Université de Lille 1

Habilitation à diriger des recherches en sciences physiques

Materials with internal contacts: theoretical and numerical studies

Matériaux à contacts internes: études théoriques et numériques

---

Document de synthèse

par

Vladislav ALESHIN

Soutenue le 12 décembre 2017 devant la commission d'examen composée de :

Rapporteur: Mr. Philippe Dufrénoy, Professeur des Universités, Université Lille1

Rapporteur: Mr. Djimédo Kondo, Professeur des Universités, Université Pierre et Marie Curie

Rapporteur: Mr. Valentin Popov, Professeur des Universités, Université Technique de Berlin

Examinateur: Mr. Alain Leger, Directeur de Recherche au CNRS (HDR), Université Bordeaux 1

Examinateur: Mr. Philippe Pernod, Professeur des Universités, Ecole Centrale de Lille

Garant de l'habilitation: Mr. Alain Merlen, Professeur des Universités, Université Lille1

Membre invité: Mr. Vladimir Preobrazhensky[1,2], [1]Professeur émérite, Ecole Centrale de Lille, [2]Institut de Physique Générale de l'Académie des Sciènes, Moscou

Content

Abstract

In this work, some mechanical and acoustic aspects related to materials with internal contacts are studied. The internal contacts here refer to a multitude of situations, in particular, when a material has some microstructure with contacting elements, consists of unconsolidated or imperfectly consolidated grains, either, finally, contains defects such as cracks, delaminations, debonding, damaged artificial joints, etc. The presence of internal contacts engenders strong nonlinear behavior and considerably modifies linear properties. In particular, in unconsolidated granular materials compressed by their own weight, contact interactions create power-law depth profiles of elastic moduli that support a specific kind of localized modes propagating along the surface in a sort on a natural waveguide (chapter 1). Further, internal contacts in imperfectly consolidated granular materials or micro-cracked materials produce significant hysteresis in the stress-strain relationship that can be attributed to adhesion- or friction-based mechanisms (chapter 2). Another case of interest is materials in which internal contacts are related to localized damage. Frictional hysteretic behavior of contact between two surfaces profiles is considered in chapter 3 from a fundamental point of view. The developed semi-analytic solution called method of memory diagrams represents an algorithmic boundary condition that has to be set at the internal boundary corresponding to a crack or delamination (implemented in chapter 4). As a result, the numerical toolbox for simulations of elastic waves or vibrations in materials with cracks of known geometry has been created. The work is concluded by a research project in which applications to nondestructive testing, to properties optimization of existing materials as well as to creation of novel materials are proposed.

Résumé

Dans ce travail, certains aspects mécaniques et acoustiques liés aux matériaux avec contacts internes sont étudiés. Les contacts internes ici se réfèrent à une multitude de situations, en particulier, lorsqu'un matériau a une microstructure avec des éléments de contact, se compose de grains non consolidés ou imparfaitement consolidés, soit, enfin, contient des défauts tels que des fissures, des délaminages ou des détachements, des joints artificiels endommagés, etc. La présence de contacts internes engendre un comportement non linéaire fort et modifie considérablement les propriétés linéaires. En particulier, dans les matériaux granulaires non consolidés comprimés par leur propre poids, les interactions de contact aboutissent à des modules élastiques qui dépendent de la profondeur selon des lois de puissance. Ces milieux supportent un type spécifique d'ondes localisées se propageant le long de la surface dans une sorte de guide d'onde naturel (chapitre 1). En outre, les contacts internes dans des matériaux granulaires imparfaitement consolidés ou dans des matériaux micro-fissurés produisent une hystérésis significative dans la relation contrainte-déformation qui peut être attribuée aux mécanismes à base d'adhésion ou de frottement (chapitre 2). Un autre cas d'intérêt est le matériau dans lequel les contacts internes sont liés à l'endommagement localisé. Le comportement hystérétique de friction de contact entre deux corps élastiques est considéré dans le chapitre 3 d'un point de vue fondamental. La solution semi-analytique développée, appelée méthode des diagrammes de mémoire, représente une condition aux limites algorithmique qui doit être posée à la frontière interne correspondant à une fissure ou à un délaminage (implémenté au chapitre 4). En conséquence, un dispositif numérique pour les simulations d'ondes élastiques ou de vibrations dans des matériaux avec des fissures de géométrie connue a été créé. Le travail est conclu par un projet de recherche dans lequel sont proposées les applications au contrôle non destructif, à l'optimisation des propriétés des matériaux existants, ainsi qu'à la création de nouveaux matériaux.

Preface

This document represents a summary of my research activities carried out between 2001-2017, after my PhD thesis defense in 2000 at the Moscow State University, faculty of physics . In 2001, I got a postdoctoral position at *Université du Maine* that allowed me to take my first steps in numerical modeling for waves in granular materials. This naturally resulted in getting into Preisach modeling, a central point of a mathematical theory for hysteresis, and, broader, into phenomenology of materials with internal contacts.

My second postdoctoral position at the *KU Leuven Campus Kortrijk* (2002-2005) was a direct continuation of work started in Le Mans. It was primarily related to consolidated materials, in particular, to wave phenomena in there, to phenomenological modeling, and to inverse problems and materials characterization. We have implemented our first ideas of nondestructive testing (NDT) on materials with microstructure as well as linear materials with localized defects (cracks, delaminations, etc). In parallel to those directions, I started a new research activity that finally became my primary area of interest - an activity related to a link between properties of microstructure or of damage and measurable characteristics such as hysteretic stress-strain curves in mechanical experiments or higher harmonics, nonlinear resonances or other indicators of acoustical nonlinearity related to internal contacts.

This question is indeed important for engineering applications such as NDT as well for from a theoretical point of view. Suppose that an experiment registered certain amount of nonlinearity in terms of a measurable response. How critical is the damage level that corresponds to that amount? Is it possible to make any lifetime predictions? The problem becomes even more challenging and significant when earlier stages of damage are concerned. Is it possible to predict failure in a safe situation far before the failure actually occurs? Finally, from a theoretical viewpoint, is it possible to attribute measurable responses to certain mechanisms and, in that sense, explain the behavior of materials with microstructure? Trying to answer these questions I found some unexplored niche that became my area of expertise and eventually my career engine.

In 2006-2007 I returned to *Université du Maine* for another postdoc related to wave phenomena in granular materials. One of the *LAUM* research school specialties is applying an advanced methodology of the classical wave theory for describing waves in granulars as much as possible without implementing detailed numerical modeling of the molecular dynamics type (account for individual beads). In 2007-2009 (*École Navale* and *ENSTA Bretagne*) my activity was devoted to underwater acoustics, in particular, to physical properties of marine sediments and to wave scattering by rough sandy sediments. I did not include those results in

the present document, but to some extent the work was along the same line: a water saturated granular material is still granular material whose properties are greatly affected by the presence of contacts between particles. The accent, however, has been made on geometric aspects of the wave-material interactions such as scattering by surface roughness. During 2007-2009 I continued to contribute into studies for mechanisms of contact nonlinearity in *KU Leuven* in the framework of a collaboration project.

Acquiring the CNRS research position in 2009 allowed me to turn back to my principal topic and realize my long-standing intention: update existing analytical solutions of contact mechanics and bring them to nonlinear acoustics and mechanics of materials. Frictional contact mechanics is a complex discipline despite the underlying physics is known since the times of Coulomb, Cauchy and Poisson; the matter is that the solutions are typically hysteretic and memory-dependent. This made my undertaking a risky business in some sense. Indeed, the success in searches for some universal rules in a tangled history-dependent contact responses is not guaranteed. Unscrambling this puzzle and finding some automated solutions was my central interest in 2009-2013. The result was the creation of the method of memory diagrams, a scheme in which all mechanical characteristics such as contact forces and displacements, surface stress distributions and local displacement distributions are expressed as a superposition of a number of basis solutions with parameters whose values depend on history. The raisin is that these parameters and, more generally, the memory in the contact system, can be presented as a simple graphic object that I named memory diagram. The memory diagram evolved following loading history in accordance to a certain set of rules. In that sense, the solution can be referred to as algorithmic analytical or semi-analytical.

These findings contributed to the creation of the MMD-FEM numerical toolbox we have developed together with Dr. Steven Delrue from KU Leuven in the framework of a European project (2012-2016) on self-healing composite materials and non destructive testing. The numerical toolbox was a principal deliverable of the theoretical workpackage intended for modeling support for nonlinear ultrasound experiments. During this period I also started to work with PhD students and to develop supervision activity.

A most intriguing question for anyone contributing into theoretical research in traditional disciplines is applications. Having a working modeling tool generally means an increased visibility of all physical processes taking place in experiments. Knowledge of the reaction of a frictional contact on acoustic or random signals, elastic waves and vibrations can be applied not only in nondestructive testing, but also in designing nonlinear acoustic metamaterials, as well as in engineering applications in transport, such as reducing friction-induced instabilities.

I am sincerely grateful to my friends and colleagues whose contribution and support are invaluable: to Vitaly Gusev, Koen Van Den Abeele, Vincent Tournat, Vladimir Zaitsev, Xavier Jacob, Laurent Guillon, Olivier Bou Matar, Steven Delrue, Vladimir Preobrazhensky, Stefano Giordano, Valentin Popov, Roman Pohrt, Michele Ciavarella, and many others. The royal "we" that I use in many instances of this document actually means nothing but a direct indication of their important participation as well as the gratitude for their presence in my scientific life.

In the main part of the manuscript describing scientific research, figures and equations are uniquely numbered as (*x*, *y*, *z*) where *x* is the chapter number, *y* is the section number, *z* is the sequential number in the section. References are marked with three first letters of the first author surname. References to publications with my co-authorship are typed in bold.

Curriculum Vitae

First and last name: Vladislav Aleshin

Date of birth: March 14, 1973

Family status: male, married

Private address: 19/02 rue Delacroix, 59493 Villeneuve d'Ascq, France

Work address: Institut d'Electronique, de Microélectronique et de Nanotechnologie, UMR CNRS 8520, Laboratoire Central Cité Scientifique, av. Poincaré CS 60069, 59652 Villeneuve d'Ascq cedex, France

Phone: (+33/0) 3 20 19 79 49 (office), (+33/0) 6 33 78 68 81 (mobile)

E-mail: **vladislav.aleshin@iemn.univ-lille1.fr, aleshinv@mail.ru**

SUMMARY: **Entered the CNRS on 1/09/2009**

Scientific interests: contact mechanics, nonlinear mechanics and acoustics, physics of materials with microstructure, NDT, numerical simulations

38 papers in peer-reviewed journals and 71 conference presentations

H-factor of 12(Google Scholar)

DIPLOMAS & DEGREES

1. **January 1996:** **M.Sc.**, Moscow State University, Faculty of Physics (graduated with honors)

   Diploma work: "Diagnostics of inhomogeneous solids by means of the laser-induced thermal waves: the inverse and stochastic problems"

2. **May 2000:** **Ph.D.**, Moscow State University, Faculty of Physics

   Thesis title: "Laser photo-thermal diagnostics of inhomogeneous solids"

RESEARCH EXPERIENCE

Oct. 2009 – current: CNRS Senior Researcher, Institute of Electronics, Microelectronics and Nanotechnology **Villeneuve d'Ascq, France**

Oct. 2008 – Oct. 2009: Associate Professor, ENSIETA (ENSTA Bretagne) **Brest, France**

Oct. 2007 – Jun. 2008: Research Engineer (fixed-term contract), Naval Academy Research Institute **Brest, France**

Jan. 2006 – Jul. 2007: CNRS Researcher (fixed-term contract), University of Maine, Laboratory of Acoustics **Le Mans, France**

Oct. 2002 – Dec. 2005: Postdoctoral researcher, Catholic University of Leuven, Campus Kortrijk **Kortrijk, Belgium**

Oct. 2001 – Aug. 2002: Postdoctoral Researcher, University of Maine, Laboratory of Acoustics **Le Mans, France**

Apr. 1996 – Jul. 2001: Research Assistant, Moscow State University, Physics Faculty **Moscow, Russia**

Jun. 1997, Oct. 1998 – Nov. 1998: Visiting research fellow at the Institute of Optics and Quantum Electronics **Jena, Germany**

TEACHING EXPERIENCE

Sep. 1996 – Jun. 2001: Teaching Assistant, Moscow State University, Physics Faculty **Moscow, Russia**

Jan. 2007 – May 2007: Teaching Assistant, University of Maine, Laboratory of Acoustics **Le Mans, France**

Mar. 2008 – June 2008: Supervising student projects at the Naval Academy Research Institute, **Brest, France**

Feb. 2009 – June 2009: Associate Professor, ENSIETA (ENSTA Bretagne) **Brest, France**

Total : 452 equivalent seminar (French *TD*) hours

SCIENTIFIC SUPERVISION[1]

Chercheur/Etudiant	Niveau	Nature	Taux	Année
Nikolay SMAGIN	postdoc	co-encadrement dans le cadre d'un projet Européen	30%	2012-2014
Kevin TRUYAERT	doctorant, KU Leuven	co-encadrement: responsable pour la partie théorique de la thèse	40%	2016-2019
Andrey TRIFONOV	doctorant, Centrale Lille,	co-encadrement: responsable	50%	2013-

[1] Partly written in French since it primarily concerns the French educational system

	soutenu le 6/04/2017	pour la partie théorique de la thèse		2016
Sergey KOSHELUK Yulia KUTLUBAEVA	doctorants en cotutelle, Moscow Technical University, soutenances prévues en 2018	co-encadrement: support en programmation scientifique, mathématiques appliquées	30%	2014-2017
Ksenia BYCHKOVA Tatiana MERZLIKINA Elena GORINENKO Margarita ZEMSKOVA	stagiaires internationales 2-4 années	support en programmation scientifique, mathématiques appliquées	30%	2015
Marjolaine VANDEPUTTE Thomas DRUCKÉ	stagiaires 1 année	responsable de stage	100%	2016
Aurélie NOÉ Emilie FERRERO	élèves 2 année	projet de voie d'approfondissement	100%	2007-2008

SCIENTIFIC PROJECTS

- **European project** ALAMSA (2012-2016), *"A life-cycle autonomous modular system for aircraft material state evaluation and restoring system"*, 10 academic and industrial partners, **function**: principal collaborator for the modeling part, writing the proposal and reports (one theoretical WP)

- **Personal project** (French *PEPS*) NONLIMETA (2015), *"Numerical laboratory for nonlinear acoustical metamaterials"*, four academic partners, **function**: project leader

- **National Research Agency (*ANR, France*) project** ANL-MEMS (2011-2013), *"Nonlinear elastic imaging techniques for MEMS reliability assessment"*, two academic partners, **function**: principal collaborator for the modeling part, writing the proposal and reports (one theoretical WP)

- ***FWO Vlaanderen* (Belgium) project** (2006-2009), *"Physical mechanisms for constitutive modeling in nonlinear elasticity and acoustics of solids with internal contacts"*, two academic partners, **function**: principal collaborator

- **Thales Underwater Systems project** (2007-2008), *"Long-range detection of buried objects"*, one industrial and one academic partners, **function**: principal collaborator

- Participation in projects (1996-2007) funded by the *ANR* (France), *Pays de la Loire* region (France), *FWO Vlaanderen* (Belgium), Russian Foundation for Fundamental Research, etc., **functions**: postdoc, PhD student

SCIENTIFIC INTERESTS

- **Contact mechanics, friction, physics of solids with microstructure and defects**
- **Elastic waves in materials**: linear and nonlinear ultrasound, nondestructive testing and material characterization, time reversal acoustics
- Applied mathematics, numerical simulations
- Laser physics, thermal physics, statistical physics, nonlinear acoustics and optics, physical fractals

OTHER ACTIVITIES

- **Member** of the French Acoustical Society, French Mechanical Society
- **Reviewer for**

Physical Review Letters	*Journal of Mechanics and Physics of Solids*
Physical Review B	*International Journal of Solids and Structures*
Physical Review E	*Journal of Acoustical Society of America*
Journal of Applied Physics	*International Journal of Non-Linear Mechanics*
Tribology Transactions	*Applied Mathematical Modelling*
Wave Motion	*Acta Acustica united with Acustica*
Ultrasonics	*European Journal of Mechanics - A/Solids*
Physical Mesomechanics	*Chaos: An Interdisciplinary Journal of Nonlinear Science*
Journal of Sound and Vibration	*Zeitschrift für Angewandte Mathematik und Mechanik*
Journal of Geophysical Research	*Geophysical Research Letters*
The Journal of Adhesion	*Iranian Journal of Science and Technology*
Facta Universitatis	*Mechanics Based Design of Structures and Machines*
ASME Journal of Tribology	*International Journal of Mechanical Sciences*

- **Book reviewer for**: Wiley
- **Expert reviewer for**: Czech Science Foundation

SPORTS AND HOBBIES: Fitness, literature

LANGUAGES: Fluent English, good French, native Russian

Publications

1. V.V. Aleshin, A.S. Chirkin. Generation of laser-induced thermal waves as a nondestructive diagnostic method. Proc. SPIE, 1995, V. 2797, p. 69.
2. V.V. Aleshin, A.S. Chirkin. Diagnostics of inhomogeneous media by means of laser-induced thermal waves: a stochastic problem Isv. RAN, seria phys., 1995, N.12, p. 55 (in Russian).
3. V.V. Aleshin, V.A. Vysloukh. Continued fraction method in inverse problem of photothermal diagnostics. Appl. Phys. A, 1997, Vol. 64(6), p. 579.
4. V.V. Aleshin, V.A. Vysloukh. On the solution of an inverse problem in photothermal diagnostics using Tikhonov's regularization method. Vestnik MGU, seria 3 (physics, astronomy), 1998, N.1, p. 35 (in Russian).
5. V. Aleshin, H.G. Walther. Inspection of inhomogeneous samples by combined laterally scanned and frequency resolved measurements. J. Appl. Phys., 1999, Vol. 86(11), p. 6512.
6. V.V. Aleshin. Inverse problem of heat capacity and thermal conductivity reconstruction in laser photothermal depth profiling. Isv. RAN, seria phys., 2000, Vol. 64, p. 2436 (in Russian).
7. V. Aleshin, H.G. Walther. Depth profiling based on laterally resolved photothermal measurements. Analytical Sciences, 2001, Vol.17, p. 402.
8. V. Gusev, V. Aleshin. Strain wave evolution equation for nonlinear propagation in materials with mesoscopic mechanical elements. J. Acoust. Soc. Am., 2002, Vol. 112(6), p. 2666.
9. V. Aleshin, V. Gusev, V. Zaitsev. Propagation of initially bi-harmonic sound waves in a 1D semi-infinite medium with hysteretic non-linearity. Ultrasonics, 2004, Vol. 42, p. 1053.
10. K. Van Den Abeele, F. Schubert, V. Aleshin, F. Windels, J. Carmeliet. Resonant bar simulations in media with localized damage. Ultrasonics, 2004, Vol. 42, p. 1017.
11. V. Aleshin, V. Gusev, V. Zaitsev. Propagation of acoustics waves of non-simplex form in a material with hysteretic quadratic nonlinearity: analysis and numerical simulations. J. Comput. Acoust., 2004, Vol. 12(3), pp. 319-354.
12. V. Aleshin, K. Van Den Abeele. Micro-potential model for stress-strain hysteresis of micro-cracked materials. J. Mech. and Phys. Solids, 2005, Vol. 53(4), p. 795.
13. V. Aleshin, K. Van Den Abeele. Micro-potential model for stress-strain hysteresis and PM space. In: The universality of nonclassical nonlinearity, with applications to NDE and Ultrasonics (chapter 11), ed. P.P. Delsanto, Springer, New York, 2006.
14. K. Van Den Abeele, S. Vanaverbeke, V. Aleshin. Multiscale approach to nonlinear and hysteretic elastodynamics in one- and two dimensions. In: The universality of nonclassical nonlinearity, with applications to NDE and Ultrasonics (chapter 9), ed. P.P. Delsanto, Springer, New York, 2006.
15. V. Gusev, V. Aleshin, V. Tournat. Acoustic waves in an elastic channel near the mechanically free surface of granular media. Phys. Rev. Lett., 2006, Vol. 96, 214301.
16. V. Aleshin, K. Van Den Abeele. Microcontact-based theory for acoustics in microdamaged materials. J. Mech. and Phys. Solids, 2007, Vol. 55, pp. 366-390.
17. V. Aleshin, K. Van Den Abeele. Friction in unconforming grain contacts as a mechanism for tensorial stress-strain hysteresis. J. Mech. and Phys. Solids, 2007, Vol.55, pp. 765-787.
18. V. Aleshin, V. Gusev, V. Tournat. Acoustic modes propagating along the free surface of granular media. J. Acoust. Soc. Am., 2007, Vol. 121 (5), pp. 2600-2611.
19. V. Aleshin, W. Desadeleer, K. Van Den Abeele. Characterization of hysteretic elasticity in materials using the integrated Preisach density. Int. J. Nonlin. Mech., 2008, Vol. 43, pp. 151-163.
20. V.E. Gusev, V. Aleshin, V. Tournat. Reflection of nonlinear acoustic waves at the mechanically free surface of an unconsolidated granular medium. Acustica-Acta-Acustica, 2008, Vol. 94, pp. 215-228.
21. X. Jacob, V. Aleshin, V. Tournat, P. Leclaire, W. Lauriks, V. E. Gusev. Acoustic probing of the jamming transition in an unconsolidated granular medium. Phys. Rev. Lett., 2008, Vol. 100, 158003.
22. V. Aleshin, K. Van Den Abeele. Preisach analysis of the Hertz-Mindlin system. J. Mech. and Phys. Solids, 2009, Vol. 57, 657–672.
23. V. Aleshin, L.Guillon. Modeling of acoustic penetration into sandy sediments: physical and geometrical aspects. J. Acoust. Soc. Am., 2009, Vol. 126 (5), pp. 2206-2214
24. V. Aleshin, K. Van Den Abeele. Frictional contact of two spheres for arbitrary 2D loading: memory diagrams and Preisach analysis. Proceedings of Meetings on Acoustics, 2011, Vol. 13, 045004.
25. V. Aleshin, K. Van Den Abeele. Hertz-Mindlin problem for an arbitrary oblique 2D loading. General solution by memory diagrams. J. Mech. and Phys. Solids, 2012, Vol. 60, pp. 14-36.
26. V. Aleshin, K. Van Den Abeele. General solutions to the mechanical contact problem. Proceedings of Meetings on Acoustics, 2012, Vol. 16, 045012.
27. K. Van Den Abeele, S. Delrue, S. Haupert, V. Aleshin. Modeling nonlinear response from distributed damage and kissing bonds. Proceedings of Meetings on Acoustics, 2012, Vol. 16, 045020.
28. V. Aleshin, K. Van Den Abeele. General solution to the Hertz-Mindlin problem via Preisach formalism. Int. J. Non-Linear Mech, 2013, Vol. 49, 15–30.

29. G.Sh. Boltachev, V. Aleshin. Shift and torsion contact problems for arbitrary axisymmetric normal stress distributions. Int. J. Sol. Struct., 2013, Vol. 50, 2894–2900.
30. V. Aleshin, O. Bou Matar, K. Van Den Abeele. Method of memory diagrams for mechanical frictional contacts subject to arbitrary 2D loading. Int. J. Sol. Struct., 2015, Vol. 60-61, 84-95.
31. V. V. Aleshin, O. Bou Matar. Solution to the frictional contact problem via the method of memory diagrams for general 3D loading histories. Physical Mesomechanics, 2016, Vol. 19, 130-135.
32. V.V. Aleshin, O. Bou Matar Contact mechanical problem for arbitrary 3D loading histories. In: High Performance and Optimum Design of Structures and Materials II, 2017, 467-478.
33. S. Delrue, V. Aleshin, M. Sorensen, L. De Lathauwer. Simulation study of the localization of a near-surface crack using an air-coupled ultrasonic sensor array. Sensors, 2017, Vol. 17 (4), 1-21.
34. V.L. Preobrazhensky, V.V. Aleshin P. Pernod. Resonance of Feshbach-type and explosive instability of magnetoelastic waves in solids. Wave Motion, submitted.
35. V.V. Aleshin, S. Delrue, A. Trifonov, O. Bou Matar, K. Van Den Abeele. Two dimensional modeling of elastic wave propagation in solids containing cracks with rough surfaces and friction - Part I: Theoretical background. Ultrasonics, 2018, Vol. 82, 11-18.
36. S. Delrue, V.V. Aleshin, K. Truyaert, O. Bou Matar, K. Van Den Abeele. Two dimensional modeling of elastic wave propagation in solids containing cracks with rough surfaces and friction – Part II: Numerical implementation. Ultrasonics, 2018, Vol. 82, 19-30.
37. V.V. Aleshin, S. Delrue, K. Van Den Abeele, O. Bou Matar. Nonlinear and hysteretic constitutive models for wave propagation in solid media with cracks and contacts. In: Nonlinear Acoustic Techniques for Nondestructive Evaluation (chapter 5), ed. T. Kundu, Springer, in press.
38. V.V. Aleshin, K. Van Den Abeele. Preisach description for solids with frictional cracks. Int. J. Nonlin. Mech., submitted.

Conferences

1. V.V. Aleshin, A.A. Kalinovskii, A.S. Chirkin, “Generation of laser-induced thermal waves as a nondestructive diagnostic method.” 15th International Conference on Coherent and Nonlinear Optics, 1995, St. Petersburg, Russia.
2. V.V. Aleshin, A.S. Chirkin. Inverse problem in laser photothermal diagnostics of inhomogeneous medium. International Conference on Computer Methods and Inverse Problems in Nondestructive Testing and Diagnostics, 1996, Minsk, Belarus.
3. V.V. Aleshin, V.A. Vysloukh, A.S. Chirkin. Continued fraction method in the inverse problem of photothermal diagnostics. 5th Russian School-Seminar "Wave Phenomena in Inhomogeneous Media",1996 , Krasnovidovo, Moscow reg., Russia.
4. V.V. Aleshin. Algorithms for solving 1D inverse problem in phothothermal diagnostics. 6th Russian School-Seminar "Wave Phenomena in Inhomogeneous Media", 1998, Krasnovidovo, Moscow reg., Russia.
5. H.G. Walther, T.T.N. Lan, V. Aleshin. Reconstruction of thermal conductivity depth profiles from photothermal measurements. 3rd International Workshop - Advances in Signal Processing for NDE of Materials, 1997, Quebec City, Canada.
6. M. Bertolotti, R. Li Voti, G.L. Liakhou, S. Paoloni, C. Sibilia, V. Aleshin, H.G. Walther. Depth profiling using laterally resolved photothermal measurements applied for the estimation of steel hardness profiles. 10th International Conference "Photoacoustic and Photothermal Phenomena", Rome, Italy, 1998.
7. H.G. Walther, V. Aleshin. Steel hardness inspection by laterally scanned and frequency resolved infrared radiometric measurements. 5th International Workshop on Advanced Infrared Technology and Applications, Venice, 1999.
8. H.G. Walther, V. Aleshin, M.C. Larciprete. Feasibility of photothermal depth profiling discussed for hardness measurements. Gordon Research Conference on Photoacoustic and Photothermal Phenomena, 1999, New London, USA.
9. V.V Aleshin. Heat capacity and thermal conductivity profiles' reconstruction in laser photothermal depth profiling of inhomogeneous solids. 7th Russian School-Seminar "Wave Phenomena in Inhomogeneous Media ", 2000, Krasnovidovo, Moscow reg., Russia.
10. H.G. Walther, V. Aleshin. Depth profiling based on laterally resolved photothermal measurements Proc. of 11th International Conference on Photothermal and Photoacoustic Phenomena, 2000, Kyoto, Japan.
11. V. Tournat, V. Aleshin, V.E. Gusev, B. Castagnède. Experimental investigations of parametric antenna operation in granular materials, 16th International Symposium on Nonlinear Acoustics, 2002, Moscow, Russia.
12. V. Aleshin, V. Gusev, V. Zaitsev. Propagation of initially bi-harmonic acoustic signals in materials with hysteretic quadratic nonlinearity. Ultrasonics International, 2003, Granada, Spain.
13. K. Van Den Abeele, F. Schubert, V. Aleshin, F. Windels, J. Carmeliet. Resonant bar simulations in media with localized damage. Ultrasonics International, 2003, Granada, Spain.

14. K. Van Den Abeele, F. Schubert, V. Aleshin. Modeling of wave distortion phenomena in media with localized microdamage. 5th World Congress on Ultrasonics, 2003, Paris, France.
15. V. Aleshin, K. Van Den Abeele. Micro-potential model for acoustical hysteresis. 18th International Congress on Acoustics, 2004, Kyoto, Japan.
16. V. Aleshin, K. Van Den Abeele. Micro-potential models for stress-strain hysteresis of microcracked media. 9th International Workshop on Nonlinear Elasticity in Materials, 2004, Karlskrona, Sweden.
17. V. Aleshin, K. Van Den Abeele. Micro-potential model for elasticity of hysteretic materials. 6th International Congress on Mathematical Modeling, 2004, Nizhni Novgorod, Russia.
18. V. Aleshin, K. Van Den Abeele. Micro-level based constitutive equations in elasticity and acoustics of materials with internal contacts. 12th International Congress on Sound and Vibration, 2005, Lisbon, Portugal.
19. V. Aleshin, K. Van Den Abeele. Physical constitutive equations for nonlinear acoustics of materials with internal contacts. 17th International Symposium on Nonlinear Acoustics, 2005, State College, Pennsylvania, USA.
20. V. Aleshin, K. Van Den Abeele. Microcontact-based theory for acoustics in microdamaged materials. 10th International Workshop on Nonlinear Elasticity in Materials, 2005, Taormina, Italy.
21. V. Aleshin, W. Desadeleer, M. Wevers, K. Van Den Abeele. Integrated Preisach density as a characterisation for rocks. 10th International Workshop on Nonlinear Elasticity in Materials, 2005, Taormina, Italy.
22. K. Van Den Abeele, S. Vanaverbeke, V. Aleshin. NEWS Nonlinear Elastic Wave Spectroscopy: Modeling nonlinear and hysteretic constitutive material behavior and nonlinear wave dynamics. Workshop on Advanced Ultrasonic Methods For Studies Of Materials, 2005, Bydgoszcz, Poland.
23. V. Aleshin, K. Van Den Abeele. Adhesion hysteretic mechanism for nonlinear acoustics of solids with internal contacts. 8ème Congrès Français d'Acoustique, 2006, Tours, France.
24. V. Gusev, V. Aleshin, V. Tournat. Dispersion des ondes acoustiques transverses horizontales en sub-surface de milieux granulaires non consolidés. 8ème Congrès Français d'Acoustique, 2006, Tours, France.
25. V. Gusev, V. Aleshin, V. Tournat. Réflexion en incidence normale d'ondes acoustiques non linéaires par la surface libre horizontale d'un milieu granulaire non consolidé. 8ème Congrès Français d'Acoustique, 2006, Tours, France.
26. V. Aleshin. Physical stress-strain constitutive equations for materials with internal contacts. Workshop (GDR 2501) “Study of Ultrasonic Propagation from an NDT Perspective”, 2006, Giens, France.
27. V. Aleshin. Adhesion and friction models for nonlinear elasticity of materials with internal contacts. International colloquium devoted to 25 years anniversary of Le Mans Laboratory of Acoustics, 2006, Le Mans, France.
28. V. Aleshin, K. Van Den Abeele. Physical friction-based model for a tensorial description of stress-strain in materials with internal contacts. 11th International Workshop on Nonlinear Elasticity in Materials, 2006, Sorrento, Italy.
29. V. Gusev, V. Aleshin, V. Tournat. Acoustic waves in an elastic channel near the free surface of a granular medium. Dygram 2006 Workshops: Granular Dynamics, Jamming, Rheology, and Instabilities, 2006, Rennes, France.
30. C. Inserra, V. Tournat, V. Aleshin, V. Gusev, B. Catagnède. On some aspects of acoustic diagnostics of unconsolidated granular media. 4th International Conference on Emerging Technologies in Non-Destructive Testing, 2007, Stuttgart, Germany.
31. P. Leclaire, X. Jacob, V. Aleshin, V. Tournat, O. Dazel, J.-F. Allard, W. Lauriks, V. Gusev. Guided acoustic modes for testing surface layers of unconsolidated granular media. 4th International Conference on Emerging Technologies in Non-Destructive Testing, 2007, Stuttgart, Germany.
32. V. Aleshin, K. Van Den Abeele. Constitutive models for solids containing rough cracks: from micro to macro. 4th International Conference on Emerging Technologies in Non-Destructive Testing, 2007, Stuttgart, Germany.
33. V. Aleshin, K. Van Den Abeele. Constitutive models for nonlinear elasticity in materials with microstructure. Ecole Thématique “Acoustique et Ondes Non Linéaires et Applications”, 2007, Oléron, France.
34. V. Tournat, V. Gusev, V. Aleshin, X. Jacob et C. Inserra. Acoustique non linéaire et milieux granulaires. École Thématique “Acoustique et Ondes Non Linéaires et Applications”, 2007, Oléron, France.
35. X. Jacob, V. Tournat, V. Aleshin, V. Gusev. Evaluation of the mechanical properties of granular media at low pressures. International Congress on Acoustics, 2007, Madrid, Spain.
36. P. Leclaire, V. Tournat, O. Dazel, V. Aleshin W. Lauriks, J.F. Allard, V. Gusev. Guided acoustic waves near the free surface of unconsolidated granular materials. International Congress on Acoustics, 2007, Madrid, Spain.
37. V. Tournat, V. Gusev, X. Jacob, C. Inserra, V. Aleshin. Linear and nonlinear acoustic waves in unconsolidated granular media: opportunities for new fundamental wave processes and quantitative evaluation. Statics and Dynamics of Granular Media and Colloidal Suspensions, 2007, Naples, Italy.

38. X. Jacob, V. Aleshin, V. Tournat, P. Leclaire, W. Lauriks, V. Gusev. Acoustic waves propagation along mechanically free surface of unconsolidated granular porous media. Acoustics'08, 2008, Paris, France.
39. L. Guillon, V. Aleshin. Analysis of acoustical transmission and reflection from a sandy stratified rough sediment using the grain shearing model. Acoustics'08, 2008, Paris, France.
40. V. Aleshin, K. Van Den Abeele. Is there physics behind the PM-space? 14th International Conference on Nonlinear Elasticity in Materials, 2009, Lisbon, Portugal.
41. V. Aleshin, L. Guillon. Statistical analysis of acoustical scattering by rough sandy marine sediments. 3rd International Conference and Exhibition “Underwater Acoustic Measurements: Technologies and Results”, 2009, Nafplion, Greece.
42. V. Aleshin, L. Guillon, A. Khenchaf. Penetration of sound into rough marine sediments: numerical analysis and statistics. 11th Experimental Chaos and Complexity Conference, 2010, Lille, France
43. V. Aleshin, K. Van Den Abeele. General solutions to the contact problem of two spheres with friction. 15th International Conference on Nonlinear Elasticity in Materials, 2010,Otranto, Italy.
44. V. Aleshin, K. Van Den Abeele. Frictional contact of two spheres for arbitrary 2D loading. 20ème Congrès Français de Mécanique, 2011, Besançon, France.
45. S. Giordano, Y. Dusch, N. Tiercelin, A. Talbi, O. Bou Matar, V.V. Aleshin, A. Merlen, V.L. Preobrazhensky, P. Pernod. Magnetic particle embedded in a piezoelectric matrix: analysis and applications. 20ème Congrès Français de Mécanique, 2011, Besançon, France.
46. V. Aleshin, K. Van Den Abeele. Frictional contact of two spheres for arbitrary 2D loading: memory diagrams and Preisach analysis. 16th International Conference on Nonlinear Elasticity in Materials, 2011, Prague, Czech Republic.
47. V. Aleshin. Contact mechanics based on Preisach analysis. GDRE workshop "Wave Propagation in Complex Media for Quantitative and Non Destructive Evaluation", 2012, Nice, France.
48. V. Aleshin. On the origin of the contact acoustical nonlinearity: general solutions to the mechanical contact problem. GDRE workshop "Nonlinearities in acoustics, specially contact nonlinearities", 2012, Oleron, France.
49. V. Aleshin. General solutions to the mechanical contact problem. GDR MePhy workshop, 2012, Agay, France.
50. V. Aleshin. Frictional contact of solids of arbitrary shapes with arbitrary loading histories. 17th International Conference on Nonlinear Elasticity in Materials, 2012, Cefalu, Italy.
51. K. Van Den Abeele, V. Aleshin, Modeling nonlinear response from distributed damage and kissing bonds (localized damage). 17th International Conference on Nonlinear Elasticity in Materials, 2012, Cefalu, Italy.
52. V. Aleshin, K. Van Den Abeele, O. Bou Matar. On general solutions to the mechanical contact problem with friction: extending the method of memory diagrams. 18th International Conference on Nonlinear Elasticity in Materials, 2013, Ascona, Switzerland.
53. O. Bou Matar, P.-Y. Guerder, H. Zhou, V. Aleshin. Nonlinear elastodynamic simulations using the Discontinuous Galerkin Finite Element Method on graphics processors. 18th International Conference on Nonlinear Elasticity in Materials, 2013, Ascona, Switzerland.
54. O. Bou Matar, V. Aleshin, A. Talbi, H. Zhou, N. Chigarev, V. Gusev, C. Ni, V. Tournat. ANL-MEMS: Techniques d'imagerie acoustique non linéaire pour l'étude de la fiabilité des MEMS. Journées Nationales en Nanosciences et Nanotechnologies, J3N 2013, 2013, Marseille, France.
55. V. Aleshin, O. Bou Matar. Elastic frictional contact problem for arbitrary surface shapes and arbitrary 2D loading history: method of memory diagrams. Contact Mechanics International Symposium, 2014, Abu Dhabi, United Arab Emirates.
56. N. Smagin, A. Trifonov, O. Bou-Matar, V. Aleshin. Time reversal coda wave mixing technique for nonlinear defects' localization. 19th International Conference on Nonlinear Elasticity in Materials, 2014, Fréjus, France.
57. V. Aleshin. Method of memory diagrams for solving frictional contact problems in 3D. 19th International Conference on Nonlinear Elasticity in Materials, 2014, Fréjus, France.
58. V. Aleshin. Method of memory diagrams for solving frictional contact problems and its application to materials with contact nonlinearity. Workshop on Advances in Tribology: Science, Technology and Education, 2015, Karlovy Vary, Czech Republic.
59. V.V. Aleshin, O. Bou Matar. Contact mechanical problem for arbitrary 3D loading histories. 12th International Conference on Surface Effects and Contact Mechanics, 2015, Valencia, Spain.
60. V. Aleshin. Frictional contact of solids subject to arbitrary loading history in 3D. GDR MePhy workshop, 2015, Agay, France.
61. V. Aleshin, O. Bou Matar. Contact mechanical models for nonlinear elasticity in materials. 20th International Conference on Nonlinear Elasticity in Materials, 2015, Bruges, Belguim.
62. O. Bou Matar, A. Trifonov, V. Aleshin. Modeling elastic wave propagation in a solid with distributed damage and kissing bonds using the Discontinuous Galerkin Finite Element Method. 20th International Symposium on Nonlinear Acoustics, 2015, Lyon, France

63. A. Trifonov, O. Bou Matar, N. Smagin, V. Aleshin. Coda wave interferometry technique for nonlinear defects' localization in composite plates. 20th International Symposium on Nonlinear Acoustics, 2015, Lyon, France
64. V. Aleshin. Modeling for nonlinear acoustic metamaterials based on contact nonlinearity. GDR META workshop, 2016, Cargèse, France.
65. S. Delrue, V. Aleshin, O. Bou Matar, K. Van Den Abeele. Modeling of elastic wave propagation in samples containing cracks with friction. 21th International Conference on Nonlinear Elasticity in Materials, 2016, Lake Tahoe, California, USA.
66. S. Delrue, V. Aleshin, O. Bou Matar, K. Van Den Abeele. 2D modeling of elastic wave propagation in solids containing closed cracks with friction. COMSOL Conference 2016 Munich, 2016, Munich, Germany.
67. V. Aleshin, S. Delrue, O. Bou Matar, K. Van Den Abeele. Modelling of acoustic waves and vibrations in materials containing frictional cracks with rough faces. Workshop "New Mathematics for a Safer World: Wave Propagation in Heterogeneous Materials", 2017, Edinburgh, UK.
68. S. Delrue, V. Aleshin. Numerical code for describing acoustic wave propagation in solids containing cracks of known geometry. 24th International Congress on Sound and Vibration, 2017, London, UK.
69. V.L. Preobrazhensky, V.V. Aleshin, P. Pernod. Feshbach resonance and explosive instability of magnetoelastic waves. 24th International Congress on Sound and Vibration, 2017, London, UK.
70. S. Delrue, V. Aleshin. 2D modeling for acoustic waves in solids with frictional cracks. 23ème Congrès Français de Mécanique, 2017, Lille, France.
71. V.L. Preobrazhensky, V.V. Aleshin, P. Pernod. Explosive instabilities of acoustic waves propagating in antiferromagnets under magnetic and elastic pumping. 23ème Congrès Français de Mécanique, 2017, Lille, France.

Scientific Research

Introduction

It is reasonably safe to state that pure, uniform and regular materials are exceptional in common life. 99% of the time mankind produces, treats and uses materials which have impurities, irregularities, inclusions, defects etc., which are inherent properties of their microstructure. Internal defects can be roughly categorized in three types: 1D dislocations, 2D internal contacts and 3D pores, voids, etc. Amongst these, the second type is the most essential in terms of material performance, since the presence of internal contacts manifests itself in the most drastic way. Indeed, influence of dislocations is negligible if we speak about seismology or building constructions, whereas pores and voids usually contribute to the most interesting material properties much less than cracks and contacts do (e.g., failure loads, acoustic and static nonlinearities, sound attenuation, etc). This makes solids with internal contacts to be an extremely important class of materials, and justifies the fact that an accurate description of their mechanical properties is critical.

Most typical examples of materials with internal contacts are unconsolidated granular materials in which the only physical link between the constituents (grains) is through internal contacts, and consolidated materials in which there exist a solid matrix whose properties are modified by the presence of contacts. In the latter class, it turn, two groups can be distinguished. In some materials, internal contacts are present as an inherent part of their structure (consolidated grainy materials such geomaterials or building construction materials). Generally speaking, all solids that are not single crystals can be regarded as materials with inherent random structure at a mesoscopic scale, i.e., a scale which significantly exceeds the atomic size but is still small compared to macroscopic dimensions. Finally, there are solids in which internal contacts appear as defects (cracks, delaminations, etc.). Studies for materials of this class form a basis for theories underlying nondestructive testing (NDT) techniques.

Research activities presented here are grouped around three major topics: unconsolidated granular materials (chapter 1), consolidated materials with internal contacts (chapter 2), and fundamental solutions to frictional mechanical problems (chapter 3) applied (chapter 4) for modeling wave propagation in structures with frictional contacts. Studies summarized in this document are unified by a general approach that can be briefly characterized as "description-explanation-creation". The description phase means that we consider a material with postulated properties and try to simulate processes and effects occurring due to the accepted material model. An example is given in chapter 1 in which

localized acoustic modes in a granular material compressed by its own weight are found. We study the waveguide effect appearing due to reflection from deeper and more rigid material layers but do pretend to answer the question about mechanisms responsible for a particular shape of the gravity-induced elastic moduli profiles. Sections 2.1-2.5 of chapter 2 about consolidated materials with internal contacts are written in accordance to the same principle. We introduce simple or more advanced constitutive models, solve wave propagation and standing wave problems in materials with a postulated model, try to retrieve model parameters from data, etc.

Attempts to attribute the revealed effects to some physical mechanisms such as crack bistability due to adhesion (section 2.6), adhesion hysteresis (section 2.7), friction (section 2.8) are discussed at the end of chapter 2 concluded by a comparison of the proposed physical models section 2.9). This part refers to the "explanatory" phase of the general approach whose objective is to contribute to understanding of the known behaviors of materials with internal contacts. Chapter 3 is entirely devoted to the explanatory phase and introduces two fundamental solutions to the frictional contact problem in mechanics; we build up a force-displacement relationship for this memory-dependent, hysteretic problem suitable for an arbitrary loading history and a wide range of contact geometries. In chapter 4, the fundamental solutions derived in chapter 3 are used as boundary conditions for the wave propagation problem in materials containing internal contacts. The corresponding numerical tool based on finite element modeling is also presented.

The next part of the document ("Positioning the research in the laboratory context") describes the impact of the developed explanatory models onto NDT techniques being elaborated in our LISC/LEMAC group in the frameworks of national and European projects.

Finally, the concluding part of the manuscript outlines the research project that can be referred to the "creation" phase. In particular, the project exploits the idea of creation of nonlinear acoustic metamaterials based on strong and controllable contact nonlinearity. Another suggestion is to produce a tunable material exhibiting a giant acoustical instability fed by magnetic pumping. At the same time, the tool elaborated in this work can be used to prevent harmful instabilities induced by friction and therefore contribute to creation of “silent” machinery and transport vehicles. The research project is an open part whose objective is to seek for collaboration in practical spheres, especially the ones designated as priorities by I-SITE science management concept recently introduced in France.

1. Guided waves in unconsolidated granular materials

1.1. General remarks

Unconsolidated granular materials represent an important class of materials with internal contacts. A central feature of this class is the absence of an elastic matrix in which contacts could be embedded. Behavior of grains in a material is impacted by two major factors: contact forces and gravity. More precisely, the interaction mechanism is unique - contact forces only, - while the gravity just modifies the forces by adding a constant level depending on a vertical coordinate of a current particle. Contact forces in granular materials form a complicated, highly inhomogeneous and highly mobile network [Mue-98] that can be visualized via modern optical methods. The mobility of grains strongly affects the materials behavior and results in extremely reach dynamic effects whose typical manifestations are formation of complex surface patterns [Dro-04], segregation of grains [Gol-09] with different properties, etc.

In comparison with consolidated materials studied below, the unconsolidated granulars show even more complex behavior despite their internal structure can be very simple and contain, for instance, just identical elastic spheres. This fact suggests using purely numerical approaches such as methods of the molecular dynamics class [Hin-05] in which each bead is simulated individually, and the number of degrees of freedom in the system is extremely high. The strength of the approach is in the possibility to imitate a wide range of dynamic effects and make a detailed prediction for material's evolution. The associated weakness is that a detailed simulation does not contribute much to our physical understanding of material's behavior.

In this chapter, we try to advance a different, more traditional approach based on solving wave equations in a material with given properties originating from experiments and theoretical modeling. We describe guided surface acoustical modes that exist near the surface of an unconsolidated granular material compressed by its own weight. The results were published in **[Ale-07e], [Gus-06a], [Gus-06b], [Gus-06c], [Jac-07], [Jac-08a], [Jac-08b], [Lec-07a], [Lec-07b], [Tou-04], [Tou-07a]**, and **[Tou-07b]**.

1.2. Theory of the guided surface acoustical modes

Basic equations

Acoustical modes we are looking for can be polarized in the vertical (saggital) (see Fig. 1.2.1) plane or they can have horizontal polarization (shear horizontal model). Out interest here is to

the case of vertical polarization since it is more suitable for experimental detention via laser vibrometry. We use the continuous medium approximation in which the specific properties of an unconsolidated granular material under gravity are given just as depth profiles of its rigidity. The typical depth (or pressure) dependence measured experimentally at high pressures [Sac-80] and obtained numerically at low pressures [God-90] has the power form:

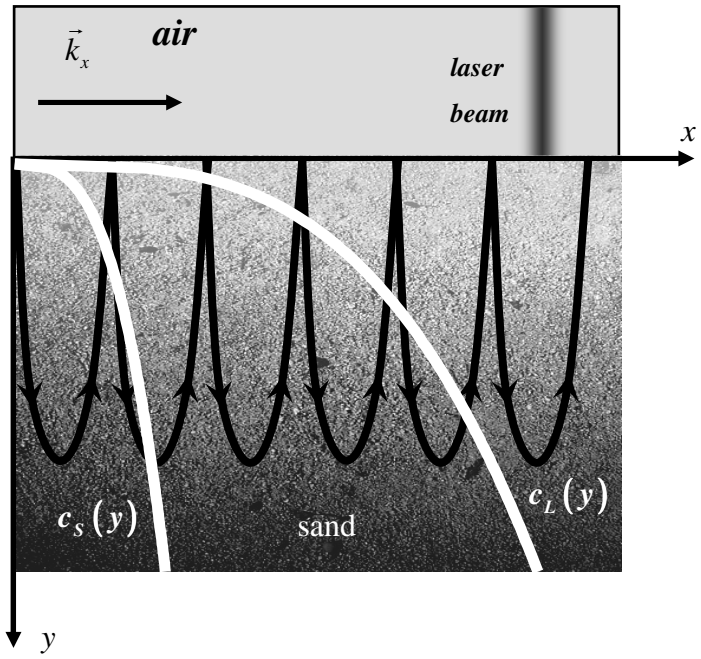

Fig. 1.2.1. Geometry of the problem. Sound velocity (in fact, elastic moduli) profiles are shown in white. Black curves illustrate rays paths for waves continuously reflected from deeper (more rigid) layers of the granular material.

$$c_L(y) = \gamma_L (\rho g y)^{\alpha_L}, \quad c_S(y) = \gamma_S (\rho g y)^{\alpha_S}, \tag{1.2.1}$$

where exponents α_L and α_S are important parameters related to the state of the granular material and γ_L and γ_S are coefficients.

A system of two Helmholtz equations for the coupled horizontal u_x and vertical u_y complex amplitude components of the displacement vector

$$\vec{U} = \{u_x(y), u_y(y)\} e^{i\omega t - ikx} \tag{1.2.2}$$

reads:

$$\begin{aligned} \left(c_S^2 u_x'\right)' + \left(\omega^2 - c_L^2 k^2\right) u_x &= ik\left[\left(c_L^2 - 2c_S^2\right) u_y' + \left(c_S^2 u_y\right)'\right] \\ \left(c_L^2 u_y'\right)' + \left(\omega^2 - c_S^2 k^2\right) u_y &= ik\left[c_S^2 u_x' + \left(\left(c_L^2 - 2c_S^2\right) u_x\right)'\right] \end{aligned}, \tag{1.2.3}$$

where primes denote the y-derivatives. The third amplitude component u_z of the total displacement is the shear horizontal wave that is governed by a similar Helmholtz equation [Ale-07e] and is not considered here.

The boundary conditions correspond to the absence of stress at the surface

$$\left[c_S^2(y)\left(u_x' - iu_y\right)\right]\Big|_{y=0} = 0,\ \left[c_L^2(y)u_y' - i\left(c_L^2(y) - 2c_S^2(y)\right)u_x\right]\Big|_{y=0} = 0, \tag{1.2.4a}$$

vanishing of the wave displacements at infinity (localization)

$$u_{x,y}\Big|_{y\to\infty} = 0, \tag{1.2.4b}$$

and the choice of normalization for the displacement:

$$u_x\Big|_{y=0} = 1 \quad . \tag{1.2.4c}$$

Substitution of Eq. (1.2.1) into Eq. (1.2.3) and substitution $i\,u_y \to u_y$ provide the following form of the Helmholtz equations:

$$\begin{aligned}
&\left(y^{2\alpha_S}u_x'\right)' + \left(\Omega^2 - \delta y^{2\alpha_L}\right)u_x = \left(\delta y^{2\alpha_L} - 2y^{2\alpha_S}\right)u_y' + \left(y^{2\alpha_S}u_y\right)' \\
&\delta\left(y^{2\alpha_L}u_y'\right)' + \left(\Omega^2 - y^{2\alpha_S}\right)u_y = -y^{2\alpha_S}u_x' - \left(\left(\delta y^{2\alpha_L} - 2y^{2\alpha_S}\right)u_x\right)'
\end{aligned} \tag{1.2.5}$$

written here for the normalized on the inverse wave number k^{-1} depth y: $y \to ky$. If the wave number k is considered known and the frequency ω is unknown, then the introduced in Eq. (1.2.5) parameter

$$\delta = \frac{\gamma_L^2}{\gamma_S^2}\left(\frac{\rho g}{k}\right)^{2\alpha_L - 2\alpha_S} \tag{1.2.6}$$

is known, and the unknown normalized frequency

$$\Omega = \frac{\omega}{\gamma_S k}\left(\frac{k}{\rho g}\right)^{\alpha_S} \tag{1.2.7}$$

has to be calculated through the solution of the eigen problem Eq. (1.2.5) with the appropriate boundary conditions derived from Eqs. (1.2.4a), (1.2.4b), (1.2.4c). The corresponding numerical algorithm has been developed [Ale-07e] which provides the shapes of the eigen functions (modes) $u_{x,y}(y)$ and dispersion parameter Ω. The latter gives the dispersion relationship in the form of the rewritten Eq. (1.2.7):

$$\omega = \Omega\gamma_S\left(\rho g\right)^{\alpha_S} k^{1-\alpha_S}. \tag{1.2.8}$$

Fast and slow waves

Although the numerical algorithm allows one to calculate all modal shapes and dispersion curves with any desired precision, for theoretical understanding of the problem it is meaningful to consider analytically the limit $c_L \gg c_S$ (i.e. $\delta \gg 1$) and show the existence of two

different mode types: fast and slow. Later on we will see from the analysis of the experimental data that this assumption is fulfilled with a reasonable accuracy (δ≈4.7-4.8).

First of all, the introduction of $\operatorname{div}\vec{u} = -iku_x + u_y'$ in the dimensional variables or $i\operatorname{div}\vec{u} = u_x + u_y'$ in the normalized variables of Eq. (1.2.5) allows us to rewrite Eq. (1.2.5) in the equivalent form:

$$\begin{aligned} \Omega^2 u_x &= \delta y^{2\alpha_L} i\operatorname{div}\vec{u} + \left(y^{2\alpha_S}\right)' u_y - y^{2\alpha_S} u_y' - \left(y^{2\alpha_S} u_x'\right)' \\ \Omega^2 u_y &= -\left(\delta y^{2\alpha_L} i\operatorname{div}\vec{u} - y^{2\alpha_S} u_x\right)' + y^{2\alpha_S} u_y + \left(y^{2\alpha_S}\right)' u_x \end{aligned} . \qquad (1.2.9)$$

where $i\operatorname{div}\vec{u}$ is a real value, or just $\Omega^2 u_x = L + S_1$ and $\Omega^2 u_y = -L' + S_2$ with

$$\begin{aligned} L &= \delta y^{2\alpha_L} i\operatorname{div}\vec{u} \\ S_1 &= \left(y^{2\alpha_S}\right)' u_y - y^{2\alpha_S} u_y' - \left(y^{2\alpha_S} u_x'\right)' . \\ S_2 &= \left(y^{2\alpha_S} u_x\right)' + y^{2\alpha_S} u_y + \left(y^{2\alpha_S}\right)' u_x \end{aligned} \qquad (1.2.10)$$

Similarly to [Cha-01] we formally calculate the limit δ»1 in these equations having in mind that the result actually depends on the behavior of the *L*-term containing only the longitudinal velocity compared to the $S_{1,2}$-terms that depend on the shear velocity only. Correspondingly, three cases are possible:

1. *L*-term is much greater than *S*-terms i.e. $|L| \gg |S_1|$ and $|L'| \gg |S_2|$;
2. *L*-term is much smaller than *S*-terms i.e. $|L| \ll |S_1|$ and $|L'| \ll |S_2|$;
3. At least one of the *S*-terms is comparable to the *L*-term i.e. $|L| \sim |S_1|$ or $|L'| \sim |S_2|$.

The second case is obviously impossible since if we neglect *L* in Eq. (1.2.9), this will produce three nontrivial differential equations for two functions u_x and u_y: two Eqs. (1.2.9) together with the equation $i\operatorname{div}\vec{u} = u_x + u_y' = 0$. In the two other cases we obtain, exactly as shown in [Cha-01], so-called fast and slow seismo-acoustic waves.

In the first case the *L*-term is high enough so that the terms $S_{1,2}$ containing the velocity c_S in Eq. (9) can be neglected:

$$\begin{aligned} \Omega^2 u_x &= i\delta y^{2\alpha_L} \operatorname{div}\vec{u} \\ \Omega^2 u_y &= -\left(i\delta y^{2\alpha_L} \operatorname{div}\vec{u}\right)' , \end{aligned}$$

or, returning back to the displacement vector $\vec{U}$ using Eq. (1.2.2):

$$\frac{\partial^2 \vec{U}}{\partial t^2} = \operatorname{grad}\left(c_L^2 \operatorname{div}\vec{U}\right). \qquad (1.2.11)$$

This equation, together with the appropriate boundary conditions that can be easily derived from Eqs. (1.2.4a)-(1.2.4c), describes the localized waves propagating along the surface with a high velocity comparable to c_L and called therefore fast waves. These modes are actually compressive since no dependence of the shear wave velocity c_S is present in Eq. (1.2.11). The ray path for such waves is shown in Fig. 1.2.1: the rays approach the surface almost normally **[Ale-07e]**, so that the vertical displacement component for these compressive waves is much higher then the horizontal one and is therefore easily detectable by normal laser incidence. In addition, in our experiments vibrating plate or rod oscillates mainly in the *x*-directions and essentially excites the longitudinal wave component.

In the last case, $L \equiv \delta y^{2\alpha_L} i \operatorname{div} \vec{u}$ is of order of S_1 or L' is of order of S_2. Since δ is high, the divergence itself is quite small and such modes closely resemble waves in an incompressible liquid. This situation can be can be considered by taking $u_x \approx -u_y'$ everywhere in Eqs. (1.2.9) except in the term L i.e. in front of the large coefficient δ. Then Eqs. (1.2.9) are transformed into the system

$$-\Omega^2 u_y' = L + \left(y^{2\alpha_S}\right)' u_y - y^{2\alpha_S} u_y' + \left(y^{2\alpha_S} u_y''\right)'$$

$$\Omega^2 u_y = -\left(L + y^{2\alpha_S} u_y'\right)' + y^{2\alpha_S} u_y - \left(y^{2\alpha_S}\right)' u_y'$$

from which the *L*-term can be easily excluded. The resulting equation of the 4th order contains only the shear velocity c_S and describes slow waves [Cha-01].

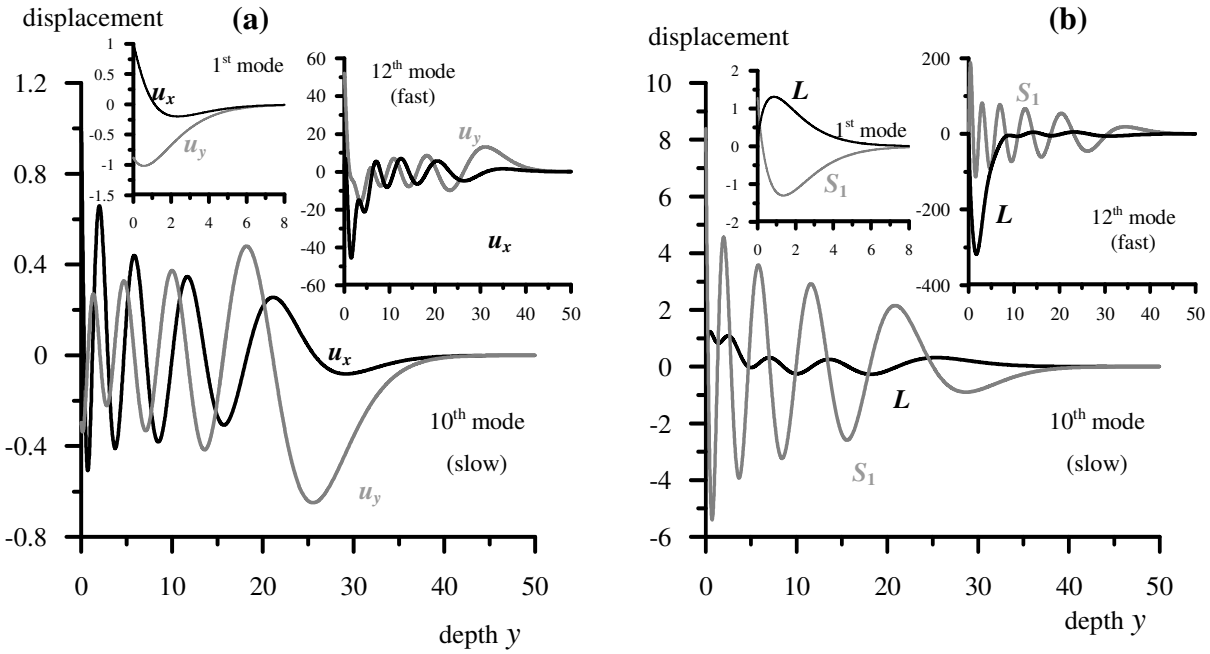

Fig. 1.2.2 (a) The displacement depth (*y*) profiles u_x and u_y for the 1st, 10th, and 12th modes. (b) The terms in the Helmholtz equation (9): *L* contains the longitudinal velocity and the

divergence, S_1 depends on the shear velocity. The parameters of the granular medium ($\gamma_{L,S}$ and $\alpha_{L,S}$) are optimized to fit the experiment: $\delta \approx 4.7$-4.8.

The numerical algorithm **[Ale-07e]** allows us to solve the system Eq. (1.2.5) describing the waves of the both types and see how the physical differences between the modes show up in the displacement depth profiles (Fig. 1.2.2a). The displacements are plotted for the normalization $u_x(0)=1$. For a typical slow mode, for instance, 10^{th}, the vertical component u_y of the surface displacement is negligible, while for a fast mode (the mode 12 in the inset in Fig 1.2.2 a), for the same horizontal component $u_x(0)=1$ the vertical one achieves the value of 52.1.

For theoretical representation of the dispersion curves it is convenient to plot the functional dependence between the parameters Ω and δ figuring in Eq. (1.2.5). In Fig. 1.2.3 (a) the gray points represent values of Ω^{1/α_S} plotted against δ. Two families of modes clearly differ in behavior: the slow modes rapidly saturate at increasing δ whereas the fast modes follow the growing asymptotes (black solid lines). It is easy to see why the saturating dependence corresponds to the slow waves: if Ω does not depend on δ and therefore on k (see Eq. 1.2.6), the frequency ω in the dispersion relation Eq. (1.2.8) is proportional to $k^{1-\alpha_S}$ and any dependence on α_L disappears. The saturated curves are almost equidistant for the chosen vertical scaling Ω^{1/α_S}, except for several low-order slow modes. For the fast modes, in the same way, the frequency ω should be proportional to $k^{1-\alpha_L}$. To satisfy this condition, one has to require for the normalized frequency Ω the proportionality $\Omega \sim k^{\alpha_S-\alpha_L} \sim \delta^{1/2}$ or $\Omega^{1/\alpha_S} \sim \delta^{1/(2\alpha_S)}$. In Fig. 1.2.3 (a) plotted for the optimized (see below) values $\alpha_L=0.309$, $\alpha_S=0.316$ such sections following the increasing asymptotes $\delta^{1/(2\alpha_S)}$ (black solid lines) can be found as well.

At the same time, the mode number 20 follows the saturating behavior already at $\delta \approx 2.5$ thus indicating a slow mode, and then at $\delta \approx 3.2$ (marked with dotted lines in Fig. 1.2.3 (a), (b)) switches to increasing asymptote typical for the fast mode, soon afterwards returning back to the horizontal dependence. The same transformation happens two times more: at $\delta \approx 4.3$ and $\delta \approx 7$. Afterwards the 20-th mode becomes slow again and always remains slow for higher δ-values. The modes of very high orders can experience even four or more of such transformations. The callout in Fig. 1.2.3(a) shows that during the transformations the modes actually do not intersect.

As we saw above, the physical difference between fast and low waves results in very different magnitudes of the vertical displacement $u_y(0)$ at the surface. Accordingly, it makes

sense to define a parameter $V = u_y(0) \Big/ \left[u_x^2(0) + u_y^2(0)\right]^{1/2}$ related to the "visibility" of the mode via vertical displacement detection system, i.e. just the projection of the polarization vector at the surface on the vertical axis. Figure 5 (b) shows that each transformation of the high-order modes into the fast mode corresponds to a peak of *V*: indeed, for the 20th mode in the range of δ greater than approximately 2.8, i.e. in the regime when the there is a distinction between fast and slow waves, the peaks in Fig. 1.2.5 (b) are located exactly below the transitions in Fig. 1.2.3 (a) marked with the dotted lines. The same happens to all other modes experiencing the transitions (not shown in Fig. 1.2.3 (b)).

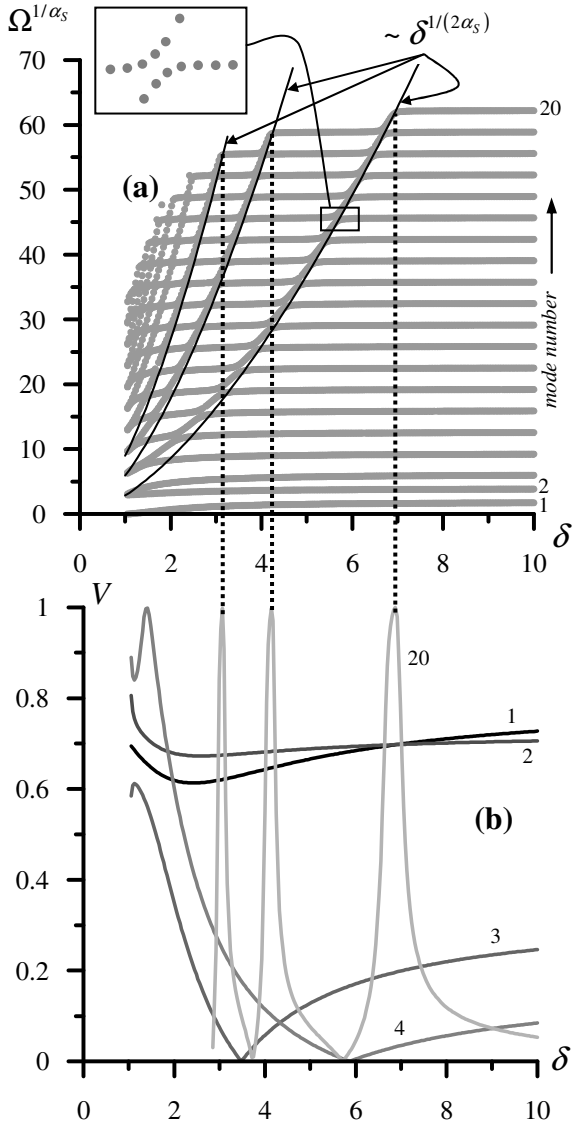

Fig. 1.2.3. (a) Theoretical curves (gray points) for the guided surface modes represented as functions $\Omega^{1/\alpha_S}(\delta)$. The saturating behavior corresponds to the slow waves; the asymptotes for the fast waves are shown with black solid lines. 20 first modes are plotted. (b) The vertical component of the surface displacement normalized on the displacement modulus, i.e.

visibility $V(\delta)$ of the modes. The modes 1-4 and 20 are plotted (the latter is shown only for δ>2.8 to illustrate the behavior at δ»1).

It is interesting to see that the saturation in Fig. 1.2.3 (a) for the lower-order modes takes place at higher δ: the first mode saturates at δ≈5 while the 20th one achieves the first slow regime already at δ=2.5-3. Another remarkable difference between modes with different orders is that low order modes are always slow at high enough δ, whereas the high modes transforms into the fast and back into the slow modes many times in the course of δ-increase. For instance, the first mode saturates considerably at δ≈6 and is for higher δ a pronounced slow mode, similarly to other low-order modes.

1.3. Experimental detection of the guided surface acoustical modes

Through experiments at frequencies (500 Hz ≤f≤ 5 kHz, an order of magnitude higher than in earlier experiments [And-04]), we are able to test near-surface layers at low pressures corresponding to the vicinity of the jamming transition. The lowest-order waveguide mode at its highest frequency f=3 kHz propagates at a velocity ~15 m/s and penetrates only ~0.5 cm beneath the surface, probing the material at pressures less than 75 Pa. This pressure value is below the lowest pressure level accessed in numerical simulations [Mak-04]. However, even at the bottom of the experimental container (Fig. 1.3.1) at a depth of 20 cm, which can be accessed through the low-frequency higher-order modes, the pressure does not exceed 7.5 kPa and is lower than in most of the earlier experiments with bulk acoustic waves. The waves are excited using a 1 mm thick aluminum plate attached to a shaker and partly buried in the granular material (Fig. 1.3.1). The vertical surface velocity is measured as a function of time and distance with the help of a laser Doppler vibrometer with a surface focused beam (sensitivity 1 mm·s^{-1}V^{-1} within the frequency band 80 Hz–20 kHz). The particle velocity is recorded every millimeter along the propagation direction from the source over a 300 mm distance. A maximum vertical velocity of 5·10^{-4} m/s at 1 kHz was observed close to the source.

As the mechanical nonlinearity of a granular medium increases on approaching the jamming point [Tou-04], we checked that the data are not influenced by the wave amplitude in the chosen range of excitation strengths. This demonstrates the existence of linear guided acoustic waves near a surface at zero pre-compression. Note, for comparison, that in a 1D chain of beads at zero pre-compression the linear acoustic waves do not exist (sonic vacuum) [Nes-01]. Using the measured signal in the time-space domain it is straightforward to perform

the time and space double Fourier transform of the signals and plot the dispersion curves for different guided acoustic modes. The experiments are performed on a granular material consisting of 150 μm diameter glass beads in a large tank of dimensions 80 cm × 50 cm × 20 cm (see Fig. 1.3.1).

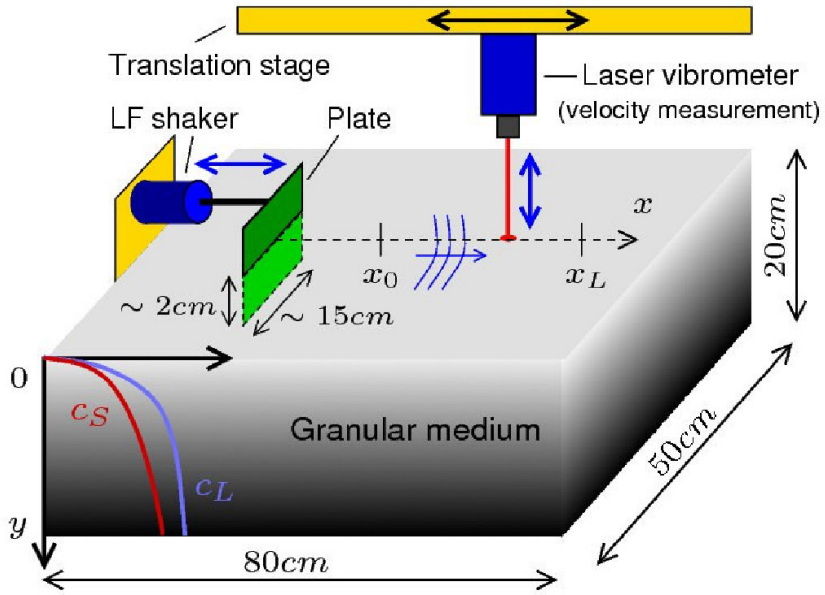

Fig. 1.3.1. Experimental setup.

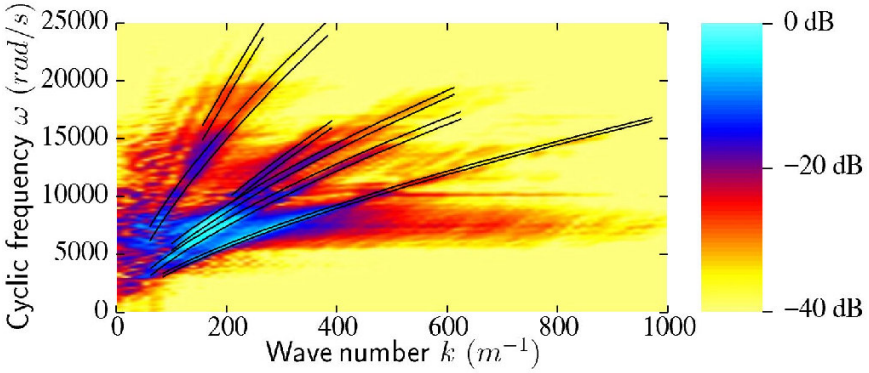

Fig. 1.3.2. Typical dispersion curves for the guided surface modes. Thin double lines indicate averages plus and minus standard deviation; these curves are obtained as a result of a statistical treatment of a number of patterns.

A typical experimentally obtained pattern in the (ω, k) domain is presented in Fig. 1.3.2. The range $0< k <$50–100 m^{-1} is probably affected by the reflection of the waves from the container walls, but the short-wave part corresponds to the modes guided in the horizontal channel [Gus-06] [Ale-07]. The dispersion relations in Fig. 1.3.2 are plotted using an intensity

scale corresponding to the logarithm of the normalized Fourier transform of the particle velocity. The measurements were repeated a number of times with different excitation functions, namely, short pulses with Gaussian spectra centered at different frequencies. For each data set, maxima of the smoothed intensity function for different k points were found. In 80% of the different experimental conditions these maxima were in good agreement with each other. We selected only these points and calculated the power-law approximation curves together with the standard deviation for each mode. In Fig. 1.3.2 the solid lines represent the mean values ± standard deviations.

1.4. Retrieving material properties

The modes' behavior analysis is of interest for theoretical understanding of physics of granular materials, but the practical purpose of this work is to retrieve the depth profiles of rigidity from acoustical measurements by matching the experimental curves plotted in Fig. 1.3.2 and theoretical dependences. At the same time, the residual error of matching indicates whether the chosen simple model is adequate to the experimental situation.

The results of fitting are shown in Fig. 1.3.3 where we plotted the experimental curves obtained by a statistical treatment of experimental 2D patterns in the (ω, k)-domain (solid lines corresponding to ± standard deviation intervals) and the following theoretical (ω, k) points: all points belonging to the first four modes, since they are found to be powerful enough to be detectable regardless their visibility, and all points for the modes higher than fourth with visibility higher than 1/2. This rule allows to easily identify the orders of all experimental modes: the four lower curves (intervals) have orders 1-4, but the two upper curves do not represent the modes number 5 and 6, as it could be expected, but correspond to modes 11-12 and 22-23. Here and everywhere the modes are numbered with respect to the number of zeroes in the profiles.

Matching of the curves is typically done via minimization of an objective function that has been introduced in our case in the following way. For the modes 1-4, if a point is within the relevant interval between the solid lines, to penalty is added to the objective function. If it is outside, then a square of the deviation from the mean is added to the function. For each highly visible point belonging to a mode higher than 4, first a nearest experimental interval is found and then the objective function is modified in the same way. Such a principle severely penalizes points coming out the corresponding intervals leaving to the points within intervals complete freedom. The minimization was performed by the principal axis method [Bre-02]

which is one of the most effective amongst methods of function optimization without knowing analytical expressions for the derivatives of the objective function.

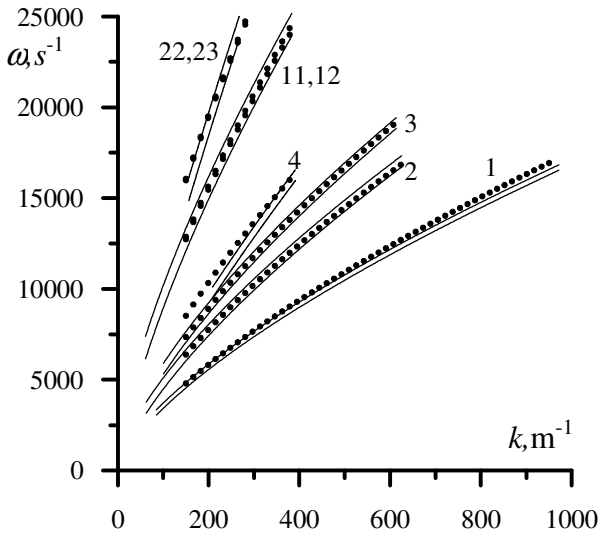

Fig. 1.3.3. Experimental dispersion curves (solid lines) represented as ± standard deviation intervals and theoretical matched fitted to them. The numbers indicate mode orders.

This procedure has provided the optimized parameters of the rigidity profiles Eq. (1.2.1): γ_S=6.42 [SI], γ_L=14.4 [SI], α_S=0.316, α_L= 0.309 with the residual value of the objective function 190 s^{-1}.

1.5. Summary

In this chapter, a specific type of localized acoustic modes is described that exists due to gravity-induced variations of sound velocity profiles vs. depth. The actual origin of the phenomena is related to the presence of internal contacts in unconsolidated granular materials. Highly nonlinear, the internal contacts are sensitive to gravity which results in an important dependence on the vertical coordinate for the linear material properties as well. Gravity-induced changes work as a natural waveguide for acoustic waves traveling in the vicinity of surfaces similarly to the surface waves in solids (Rayleigh waves). However, since the physical mechanism of localization is different, the behavior of those two kinds of localized modes is also different. In particular, there is a theoretically infinite number of modes in the gravity-indeed granular waveguide, whereas the Rayleigh wave is unique simple mode, etc.

Our linear theory and numerical simulations show how to retrieve properties of the granular material from experimentally measured wave data.

2. Consolidated materials with internal contacts: behavior and mechanisms

2.1. Context and concept

This chapter is concerned with consolidated materials with internal contacts present in their structure. They can have common features with the unconsolidated granular materials addressed in the previous chapter, since the both classes have grains with mechanical contacts between them. However, the present case largely differs as the mobility of grains playing an important role for the unconsolidated granulars is practically absent here. At the same time, grainy microstructure means the presence of impurities, irregularities, inclusions, defects, poses, voids, etc., whose behavior significantly alters the materials performance compared to homogeneous media. Most well-known examples (see Fig 2.1.1) of the considered class are geomaterials, such as volcanic (granite, basalt, etc.) and sedimentary rocks (sandstones and limestones, slates, etc), as well as artificial materials such as concrete, mortar, and roofing slate used in construction. Other examples are polycrystalline metals and alloys which also have a grainy microstructure. Complex crack networks (Fig. 2.1.2) in microcracked materials can be visualized [Nem-01] by filing the cracks with Wood's metal and then using the scanning electron microscopy (SEM).

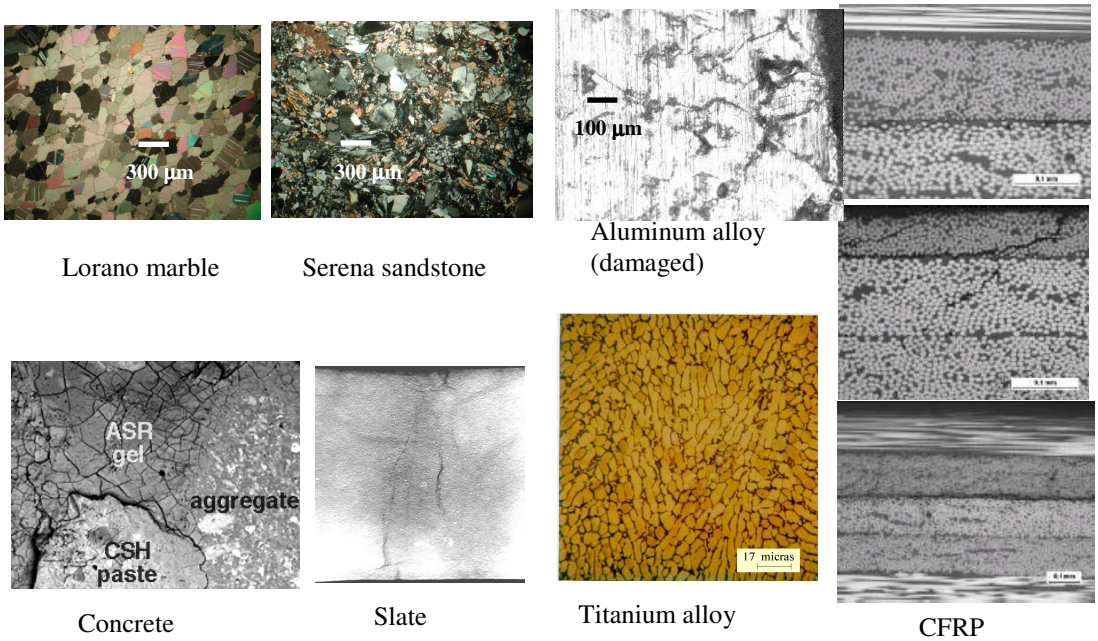

Fig. 2.1.1. Examples of consolidated materials with internal contacts

There is a huge and growing number of researchers and engineers who simulate deformations, acoustics, damage, fatigue and other processes in such materials. The range of

applications covers ultrasonic quality inspection of machinery components, seismology and geological survey, damage assessment and monitoring of constructions and historical monuments, visualization of osteoporosis of human bones, etc. Many of these complicated 3D problems can be successfully solved with the help of modern computers and numerical methods, but only if a material model and the corresponding constitutive equations are adequately given. Constitutive models are needed everywhere and anytime one studies the response of a microstructured material following a static or dynamic impact. They are particularly essential when nonlinear effects are investigated.

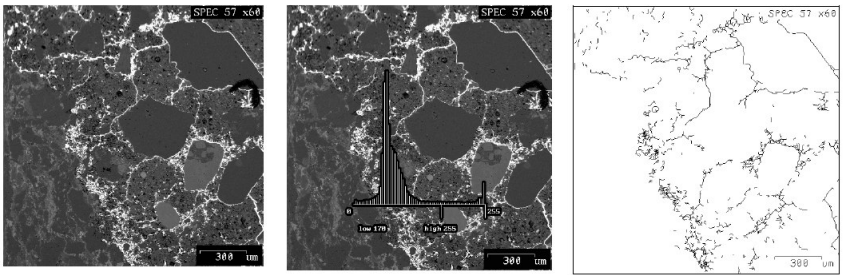

(a) **(b)** **(c)**

Fig. 2.1.1. (a) SEM backscatter image; (b) establishing threshold in histogram; (c) binary-thinned image of the crack network in concrete.

Many material models have been developed for particular cases in a semi-empirical or purely empirical way. Recently some unifying concepts appeared in nonlinear acoustics accounting for effects such as hysteresis and memory, but they remain most of the time completely phenomenological. A detailed description of the behavior of materials with microstructure is, however, not possible without understanding the underlying physical processes: adhesion and friction in the contacts, breakage and healing of contacts, etc. Despite the multitude of researches working on this and related topics, such a detailed "bottom-up" description is still missing.

Models proposed for description of consolidated materials with internal contacts should successfully describe existing experiments that, in their turn, can be categorized into three classes: quasi-static (mechanical tests), dynamic (acoustics), and acousto-elastic tests combining the two previous classes. A unifying feature immediately seen as long as a considerable mechanical excitation is applied to the material is the stress-strain hysteresis (Fig. 2.1.2). So any successful model should at least describe a hysteretic mechanical response that can be due to various factors taken into account.

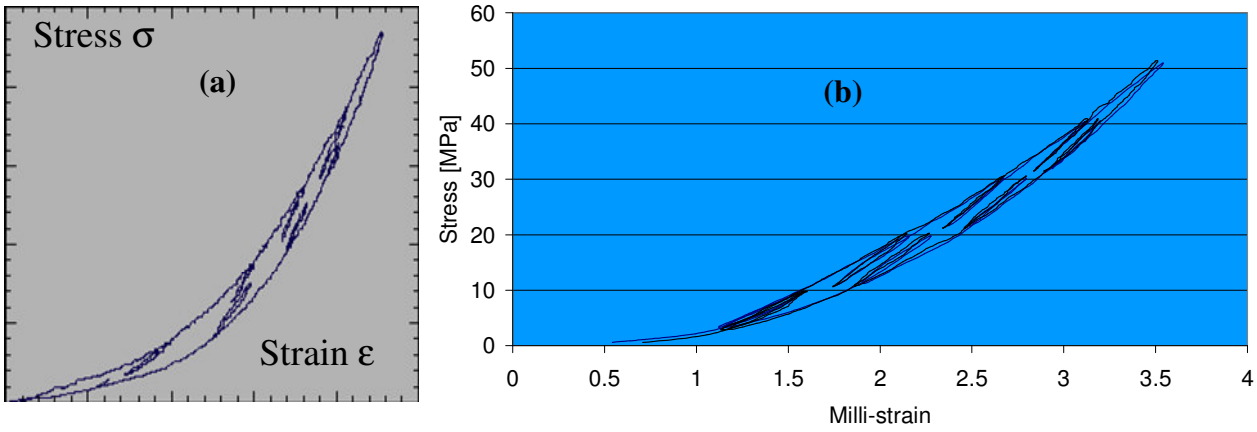

Fig. 2.1.2. Typical hysteresis in stress-strain relationship (mechanical tests on sandstones), [Ost-01].

A central phenomenological approach to hysteresis is the Preisach formalism [Pre-35], [Kra-83], [May-85], [May-91], [Ort-92], [McC-96] discussed in section 2.2. It is based on a concept of hysteretic elements that switch between two states depending on an input parameter. The states are characterized by their particular output supposed to be equal 0 or 1 for simplicity. The actual output of the system is calculated as a sum of all particular outputs of various hysteretic elements taken with different weight coefficients. The advantage of the approach is in the relative simplicity of output calculations for any history (also called protocol) of the drive parameter. The Preisach model is quasi-static i.e. the result does not depend of the protocol execution rate. In reality, many systems can be approximately regarded as belonging to the Preisach class. To check whether a particular model is a Preisach system or not, there exist two necessary and sufficient criterions. If both of them are fulfilled, we can make use of advantages of Preisach description and easily calculate the response by applying the standard algorithm. In our study we consider only 1D (scalar models) while vector [May-91] and tensorial [Hel-98], [Hel-01] Preisach models can be found in literature as well. At the end of this chapter we show how to extend the developed theory to the case of general tensorial loading.

In section 2.3 we show that a number of traditional models for hysteretic response of materials with internal contacts can be considered as particular cases of the Preisach representation. Section 2.4 contains a description of nonlinear phenomena occurring in materials with Preisach hysteresis. As a conclusion, we will see that the Preisach formalism can do everything that the traditional models do and much more. The Preisach representation is more general, flexible and suitable for any excitation protocol which is especially important

in acoustics and ultrasonics. The other side of the coin is a high number of free parameters in the Preisach description. One possible approach would be to retrieve them from data which is discussed in section 2.5. Another opportunity is presented by physical models that allow us to theoretically calculate free parameters of the Preisach description. In sections 2.6-2.8 three physical models based on different assumptions are described. Section 2.9 contains a summary of the three physical approaches and some conclusions about strengths and weaknesses of each of them.

2.2. General Preisach description

The Preisach system [Pre-35], [Kra-83], [May-85] is a mathematical formalism describing rate-independent hysteresis, in which a hysteretic function $y_H(x)$ is represented as a sum (integral) of elementary contributions $\hat{\gamma}$ from two-state hysteretic elements (x is the drive parameter, y is the response). These hysteretic elements (see Fig. 2.2.1(a)) are characterized by two values x_c and x_o ($x_c \leq x_o$) of input x and have the following property:

- if $x > x_o$ then $\hat{\gamma} = 0$, and the element (x_o, x_c) is said to be open;
- if $x < x_c$ then $\hat{\gamma} = 1$, and the element (x_o, x_c) is said to be closed;
- if $x_c < x < x_o$ then the state of the element is determined by its history, i.e., the value of $\hat{\gamma}$ is the same as its value at the previous moment of time.

The contributions of the individual elements with different arguments (x_o, x_c) are taken with weight coefficients $\Pi(x_o, x_c)$. The distribution $\Pi(x_o, x_c)$ in the Preisach space i.e. in the (x_o, x_c)-plane is called Preisach density which represents a portrait of the system and is therefore independent of the drive parameter evolution. Since $x_o \geq x_c$ only elements below the diagonal $x_c = x_o$ are to be considered. In this representation, it is straightforward to identify the configuration of the areas containing open and closed elements corresponding to the above mentioned properties (see Fig. 2.2.1(b)). For a given input x, all elements to the left of the vertical line $x_o = x$ are open, and all elements above the horizontal line $x_c = x$ are closed. These areas are shown in Fig. 2.2.1(b) in light gray and dark gray, respectively. The state of the elements in the remaining area (hatched) depends on their history, i.e., on the protocol of the drive parameter x, and the above rule tells how exactly. Since for increasing values of x the thick vertical line in Fig. 2.2.1(b) shifts to the right and for decreasing x the thick horizontal line shifts downward, each time correspondingly changing the state of elements, the resulting pattern (Fig. 2.2.1(c)) will consist of two areas, one fully open and the other fully closed, divided by the staircase line $V_1, V_2, \ldots, V_n \ldots$ The vertices V_n of the staircase line correspond to particular extrema of the x-protocol.

The hysteretic response function $y_H(x)$ is then found as the integral over the elementary contributions weighted by the Preisach density Π:

$$y_H(x) = \int_{-\infty}^{+\infty} dx_o \int_{-\infty}^{x_o} \hat{\gamma}(x_o, x_c, x)\,\Pi(x_o, x_c)\,dx_c \tag{2.2.1}$$

As mentioned before, $\hat{\gamma}$ differs from zero and equals 1 only for closed elements. For a given protocol $x(t)$, the above rule of switching determines the actual configuration of closed elements Ω (dark gray in Fig. 2.2.1(b) and 2.2.1(c)) and integral Eq. (2.2.1) can be rewritten as

$$y_H(x) = \iint_{\Omega} \Pi(x_o, x_c)\,dx_o dx_c\,. \tag{2.2.2}$$

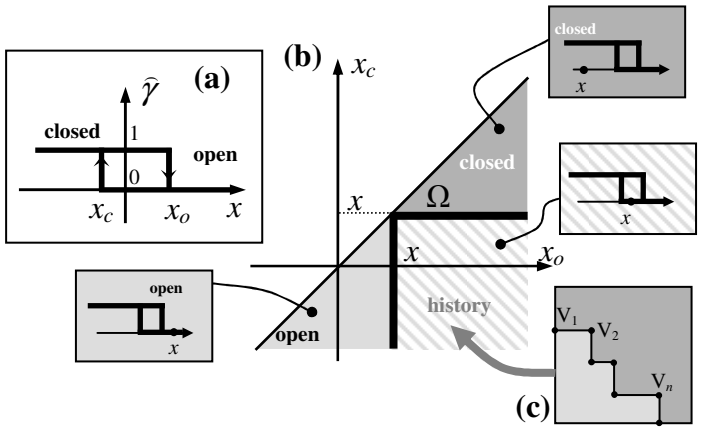

Fig. 2.2.1. (a) Elementary hysteretic element characterized by the control parameter values x_c and x_o. (b) The Preisach (x_o,x_c)-space with three identifiable areas: lower triangle with open elements (light gray), upper triangle with closed elements (dark gray), and rectangle where the state of the elements is determined by the history of the system (hatched). The insets illustrate the relative position of the current value of the control parameter x with respect to the switching parameters x_c and x_o. (c) A typical configuration of the history-dependent part of the Preisach space.

A more detailed description of the evolution of the Preisach system is given, for instance, by [Kra-83]. In order to link this phenomenological formalism to particular physical models for micro-cracked solids we need to evaluate the following necessary and sufficient properties of the Preisach system, as formulated in [May-85].

A model of hysteresis represents a Preisach system if and only if the following two criteria are fulfilled:

- *Criterion A*: "Each local maximum erases the vertices V_n whose x_o-coordinates are below this maximum value, and each local minimum removes the vertices V_n whose x_c-coordinates are above this minimum."
- *Criterion B*: "All hysteresis loops corresponding to the same extremal values of the input parameter x are congruent."

The first criterion (A) implies that not all extrema of the control parameter x are kept in memory as vertices V_n of the staircase line: some of the vertices are erased by the later extrema. In Fig. 2.2.2(a) we illustrate the stored and erased extremum points that will yield the corresponding stored and erased vertices for an arbitrary protocol $x(t)$. In particular, the local maximum at t=4 exceeds the local maximum at t=2 thus erasing the pair of extremum points at t=2 and t=3. Similarly, the pair at t=5 and t=6 are removed by the local minimum at t=7. This means that the protocol in which the points t=1 and t=4, as well as the points t=4 and t=7, are connected with the straight line (dashed line in Fig. 2.2.2 (a)) is equivalent in the sense that it will bring the system to the same state (at t=7) as in the original protocol. The presence or absence of the erased section has no impact on the further evolution of the system.

In addition, the criterion A is equivalent to the end-point memory property [Ost-01] that means that after leaving an inner loop at a certain value of the control parameter the hysteresis curve has the same tangent as immediately before entering this inner loop. This behavior is directly observed in Fig. (2.1.1).

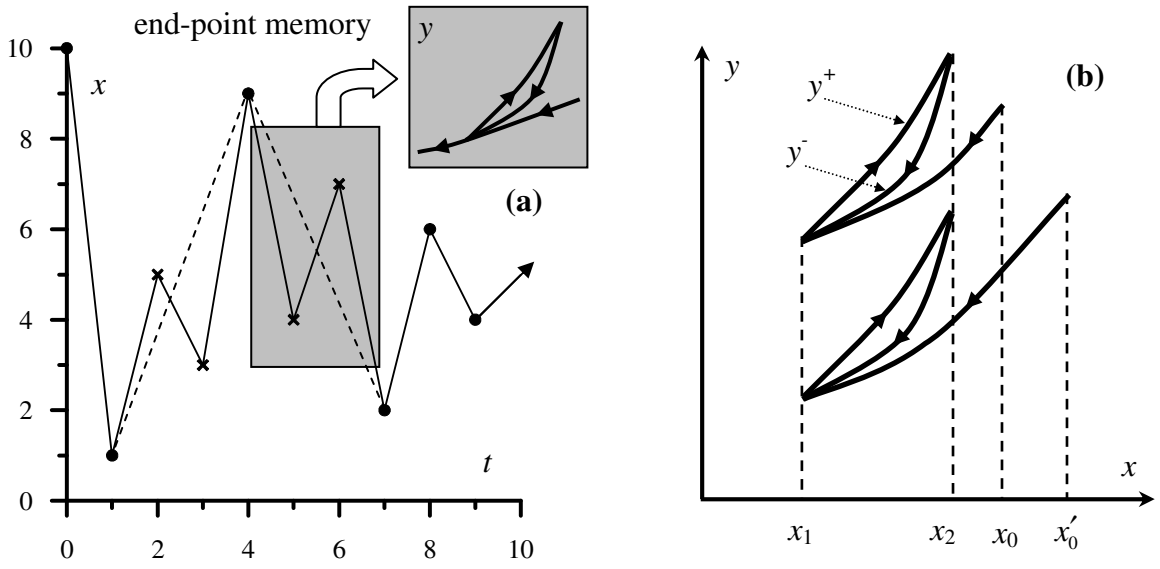

Fig. 2.2.2. Illustration of the Mayergoyz identification theorem: (a) Filled circles correspond to the extrema of the input protocol $x(t)$ which are stored in memory at the final moment t=10. The crosses are intermediate extrema points which have been erased. The dashed lines

indicate an equivalent protocol resulting in the same final state of the system; (b) Loops confined between identical x_1 and x_2 values are congruent, independently of how they were obtained.

The second criterion (B) requires that any two closed loops confined between the same extremal values of the protocol have the same shape – no matter how complicated the protocol is. This actually means that, in the Preisach system, the *shape* of the curve $y(x)$ after passing an extremum point is determined by this extremum point only. At the same time, an overall 'vertical' *shift* of the curve is influenced by all memorized extrema of the protocol. Indeed, as shown in Fig. 2.2.2 (b), if the shape of the section $x_1 \rightarrow x_2$ is determined not only by the previous extremum x_1, but, for instance also depends on whether the second last extremum was x_0 or x_0', such sections cannot be congruent. Changing x_0 to x_0' will only shift the loop as a whole without distorting its shape. Of course, one always has to keep in mind that the loops must be closed, i.e. start and end at the same point. Note that the above criteria are formulated independently of the Preisach space (x_o, x_c) itself.

The total system response can be viewed as a sum of the hysteretic contribution and an ordinary, non-hysteretic function $y_{NH}(x)$,

$$y(x) = y_{NH}(x) + y_H(x). \tag{2.2.3}$$

The Preisach formalism allows one to deduce an important property that links hysteresis curves i.e. experimental data with the Preisach density. Consider an individual closed loop whose up-going branch is denoted y^+ and down-going branch is y^-. Then from Eqs. (2.2.2)- (2.2.3) it follows that for the loop "thickness"

$$\Delta y(x, x_1, x_2) \equiv y^+ - y^- = \int_x^{x_2} dx_o \int_{x_1}^{x} \Pi(x_o, x_c)\, dx_c\,, \tag{2.2.4}$$

and therefore the Preisach density can be found from the loop shape by double differentiation:

$$\frac{\partial \Delta y(x, x_1, x_2)}{\partial x \partial x_2} = \Pi(x_2, x), \tag{2.2.5}$$

where after calculation of the density the arguments x_2 and x have to be substituted with the common arguments x_o, x_c.

This simple result allows an easy check if a given model belongs to the class of Preisach systems or not. First we have to make sure that for a given model or experimental data the criterions A and B are fulfilled. Then the Preisach density $\Pi(x_o, x_c)$ and other important characteristics such as the non-hysteretic contribution $y_{NH}(x)$ can be determined.

Finally, using the known algorithm that keeps track on the staircase line V_1, V_2, … ,V_n in Fig. 2.2.1, its is straightforward to calculate the system response for any excitation protocol.

This feature represents a major benefit of using the Preisach description. The automated calculation of the response is especially important for acoustical excitations that can contain millions of extrema per second. Another advantage of the approach is in its predictive power; as soon as the key parameters of the description are identified on the basis of one particular protocol, the model can be used for generating data for another protocol.

The general estimation of the Preisach approach is that it represents an easy-to-use and universal predictive model but does not provide any physical explanation to the encountered effects. In addition, the model has a large number of parameters (one function of two variables as a portrait of the system) that have to be identified directly from data or, better, from some physical modeling of the system followed by experiment-theory comparison.

Below we show that a number of traditional hysteresis models used in nonlinear acoustics and mechanics for many years represent, in fact, a particular case of the Preisach system.

2.3. Preisach description and other models

Traditionally, a number of simple models have been used to quantify hysteretic effects in materials with internal contacts. Their typical feature is a closed-form expression for up-going and down-going branches of the stress-strain hysteresis and a limited applicability - typically they can be used only for a periodic protocol that has only one pair of extrema per period (so-called simplex signal), and the absolute values the extrema are equal. A common example of such a protocol is a sinewave. Here we consider three particular models: quadratic hysteretic [Naz-15], Davidenkov [Dav-38], and Granato-Lücke [Gra-56] models.

For the quadratic hysteretic model, the up-going and down-going branches are given by expressions

$$\begin{cases} \sigma^{+}(\varepsilon) = K_0\left(\varepsilon + \beta\varepsilon^2 + \alpha\left((\Delta\varepsilon)^2 - \frac{1}{2}(\Delta\varepsilon + \varepsilon)^2\right)\right) \\ \sigma^{-}(\varepsilon) = K_0\left(\varepsilon + \beta\varepsilon^2 - \alpha\left((\Delta\varepsilon)^2 - \frac{1}{2}(\Delta\varepsilon - \varepsilon)^2\right)\right) \end{cases}, \qquad (2.3.1)$$

where σ is stress, ε is strain, $\Delta\varepsilon$ is the strain amplitude, and K_0, α, β are model parameters. This expression does not answer the question about the system's reaction on a signal different from the simplex sinewave type. Hence, it is impossible to check the criterions A and B since no pair of different loops corresponding to the extrema [$-\Delta\varepsilon$, $\Delta\varepsilon$] can be obtained; there is only a unique loop defined by Eq. (2.3.1). However, it is possible to construct a Preisach system

that will to the same as the quadratic hysteretic model for a sinewave-type signal and will also be applicable other, more complex excitation protocols. Using the procedure outlined above and, in particular, Eq. (2.2.5), we calculate the Preisach density and the non-hysteretic contribution in the form

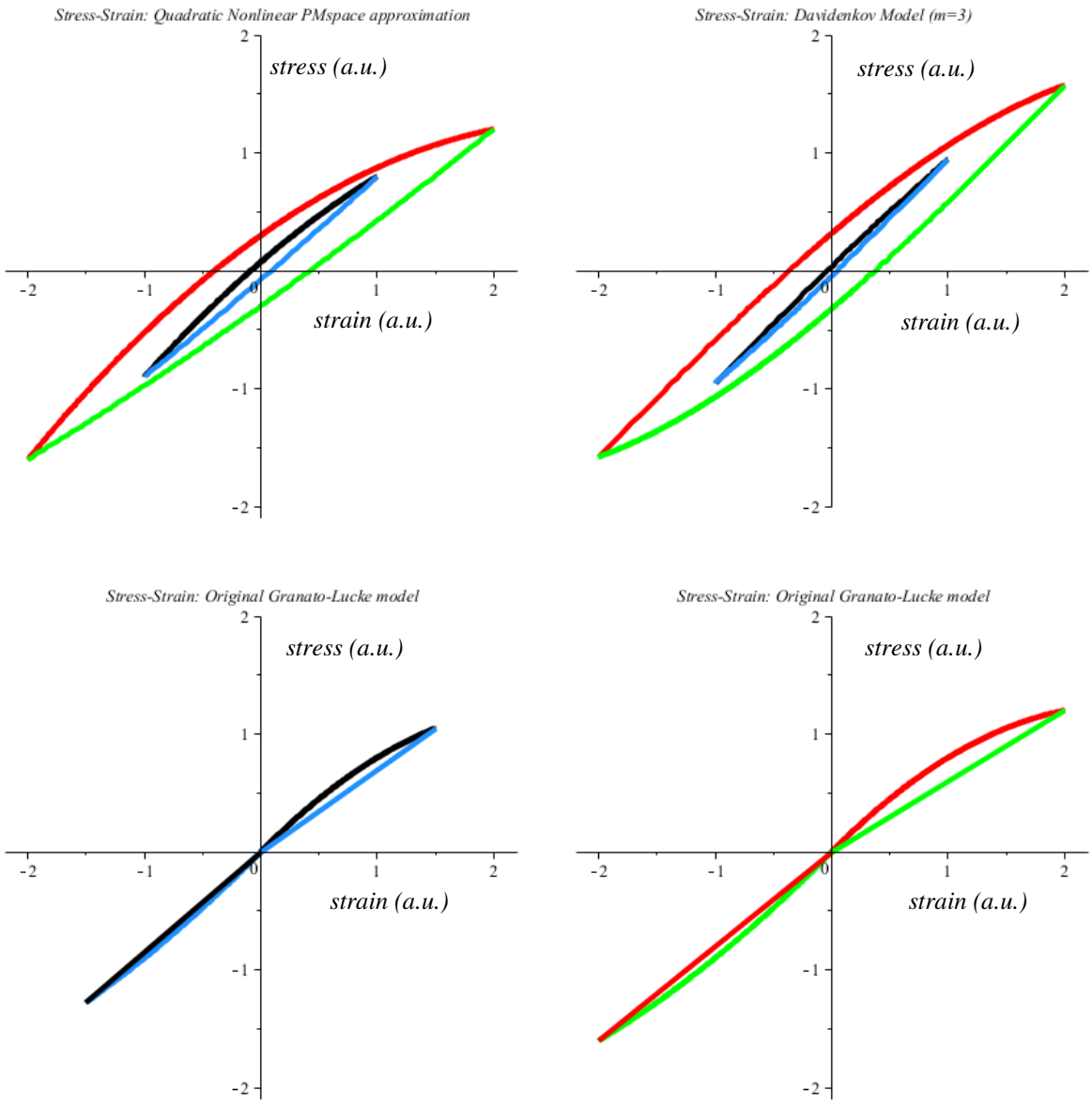

Fig. 2.3.1. Typical stress-strain relationships for the traditional quadratic hysteretic, Davidenkov, and Granato-Lücke models. Various colors correspond to up-going and down-going loop branches for two (lower and higher) arbitrary amplitudes.

$$\begin{aligned} &\Pi(\varepsilon_o, \varepsilon_c) = \alpha \\ &\sigma_{NH}(\varepsilon) = K_0\left(\varepsilon + \beta\varepsilon^2\right) \end{aligned} \tag{2.3.2}$$

that completely reflects the name of the model: there is a quadratic non-hysteretic contribution and the simplest (constant) density.

The same exercise can be repeated for the pioneering Davidenkov model

$$\begin{cases} \sigma^{+}(\varepsilon) = K_0\left(\varepsilon + \dfrac{\alpha}{m}\left(2^{m-1}(\Delta\varepsilon)^m - (\Delta\varepsilon+\varepsilon)^m\right)\right) \\ \sigma^{-}(\varepsilon) = K_0\left(\varepsilon - \dfrac{\alpha}{m}\left(2^{m-1}(\Delta\varepsilon)^m - (\Delta\varepsilon-\varepsilon)^m\right)\right) \end{cases}, \tag{2.3.3}$$

with the result

$$\begin{aligned} &\Pi(\varepsilon_o,\varepsilon_c) = \alpha(m-1)\left(\varepsilon_o - \varepsilon_c\right)^{m-2} \\ &\sigma_{NH}(\varepsilon) = K_0\varepsilon \end{aligned}. \tag{2.3.4}$$

The Granato-Lücke model provides different explicit expressions for positive and negative strain and strain rate,

$$\sigma(\varepsilon) = \begin{cases} K_0^{+}(\varepsilon - \dfrac{\gamma_1}{m}\varepsilon^m) & if \quad \varepsilon \ge 0, \dot{\varepsilon} \ge 0 \\ K_0^{+}(\varepsilon + \dfrac{\gamma_2}{m}\varepsilon^m - \dfrac{\gamma_1+\gamma_2}{m}(\Delta\varepsilon)^{m-1}\varepsilon) & if \quad \varepsilon \ge 0, \dot{\varepsilon} \le 0 \\ K_0^{-}(\varepsilon + \dfrac{\gamma_3}{n}\left|\varepsilon\right|^n) & if \quad \varepsilon \le 0, \dot{\varepsilon} \le 0 \\ K_0^{-}(\varepsilon - \dfrac{\gamma_4}{n}\left|\varepsilon\right|^n - \dfrac{\gamma_3+\gamma_4}{n}(\Delta\varepsilon)^{n-1}\varepsilon) & if \quad \varepsilon \le 0, \dot{\varepsilon} \ge 0 \end{cases}. \tag{2.3.5}$$

The parameters of the Preisach description also have different analytical forms in different quadrants:

$$\begin{cases} \Pi(\varepsilon_o,\varepsilon_c) = \dfrac{\gamma_1+\gamma_2}{m}(m-1)\left(\varepsilon_o\right)^{m-2} & if \quad \varepsilon_o \ge \varepsilon_c \ge 0 \\ \Pi(\varepsilon_o,\varepsilon_c) = \dfrac{\gamma_3+\gamma_4}{n}(n-1)\left|\varepsilon_c\right|^{n-2} & if \quad \varepsilon_c \le \varepsilon_o \le 0 \end{cases} \tag{2.3.6a}$$

$$\begin{cases} \sigma_{NH}(\varepsilon) = K_0^{+}\left(\varepsilon + \left(\dfrac{\gamma_2}{m} - \dfrac{\gamma_1+\gamma_2}{m^2}\right)\varepsilon^m\right) & if \quad \varepsilon \ge 0 \\ \sigma_{NH}(\varepsilon) = K_0^{-}\left(\varepsilon - \left(\dfrac{\gamma_4}{n} - \dfrac{\gamma_3+\gamma_4}{n^2}\right)\left|\varepsilon\right|^n\right) & if \quad \varepsilon \le 0 \end{cases} \tag{2.3.6b}$$

Hysteresis loops corresponding to the model definitions Eqs. (2.3.1), (2.3.3), and (2.3.5) as well as the corresponding Preisach characteristics Eqs. (2.3.2), (2.3.4), (2.3.6a), (2.3.6b) are plotted in Fig. 2.3.1 for some particular values of each model parameters and two arbitrary values of the excitation amplitude.

The results discussed here **[Van-12]** show that the Preisach description is a broader concept than the traditional models for acoustical hysteresis and can be used instead of them.

2.4. Waves in materials with Preisach hysteresis

The objective of this chapter is to study nonlinear effects that occur when an acoustic wave propagates through a material with hysteretic properties. We analyze these manifestations in two cases: (a) when a harmonic wave of frequency ω or a wave having components at ω and 2ω frequencies infinitely propagate through a 1D material with Preisach hysteresis **[Gus-02]**, **[Ale-04a]**, **[Ale-04c]**, **[Ale-03]** and (b) when a 1D resonant bar of a material with Preisach hysteresis is excited with a harmonic signal **[Van-03]**, **[Van-04]**, **[Van-06]**.

Propagation problem

Nonlinear effects in 1D hysteretic medium can be modeled by the 1D wave equation

$$\rho_0\left(\frac{\partial^2 u}{\partial t^2}-c_0^2\frac{\partial^2 u}{\partial x^2}\right)=\frac{\partial \sigma_H}{\partial x} \tag{2.4.1}$$

written for the particle displacement u (parallel to the direction of the wave propagation). Here c_0 is the sound velocity, σ_H is a contribution to the stress due to presence of hysteretic elements. So in this model we do not take into account "classical" nonlinearity of reversible type, concentrating on hysteretic nonlinearity only. In other words, from the point of notations introduced in Eq. (2.2.3), we consider y_H only and neglect y_{NH}.

Using the well-known method of a slowly varying wave profile (multiple scale technique) described, for example, in [Rud-76], we arrive to the "shortened" evolution equation for slowly varying profile of strain $\varepsilon \approx \partial u/\partial x$ for the wave propagating in the positive direction of x-axis

$$\frac{\partial \varepsilon}{\partial x}+\upsilon\left(x,\tau\right)\frac{\partial \varepsilon}{\partial \tau}=0\,. \tag{2.4.2}$$

Here $\tau = t - x/c_0$ denotes "fast" time in the accompanying system of the coordinates, x is "slow" evolution coordinate, and

$$\upsilon\left(x,\tau\right)=-\frac{1}{2\rho_0 c_0{}^3}\frac{\partial \sigma}{\partial \varepsilon}\,. \tag{2.4.3}$$

If $\upsilon\left(x,\tau\right)$ were constant, Eq. (2.4.3) would correspond to a wave that propagates to the right without distorting its shape, as it occurs if we neglect any nonlinearity and assume $\partial\sigma/\partial\varepsilon = E = const$. However, account for hysteretic nonlinearity means that

$$\frac{\partial \sigma}{\partial \varepsilon}=E+\frac{\partial \sigma_H}{\partial \varepsilon},\quad E=\rho_0 c_0^2\,, \tag{2.4.4}$$

and the wave shape will be distorted during propagation.

As it was mentioned in section 2.2, there exist a known algorithm that keeps track on the evolution of the staircase line V_1, V_2, … ,V_n… in Fig. (2.2.1) and therefore completely

determines the evolution of the Preisach system. This algorithm has been implemented, and the hysteretic contribution $\partial\sigma_H / \partial\varepsilon$ in Eqs. (2.4.3) and (2.4.4) has been evaluated for an arbitrarily changing signal $\varepsilon(\tau)$ and for a constant Preisach density Π_0. The latter assumption is supported by the fact that, as we shall see, a nontrivial Preisach density distribution shows up at high mechanical strains (section 2.5) while typical acoustical excitations are several orders less.

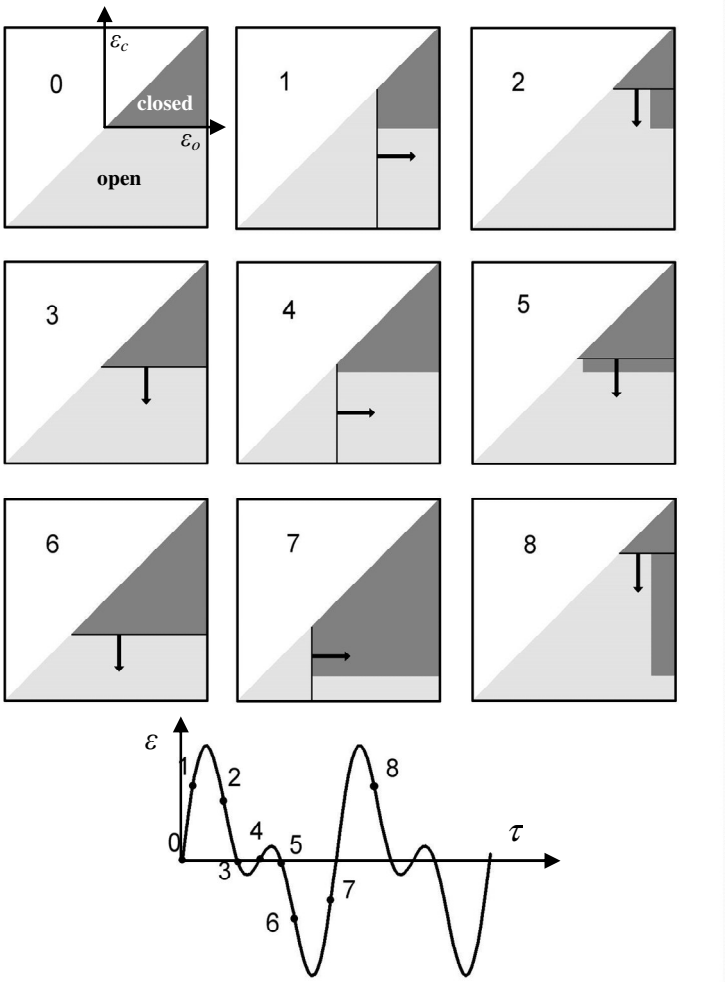

Fig. 2.4.1. Example of Preisach system evolution. Configurations 0-8 of open (light gray) and closed (dark gray) areas in the Preisach space correspond to points 0-8 of the input signal $\varepsilon(\tau)$ that plays a role of $x(t)$ in the general description in section 2.2. The coordinate axes (ε_o, ε_c) are shown on the first portrait 0 only.

Fig. 2.4.1 illustrates the work of the algorithm. In the lower set, a two-frequency signal $\varepsilon(\tau)$ is plotted; the upper part contains a number of state portraits (i.e. configurations of open and closed zones) that correspond to points 0-8 marked in the input protocol $\varepsilon(\tau)$ below. The state portraits include "switching lines" $\varepsilon_o=\varepsilon$ for opening and $\varepsilon_c=\varepsilon$ for closing, with ε, the current strain value (see the lower set). Opening that occurs for increasing $\varepsilon(\tau)$ is drawn in

portraits 1, 4, and 7, in which the vertical switching line moves to the right changing the state of all swept elements to "open" (light gray). In contrast, for closing (portraits 2, 3 ,5, 6, and 8) the switching line becomes horizontal (ε_c=ε) and it moves downward switching elements to "close" (dark gray). It is remarkable that thus relatively simple procedure imitates a behavior of a wide variety of hysteretic systems.

Implementation of the above procedure in the Preisach space allows one to numerically solve the evolution equation Eq. (2.4.2) for the slow amplitude. Hysteretic nonlinearity results in wave profile transformations shown in Fig. 2.4.2 at different distances x normalized on a characteristic value x_{nl} given by

$$x_{nl} = \frac{2T\rho_0 c_0^3}{\Pi_0 \varepsilon_0}, \tag{2.4.5}$$

where ε_0 and T is the amplitude and period of the signal. With increasing x, nonlinear transformations are accumulated. In particular, a sinewave (set (a)) finally becomes a symmetric saw tooth profile while, as it is well-known [Rud-76], for a classical (polynomial) acoustical nonlinearity, the saw tooth profile is asymmetric and includes vertical fronts (shock wave). An initially bi-harmonic signal of a complex type (more than a pair of extrema per period) finally becomes simplex (set (b)). In general, the dynamics of ω and 2ω-wave interaction is quite complex; one wave can improve propagation conditions for another wave and vice versa.

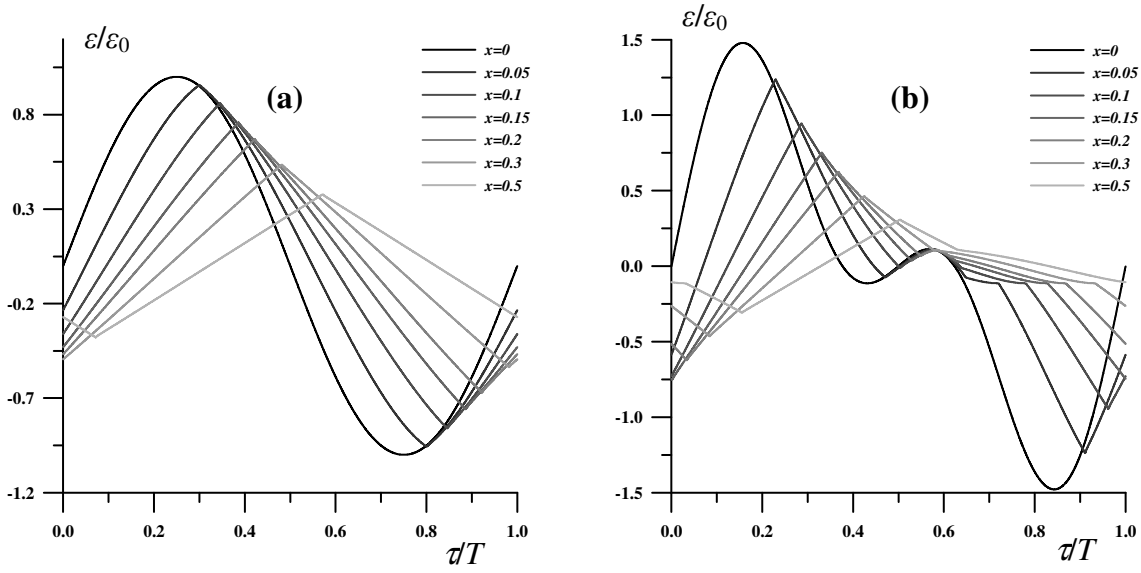

Fig. 2.4.2. Transformations of initially harmonic (a) and bi-harmonic (b) profiles.

Resonance problem

In order to observe strong nonlinear effects similar to those depicted in Fig. 2.4.2, high propagation distances are needed, since the expression Eq. (2.4.5) for x_{nl} contains weak nonlinear parameter Π_0 in the denominator. In practice, comparison with experimental results is much easier when a standing wave is considered instead of wave propagation. In **[Van-04]**, a similar simulation has been reported for a resonant bar with material parameters typical for sandstones. Figs. 2.4.3 (a) and (b) illustrate frequency sweeps for resonances of the fundamental and 3rd harmonics of the particles velocity; in both cases the resonance frequencies become smaller when the amplitude increases i.e. the nonlinearity has softening character. Fig. 2.4.3 (c) shows the dependence of this resonance frequency shift on the amplitude of the particles velocity both calculated for the fundamental harmonics. It is found that this simulated dependence is linear. The second important indicator is presented in Fig. 2.4.3 (d); the dependence of the 3rd harmonic amplitude on the amplitude of the fundamental one is quadratic. These two characteristic dependencies are in good agreement with known experimental data published in [Ost-01]. This fact is a strong argument for the adequacy of the Preisach model for consolidated materials with internal contacts.

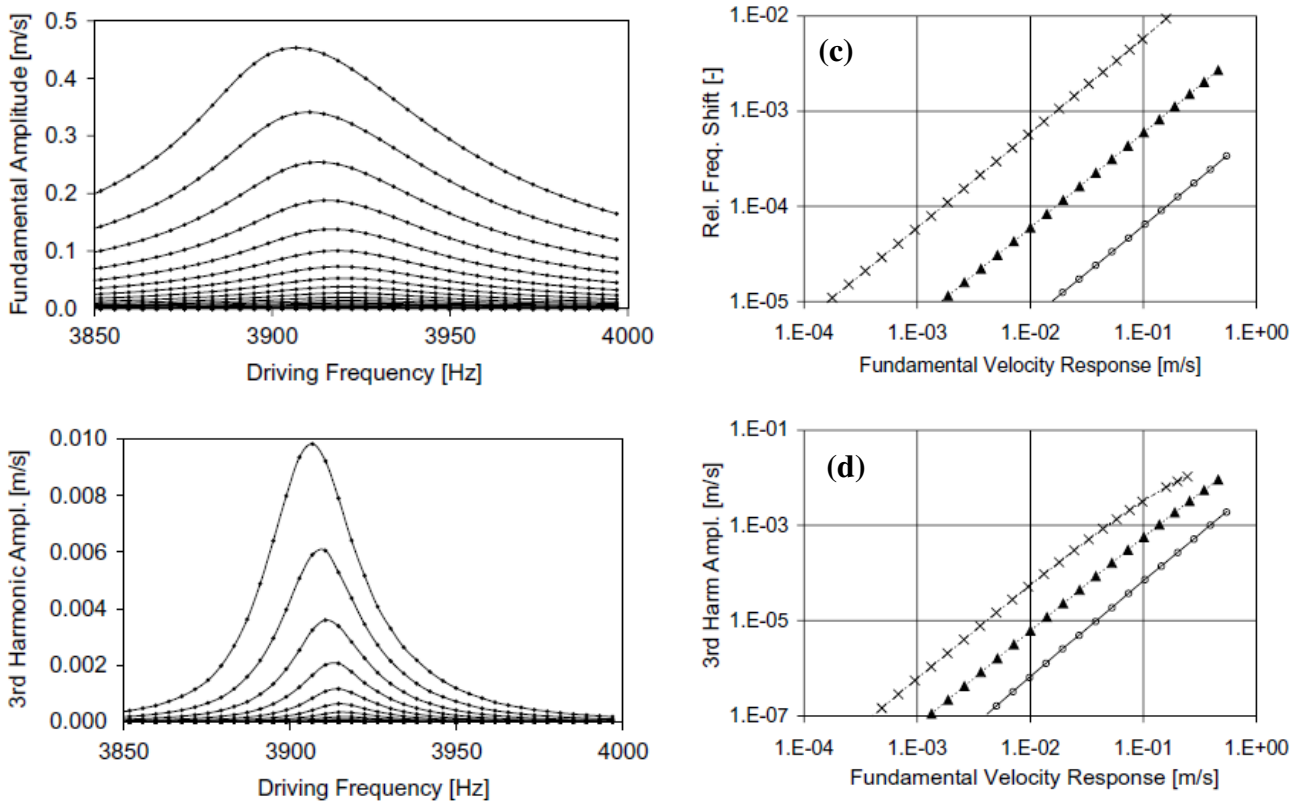

Fig. 2.4.3. Resonance curves for the fundamental (a) and 3rd (b) harmonics. Resonance frequency shift (c) and the 3rd harmonic amplitude as a function of the fundamental

harmonics amplitude. The linear (c) and quadratic (d) dependencies are key characteristics of hysteretic systems of the considered kind and are confirmed experimentally.

2.5. Retrieving Preisach density from data

Integrated Preisach density

The flexibility of the Preisach model is both its strength and disadvantage. The latter is due to the fact that it has a high number of free parameters (actually one 2D function and one 1D function) that has to be determined. One of possibilities is to retrieve these system portraits directly from data. Here (and in **[Ale-08]**, **[Ale-05a]**) we present a method of calculation of the Preisach density (2D function) and the non-hysteretic contribution (1D function) from stress-strain curves measured for a number of materials using a specific loading protocol. It is suggested to use the integrated Preisach density that is also linked to data as the original Preisach density (Eq. 2.2.5) but this link does not contain the ill-conditioned operation of double differentiation.

In this section (section 2.5) we adopt the following convention: stress is positive in compression. The usual definition of the stress requires just adding the minus sign in front of each stress-related characteristics.

The integrated density $H(\sigma_o,\sigma_c)$ is defined as

$$H(\sigma_o,\sigma_c)=\int_{\sigma_c}^{\sigma_o} dx \int_{\sigma_c}^{x} \Pi(x,y)\,dy \tag{2.5.1}$$

through the ordinary density $\Pi(\sigma_o,\sigma_c)$ which means that the former is obtained from the latter by integration over the triangle defined by the corners (σ_o,σ_c), (σ_o,σ_o) and (σ_c,σ_c) (see also Fig. 2.5.3). Then the principal Eq. (2.2.2) of the Preisach model that contains integration oven the open area delimited by the staircase line V_1, V_2, … ,V_n (Fig. 2.2.1) is replaced by a simple expression

$$\varepsilon_H = H(V_1)-H(V_2)+H(V_3)-...\pm H(V_n) \tag{2.5.2}$$

where the integration has already been done and the integrated densities are calculated at the vertices V_1, V_2, … ,V_n.

Inversion procedure

In order to estimate the integrated density distribution, we use a specific protocol depicted in Fig. 2.5.1(a) defined by N stress levels. The corresponding stress-strain curve contains all loops that can be formed by stress variations between these levels. Each of the loops

correspond to a triangle located inside the largest triangle in Fig. 2.5.1(b) "activated" in the Preisach space while tracing those loops.

The proposed scheme allows one to maximize information obtained from a 1D curve for retrieving a 2D surface. Indeed, an infinitely large N means that the stress-strain curve sweeps practically whole coordinate plane (σ, ε). However, in practice, the number N should not be too high because of experimental errors limiting the resolution of the smaller loops. The total number of loops in the protocol in Fig. 2.5.1(a) i.e. the total number of triangles in Fig. 2.5.1(b) is $N_L=N(N+1)/2$.

As if follows from the Preisach description and, in particular, from Eq. (2.2.4) for a loop thickness, thicknesses of N_L loops present in the protocol correspond to the integrals of the Preisach density over the relevant rectangles in the Preisach space. This fact is illustrated in Fig. 2.5.2. In the set (a), a particular loop is plotted (we no not show the whole stress-strain dependency for the protocol Fig. 2.5.2(a) since it is too massy). Its thickness $\Delta\varepsilon$ equals the density integral over the hatched rectangle shown in the set (b).

In our approach, we measure the thicknesses $\Delta\varepsilon$ from the available stress-strain data for all σ-levels at the grid points in the Preisach space. For an $N\times N$ grid with $N_L=N(N+1)/2$ possible triangles and the corresponding N-level stress protocol, the maximum number of possible "non-zero" thickness measurements is $N_M=N(N^2-1)/6$. This means that each N-level protocol gives us the density integrals over N_M rectangles, overlapping as well as non-overlapping. Once these values are

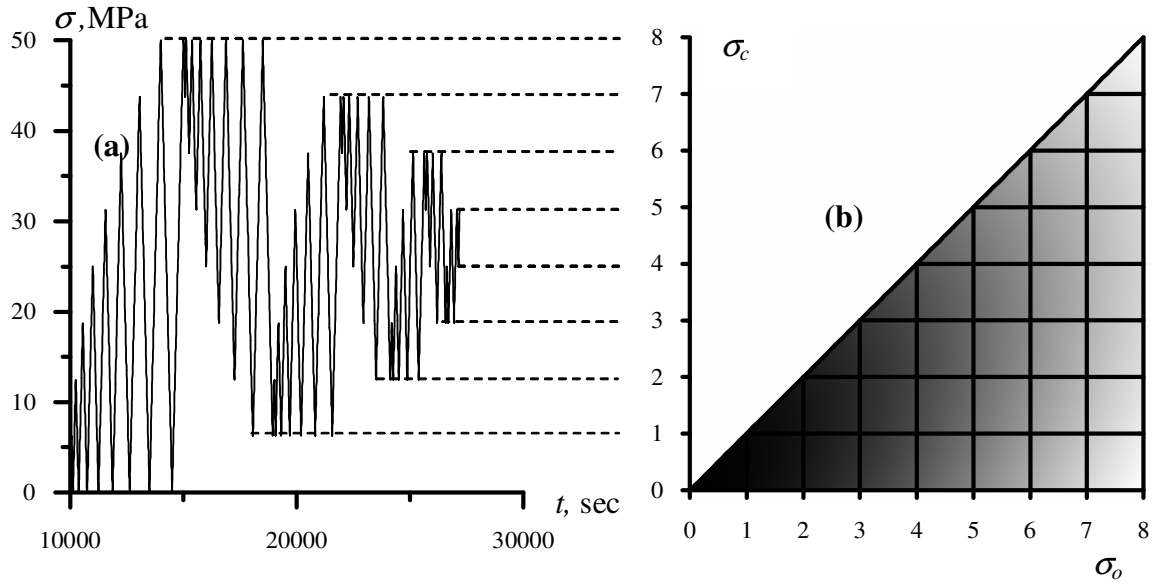

Fig. 2.5.1. Specific N-level stress protocol (with N=8) used in the reconstruction algorithm (left figure). Each individual compression-decompression cycle uniquely corresponds to one of the possible triangles composed by any two grid lines (shown at the right).

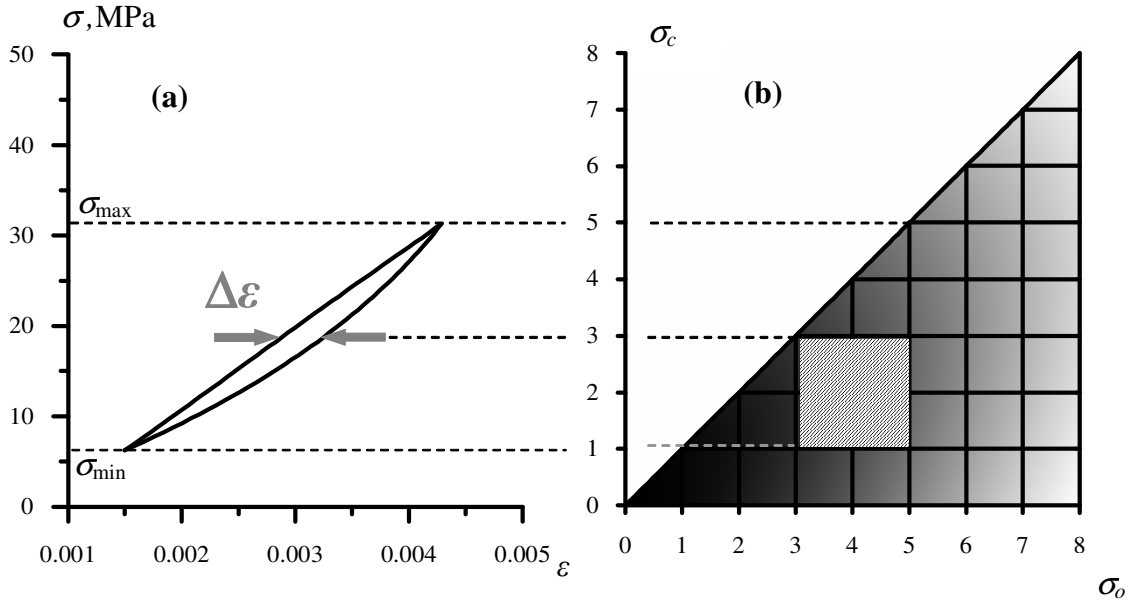

Fig. 2.5.2. (a) Strain thickness $\Delta\varepsilon$ at constant stress value σ for a typical hysteretic loop in the stress-strain relationship (left figure) and the corresponding rectangle in the Preisach space (b). The Preisach density integral over this rectangle equals $\Delta\varepsilon$. The corners of the rectangle are defined by the highest and the lowest stress values of the loop as well as the stress σ at which $\Delta\varepsilon$ is measured. Here, N=8.

known, it is possible to infer the integrals over the individual 1×1 squares in the Preisach space (called here blocks or bins). The number of such bins is $N_B=N(N-1)/2$. Note that the number of unknown bin integrals N_B is always smaller then the number N_M of known data points (i.e. loop thickness measurements, or rectangles (bins combinations)), except in the trivial case for N=2, when both numbers equal 1. As a consequence, we have an over-determined system of linear equations that can be solved by minimizing the corresponding objective function:

$$F=\sum_{i=1}^{N_M}\left(\Delta\varepsilon_i-\sum_{k,l\in i}I_{k,l}\right)^2, \qquad (2.5.3)$$

where $\Delta\varepsilon_i$ is the result of i-th thickness measurement and $\sum_{k,l\in i}I_{k,l}$ represents the summation of all bin integrals (i.e., density integrals over the $(k,l)^{\text{th}}$ bin) belonging to the corresponding i-th rectangle. The residual value of the objective function can be used as a criterion for whether we have a good Preisach system or a system that significantly deviates from the ideal one.

The problem of calculating the individual bins values from their combinations basically requires the subtraction of two closely valued positive numbers, each known with

some finite precision. In that case, the relative error of the result is much higher than the relative errors of the individual components. In other words, the discussed problem is a coarse-grid analog of the continuous differentiation given by Eq. (2.2.5).

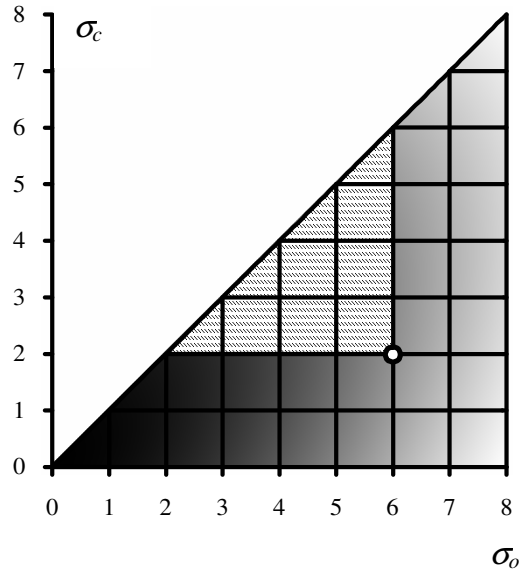

Fig. 2.5.3. The integral Preisach density at the marked grid point (σ_c,σ_o) is the sum of the Preisach density integrals for all bins (square and triangular) in the hatched triangle.

However, in our approach, we try do retrieve the integrated Preisach density which means that we do not really need the bin values themselves, but only a specific combination of them corresponding to the points where the integrated density is calculated (grid points). To find the integrated density in a given grid point (σ_o,σ_c) we must collect all bins located at the upper-left hand side from that point (see Fig. 2.5.3). Summing all the bin integrals, we avoid the above mentioned instability problem since the sum of positive numbers has a small relative error.

Note that, despite the fact that we combine the bins in the integrated density reconstruction algorithm, reducing the relative error, it is still advisable to stabilize the process of deriving the bins themselves. A typical regularization technique [Tik-77] consists in considering a stabilizing addition to the objective function (Eq. 2.5.3) of the kind

$$F' = F + \alpha \sum_{k,l} \left(I_{k,l} - I_{k+1,l} \right)^2 + \alpha \sum_{k,l} \left(I_{k,l} - I_{k,l+1} \right)^2 , \qquad (2.5.4)$$

which penalizes large differences between neighboring bins and smoothens the coarse-grained Preisach density. The stabilizing parameter α must be predetermined depending on the noise value.

As seen in Fig. 2.5.3, the integral density $H(\sigma_c,\sigma_o)$ consists of individual square bins, and small triangular bins which are located at the diagonal $\sigma_c=\sigma_o$. To estimate the integrals in the triangular bins, we assume that the Preisach density has a constant value in each triangular bin (N in total). This is, of course, not exactly true and may lead to errors which will be discussed later. From Eq. (2.2.4) rewritten as

$$\Delta\varepsilon = \left|\varepsilon^{\uparrow}(\sigma) - \varepsilon^{\downarrow}(\sigma)\right| = \int_{\sigma}^{\sigma_{\max}} d\sigma_o \int_{\sigma_{\min}}^{\sigma} \rho(\sigma_o,\sigma_c)\, d\sigma_c \,. \tag{2.5.5}$$

with $\varepsilon^{\uparrow}(\sigma)$ and $\varepsilon^{\downarrow}(\sigma)$, the up-going and down-going loops branches, it follows that the area inside any closed stress-strain loop (see Fig. 2.5.2. (a)), assuming a constant Preisach density Π_0, is

$$A = \int_{\sigma_{\min}}^{\sigma_{\max}} \Delta\varepsilon \, d\sigma = \Pi_0 \left(\sigma_{\max} - \sigma_{\min}\right)^3 \big/ 6 \,. \tag{2.5.6}$$

Thus, by measuring the areas A for all the smallest stress-strain loops, one easily obtains the integral density values $\Pi_0(\sigma_{\max}-\sigma_{\min})^2/2=3A/(\sigma_{\max}-\sigma_{\min})$ related to the triangular bins. Here Π_0, $\sigma_{\max}$ and $\sigma_{\min}$ are, of course, different for different triangular bins.

Finally, after calculating the integrated density $H(\sigma_o,\sigma_c)$ at discrete grid points, we interpolate the ready set of points with a smooth function to get the integrated density distribution everywhere in the (σ_c,σ_o) space, which can be used to obtain the hysteretic contribution to the total strain following an arbitrary stress protocol.

The non-hysteretic component $\varepsilon_{NH}(\sigma)$ can also be reconstructed once the integrated density is found. To do this, we consider, for instance, an up-going curve $\varepsilon^{\uparrow}(\sigma)$ for the largest loop of the protocol and note that

$$\varepsilon^{\uparrow}(\sigma) = \varepsilon_{NH}(\sigma) + H(\sigma,\sigma_{\min}) \,. \tag{2.5.7}$$

Alternatively, we can also consider the down-going curve with

$$\varepsilon^{\downarrow}(\sigma) = \varepsilon_{NH}(\sigma) + H(\sigma_{\max},\sigma_{\min}) - H(\sigma_{\max},\sigma) \,. \tag{2.5.8}$$

Using both the measured up-going and down-going branches and with the known integrated density values, we retrieve $\varepsilon_{NH}(\sigma)$ twice. Certainly, for an ideal Preisach system these two values must coincide. For realistic cases, they deviate with a discrepancy characterizing the validity of the discussed Preisach modeling.

In conclusion, the algorithm of the integrated Preisach density computation can be summarized as follows:

- Choose *N* and execute the corresponding stress protocol depicted in Fig. 2.5.1(a).
- Measure the thicknesses of all loops at the grid points.
- Minimize the objective function (Eq. 2.5.4) to get all square bins.
- Measure the areas of the smallest loops to get all triangular bins.
- Collect all bins related to the integrated density at the grid points.
- Interpolate the discrete set of integrated density points to obtain the integrated density distribution everywhere in the (σ_o,σ_c) space.
- Determine the non-hysteretic contribution using Eq. (2.5.7) or Eq. (2.5.8).

Application to experimental data

We now apply the reconstruction method to real experimental data resulting from uniaxial compression test on several hysteretic materials (natural building stones). Cylindrical samples (with a length of about 50mm, and a diameter of 25mm) were loaded using the MTS 810 TestStar load frame (Fig. 2.5.4 (a)) capable of loading up to 100kN. Strain was measured by means of two dynamic strain gauge extensometers (Instron 2620-603 with gauge length 10 mm (Ext1) and 25 mm (Ext2)).

Figs. 2.5.4 (b) and (c) illustrate two loops of the stress-strain curve for Serena sandstone. The large loop (0→58MPa→0) switches all the hysteretic elements contained in the covered pressure range. This loop evidently shows the largest difference between up-going and down-going curves. The inset represents one of the smallest loops obtained at the highest ambient pressure (58MPa→51MPa→58MPa). Since at such high pressures, almost all micro-slippage in the contacting asperities inside the rocks is disabled, this loop is considerably less hysteretic than the others. Correspondingly, the two loops in Figs. 2.5.4 (b) and (c) are the most and the least hysteretic ones within the protocol.

The largest loop (0→58MPa→0) was used to retrieve the non-hysteretic contribution $\varepsilon_{NH}(\sigma)$ according to Eqs. (2.5.7)-(2.5.8) (see Fig. 2.5.4 (d)). As mentioned, the algorithm enables to reconstruct the non-hysteretic dependence twice, based on either the up-going or the down-going branches of the largest loop. Good coincidence between the inverted data points (large and small crosses) confirms the validity of the Preisach model for this material.

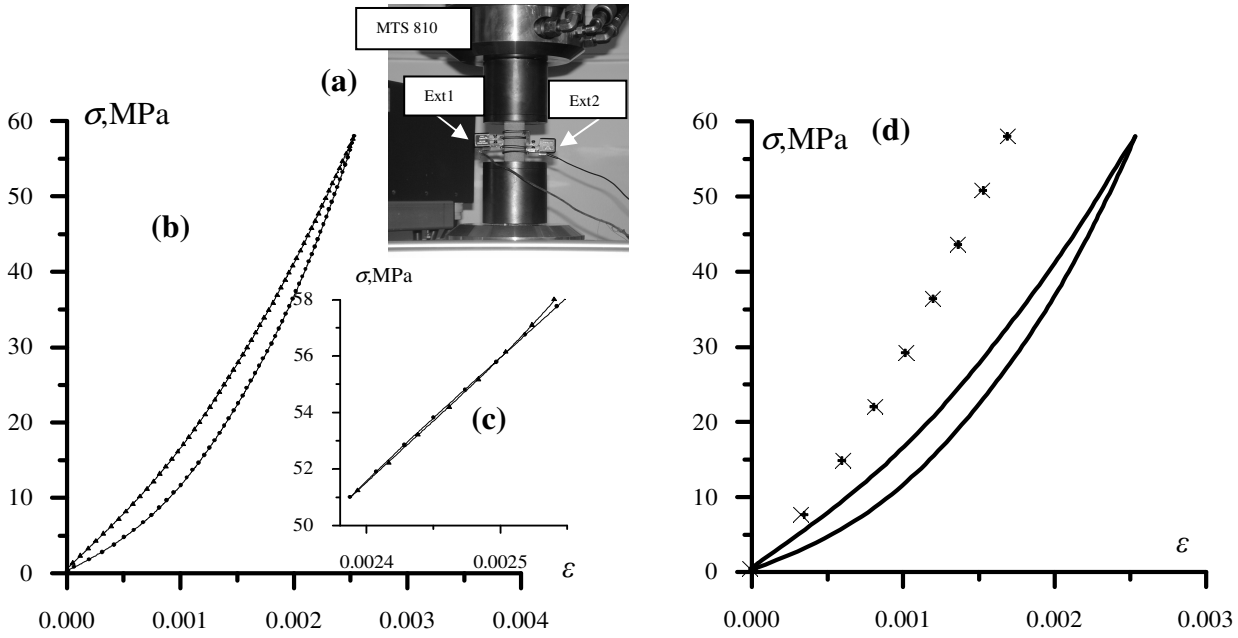

Fig. 2.5.4. (a) Experimental setup for cyclic uniaxial compression tests on cylindrical rock samples. (b) Experimental data corresponding to the largest loop of the 8-level stress protocol (0→58MPa→0) and (c) of one of the smallest loops (58MPa→51MPa→58MPa) for a sample of Serena sandstone (each 20th point plotted). The solid lines represent polynomial approximation of 3rd and 5th degree for the small and the large loop, respectively. (d) Non-hysteretic contribution $\varepsilon_{NH}(\sigma)$ (points) and the largest hysteretic loop (solid lines) in the stress-strain behavior of Serena sandstone. The small crosses correspond to the up-going curve (Eq. 2.5.7) and the large ones are obtained from the down-going curve (Eq. 2.5.8).

In Fig. 2.5.5 we have plotted two integrated Preisach portraits, one for a sandstone (Serena) and one for a bioclastic limestone (Lecce). The petrographic parameters (type and size of grains, pores and interstices) of these two rocks are considerably different, as well as their physical properties. In particular, the ultimate compression strength values differ about a factor 9. As a result, the hysteretic portraits are considerably different too: the integrated Preisach densities have distinctive parameters and shapes.

As a final point in the analysis, we investigate the prediction power of the considered methodology. Fig. 2.5.6 illustrates the actual measurement of the stress-strain curve together with the predicted behavior that was calculated using Eq. (2.5.1), Eq. (2.5.2) and the reconstructed integral density for Sander sandstone (similar to Fig. (2.5.5), not shown here). The agreement is most satisfactory. The experimental and predicted shapes only weakly

deviate from each other, with the major difference being a constant shift. This effect can be attributed to the fact that successive cycles are never perfectly repeatable.

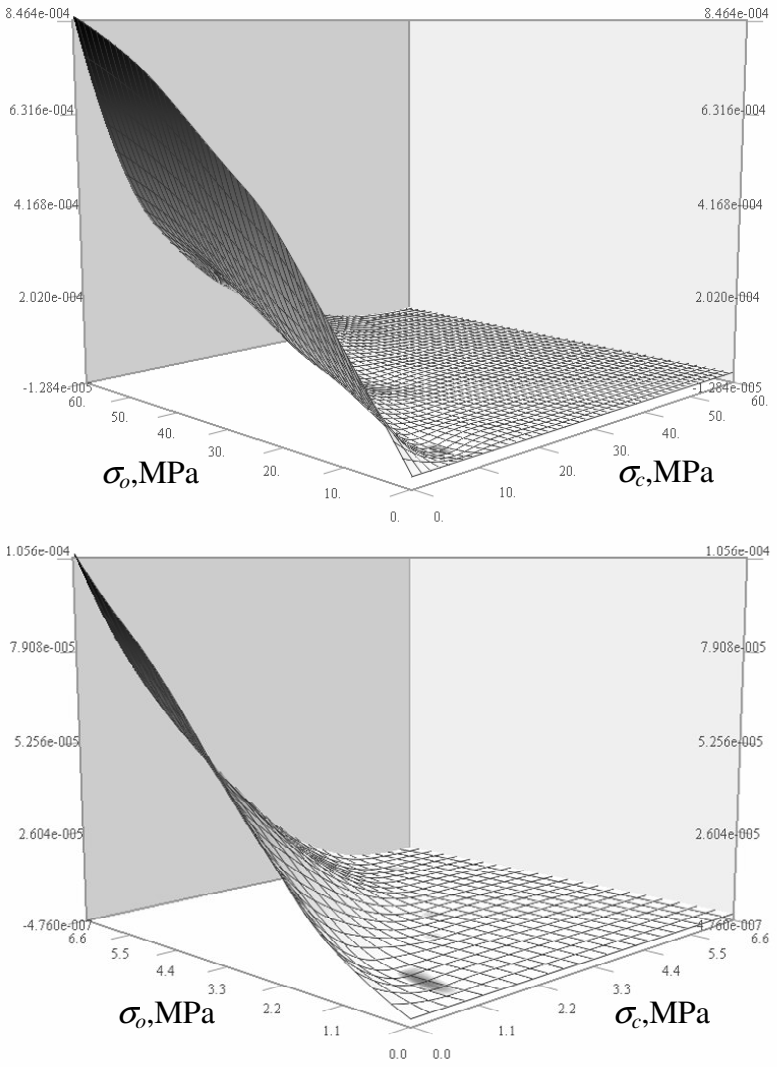

Fig. 2.5.5. Reconstructed integrated Preisach density distributions for two very different rocks (Serena sandstone and Lecce limestone).

The study presented here is purely phenomenological and suggests just a data processing procedure. A deeper insight into the nature of consolidated materials with internal contacts would require some physical modeling for reasons of hysteresis and their influence on measurable parameters. In the next sections of this chapter such attempts are discussed.

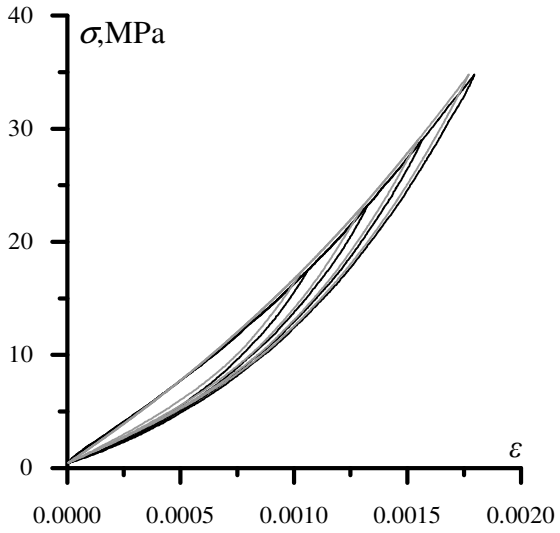

Fig. 2.5.6. Prediction of additional loading-unloading cycles made for Sander sandstone. Black is actual experimental data, gray is a prediction based on the reconstructed integral Preisach density.

2.6. Micropotential model for hysteresis

There can be several physical reasons that produce hysteretic behavior. One of them is the presence of double-well potentials corresponding to internal structure interactions. Each of such potentials can be responsible for interaction between particular structure elements. The state of the subsystem corresponding to these structure elements is then described as a point trapped in one of two minima of the double-well potential. External action modifies the potential function shape; in some situations one of two minima can disappear. In that case, the subsystem is forced to stay in the remaining minimum that corresponds to opening or closing an element in the Preisach representation.

A multitude of structure elements correspond to a multitude of subsystems. The simplest way of obtaining of the material response is to assume that the subsystems do not interact so that the total response equals the sum of subsystems responses. This assumption is analogous to summation of elements contributions (Eq. (2.2.1) or (2.2.2)) in the Preisach model. Thus the key part of the theory is to identify a physical mechanics that can be responsible for a double-well potential.

In this section (as well as in **[Ale-05b]**, **[Ale-06a]**, **[Ale-04b]**, **[Ale-04d], [Ale-04e]**) it is demonstrated that such en effect can be attributed to adhesion of internal crack faces. Smallest cracks in a material can have sizes comparable to an interatomic distance that allows one to describe the interface interaction using potentials of Lennard-Jones type with a

pronounced minimum corresponding to a strong pull-off force with a characteristic magnitude comparable to the one of an intact material. Further, the presence of roughness considerably (several orders of magnitude) weakens the pull-off adhesion force and smoothens the corresponding potential minimum. On the other hand, cracks can have some "natural" rest aperture considerably exceeding the adhesion force range. As a result, a double-well potential can occur with a depth of wells comparable to strain energy in an acoustic wave (section 2.4) or in a static deformation field (section 2.5). In that case, the material will show hysteretic behavior. Below we describe a situation in which a double-well potential can appear.

Straining a material containing cracks produces three potential energy components. One of them, P_{bulk}, is related to deformation energy of the intact material. The presence of cracks means that in the vicinity of crack tips high local strains and the related strain energy P_{loc} arises. Finally, if crack lips are in contact, contact interaction energy P_{cont} should also be taken into account. It is important to mention that the spatial distributions of those energies have almost non-intersecting supports. This means that the total potential energy of the material, P, can be obtained by the simple summation,

$$P = P_{cont} + P_{loc} + P_{bulk} . \tag{2.6.1}$$

Below we estimate these three contributions separately starting with the contact term P_{cont}.

Contact interactions via Lennard-Jones potential

For most materials, the interaction potential w (per unit of surface) for two half-spaces, separated by a distance ξ, is given by [Izr-85]:

$$w(\xi) = \frac{H}{12\pi}\left(-\frac{1}{\xi^2} + \frac{a_0^6}{60}\frac{1}{\xi^8}\right). \tag{2.6.2}$$

Here, H is the Hamaker constant of the material, and a_0 is the atomic size. The Hamaker constant H for most materials ranges from 0.4 to $4\cdot10^{-19}$ J. In the example that will be discussed later, we will use $H = 10^{-19}$ J.

The potential energy $w(\xi)$ describes strong repulsion at small separation distances $\xi < 15^{-1/6} a_0 \approx 0.64 a_0$ and attraction (adhesion) at larger distances which diminishes as the distance increases. This result can be obtained by integration of the Lennard-Jones potential (also referred to as the 6-12 potential or the potential of the Van der Waals force).

The assumption of almost plain elementary cracks consequently yields a simple form for the potential energy (per unit of surface) of such a crack:

$$W(g) = \int_0^\infty w(\xi)\varphi(\xi)d\xi . \tag{2.6.3}$$

Here, we have introduced the distribution function $\varphi(\xi)$ of the local random gap ξ between crack faces, with mean value g and standard deviation D, such that:

$$g = \int_0^\infty \xi\, \varphi(\xi) d\xi, \qquad D^2 = \int_0^\infty \xi^2\, \varphi(\xi) d\xi - g^2 . \tag{2.6.4}$$

In many research studies dealing with rock joints, the local gap between rough surfaces in contact is assumed to have a lognormal distribution:

$$\varphi(\xi) = \frac{e^{\kappa/2}}{g\sqrt{\pi^{\,k}}} \exp\left(-\tfrac{1}{\kappa} \ln^2 \left(\frac{\xi}{g} e^{3\kappa/4} \right) \right), \tag{2.6.5}$$

where κ is a parameter which links the standard deviation D and the average g through the following expression:

$$D = g\, e^{-3\kappa/4} \sqrt{e^{2\kappa} - e^{3\kappa/2}} . \tag{2.6.6}$$

Inverting Eq. (2.6.6) with respect to κ and substituting it into Eq. (2.6.5), we obtain an explicit form of the distribution $\varphi(\xi)$ as a function of the average gap g and the standard deviation D (r.m.s roughness) The integral Eq. (2.6.3) can then be expressed as follows in terms of g and D:

$$W(g) = \frac{H}{12\pi} \gamma^3 \left(-\frac{1}{g^2} + \frac{a_0^6}{60} \frac{\gamma^{33}}{g^8} \right), \tag{2.6.7}$$

where

$$\gamma = 1 + (D/g)^2 . \tag{2.6.8}$$

This modified Lennard-Jones potential has a minimum (g_{LJ}, W_{LJ}) whose dependence of the r.m.s. roughness is depicted in Fig. 2.6.1. Set (a) shows that g_{LJ}, the distance between two half-spaces with rough and adhesive surfaces, growths approximately as much as D which is not surprising al long as g_{LJ} greatly exceeds the atomic distance a_0. Set (b) illustrates an important effect of strong weakening of the potential well depth - W_{LJ} for increasing roughness (well-known "adhesion paradox" discussed in [Ful-75]). In other words, while the ordinary Lennard-Jones potential correspond to the intact material and finally determines the material tensile strength, the modified potential Eq. (2.6.7) corresponds to several order weaker pull-off stress that can be comparable to typical acoustical or mechanical excitations (sections 2.4 and 2.5).

Accepting that each representative volume of the material contains many cracks with identical parameters, we finally write for the contact (adhesive) interaction potential energy per unit volume

$$P_{cont} = S_V W(g) \tag{2.6.9}$$

where S_V is the total area of cracks per unit volume.

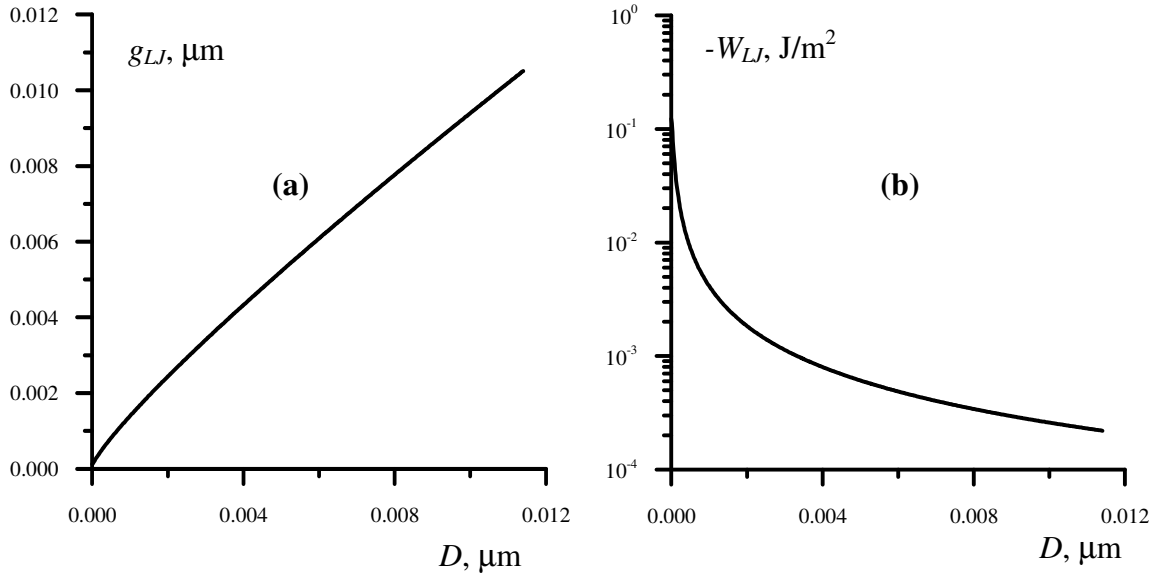

Fig. 2.6.1. Minimum position g_{LJ} (a) and value W_{LJ} (b) of the adhesive potential $W(g)$ as a function of r.m.s. roughness D.

Potential of local deformations

The second component P_{loc} of the potential energy is related to the fact that changing the average crack aperture produces elastic deformations in the vicinity of a crack. This potential energy can be estimated in the following way [Zai-00]. Suppose that a uniform normal stress σ is applied to the faces of a crack of radius R surrounded by an intact material having elastic constants E (Young's modulus) and ν (Poisson's ratio). The elastic energy in that system [Sne-65]

$$U = \frac{8\left(1-\nu^2\right)R^3}{3E}\sigma^2 \tag{2.6.10}$$

corresponds to certain distribution of the crack opening displacement. We, however, shall consider this system as not distributed lamped but lumped, namely as a spring with an elastic constant k. The string extension a is induced by the force $F=ka$. On the other hand, $F=\pi R^2\sigma$. The potential energy of the spring

$$U = \frac{ka^2}{2} = \frac{F^2}{2k} \tag{2.6.11}$$

can be rewritten as

$$U = \frac{3\pi}{64}\frac{E}{\left(1-\nu^2\right)}\left(2\pi R\right)a^2. \tag{2.6.12}$$

In our simple consideration, the spring with the elongation a replaces a crack with a current mean gap g that, in the absence of any neither external action nor adhesion, takes a value G that we shall call "rest gap" hereafter. This means that

$$a = g - G \tag{2.6.13}$$

and Eq. (2.6.12) takes the form

$$U = U(g) = \frac{3\pi}{64}\frac{E}{(1-\nu^2)}(2\pi R)(g-G)^2. \tag{2.6.14}$$

The result Eq. (2.6.14) is obtained for a single crack. Assuming that each representative volume contain a large number of non-interacting cracks, we finally obtain the local strain energy per unit volume as

$$P_{loc} = \frac{L_V}{2\pi R}U(g) = L_V\frac{3\pi}{64}\frac{E}{(1-\nu^2)}(g-G)^2 \tag{2.6.15}$$

where L_V is the total length of crack tips (total perimeter of cracks) per unit volume.

In order to estimate the third component P_{bulk} of the potential energy we remark that total deformation of the material is due to two factors: strain γ of the intact material zones and changes of the crack apertures i.e.

$$\varepsilon = \gamma + S_V(g-G). \tag{2.6.16}$$

Hence, the bulk potential energy (per unit volume)

$$P_{bulk} = \tfrac{1}{2}E\gamma^2 = \tfrac{1}{2}E\left(\varepsilon - S_V(g-G)\right)^2 \tag{2.6.17}$$

The quantities P_{cont} and P_{loc} contain purely geometric parameters S_V and L_V related to cracks geometry and density or, finally, to the degree damage in the material. These parameters can be retrieved by a statistical analysis of thin slices [Nem-01]. We will use $S_V = 10^3$ m^{-1} and $L_V = 10^8$ m^{-2} as a rough estimation.

Evolution equations and double-well potentials

To write out the evolution equations in a rigorous manner it is convenient to use the Lagrangian formalism. The Lagrangian of the system has the form

$$L(u, u_x, u_t, g, g_x, g_t) = \tfrac{1}{2}\rho_0 u_t^2 - P_{bulk}(u_x, g) - P_{loc}(g) - P_{cont}(g) \tag{2.6.18}$$

i.e.

$$L(u, u_x, u_t, g, g_x, g_t) = \tfrac{1}{2}\rho_0 u_t^2 - \tfrac{1}{2}E\left(u_x - S_V(g-G)\right)^2 - C(g) \tag{2.6.19}$$

where $C(g)$ groups all terms related to cracks:

$$C(g) = S_V \frac{H}{12\pi}\left(1+\left(D/g\right)^2\right)^3\left(-\frac{1}{g^2}+\frac{a_0^6}{60}\frac{\left(1+\left(D/g\right)^2\right)^{33}}{g^8}\right)+L_V\frac{3\pi}{64}\frac{E}{\left(1-\nu^2\right)}\left(g-G\right)^2 \tag{2.6.20}$$

Then Lagrange equations

$$\begin{cases}\dfrac{\partial}{\partial t}\left(\dfrac{\partial L}{\partial u_t}\right)+\dfrac{\partial}{\partial x}\left(\dfrac{\partial L}{\partial u_x}\right)-\dfrac{\partial L}{\partial u}=0\\ \dfrac{\partial}{\partial t}\left(\dfrac{\partial L}{\partial g_t}\right)+\dfrac{\partial}{\partial x}\left(\dfrac{\partial L}{\partial g_x}\right)-\dfrac{\partial L}{\partial g}=0\end{cases} \tag{2.6.21}$$

produce an obvious result for the evolution equation:

$$\rho_0 u_{tt} = E u_{xx} - E S_V g_x \tag{2.6.21}$$

that actually coincides with Eq. (2.4.1). The gap g in there is obtained as a solution of the Lagrange equation $\partial L/\partial g = 0$ i.e. by minimizing the potential energy

$$P\left(g\right) = C\left(g\right) + \tfrac{1}{2}E\left(u_x - S_V(g-G)\right)^2. \tag{2.6.22}$$

As we can see, that the evolution of the system is determined by the character of the potential $P(g)$. Depending of its parameters, it can have one or two minima. It is necessary to consider its structure in more detail.

In the absence of external action (u_x=ε=0) Eq. (2.6.22) takes the form

$$P\left(g\right) = C\left(g\right) + \tfrac{1}{2}ES_V^2\left(g-G\right)^2 \tag{2.6.23}$$

which represents the sum of the modified Lennard-Jones potential $W(g)$ with a minimum g_{LJ} (Fig. 2.6.1) and the quadratic function centered on G. A numerical analysis Eq. (2.6.23) shows that $P(g)$ have two minima if the roughness parameter D does not exceed a critical value D_{cr} ($D < D_{cr}$). Large values of D mean that roughness totally eliminates the adhesion effect so that no potential minimum corresponding to adhesion is present. For $D < D_{cr}$, due to summation the actual positions of minima shift but the general sense of Eq. (2.6.23) remains unchanged. It defines a system that can be found in one of two states, "closed" i.e. with a close to g_{LJ}, the adhesive minimum, and "open" i.e. with g close to G, the "natural" unperturbed gap.

Suppose now that some external action appears that produces strain ε. Then, in order to get rid of G in the expression Eq. (2.6.22), it is convenient to introduce

$$s = \varepsilon + S_V\left(1+\alpha\right)G. \tag{2.6.24}$$

instead of ε. By omitting unnecessary constants, the potential $P(g)$ becomes

$$P'(g) = W(g) + ES_V(1+\alpha)g^2/2 - Esg, \tag{2.6.25}$$

where

$$\alpha = \frac{3\pi}{32}\frac{1}{1-\nu^2}\frac{L_V}{S_V^2} \tag{2.6.26}$$

is a characteristics of a cracking in the material.

Here we consider the case $D < D_{cr}$ otherwise a double-well potential does not appear. So, if the adhesion effect is strong enough ($D < D_{cr}$), one minimum or two minima may exist depending on the magnitude of s. This fact actually determines the hysteretic character of the problem. For high $s<s_c$ there is only one minimum (curve (a) in Fig. 2.6.2) located at small gap values g ($g \approx g_{LJ}$ of the adhesive potential, see Fig. 2.6.1 (a)). In the same way, for $s>s_o$ there is only one minimum located at higher gaps $g \approx G + \varepsilon / S_V$ (curve (c)). In an intermediate situation $s_c<s<s_o$, both minima are present (curve (b)) so the state of the system depends on its history. The system will keep staying in the state it was before as long as possible. When this minimum disappears the system is forced to switch to the other state. This behavior fully coincides with the rules of switching introduced in section 2.2 for a hysteretic element $\hat{\gamma}$.

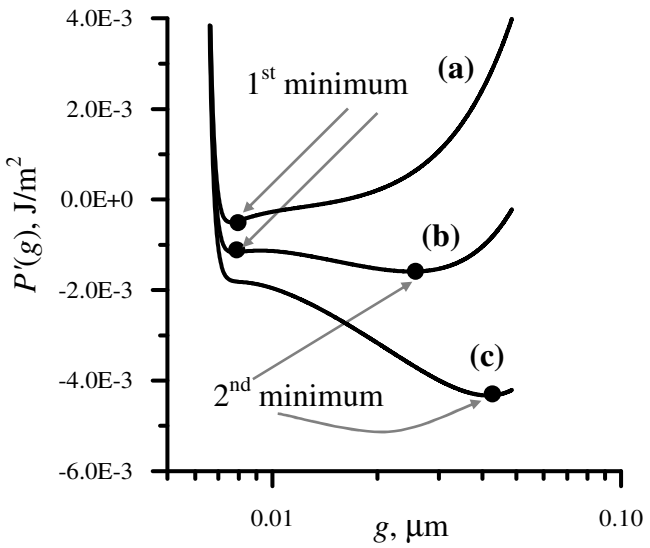

Fig. 2.6.2. Three possible configuration of the potential $P'(g)$ depending on the value of the strain: (a) the only 1st minimum (in the adhesive zone) when $\varepsilon < \varepsilon_c$, (b) double-well potential with both 1st and 2nd minima present (when $\varepsilon_c < \varepsilon < \varepsilon_o$), (c) the only 2nd minimum when $\varepsilon_o < \varepsilon$.

The only difference is the rectangular shape Fig. 2.2.1 (a) of the element $\hat{\gamma}$ and a nontrivial hysteretic form of the solution $g(s)$ depicted in Fig. 2.6.3. The critical values ε_c and

ε_o can be calculated from the critical values s_c and s_o of the auxiliary parameter s shown in Fig. 2.6.3 using Eq. (2.6.20):

$$s_{s,o} = \varepsilon_{s,o} + S_V \left(1+\alpha\right) G . \tag{2.6.27}$$

The difference $\Delta s = s_o - s_c = \varepsilon_o - \varepsilon_c$ can be interpreted as a characteristic of the "strength" of a crack: "weak" cracks switch at small strain excursions and "strong" ones change states at large strain amplitudes. The more rough the coasts of a crack, the weaker it is, until the r.m.s. roughness D exceeds a critical value D_{cr} (which equals $7.30 \cdot 10^{-3}$ μm in our example with the chosen values of parameters S_V, L_V, H, E). For $D > D_{cr}$ the dependency $g(s)$ becomes non-hysteretic. In this case only the second minimum of the potential $P'(g)$ is present. Thus, the highest difference Δs is reached for zero roughness (maximum $\Delta s \approx 0.2$ in our example), and $\Delta s \to 0$ at $D \to D_{cr}$.

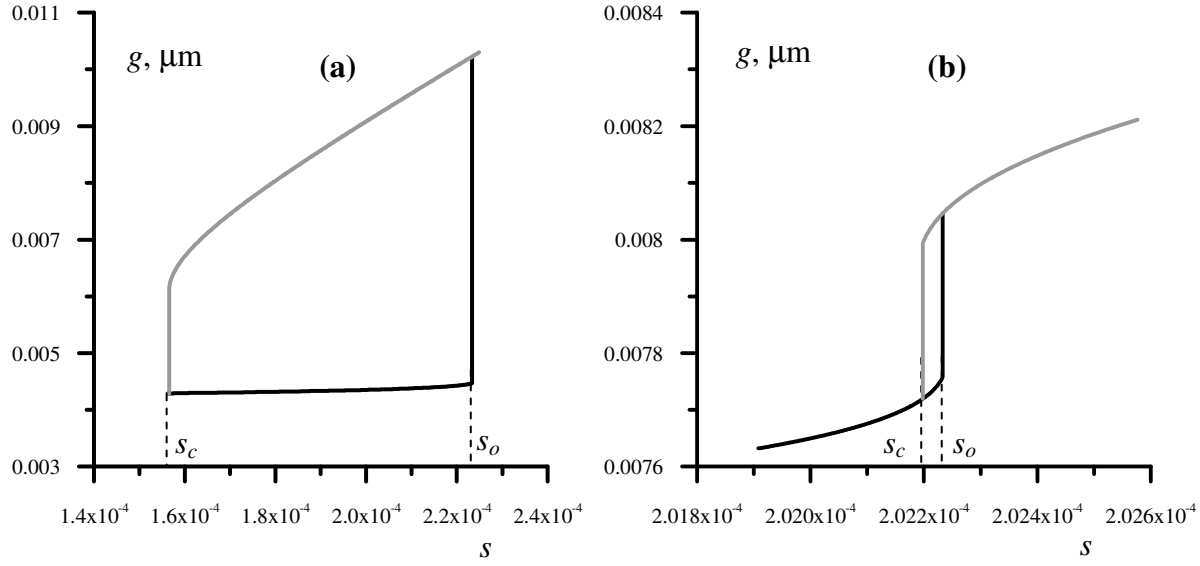

Fig. 2.6.3. Hysteretic aperture for a "strong" (a) and "weak" crack. The "strength" or "weakness" depend on the difference s_o-s_c=ε_o-ε_c that equals the strain variation necessary to switch the crack.

Introducing an ensemble of elements and Preisach density

We have demonstrated that a crack with rough surfaces and adhesion can behave as a bistable element. However, in the Preisach description, an ensemble of such hysteretic elements with different critical parameters must be present. In order to get such an ensemble we have to assume that cracks in a material vary with respect to their rest gaps G and r.m.s. roughness D. Denoting this distribution $\varphi(G,D)$ and accepting that cracks do not interact, we rewrite Eq. (2.6.16) in the form:

$$\rho_0 u_{tt} = E u_{xx} - E S_V \frac{\partial}{\partial x} \int \varphi(G,D)\, g(G,D)\, dG dD\,. \qquad (2.6.28)$$

The resulting Preisach distribution for a uniform distribution $\varphi(G,D)$ is shown in Fig. 2.6.4. Only elements with $-10^{-6} < \varepsilon_o, \varepsilon_c < 10^{-6}$ are plotted. The picture has been obtained with the Monte-Carlo method in which the number of points located in a small rectangle $[\varepsilon_c, \varepsilon_c + \Delta\varepsilon_c] \times [\varepsilon_o, \varepsilon_o + \Delta\varepsilon_o]$ characterize the local value of the density.

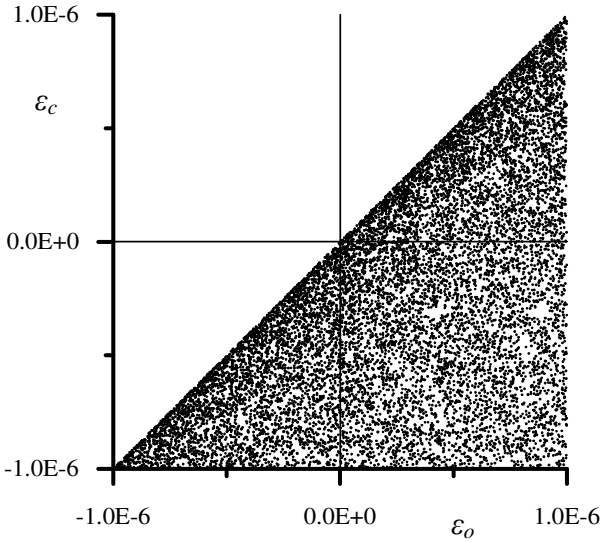

Fig. 2.6.4. The Preisach density $\Pi(\varepsilon_o, \varepsilon_c)$ obtained in the framework of the micro-potential model with a uniform distribution of cracks over G and D (only elements with $-10^{-6} < \varepsilon_o, \varepsilon_c < 10^{-6}$ are plotted).

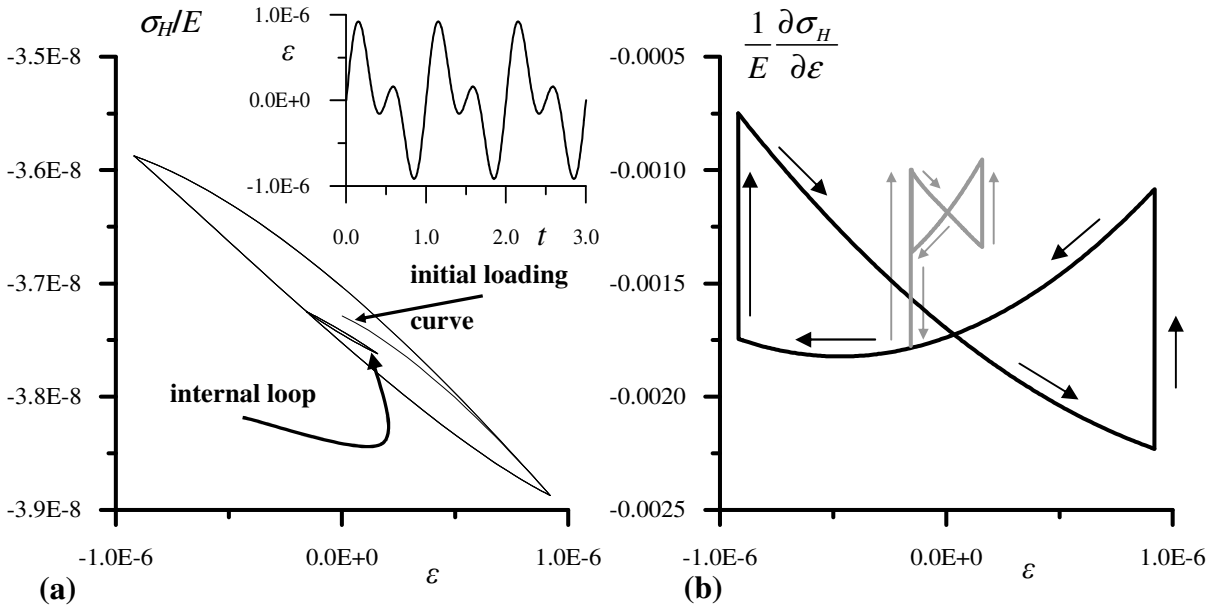

Fig. 2.6.5. Stress-strain relation (a) for a strain excitation $\varepsilon(t) = (0.55 \sin 2\pi t + 0.5 \sin 4\pi t) \cdot 10^{-6}$. An inner loop is observed due to the presence of local extrema in $\varepsilon(t)$. (b) The respective elastic modulus demonstrates a "bow-tie" behavior.

A more practical result of the model is the hysteretic stress-strain relationship and the hysteretic dependency of the effective elastic modulus. The latter shows a "bow-tie" behavior similar to known experimental results [Tut-98], [Boi-97].

It is worth noting that the variability in parameters of individual cracks is not a unique explanation for the Preisach ensemble of elements. The ensemble can exist due to other reasons such as different crack orientation considered in the next sections.

2.7. Adhesion hysteresis model

In this section, an alternative explanation of hysteresis in materials with internal contacts is presented (see also **[Ale-07a], [Ale-05c]), [Ale-05d], [Ale-05e], [Ale-06b], [Ale-06c], [Ale-07b], [Ale-07c], [Ale-09b]**). As it was mentioned, the ensemble of Preisach elements can be attributed to a distribution of cracks orientations. In addition, hysteresis can exist not only at the level of a crack in the form of the bistability due to the summation of the adhesive and elastic potentials. Hysteresis can be observed at the level of an individual asperity that is described by a variety of models of the Johnson-Kendall-Roberts (JKR) type [Joh-85] which include formation and breaking of an adhesive neck. Below those arguments are considered in more detail.

Mesoscopic mechanics

Suppose that a large number of penny-shaped cracks with different orientations given by the spherical angles θ, φ are embedded into a volume filled with an intact material. Due to external loading, each crack experiences a normal displacement $a_{\theta,\varphi}$. Here we neglect tangential crack faces displacements and possible frictional effects and write for the strain components arising due to normal displacements only:

$$\varepsilon_{xx} = \gamma_{xx} - S_V \int_0^{\pi/2} d\theta \int_0^{\pi} d\varphi a_{\theta\varphi} \Psi(\theta,\varphi) \sin^3\theta \cos^2\varphi,$$

$$\varepsilon_{yy} = \gamma_{yy} - S_V \int_0^{\pi/2} d\theta \int_0^{\pi} d\varphi a_{\theta\varphi} \Psi(\theta,\varphi) \sin^3\theta \sin^2\varphi, \qquad (2.7.1)$$

$$\varepsilon_{zz} = \gamma_{zz} - S_V \int_0^{\pi/2} d\theta \int_0^{\pi} d\varphi a_{\theta\varphi} \Psi(\theta,\varphi) \cos^2\theta \sin\theta.$$

Here $\Psi(\theta,\varphi)$ is the orientation distribution and γ_{ii} are the components of the strain tensor for the intact material. The off-diagonal components are not modified since we neglect shearing of the cracks. The minus signs appeared in Eq. (2.7.1) since we define $a_{\theta,\varphi}$ to be positive in compression.

In the sake of simplicity we consider a bar with an isotropic orientation of cracks, i.e. $\Psi(\theta,\varphi)=(2\pi)^{-1}$, and assume that the stress is applied in the z-direction only (unconfined case, i.e. the Young's problem). Then the φ-dependence disappears ($a_{\theta\varphi}=a_\theta$) and the only strain component $\varepsilon=\varepsilon_{zz}$ of interest reduces to

$$\varepsilon = \gamma - S_V \int_0^{\pi/2} a_\theta \cos^2\theta \sin\theta d\theta \tag{2.7.2}$$

with $\gamma=\gamma_{zz}$.

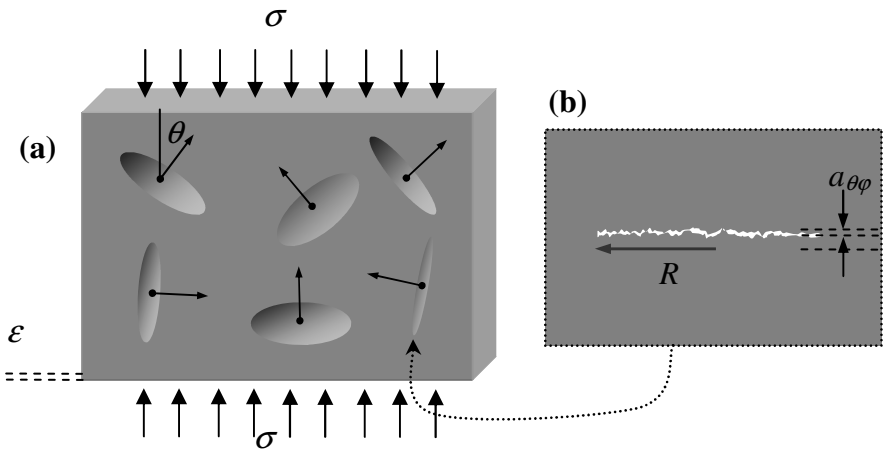

Fig. 2.7.1. (a) Generic medium with penny-shaped cracks (intergranular contacts) at different orientations. One of the cracks of radius R is shown in detail (b). The aperture change (normal displacement of the crack faces) $a_{\theta\varphi}$ is an evolving variable and depends on the orientation angles θ and φ.

In order to use the Lagrange equations as it was done in the previous section, it is necessary to obtain the potential energy (per unit of volume) of the system. We take into account the uniform crack orientation distribution and write

$$P = P_{bulk} + S_V \int_0^{\pi/2} \left(P_{loc} + P_{cont}\right) \sin\theta d\theta, \tag{2.7.3}$$

where P_{bulk} the strain energy density in the intact material, and P_{loc} and P_{con} are local strain energy and contact deformation energies per unit crack surface. Here $\sin\theta$ comes from integration of the orientation distribution over a solid angle. Similarly to the previous section, the expression for P_{bulk} and P_{loc} read:

$$P_{bulk} = \tfrac{1}{2} E\gamma_Z^2 = \tfrac{1}{2} E\left(u_z - S_V \int_0^{\pi/2} a_\theta \cos^2\theta \sin\theta d\theta\right)^2 \tag{2.7.4}$$

$$P_{loc}(a_\theta) = \frac{3\pi}{32}\frac{E}{1-\nu^2}\frac{1}{R}a_\theta^2, \tag{2.7.5}$$

whereas the contact interaction energy can be expressed through the normal contact interaction force (per unit crack surface) as

$$P_{cont}\left(a_\theta\right) = \int_0^{a_\theta} N\left(a\right) da\,. \tag{2.7.6}$$

The details of the derivation are similar to the previous case and are omitted here. Substituting the relevant terms into the Lagrange equations produces the wave equation

$$\rho_0 u_{tt} = \frac{d\sigma}{d\varepsilon} u_{zz} \tag{2.7.7}$$

where the derivative $d\sigma/d\varepsilon$ of the stress-strain relationship contains nonlinear terms that correspond to non-quadratic terms of the potential energy. Calculation of $d\sigma/d\varepsilon$ requires the evaluation of normal displacement a_θ for all crack orientations that can be done using the force balance equation directly following from the Lagrange formalism:

$$\sigma \cos^2\theta + \frac{3\pi}{16}\frac{E}{1-\nu^2}\frac{a_\theta}{R} + N\left(a_\theta\right) = 0\,. \tag{2.7.8}$$

Normal contact interactions with adhesion

We assume the JKR interaction law for the normal reaction curve $N\left(a_\theta\right)$. However, the JKR interaction is defined for a pair of spherical asperities while here we deal rather with a continuous surface roughness of the internal crack faces. To overcome this difficulty, it is suggested to use the decomposition procedure proposed by Whitehouse and Archard in [Whi-70]. As illustrated in Fig. 2.7.2, the procedure relies on the substitution of a real surface $\xi\left(\vec{\beta}\right)$ characterized by a Gaussian distribution $\varphi(\xi)$ of random heights ξ

$$\varphi\left(\xi\right) = \tfrac{1}{\sqrt{2\pi D^2}} \exp\left(-\tfrac{1}{2}\xi^2/D^2\right), \tag{2.7.9}$$

and an exponential correlation function

$$K\left(\beta\right) = \left\langle \xi\left(x\right)\xi\left(x+\beta\right)\right\rangle = \exp\left(-\beta/\beta^*\right) \quad , \tag{2.7.10}$$

by an effective system consisting of a rigid flat surface and a set of spherical asperities with a dual distribution of peaks with heights ζ and curvatures C in the following form:

$$\phi\left(\zeta, C\right) = \tfrac{3}{10\pi\sqrt{2}l^2}\tfrac{1}{D}\exp\left(-\tfrac{1}{2}\left(\zeta/D\right)^2\right)\exp\left[-\left(\zeta/D-\tfrac{1}{2}C\right)^2\right]\mathrm{erf}\left(\tfrac{1}{2}C\right). \tag{2.7.11}$$

In Eq. (2.7.9), D stands for the standard deviation of the surface roughness (r.m.s. roughness), while in Eq. (2.7.10), β^* denotes the roughness correlation radius. Both parameters have the dimension of a length. C is a normalized curvature, linked to the sphere radius r, the roughness standard deviation s and the sampling interval l which is presupposed to be l=2.3β^* in [Whi-70],

$$C = \frac{l^2}{rD}. \qquad (2.7.12)$$

In this effective system the collection of deformable spheres is pressed against the flat rigid surface. The distribution function Eq. (2.7.11) has the sense of the number of peaks per unit surface with coordinates in the range (ζ, ζ+$d\zeta$) and the normalized curvatures in the range (C, C+dC).

The Whitehouse-Archard contact mechanics model combines the above mentioned decomposition procedure with Hertzian force interactions [Lan-93]. In fact, the classical Hertz law describes the elastic interaction of two spheres with differing radii, and thus, in particular, also the interaction of a deformable sphere with a hard wall. In the present model, instead of the Hertzian force, we use of Johnson-Kendall-Roberts mechanics (JKR) [Joh-85] which takes into account adhesion effects and, in particular, adhesion hysteresis, on top of the Hertzian contact law. Below this is explained in more detail.

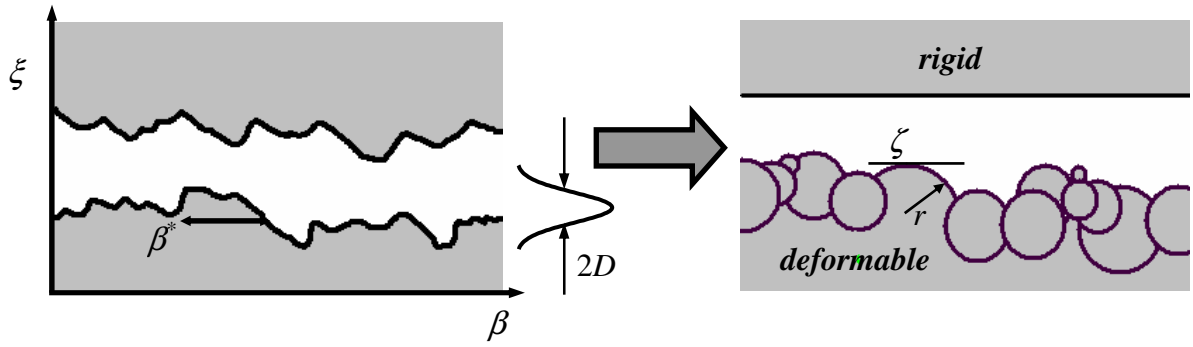

Figure 2.7.2. Illustration of the decomposition procedure by Whitehouse and Archard. Two continuously rough surfaces with a given correlation radius β^* and a roughness standard deviation s (at the left) are substituted by a collection of spheres with various peak coordinates ζ and radii r. The collection of deformable spheres is pressed against a flat rigid surface.

As mentioned before, the main goal of the present study is to demonstrate the fact that the macroscopic hysteresis properties observed in the constitutive equation for the elasticity of materials can be obtained from the hysteretic force-displacement relationship existing at the microcontacts (asperities in contact). To do this, we have chosen the JKR adhesion mechanics [Joh-85]. It is certainly not the most modern and not the most precise model, with a quite limited range of applications (very soft and compliant systems), but definitely one of the simplest, and for the sake of simplicity, we will reduce it even more.

In the JKR model, the normalized force f of a deformable sphere with radius r interacting with a flat rigid surface at a normalized displacement (interference) δ is given by the following two equations in a parametric form:

$$f = c^3 - c\sqrt{6c}, \quad \delta = c^2 - \tfrac{2}{3}\sqrt{6c}\,. \tag{2.7.13}$$

Here, c is the normalized microcontact radius (see Fig. 2.7.3). The normalization constants are:

$$\delta_0 = \left(\frac{3\pi\Gamma\left(1-\nu^2\right)}{4E}\right)^{\frac{2}{3}} r^{\frac{1}{3}}, \quad f_0 = \pi r\Gamma \tag{2.7.14}$$

for the spatial variables δ and c, and for force f, respectively. Here Γ is the surface energy.

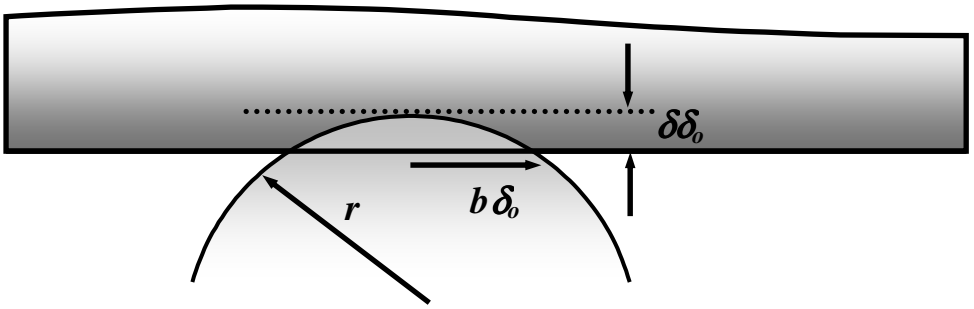

Fig 2.7.3. Contact between a deformable spherical asperity (shown undistorted) and a hard flat surface.

The typical behavior of the force-displacement curve for the JKR mechanics is hysteretic (Fig. 2.7.4 (a)): if the interference δ increases from highly negative values (large separation between the bodies), the contact is absent till δ=0, where it suddenly forms with a negative force due to the adhesive attraction. Further increase of the displacement asymptotically follows a Hertzian-type contact law. If, inversely, the interference decreases from highly positive values (high compression), then a neck is formed at δ=0. At a critical interference $\delta = -\delta_n = -6^{1/3}/2$, the neck breaks, the contact disappears, and the force returns to zero.

For the use in the numerical modeling, we will simplify the JKR model even further and neglect the non-trivial behavior of the force while the neck exists. Doing so, we obtain a simplified adhesion mechanics model in which the force is assumed to be constant during the existence of the neck. A best fit to the JKR model yields $\Delta f = 1.21$. The advantage of the simplification is that we can easily decompose the force-displacement curve in a hysteretic and a non-hysteretic part in the following way:

$$f(\delta) \approx f_{NH}(\delta) + f_H(\delta) \tag{2.7.15}$$

with

$$f_{NH}(\delta) = \begin{cases} \delta^{3/2} & if\ \delta > 0 \\ 0 & if\ \delta < 0 \end{cases} \tag{2.7.16}$$

and

$$f_H(\delta)=\begin{cases}0 & \text{if } \delta<-\delta_n\\ -\Delta f & \text{if } \delta>0\\ 0 & \text{if } -\delta_n<\delta<0 \text{ and } \delta \text{ is increasing}\\ -\Delta f & \text{if } -\delta_n<\delta<0 \text{ and } \delta \text{ is decreasing}\end{cases} \tag{2.7.17}$$

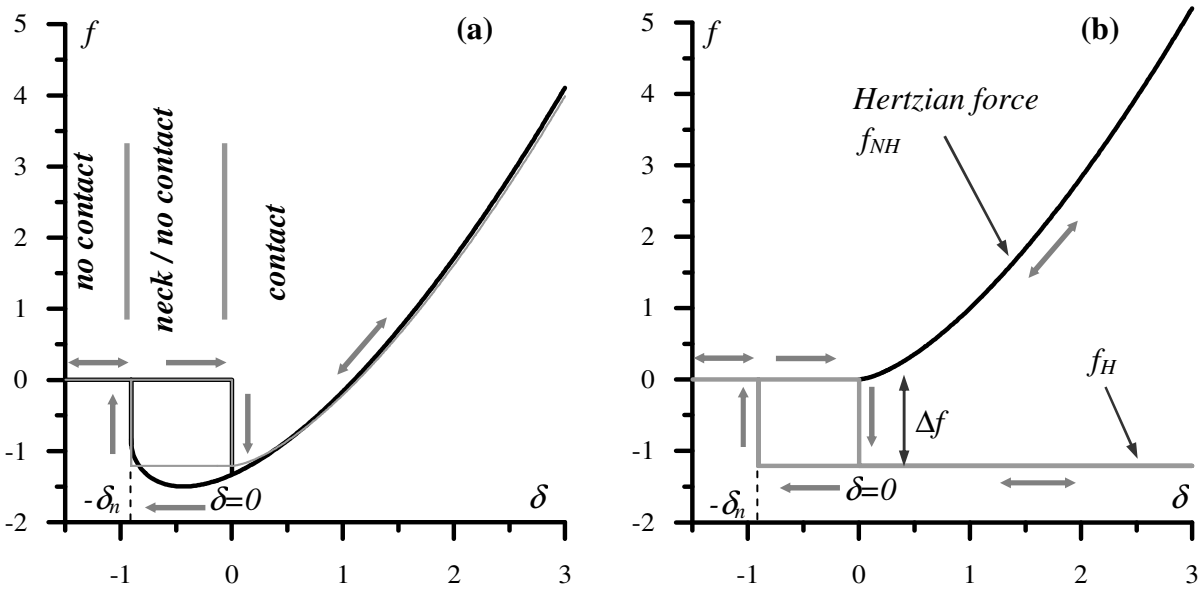

Figure 2.7.4. (a) JKR contact mechanics: the thick black line shows the force-displacement relationship $f(\delta)$ taking into account the microscopic adhesion hysteresis. (b) The simplified hysteretic (gray) and the non-hysteretic (Hertzian, black line) force components are displayed individually.

Note that the non-hysteretic component exactly corresponds to the Hertz solution and that the hysteretic force has a purely rectangular form (Fig. 2.7.4(b)).

This result completes the microscopic level of our description. We now return to the contact mechanics equations on the mesoscopic level, and proceed later to the macroscopic stress-strain equation. Having defined the force acting on an individual asperity in contact, together with the statistics of the asperities themselves, the force-displacement relationship for a rough surface yields:

$$N=\int_0^\infty\int_0^\infty \phi(\zeta,C)\, f_0 f(\delta)\big|_{\delta=(\zeta-g)/\delta_0}\, d\zeta\, dC\,, \tag{2.7.18}$$

where g is the average gap between crack faces (mean width of an intergranular contact). The normalization constants f_0 and δ_0 (depending on r) are taken from Eq. (2.7.14), and the radius r of the current asperity is linked to curvature C through Eq. (2.7.12).

Since $f(\delta)$ can be split into a hysteretic and a non-hysteretic component, we can also rewrite the above integral (Eq. 2.7.18) in the form of a sum of N_{NH} and N_H, where the non-hysteretic component

$$N_{NH} = \int_0^\infty dC \int_a^\infty d\zeta\, f_0 \phi(\zeta, C) \left((\zeta - g)/\delta_0\right)^{3/2} = \frac{\sqrt{2}}{5\pi} \frac{E}{1-\nu^2} \frac{D}{l} \psi\left(g/D\right) \tag{2.7.19}$$

in which [Oni-73]

$$\psi(x) = \int_0^\infty dC \int_x^\infty dy \exp\left(-\tfrac{1}{2} y^2\right) \exp\left[-\left(y - \tfrac{1}{2} C\right)^2\right] \operatorname{erf}\left(\tfrac{1}{2} C\right) (y - x)^{3/2} \tag{2.7.20}$$

is a known single variable function plotted in Fig. 2.7.5.

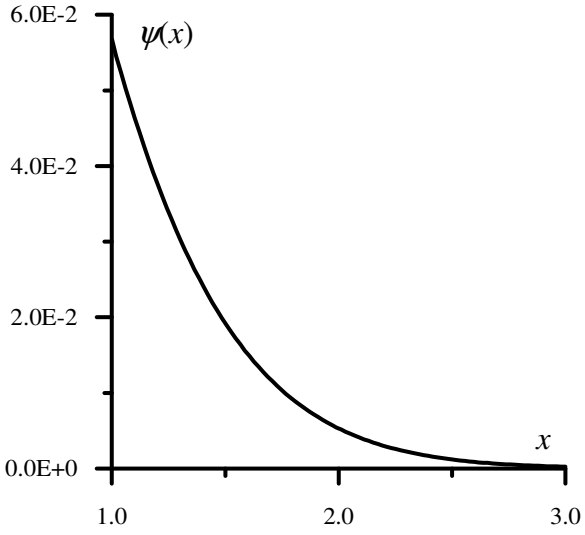

Figure 2.7.5. Function $\psi(x)$ (Eq. 2.7.20) characterizing the non-hysteretic component N_{NH} (Eq. 2.7.19) of the force-displacement.

In Eq. (2.7.8) the contact force is defined as a function of the normal displacement between crack faces $a=g-G$ (corresponds to Eq. (2.6.13) of the previous section). Hence, the expression for the non-hysteretic force finally reads:

$$N_{NH}(a) = \int_0^\infty dC \int_a^\infty d\zeta\, f_0 \phi(\zeta, C) \left((\zeta - g)/\delta_0\right)^{3/2} = \frac{\sqrt{2}}{5\pi} \frac{E}{1-\nu^2} \frac{D}{l} \psi\left(\frac{a+G}{D}\right). \tag{2.7.21}$$

The Gaussian distribution Eq. (2.7.9) for rough surface heights produces a common problem: a non-zero interaction force exists even if crack faces are infinitely separated. In practice, the problem can be solved by setting $\psi(x)=0$ for x exceeding some accepted critical value of order of 2-3 standard deviations D. We also assume that this critical value corresponds to the rest aperture G i.e. in the unstrained state crack faces are about to tough each other (or touch each other at one point). Note that this assumption is different from the one accepted in the

previous section where a distributions over G was postulated (all crack have different rest apertures).

In section 2.8 other expressions for the non-hysteretic normal reaction force are derived based on more modern approaches in contact mechanics.

Preisach description for aligned cracks

The hysteretic contribution N_H will also be expressed as a function of the normal displacement a but in a history-dependent manner, because it contains the function $f_{NH}(\delta)$ which can take on one of two values for $-\delta_n<\delta<0$, depending on the δ-history. In order to calculate this term in the most computationally economical way, we define two new dimensionless variables a_c and a_o instead of ζ and C:

$$a_c = \zeta/D, \quad a_o = \zeta/D + (\lambda/C)^{1/3}, \tag{2.7.22}$$

with

$$\lambda = 3\left(\frac{3\pi\Gamma(1-\nu)^2 l}{4ED^2}\right)^2, \tag{2.7.23}$$

and also introduce the dimensionless normal displacement $a^*=a/D$.

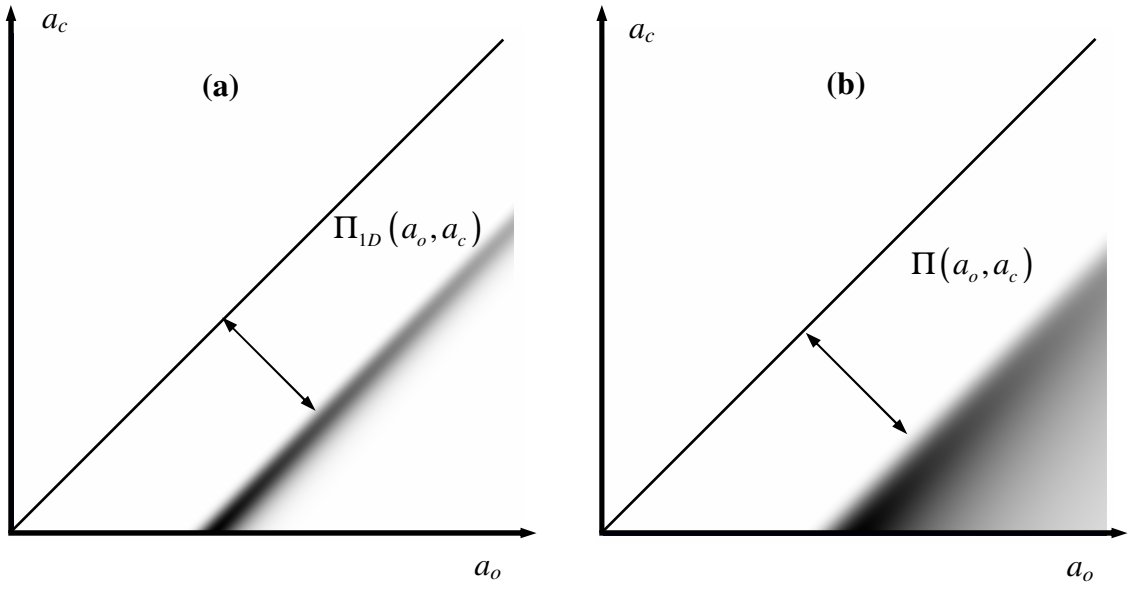

Fig 2.7.7. Grayscale plot of the hysteretic density for an individual penny-shape crack with a rough surface in the material (a) and for a statistical ensemble of diversely oriented cracks with an isotropic distribution (b). The width of the empty band (marked with the double arrow) in both figures depends on λ. It increase if λ increases.

If is straightforward to show, for an asperity with given parameters ζ and C (or a_c and a_o), that the neck of the contact breaks when the dimensionless normal displacement a^* exceeds a_o upon increasing a^* (i.e. decreasing δ), and that the contact appears when a^* becomes less than a_c upon decreasing the aperture a (i.e. increasing δ). This evolution rule fully corresponds to the Preisach system definition in the space (a_o,a_c) in which the hysteretic force is determined by the integral on elements in the Preisach space:

$$N_H(a) = -\iint\limits_{\Omega(a/D)} \Pi_{1D}(a_o, a_c)\, da_o da_c \tag{2.7.24}$$

where $\Pi_{1D}(a_o, a_c)$ is a density distribution that can be derived from the dual distribution Eq. (2.7.11) of the peak heights and curvatures sitting in Eq. (2.7.18). In fact, $\Pi_{1D}(a_o, a_c)$ should be regarded as the hysteretic contribution to the contact force from all asperities with characteristics (a_o,a_c) in the range (a_o, a_o+da_o) and (a_c, a_c+da_c) belonging to a single crack:

$$\Pi_{1D}(a_o, a_c) = \tfrac{9}{10\sqrt{2}} \tfrac{\Gamma}{D} \Delta f \exp\left(-\tfrac{1}{2}a_c^2\right) \exp\left(-\left(a_c - \tfrac{1}{2}C\right)^2\right) \operatorname{erf}\left(\tfrac{1}{2}C\right) / (a_o - a_c)\Big|_{C=\lambda/(a_o-a_c)^3}. \tag{2.7.25}$$

The structure of this density is illustrated in the grayscale plot in Fig. 2.7.7 (a). A nonzero density is localized in a narrow band. The offset from the diagonal is only controlled by parameter λ defined in Eq. (2.7.23). The band width is a function of λ as well: the larger λ, the larger are both the offset and the band width.

The integration in Eq. (2.7.24) must be performed over the area $\Omega(a)$ which contains only the asperities in contact experiencing a nonzero interaction force. The argument of Ω (the normal normalized displacement a/D) specifies the variable that is responsible for switching the points in (a_o, a_c)-space and whose history the system remembers.

This completes the derivation of the force-displacement relation for a contact between rough surfaces. We now move from the mesoscopic scale of our model to the macroscopic part of analysis. By substituting the obtained expressions Eq. (2.7.23) and Eq. (2.7.24) for $N(a_\theta)$=$N_{NH}(a_\theta)$+$N_H(a_\theta)$ into the equilibrium condition Eq. (2.7.8) the latter takes on the following form:

$$\sigma \cos^2\theta = \frac{3\pi}{16}\frac{E}{1-\nu^2}\frac{a_\theta}{R} - \frac{\sqrt{2}}{5\pi}\frac{E}{1-\nu^2}\frac{D}{l}\psi\left(\frac{a_\theta + G}{D}\right) + \iint\limits_{\Omega(a_\theta/s)} \Pi_{1D}(a_o, a_c)\, da_o da_c\,. \tag{2.7.26}$$

Remember that here the dimensional aperture a_θ depends on the orientation angle θ.

It is convenient to rewrite this equation by expanding all non-hysteretic terms in a Taylor series, which is possible since the nonlinearity for small aperture changes is expected to be weak. The expansion yields:

$$\sigma\cos^2\theta = K\left[a_\theta^* + \beta_2\left(a_\theta^*\right)^2 + \beta_3\left(a_\theta^*\right)^3 + \beta_4\left(a_\theta^*\right)^4\right] + \iint\limits_{\Omega\left(a_\theta^*\right)} \Pi_{1D}\left(a_o, a_c\right) da_o da_c \,. \tag{2.7.27}$$

Preisach description for diversely oriented cracks

Finally, we obtain the macroscopic stress-strain relation as the solution of the following set of equations:

$$\varepsilon = \sigma/E + S_V D \int_0^{\pi/2} a_\theta^* \cos^2\theta \sin\theta d\theta \,, \tag{2.7.28}$$

$$\sigma\cos^2\theta = Ka_\theta^* + \Phi_{NL}\left(a_\theta^*\right), \tag{2.7.29}$$

where $\Phi_{NL}(a_\theta{}^*)$ summarizes all nonlinear contributions to the force opposing the stress: the higher order terms in the polynomial expansion in Eq. (2.7.27) and the hysteretic component represented by the double integral.

$$\Phi_{NL}\left(a_\theta^*\right) = K\left[\beta_2\left(a_\theta^*\right)^2 + \beta_3\left(a_\theta^*\right)^3 + \beta_4\left(a_\theta^*\right)^4\right] + \iint\limits_{\Omega\left(a_\theta^*\right)} \Pi_{1D}\left(a_o, a_c\right) da_o da_c \tag{2.7.30}$$

Further simplification of the solution Eqs. (2.7.28)-(2.7.29) using the first order perturbation method with a small parameter

$$\alpha = \frac{S_V DE}{5K} \,. \tag{2.7.31}$$

provides the following form:

$$\varepsilon = \frac{1+\alpha}{E}\sigma - \frac{5\alpha}{E}\left(\iint\limits_{\Omega\left(\frac{\sigma}{K}\right)} \rho\left(a_o, a_c\right) da_o da_c + \tfrac{K}{7}\beta_2\left(\tfrac{\sigma}{K}\right)^2 + \tfrac{K}{9}\beta_3\left(\tfrac{\sigma}{K}\right)^3 + \tfrac{K}{11}\beta_4\left(\tfrac{\sigma}{K}\right)^4\right) \tag{2.7.32}$$

where the hysteretic density ρ is expressed as

$$\Pi\left(a_o, a_c\right) = \int_0^{\pi/2} \Pi_{1D}\left(a_o\cos^2\theta, a_c\cos^2\theta\right)\cos^4\theta\sin\theta d\theta \,. \tag{2.7.33}$$

In Fig. 2.7.7, we plotted both hysteretic densities: Π_{1D} (plot (a)) for a set of individual penny-shaped cracks with the same orientation normal to the applied stress and Π (plot (b)) for a statistical ensemble with isotropic orientation, corresponding to Eqs. (2.7.25) and (2.7.33), respectively. We observe that the presence of cracks with oblique orientations increases the number of elements that switches at higher stresses. The larger the angle, the further the elements are located away from the diagonal. This is a direct influence of the factor $\cos^2\theta$ in Eq. (2.7.8) which reflects the fact that inclined cracks are less sensitive to the given stress. As a result, the width of the band containing the nonzero density of hysteretic elements increases considerably.

Qualitative comparison with experimental data and discussion

Now we proceed to the simulation of an acoustical experiment. In the 1D case, the simulation of a longitudinal standing wave in an acoustical resonator simply involves solving the wave equation on a 1D interval with a harmonic stress excitation at one edge and a stress-free condition at the other end. The contact parameters S_V, D, R, and β^* were adjusted in the course of the simulations to match the experimentally measured data obtained from a SIMONRUS experiment (Single Mode nonlinear Resonance Ultrasonic Spectroscopy [Ten-04]).

The study of the nonlinear elastic behavior of geomaterials [Ten-04] shows experimentally for two different rocks that three regimes can be distinguished in the behavior of the resonant frequency as a function of the strain amplitude: a region with almost no change in the frequency for small strain amplitudes, a quadratic dependence for moderate strains (~10^{-7}) and a linear shift for larger amplitudes. In general our numerical simulations show a similar dependence, with some differences however (Fig. 2.7.8 (a)).

For small strain amplitudes (less than or of the order of the width of the empty band near the diagonal in the hysteretic density), we predict a slight frequency increase which is usually not reported in the experiments. The frequency increase in the simulation is due to the non-zero cubic nonlinearity β_3 in the non-hysteretic contribution to $\Phi_{NL}(a)$ which causes a hardening effect. Note that the quadratic nonlinear term, with nonlinearity parameter β_2, does not modify the resonant frequency in the first order of the perturbation theory, and the influence of the fourth order nonlinear term is also negligible. So the impact of the non-hysteretic nonlinearity (anharmonicity of the intergranular potential) on the resonant frequency is mainly due to the cubic term. Based on available experimental observations, we performed a matching of the remaining non-hysteretic parameters such that the hardening effect is minimized (S_V=5·10^4 m^{-1}, D=1.8 nm, β^*=15 nm). By and large, one can expect that this hardening effect is considerably overestimated by the model. Indeed, all known contact mechanics models generally match at best the fundamental behavior of the force-displacement relation. However, subtle things as the cubic term in the expansion of these relationships can differ considerably from the true values and this may have a major impact on the simulation results.

The second slight difference is the behavior of the resonant frequency at high strain amplitudes. The general character of a linear reduction is confirmed by various experiments. In our model, however, we see a tendency towards saturation (Fig. 2.7.8(a)). The saturation is due to the fact that the hysteretic density in the non-zero band of the Preisach space is decaying away from the diagonal **[Van-04]**, [Van-05a]. This effect is more pronounced for materials with delaminations and preferential orientations of cracks leading to densities

similar to Fig. 2.7.7(a). Observations of this saturation effect were already reported for concrete and composites samples subjected to cyclic 3 point-bending fatigue ([Van-00a] and [Van-05b]).

Figure 2.7.8(b) illustrates the behavior of the second and third harmonics versus the fundamental strain component. The third harmonic is dominating as is typically observed in materials of this kind. The second harmonic can be perfectly fitted with a parabolic curve, since it is almost not affected by the hysteresis and arises due to the quadratic nonlinearity. Indeed, it is known that purely hysteretic stress-strain relationships do not produce even harmonics [Ber-98], in the case of constant hysteretic density. Even harmonics can be generated if the Preisach density is considerably asymmetric in the diagonal $a_c=a_o$ direction **[Gus-02]**.

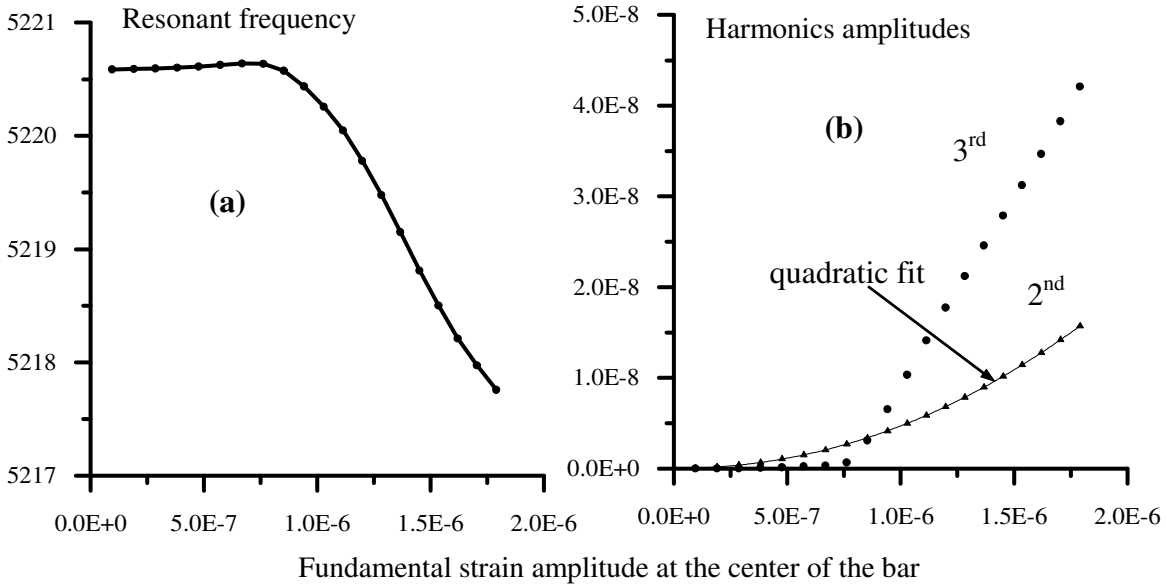

Fig. 2.7.8. Simulation of a resonant bar experiment, showing the dependence of the resonant frequency (a) and of the harmonic's amplitudes (b) on the fundamental strain amplitude in the center of a resonating bar. The material constants used for the simulation are E=20 GPa, ν=0.35, R=20 μm, Γ=4.4 J/m^2, S_V=5·10^4 m^{-1}, D=1.8 nm, β^*=15 nm.

Many experiments show that the third harmonics also behaves as the square of the strain amplitude ([Naz-00], [Van-00b]) at least for high enough strains. In our simulations, the third harmonic characteristic does not allow a simple polynomial fit. Its amplitude dependence is clearly influenced by the nontrivial hysteretic density. It is likely that the predicted density located far away from the diagonal is underestimated in the model and that therefore the simulated hysteresis contribution at high strains is weaker than in reality.

2.8. Hysteresis in solids with dry friction

In this section we present the third example **[Ale-07d], [Ale-06d], [Ale-07d], [Ale-06c], [Ale-07b], [Ale-07c], [Ale-09b]** of possible physical mechanisms underlying the Preisach description that considerably differs from the other two. It takes into account friction and neglects adhesion. Since friction is involved, it essentially uses tangential contact interactions in addition to normal ones. Finally, the Preisach hysteresis also appears here but not as a result of a double-well potential existing in the system. Moreover, the Preisach elements can not be attributed to bistable cracks nor asperities. Hysteresis appears as a collective effect of a system of frictional crack having different orientations. For any external loading at the level of a sample, a local loading state at the level of a crack considerably differs for each crack because of the orientation distribution. Depending on orientation, local normal and tangential stresses applied to crack faces can drastically vary. The orientation effect results in the fact that, at a given external loading state, interfaces of some cracks slide while interfaces of other ones do not. We will show that the collective behavior of a set of diversely oriented cracks produces the Preisach hysteresis.

Mesoscopic mechanics

The geometry of the problem is shown in Fig. 2.8.1. As previously, we consider a set of penny-shaped cracks of equal (for simplicity) radius R having some orientation distribution over spherical angle θ. At a mesoscopic level, each crack is embedded into an infinite volume of material with certain linear elastic properties. At the microscopic scale, cracks have rough surfaces having proper contact interaction laws that include roughness statistics.

The mesoscopic equilibrium equations are similar to Eq. (2.7.8) but contain the tangential component in addition to the normal one,

$$\begin{cases} -\Sigma_n = k_n a\left(N\right) + N \\ -\Sigma_t = k_t b + T \end{cases}, \tag{2.8.1}$$

where $a(N)$ is the normal force-displacement relationship for contact of rough surfaces, N and T are normal and tangential (frictional) forces per unit area, and $k_n a$, $k_t b$ are effective "restoring forces" arising from local deformation of material in the vicinity of crack tips that opposes any attempts to create nonzero displacements a and b. Here coefficients k_n and k_t are given by

$$k_n = \frac{3\pi}{16}\frac{E}{R\left(1-\nu^2\right)},\ k_t = \frac{3\pi}{16}\frac{E}{R\left(1+\nu\right)}. \tag{2.8.2}$$

The expression for the normal coefficient coincides with the previously used Eq. (2.7.8) and with the calculation by Lawn and Marshall (see [Law-98] and references therein). The form of

the tangential coefficient follows from the findings [Bil-68] which guarantee the identity of solutions for normal and tangential problems by means of a substitution $b \to a/(1-\nu)$. The identical expressions for coefficients k_n and k_t have been used in [Zai-00].

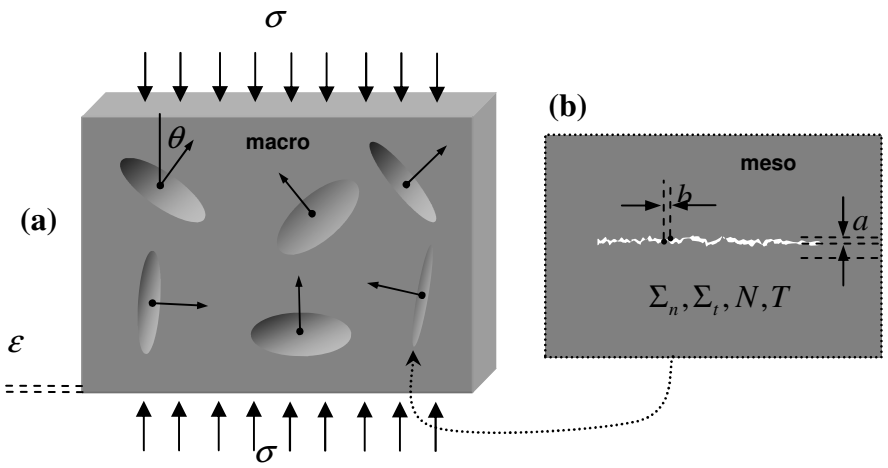

Fig. 2.8.1. (a) Macroscale: elastic material containing a large number of diversely oriented independent penny-shaped cracks. (b) Mesoscale: single crack imbedded in an infinite volume of material. N and T are contact forces, Σ_n and Σ_t are stresses applied to crack faces. Microscale corresponds to asperities on rough contact surfaces and is not shown.

In Eq. (2.8.2) $a(N)$ is the normal reaction curve for the contact between rough surfaces; its physical origin is in the compressive deformations of asperities. Friction force T per unit area is the assumed to be of Coulomb type which means that there is no simple functional relation between T and b. The frictional force is hysteretic and depends on history of the both displacements a and b, in contrary to the dependency between a and N which, for systems without adhesion and adhesion, is biunique. The Coulomb law for the friction force reads:

$$T = \begin{cases} \mu N \operatorname{sgn}(F), & if\ |F| \geq \mu N, \\ F, & if\ |F| \leq \mu N, \end{cases} \tag{2.8.3}$$

where

$$F = -\Sigma_t - k_t b\,. \tag{2.8.4}$$

Eqs. (2.8.1)-(2.8.4) govern the evolution of the system at the level of an individual crack that, in accordance to Eq. (2.8.3) can be found in ore of two states: slip (upper line in Eq. (2.8.3)) or stick (lower line). In the former case, the value of the friction force T is fixed by the Coulomb friction law, and the second Eq. (2.8.1) becomes equation for the tangential displacement b. In the case of stick, in contrast, the displacement b is known and equals the displacement value b_{old} at the previous moment of time, so that the second Eq. (2.8.1)

becomes equation for the friction force T. In both cases, Eqs. (2.8.1) can be solved if mesoscopic stresses Σ_n and Σ_t are given.

Consider now the case of uniaxial stress compression where $\sigma_{zz} \equiv \sigma$ is the only nonzero component of the macroscopic stress tensor. It is straightforward (see **[Ale-07d]**) to obtain the connection between σ and stresses Σ_n and Σ_t related to a crack having the angle θ between its normal and stress axis z:

$$\Sigma_n = \sigma \cos^2 \theta, \; \Sigma_t = \sigma \cos\theta \sin\theta . \tag{2.8.5}$$

The solution to the mesoscopic-level equations (Eqs. (2.8.1)-(2.8.5)) provides the effective displacements a and b related a crack with orientation angle θ. Those displacements pay an additional contribution into the total strain tensor. In particular, the zz-component of the total strain

$$\varepsilon_{zz} \equiv \varepsilon = \frac{\sigma}{E} - S_V \int_0^{\pi/2} \sin\theta \cos\theta \left(a\cos\theta + 2b\sin\theta \right) d\theta \tag{2.8.6}$$

is obtained **[Ale-07d]** by integrating for all cracks with the different orientation angles θ. As previously, S_V is the total area of cracks per unit of volume. Eqs. (2.8.1)-(2.8.6) fully determine the stress-strain relationship in the crack friction model in the case of uniaxial stress compression.

Consider the hysteretic part of the nonlinear strain component γ and prove that the crack friction model belongs to the class of the Preisach systems. In the integrand in Eq. (2.8.6) the first term is related to normal contact interaction. It can be calculated directly from the load-displacement curve $a(N)$ and the first balance equation Eq. (2.8.1). Since we neglect adhesion, plasticity and any other factors that may lead to hysteretic in the normal contact interaction, the first term provides fully reversible (non-hysteretic) contribution. Hysteresis is contained only in the second, friction-related term of Eq. (2.8.6)

$$\varepsilon_b = -2S_V \int_0^{\pi/2} b \sin^2\theta \cos\theta d\theta . \tag{2.8.7}$$

The calculation is more compact in the case when the entire normal "external" stress σ is equilibrated only by contact interaction, and the influence of the restoring force i.e. of deformation of the surrounding intact material is negligible (an original system that contains both contributions can be considered analogously). Thus, the final form of the balance equations (2.8.1) is

$$\begin{cases} -\sigma \cos^2\theta = N \\ -\sigma \cos\theta \sin\theta = k_t b + T \end{cases} . \tag{2.8.8}$$

Note that for stress compression tests σ is negative, *N*, *a*, and *b* are positive, while *T* can have any sign.

Loading and unloading of a collection of cracks

A simple example that illustrates the behavior of the crack friction model is a loading-unloading protocol in which σ changes from 0 to its minimum value σ_m and then increases back to 0. Suppose then that there is a critical orientation angle for which the crack faces start sliding i.e. both conditions in Eq. (2.8.3) are satisfied simultaneously:

$$T = F = \operatorname{sgn}(F)\mu N, \tag{2.8.9}$$

and, in addition, b=0. Combining these conditions results in the known expression

$$\operatorname{tg}\theta_0 = \mu. \tag{2.8.10}$$

This means that for angles smaller than θ_0 the tangential displacement b=0 while, for larger angles, it can be determined from the slip condition T=μN:

$$b = -\begin{cases} 0, & if\ 0 \le \theta \le \theta_0 = \operatorname{arctg}\mu \\ \dfrac{\sigma}{k_t}\left(\sin\theta\cos\theta - \mu\cos^2\theta\right), & if\ \theta_0 < \theta \le \frac{\pi}{2} \end{cases}. \tag{2.8.11}$$

The hysteretic strain component $\varepsilon_b \equiv \varepsilon_L$ for loading consequently becomes

$$\varepsilon_L = \frac{2S_V}{k_t}\sigma\int_{\theta_0}^{\pi/2}\left(\sin\theta\cos\theta - \mu\cos^2\theta\right)\sin^2\theta\cos\theta d\theta.$$

In the following we will need functions

$$\begin{aligned} P(\theta) &= \int_{\theta_0}^{\theta}\left(\sin\theta' + \mu\cos\theta'\right)\sin^2\theta'\cos^2\theta' d\theta' \equiv \\ &\equiv \left(-\tfrac{1}{3}\cos^3\theta' + \tfrac{1}{5}\cos^5\theta' - \tfrac{1}{5}\mu\sin\theta'\cos^4\theta' + \tfrac{1}{15}\mu\cos^2\theta'\sin\theta' + \tfrac{2}{15}\mu\sin\theta'\right)\Big|_{\theta_0}^{\theta} \end{aligned}, \tag{2.8.12}$$

and

$$\begin{aligned} Q(\theta) &= \int_{\theta_0}^{\theta}\left(\sin\theta' - \mu\cos\theta'\right)\sin^2\theta'\cos^2\theta' d\theta' \equiv \\ &\equiv \left(-\tfrac{1}{3}\cos^3\theta' + \tfrac{1}{5}\cos^5\theta' + \tfrac{1}{5}\mu\sin\theta'\cos^4\theta' - \tfrac{1}{15}\mu\cos^2\theta'\sin\theta' - \tfrac{2}{15}\mu\sin\theta'\right)\Big|_{\theta_0}^{\theta} \end{aligned} \tag{2.8.13}$$

where $\operatorname{tg}\theta_0 = \mu$. With this definition, ε_L simply reads:

$$\varepsilon_L = \frac{2S_V}{k_t}Q\left(\tfrac{\pi}{2}\right)\sigma. \tag{2.8.14}$$

Suppose now that σ increases from negative σ_m to lower absolute values. Condition

$$b = b_{old} = -\frac{\sigma_m}{k_\tau}\left(\sin\theta\cos\theta - \mu\cos^2\theta\right),$$

together with Eq. (2.8.9) (in which sgn(F)=-1 since slip changes direction) define a new critical orientation angle $\theta=\theta^*$ for which the crack faces are about to slide,

$$\operatorname{tg}\theta^* = \mu\frac{\sigma_m+\sigma}{\sigma_m-\sigma}. \tag{2.8.15}$$

Two angles θ_0 and θ^* (obviously, $\theta_0\le\theta^*$) define three intervals in the angular range $0\le\theta\le\pi/2$ such that

$$b=-\begin{cases} 0, & if\ 0\le\theta\le\theta_0=\operatorname{arctg}\mu \\ \dfrac{\sigma_m}{k_t}\left(\sin\theta\cos\theta-\mu\cos^2\theta\right), & if\ \theta_0<\theta\le\theta^*=\operatorname{arctg}\left(\mu\dfrac{\sigma_m+\sigma}{\sigma_m-\sigma}\right) \\ \dfrac{\sigma}{k_t}\left(\sin\theta\cos\theta+\mu\cos^2\theta\right), & if\ \theta^*<\theta\le\frac{\pi}{2} \end{cases}. \tag{2.8.16}$$

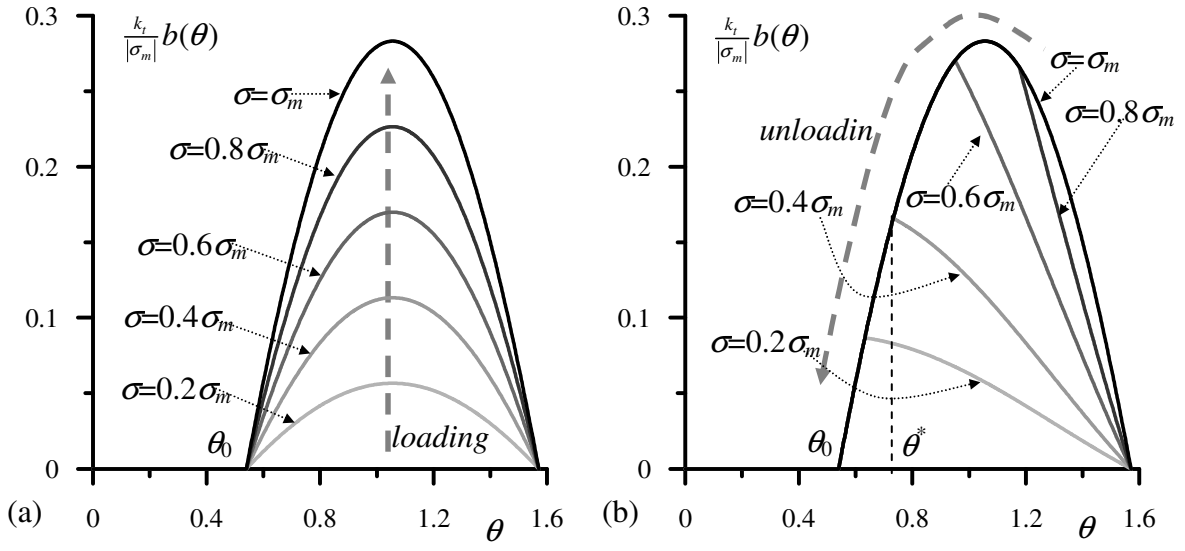

Fig. 2.8.2. The distribution of the normalized tangential displacement $\frac{k_t}{|\sigma_m|}b(\theta)$ as a function of the orientation angle θ for a simple compressive loading-unloading protocol: (a) initial loading phase (σ decreasing from 0 to σ_m, cracks with $\theta_0<\theta<\pi/2$ slide; (b) unloading phase (σ increasing from σ_m to 0, cracks with $\theta^*<\theta<\pi/2$ slide. In both sets, the gray scale of the lines is darker for larger values of $|\sigma|$ (σ is negative in compression). Darker curves are plotted on top of the lighter ones and can mask them.

The distributions of the normalized tangential displacement $\frac{k_t}{|\sigma_m|}b(\theta)$ for initial loading (Eq. (2.8.11)) and for unloading (Eq. (2.8.16)) are shown in Fig. 2.8.2 for μ=0.6. In these two cases, the evolution of the angular tangential displacement distribution is substantially different. For the initial loading (σ decreasing from 0 to σ_m) the entire interval $\theta_0<\theta\le\frac{\pi}{2}$ is

activated at once, even when the applied stress is small. During the unloading process (σ increasing from σ_m to 0), cracks almost parallel to the loading axis are activated first. As long as the stress increases (i.e. pressure drops), the lower limit θ^* of the activated range $\theta^* < \theta \le \frac{\pi}{2}$ decreases and finally becomes equal to θ_0 when the material is fully unloaded.

The integral for the hysteric strain contribution ε_U

$$\varepsilon_U = \frac{2S_V}{k_t}\sigma_m \int_{\theta_0}^{\theta^*} \left(\sin\theta\cos\theta - \mu\cos^2\theta\right)\sin^2\theta\cos\theta d\theta + \frac{2S_V}{k_t}\sigma \int_{\theta^*}^{\pi/2} \left(\sin\theta\cos\theta + \mu\cos^2\theta\right)\sin^2\theta\cos\theta d\theta$$

for unloading is consequently transformed into:

$$\varepsilon_U = \frac{2S_V}{k_t} Q\left(\theta^*\right)\sigma_m + \frac{2S_V}{k_t}\left[P\left(\tfrac{\pi}{2}\right) - P\left(\theta^*\right)\right]\sigma . \qquad (2.8.17)$$

Checking criterions of the Preisach representation

Our next task is to extend those considerations to arbitrary stress-protocol and finally check the fulfillment of the criterions A and B of the Preisach system (see section 2.2).

First let us consider a specific type of protocol that contains a decreasing sequence of maxima and increasing sequence of minima as shown in Fig. 2.8.3 (a). This protocol has *n* extrema: the sequence σ_1, σ_3, σ_5… of minima and the sequence σ_2, σ_4 … of maxima. Each extremum σ_i corresponds to a critical point θ_i in θ-axis at which the lateral displacement distribution has a discontinuous derivative:

$$\operatorname{tg}\theta_i = \begin{cases} \mu\dfrac{\sigma_i + \sigma_{i+1}}{\sigma_i - \sigma_{i+1}} & \text{for odd } i \\ \mu\dfrac{\sigma_{i+1} + \sigma_i}{\sigma_{i+1} - \sigma_i} & \text{for even } i \end{cases}, \; i=1\ldots n\text{-}1$$

or just

$$\operatorname{tg}\theta_i = -\mu\frac{\sigma_i + \sigma_{i+1}}{\left|\sigma_i - \sigma_{i+1}\right|}, \; i=1..n\text{-}1. \qquad (2.8.18)$$

The last critical angle θ^* is defined as

$$\operatorname{tg}\theta^* = -\mu\frac{\sigma_n + \sigma}{\left|\sigma_n - \sigma\right|}, \qquad (2.8.19)$$

so that if we formally denote $\sigma_{n+1} \equiv \sigma$ and $\theta_n \equiv \theta^*$, Eq. (2.8.18) will hold for $i=1\ldots n$.

Note that for the chain of extrema depicted in Fig. 2.8.3(a) the sequence θ_i increases. The corresponding distribution $b(\theta)$ reads:

$$b(\theta) = -\begin{cases} 0, & \text{if } 0 \le \theta < \theta_0 = \arctan(\mu) \\ \sigma_1 / k_t \left(\cos\theta \sin\theta - \mu \cos^2\theta\right), & \text{if } \theta_0 \le \theta < \theta_1 \\ \sigma_2 / k_t \left(\cos\theta \sin\theta + \mu \cos^2\theta\right), & \text{if } \theta_1 \le \theta < \theta_2 \\ \sigma_3 / k_t \left(\cos\theta \sin\theta - \mu \cos^2\theta\right), & \text{if } \theta_2 \le \theta < \theta_3 \\ \quad ... & \\ \sigma_n / k_t \left(\cos\theta \sin\theta \pm \mu \cos^2\theta\right), & \text{if } \theta_{n-1} \le \theta < \theta^* \\ \sigma / k_t \left(\cos\theta \sin\theta \mp \mu \cos^2\theta\right), & \text{if } \theta^* \le \theta < \frac{\pi}{2} \end{cases}, \qquad (2.8.20)$$

where the upper sign corresponds to an even n and to lower one corresponds to an odd one. The form of Eq. (2.8.20) ensures the continuity of distribution $b(\theta)$ at points θ_i. Sliding always happens for the cracks with the angles θ in the last interval $\theta_n<\theta<\pi/2$. All other cracks do not slide. The distribution $b(\theta)$ corresponding to the protocol from Fig. 2.8.3(a) for n=5 is illustrated in Fig. 2.8.3(b).

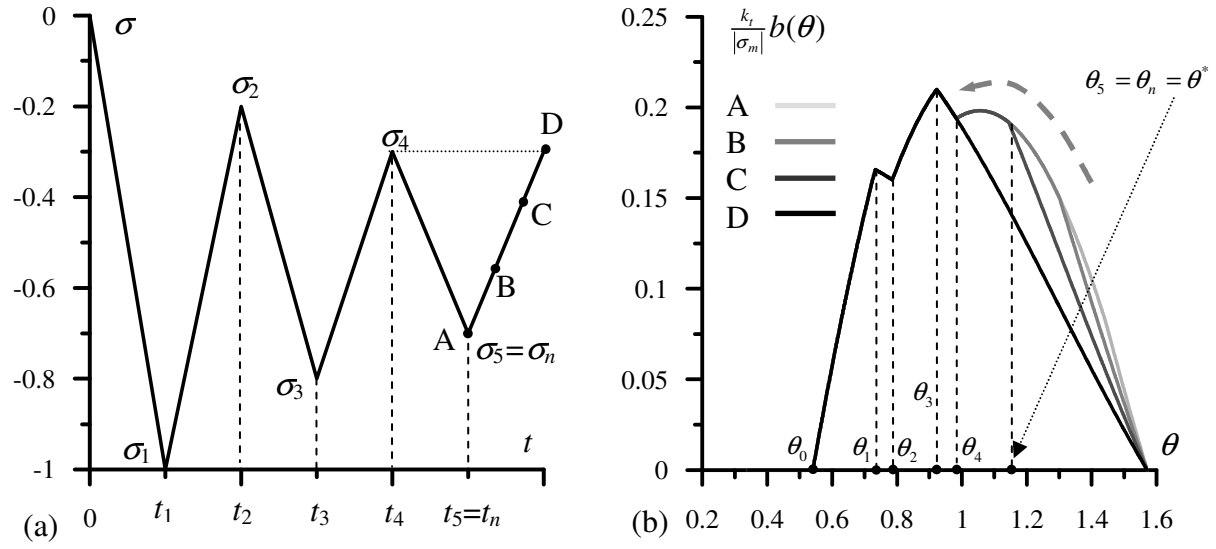

Fig. 2.8.3. (a) Exemplary protocol $\sigma(t)$ containing n=5 extrema with decreasing maxima and increasing minima. (b) The corresponding distribution of the normalized tangential displacement $\frac{k_t}{|\sigma_m|} b(\theta)$ with explicit indications of the critical points $\theta_0, \theta_1, ..., \theta_4 = \theta_{n-1}$ and $\theta^* = \theta_n$. The cracks with orientation angles ranging from θ^* to $\pi/2$ slide, while the cracks with orientation angles less than θ^* do not, i.e. they are stuck. The points A to D in set (a) correspond to the four gray curves in set (b). Darker curves are plotted on top of lighter ones and can mask them.

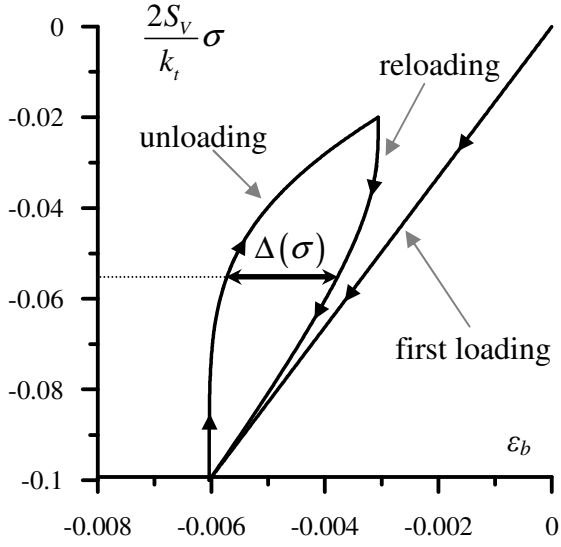

Fig. 2.8.4. Illustration for the stress dependency of the hysteretic strain component due to the tangential displacement of crack faces (following Eqs. (2.8.21), (2.8.22)) for a process containing an initial (monotonic) loading, followed by an (monotonic) unloading and a (monotonic) reloading phase. The thickness $\Delta(\sigma)$ of the closed loop measured at the level σ is a quantity that will be used to calculate the Preisach density.

It is straightforward to calculate the integrals in Eq. (2.8.7) and get

$$\begin{aligned}\varepsilon_b = \tfrac{2S_V}{k_t}\{&Q(\theta_1)\sigma_1 + \left[P(\theta_2)-P(\theta_1)\right]\sigma_2 + \left[Q(\theta_3)-Q(\theta_2)\right]\sigma_3 + \ldots \\ &\ldots + \left[P(\theta^*)-P(\theta_{n-1})\right]\sigma_n + \left[Q\left(\tfrac{\pi}{2}\right)-Q(\theta^*)\right]\sigma\}\end{aligned} \tag{2.8.21}$$

and

$$\begin{aligned}\varepsilon_b = \tfrac{2S_V}{k_t}\{&Q(\theta_1)\sigma_1 + \left[P(\theta_2)-P(\theta_1)\right]\sigma_2 + \left[Q(\theta_3)-Q(\theta_2)\right]\sigma_3 + \ldots \\ &\ldots + \left[Q(\theta^*)-Q(\theta_{n-1})\right]\sigma_n + \left[P\left(\tfrac{\pi}{2}\right)-P(\theta^*)\right]\sigma\}\end{aligned} \tag{2.8.22}$$

for even and odd n, respectively (see illustration in Fig. 2.8.4). Equations (2.8.21)-(2.8.22) represent the desired stress-strain relationship for a specific protocol in which the critical points θ_i form an increasing sequence $\theta_0<\theta_1<\ldots<\theta_n=\theta^*$ i.e. during the evolution process in which they can only be added but never erased. Using this solution, it is easy to prove the fulfillment of the Preisach criterions. Indeed, Eqs. (2.8.21)-(2.8.22) have the following remarkable property: its is only the last term that depends on σ (by means of θ^* and σ itself). This means that the shape of the hysteretic curve after the last n-th extremum determined only by the terms

$$\varepsilon_L = \tfrac{2S_V}{k_t}\left\{P(\theta^*)\sigma_n + \left[Q\left(\tfrac{\pi}{2}\right)-Q(\theta^*)\right]\sigma\right\} \tag{2.8.23}$$

for even n corresponding to a loading branch and

$$\varepsilon_U = \frac{2S_V}{k_t}\left\{Q\left(\theta^*\right)\sigma_n + \left[P\left(\tfrac{\pi}{2}\right) - P\left(\theta^*\right)\right]\sigma\right\}, \qquad (2.8.24)$$

for odd n that corresponds to unloading. The other terms represent just additive constants. Since according to Eq. (2.8.19) θ^* is expressed through the last extremum σ_n and the current stress σ, we see that the shape of this section of the hysteretic curve is determined by the last extremum only. Consequently, two hysteretic loops located between the same values of σ are congruent, i.e. the criterion B of the Preisach system is fulfilled.

Further, the above considerations referred the situation when the sequence of stress maxima decreases and the sequence of stress minima increases, i.e. no memory points are erased. If now the current stress σ reaches the value of the previously memorized extremum σ_{n-1}, then θ^* reaches θ_{n-1}. Therefore the corresponding line in Eq. (2.8.20), namely

$$\sigma_n / k_t \left(\cos\theta \sin\theta \pm \mu \cos^2\theta\right), \text{ if } \theta_{n-1} \le \theta < \theta^*$$

disappears. Then the lines just above and just below this erased line contain the identical expressions:

$$\sigma_{n-1} / k_t \left(\cos\theta \sin\theta \mp \mu \cos^2\theta\right), \text{ if } \theta_{n-2} \le \theta < \theta_{n-1}$$

and

$$\sigma / k_t \left(\cos\theta \sin\theta \mp \mu \cos^2\theta\right), \text{ if } \theta^* \le \theta < \tfrac{\pi}{2},$$

in which $\sigma=\sigma_{n-1}$ and $\theta^*=\theta_{n-1}$. This means that the two last memory points σ_n and σ_{n-1} are actually erased and a new n equals n-2. Sliding cracks are located again in the angle range $\theta^*<\theta<\pi/2$ but with a new θ^*. Erasing two vertices in the protocol $\sigma(t)$ justifies the fulfillment of the criterion A of the Preisach system.

Note that in the above situation the hysteretic dependence $\varepsilon_H(\sigma)$ forms an inner loop which closes when σ reaches this previous extremum. On leaving the loop the curve $\varepsilon_b(\sigma)$ passes the initial point of the loops with the same tangent as it had just before entering the loop. This property is called end-point memory and is also a characteristic feature of Preisach systems.

Calculating the Preisach density

For compression experiments it is more convenient to define the Preisach element as paying contribution -1 in the closed state and contribution 0 in the open state (compare to Fig. 2.2.1). We will use the fact that for Preisach systems the thickness of a loop equals the corresponding integral of the Preisach density (see also Eq. (2.2.4)):

$$\Delta\varepsilon\left(\sigma,\sigma_{n-1},\sigma_n\right)=\int_{\sigma}^{\sigma_n}d\sigma_c\int_{\sigma_{n-1}}^{\sigma}\Pi\left(\sigma_o,\sigma_c\right)d\sigma_o\,, \tag{2.8.25}$$

for the loop confined between σ_{n-1} and σ_n, where $\sigma_{n-1}<\sigma_n$. Double derivation of Eq.(2.8.25) immediately yields

$$\frac{\partial^2\Delta\varepsilon\left(\sigma,\sigma_{n-1},\sigma_n\right)}{\partial\sigma_n\,\partial\sigma}=\Pi\left(\sigma_n,\sigma\right).$$

The thickness of the loop $\Delta\varepsilon(\sigma,\sigma_{n-1},\ \sigma_n)$ is the difference between the unloading branch Eq. (2.8.24) and the loading branch Eq. (2.8.23) in which n should be substituted by n-1 as well as in the definition of θ^*. It is evident that not all the terms in this difference will contribute to the Preisach density; only the terms depending both on σ and σ_n will do and the other ones disappear after the double differentiation. It is straightforward to obtain

$$\Pi\left(\sigma_n,\sigma\right)=\frac{2S_V}{k_\tau}\frac{\partial^2}{\partial\sigma_n\,\partial\sigma}\left(Q\left(\theta^*\right)\sigma_n-P\left(\theta^*\right)\sigma\right), \tag{2.8.26}$$

with θ^* defined according to Eq. (2.8.19). After cumbersome but elementary calculations, we arrive at the following closed form analytical expression for the Preisach density:

$$\Pi\left(\sigma_o,\sigma_c\right)=\frac{8\mu^4S_V}{k_\tau}\frac{\sigma_c\sigma_o(\sigma_c-\sigma_o)^2(\sigma_c+\sigma_o)^2}{\left((\sigma_c-\sigma_o)^2+\mu^2(\sigma_c+\sigma_o)^2\right)^{7/2}}\,, \tag{2.8.27}$$

in which arguments $\left(\sigma_n,\sigma\right)$ are replaced by a more traditional pair $\left(\sigma_o,\sigma_c\right)$. Note that $\Pi(\sigma_o,\sigma_c)$ has a singularity at $\sigma_c=\sigma_o=0$, and that the density is zero on the diagonal. The factorized value $\sigma_c\Pi(\sigma_o,\sigma_c)$ depends on the ratio σ_o/σ_c only.

The hysteretic contribution to the principal equation of the Preisach method (see Eq. (2.2.2)) finally transforms into

$$\varepsilon_b\left(\sigma\right)=-\iint_{\Omega}\Pi\left(\sigma_o,\sigma_c\right)d\sigma_o d\sigma_c\,, \tag{2.8.28}$$

where it is taken into account that only closed elements forming an area Ω demarcated by a staircase line of memorized stress reversal points contribute into the integral, and that their contribution equals -1 (see the above remark). The derived Preisach density $\Pi\left(\sigma_o,\sigma_c\right)$ is defined only for $\sigma_c<0$, $\sigma_o<0$ (see Fig. 6a), since the cracks in the considered model are not pre-stressed and only experience a nonlinear behavior in compression. In the initial state (σ=0) all elements are open. The regulation of the open and closed areas corresponding to the initial loading, subsequent unloading and reloading process considered in the example shown in Fig. 2.8.4 are displayed in Fig. 2.8.5 (b)-(d).

It is straightforward to check that the stress dependency of ε_b does not contain any non-hysteretic (i.e. reversible) contribution. Indeed, in order to prove the validity of Eq. (2.8.28) in which non non-hysteretic term is present, it is enough to rewrite it for the initial loading curve and then compare it to Eq. (2.8.14). Differentiating both equations with respect to σ produces the following expression:

$$\frac{2S_V}{k_t}Q\left(\tfrac{\pi}{2}\right)=\frac{8\mu^4 S_V}{k_\tau}\int_{\sigma}^{0}\frac{\sigma_o\sigma\left(\sigma_o^2-\sigma^2\right)^2}{\left(\mu^2\left(\sigma_o+\sigma\right)^2+\left(\sigma_o-\sigma\right)^2\right)^{7/2}}d\sigma_o\,.$$

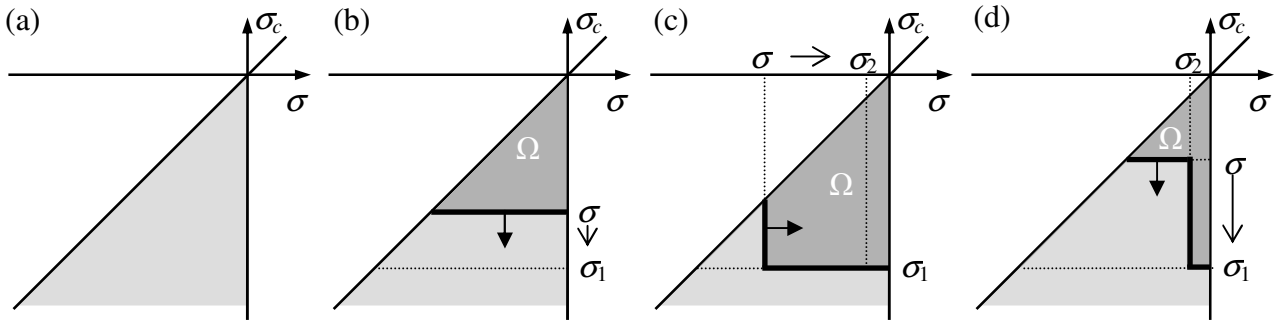

Fig. 2.8.5. Various configurations of open (light gray) and closed (dark gray) Preisach space elements corresponding to an initial loading, subsequent unloading and reloading processes (Fig. 2.8.4): (a) initial state, (b) first loading, (c) unloading, and (d) reloading.

After some calculations, it can be shown that this expression actually represents an identity in which σ cancels out.

Finally, the full stress-strain relation, accounting for the non-hysteretic contribution from the intact medium, the non-hysteretic contribution of the normal displacements of the distributed cracks and the Preisach representation of tangential crack displacements contribution of the crack friction model under uniaxial stress compression, is obtained as

$$\varepsilon_{zz}=\frac{\sigma}{E}-S_V\int_0^{\pi/2}\sin\theta\cos^2\theta\, a(N)\Big|_{N=-\sigma\cos^2\theta}d\theta-\iint_{\Omega}\Pi\left(\sigma_o,\sigma_c\right)d\sigma_o d\sigma_c \qquad (2.8.29)$$

with E the Young's modulus of the intact material, $a(N)$ the normal displacement for the contact of two half-spaces with rough surfaces compressed by a normal force N per unit nominal area, and $\Pi(\sigma_o,\sigma_c)$ the Preisach density given by Eq. (2.8.27).

By following an analogous reasoning, an expression for the transversal strain ε_{xx} affected by the presence of cracks can be obtained. Analogously to ε_{zz}, the transversal crack-induced component ε_{xx} is given by

$$\varepsilon_{xx} = -\nu\frac{\sigma}{E} - \tfrac{1}{2}S_V\int_0^{\pi/2}\sin^2\theta\left(a\sin\theta - 2b\cos\theta\right)d\theta\,, \qquad (2.8.30)$$

and therefore the final expression for the transversal strain, accounting for the reversible as well as nonreversible (Preisach) contributions, reads

$$\varepsilon_{xx} = -\nu\frac{\sigma}{E} - \tfrac{1}{2}S_V\int_0^{\pi/2}\sin^3\theta\, a(N)\Big|_{N=-\sigma\cos^2\theta}d\theta + \tfrac{1}{2}\iint_{\Omega}\Pi(\sigma_o,\sigma_c)\,d\sigma_o d\sigma_c\,, \qquad (2.8.31)$$

where the same Preisach density (Eq. (2.8.27)) should be used as in Eq. (2.8.29) for the longitudinal strain.

In summary, Eqs. (2.8.29) and (2.8.31) represent the longitudinal and transversal strain responses in the crack friction model expressed in the Preisach formalism and applied to uniaxial stress compression. These expressions can be used for any arbitrary uniaxial stress protocol.

Note that the calculations can be organized either using the Preisach formalism either on the basis of the original mechanical equations Eqs. (2.8.1)- (2.8.6).

Our crack friction model has a substantial predictive power and can be directly checked by experiment. This check is performed by fitting experimental curves with model data calculated for guessed values of model parameters. Modeling is considered successful if the experimental results can be reproduced by taking reasonable values of a restrained number of parameters.

First of all, we have to define which model parameters can be matched and which ones are known and fixed. Data are available for several sandstones (section 2.5) for which a typical value of the friction coefficient μ=0.8. Elastic constants E and ν for the intact material are, however, not known since materials of the chosen class are always "damaged" i.e. have internal contacts intrinsically. The degree of damage, parameter $S_V R$, is also not known *a priori*. Besides, we have to explicitly specify the normal reaction curve $a(N)$ or $N(a)$ that depends on statistics of internal crack faces roughness. To model the normal contact reaction, two possibilities have been considered: theoretical modeling uses a known distribution $\varphi(\xi)$ of a random gap between crack faces, and a purely numerical approach.

Normal contact interactions: theoretical approach

Modeling of a force-displacement relationship corresponding to normal loading of contacts with rough surfaces is an extensive research topic since 1950s-1970s. In particular, in the model proposed by Whitehouse and Archard [Whi-70], the concept of asperities is explicitly introduced and a distribution of asperities over heights and radii is deduced. The assumption that all asperities have equal radii but different heights produced the classical model by

Greenwood and Williamson [Gre-66]. In our approach, we try to avoid using the concept of asperity and preserve the continuous character of roughness. This is the "more modern" approach to normal contact reaction modeling that was mentioned at the end of section 2.7.

Contact of rough surfaces can be described using three different parameters related to the contact area: the nominal contact area A_n defined by replacing rough surfaces by ideally plane ones, the real (atomic) contact area A, and the geometric (truncated) contact area A_g obtained in a virtual situation when rough profiles can freely penetrate into each other or, equivalently, when all roughness elements of each surface located higher than a certain height are virtually cut off. As can be observed, the real atomic contact area A between two bodies with rough surfaces is only a small part of the nominal area A_n.

The proportionality $A \sim N$ was proposed by Bowden and Tabor in 1939 [Bow-39]; a more recent discussion on the proportionality can be found in [Car-08]. Both empirical and theoretical arguments suggest that

$$A = \frac{2\kappa\left(1-\nu^2\right)}{Eh'} N , \tag{2.8.32}$$

with h' equal to the root mean square of the random surface slope, and $\kappa \approx 2$ (see [Hyu-07] and references therein for experiments, [Per-02] for theory, [Pag-10] for the discussion on the coefficient κ, [Pag-14] for theoretical and numerical examples).

Further, we introduce the random gap ξ between the surfaces (2ξ is the full gap, ξ is related to one body) and denote $\varphi(\xi)$ as its distribution. Then it is easy to express the ratio A_g/A_n from purely geometric consideration as

$$\frac{A_g}{A_n} = \int_0^a \varphi(\xi)\, d\xi . \tag{2.8.33}$$

Finally, the real and geometric contact areas can be linked by a model relationship. In particular, if all microcontact spots are approximated by strained spheres, a simple relation

$$\frac{A}{A_g} \equiv \upsilon = \frac{1}{2} \tag{2.8.34}$$

follows from the Hertz theory [Lan-93]. For non-spherical shapes of asperities, the value of υ can deviate from 1/2. Combining Eqs. (2.8.32) - (2.8.34) we obtain an analytical expression linking N and a,

$$N(a) = \frac{\upsilon h' E}{2\kappa\left(1-\nu^2\right)} \int_0^a \varphi(\xi)\, d\xi, \quad a \geq 0 . \tag{2.8.35}$$

A possible model form for the distribution of the random gap is the Rayleigh distribution

$$\varphi(\xi) = \frac{\xi}{D^2} e^{-\frac{\xi^2}{2D^2}}, \tag{2.8.36}$$

which has no particular physical meaning but realistic behavior.

In case of negative normal displacement a, we set N equal to zero which actually corresponds to the absence of adhesion. Equation (2.8.35) means that the normal reaction of a crack section is determined by the gap (aperture) distribution which, in turn, depends on the nature of a crack. For weak acoustical excitations, it is possible to simplify Eq. (2.8.35) approximating the distribution $\varphi(\xi)$ by its tangent at ξ=0. As such, three cases can be distinguished: a vertical tangent, a horizontal one, or a tangent with inclination angle between 0 and $\pi/2$. A vertical tangent implies that even for a small compressive displacement a, a non-zero contact area will be immediately formed. In practice, this refers to highly conforming surfaces at the atomic level. Secondly, a horizontal tangent refers to an essentially open crack in which points in atomic contact practically do not appear. Finally, an intermediate tangent inclination coefficient k ($0<k<\infty$) results in the approximation $\varphi(\xi) \approx k\xi$ which yields the following result:

$$N(a) = \frac{\upsilon h' E k}{4\kappa\left(1-\nu^2\right)} a^2, \quad a \geq 0 \tag{2.8.37}$$

that will be used later in chapter 4 so that here it deserves more comment.

The same second-order dependency ($N(a) \sim a^2$) has been introduced by Biwa et al. [Biw-04] based on existing experimental data for aluminum-aluminum contact. The same dependency has been used by Yuan et al. [Yua-15] for modeling the nonlinear interaction of a compressive wave with a soft contact interface between two solid blocks of aluminum. This suggests that the quadratic dependency is a possible approximation for two globally plane surfaces with uncorrelated roughness brought into contact. As an extension we will assume in chapter 4 that Eq. (2.8.37) is also approximately valid for fatigue cracks since the internal stresses released during cracking and the associated microscopic displacements result in a similar loss of conformity at the atomic scale. Microscale composite roughness that mainly contributes to the acoustic response can thus be considered as uncorrelated.

The quadratic approximation is not the only possible form for modeling the normal load-displacement relationship. In [Poh-12] and [Poh-13], it is shown that rough surfaces with various fractal dimensions correspond to different powers in approximation of the kind of Eq. (2.8.37). Nevertheless, based on experiments [Biw-04], we here accept Eq. (2.8.37) as a possible model equation for the normal reaction curve in acoustics.

Normal contact interactions: numerical approach

An alternative possibility is to obtain $N(a)$ just by matching. Assuming that application of a normal load p_{max} (maximum of the applied stress protocol) to a crack results in a the appearance of the normal displacement a_0, we consider a normalized curve $N(a)/p_{max}$ as a function of a/a_0. This curve connects two points: (0,0) and (1,1). To represent the curve with a sufficient precision we introduce three intermediate points (0.25, y_2), (0.5, y_3), and (0.75, y_4) (see Fig. 2.8.6), and then add y_2, y_3, y_4 into the list of parameters to match.

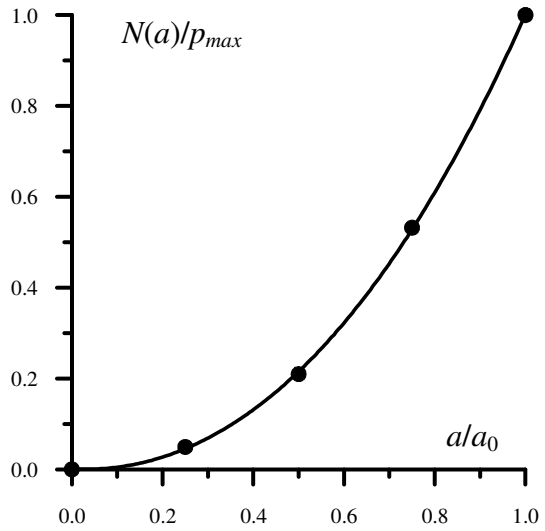

Fig. 2.8.6. Points (0, 0), (0.25, y_2), (0.5, y_3), (0.75, y_4), and (1, 1) on the normalized normal reaction curve $N(a)/p_{max}$ as a function of a/a_0 obtained as a result of matching to data for Serena sandstone. Solid line is 3rd order polynomial fit.

Quantitative comparison of model and data

Now we proceed to the concluding part and discuss the results of matching. Two sets of free parameters were considered: the set $S_1=\{E, \nu, S_V R, D/R, h'\}$ and the set $S_2=\{E, \nu, S_V R, a_0/R, y_2, y_3, y_4\}$. The first option S_1 corresponds to the postulated normal interaction model Eq. (2.8.35) with the guessed gap distribution Eq. (2.8.36) while the second option do not use any model considerations and therefore has more shape parameters (four instead of two). In Fig. 2.8.7 the matching results are illustrated: plot (a) shows the experimental and theoretical curves for the set S_1 of parameters while the plot (b) is drawn for the same experiment and the theoretical data obtained with the set S_2 of parameters.

First of all, the both methods of parameters retrieving produce the same values $E\approx 50$ GPa, $\nu\approx 0.2$, and $S_V R\approx 2$ of parameters common for the both sets. The retrieved Young's modulus $E\approx 50$ GPa is approximately twice higher than typical measured values for

sandstones [Fin-11]. This is not surprising since here E characterizes the elasticity of intact material i.e. the elasticity of grains but not of a whole material with grainy microstructure and internal contacts. A rough estimation of Young's modulus of the material made with Fig. 2.8.7 in which all nonlinear effects are neglected would be 50 MPa / $2.5 \cdot 10^{-3}$ = 25 GPa that corresponds to typical values from literature [Fin-11] or our previous measurements **[Ale-08]**. The estimated value $\nu \approx 0.2$ is close to the known data.

The remaining parameters in sets S_1 and S_2 are different; the final matching quality (residual error) in Figs. 2.8.7 (a) and (b) is different too. However, the difference of the reconstruction quality is mainly due to the non-hysteretic component of the stress-strain dependency or, finally, to the normal reaction curve $N(a)$. The S_1-reconstruction uses the pre-determined shape (Eqs. 2.8.35 - 2.8.36) of $N(a)$ whereas the S_2-reconstructuion matches the shape of the curve more locally and precisely (Fig. 2.8.7). The reconstructed values $D/R \approx 10^{-3}$, $h' \approx 0.8$ (S_1-method) are based on a guessed Rayleigh distribution Eq. (2.8.36) of the random gap between cracks faces and lead to a moderate reconstruction quality in Fig. 2.8.7 (a) and therefore should not be much trusted. In addition, the r.m.s slope $h' \approx 0.8$ is too high for quasi-planar cracks and may cause plastic deformations ignored in this study.

As a conclusion, we keep $E \approx 50$ GPa, $\nu \approx 0.2$, and $S_V R \approx 2$ for the considered material. Assuming the $R \approx 2 \cdot 10^{-5}$ m for Serena sandstone with the grain size about 10^{-5} -10^{-4} m we get $S_V = 10^5$ m^{-1}. This estimation has the same order of the values that $S_V = 5\ 10^4$ m^{-1} used in the previous section for qualitative comparison to known data for acoustical resonance and harmonic generation for another material (Fig. 2.7.8).

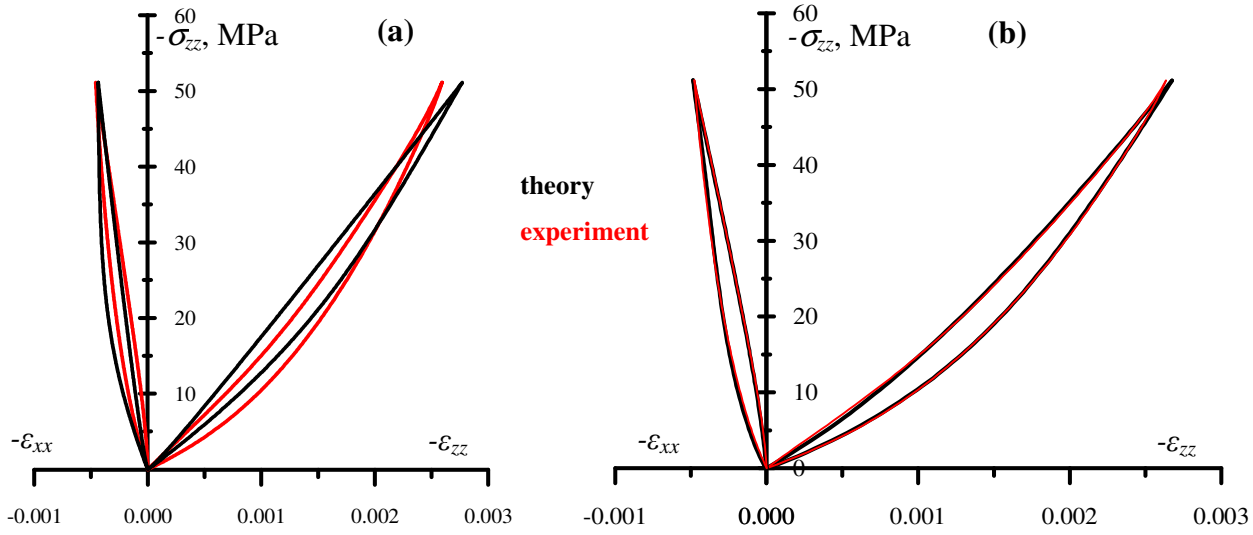

Fig. 2.8.7. Uniaxial stress compression-decompressions tests on Serena sandstone (red) and model results with fitted parameters. (a) Fitted parameters $\{E,\ \nu,\ S_V R,\ D/R,\ h'\}$; (b) fitted parameters $\{E,\ \nu,\ S_V R,\ a_0/R,\ y_2,\ y_3,\ y_4\}$.

The model developed here has a considerable predictive power. In other words, once the model parameters are optimized for some simple protocol as loading-unloading depicted in Fig. 2.8.7, the model becomes capable of reproducing data for another protocol with a good precision. This fact is illustrated in Fig. 2.8.8; theoretical (black) curves practically coincide with experimental data (red) for two complex protocols including internal loops i.e. partial loadings-unloadings or a sequence of loops of decreasing amplitude.

Below we give a short comparison of theoretical approaches described in chapter 2 and outline some prospects.

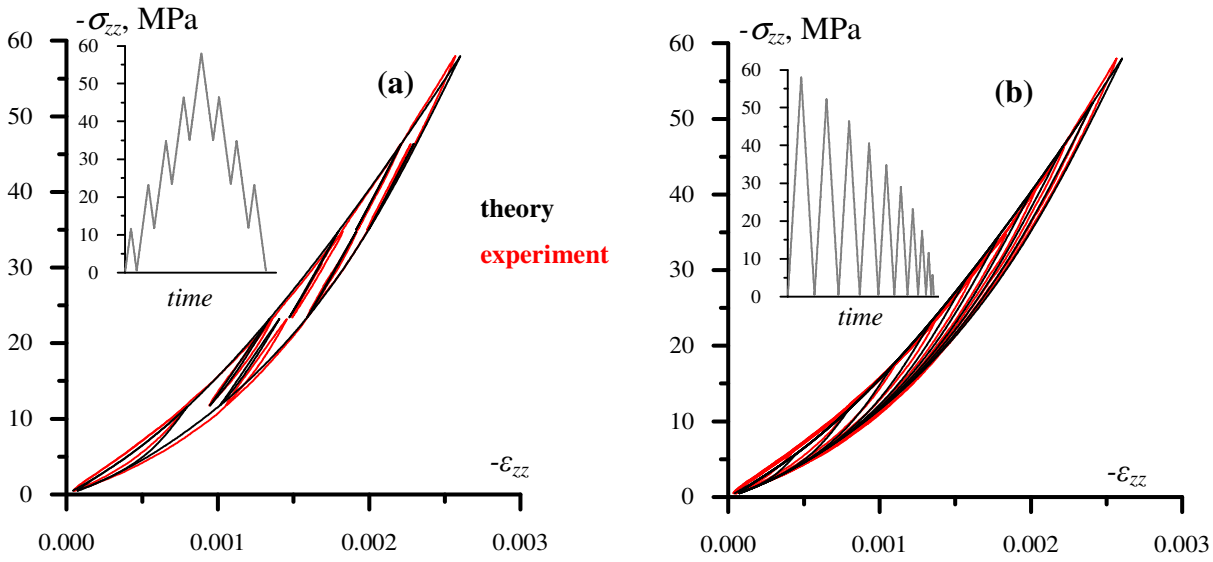

Fig. 2.8.8. Theory-experiment agreement for two uniaxial stress compression protocols: (a) set of partial loadings-unloadings i.e. "inner loops", (b) sequence of loops with a decreasing amplitude. Fitted parameters are $\{E,\ \nu,\ S_V R,\ a_0/R,\ y_2,\ y_3,\ y_4\}$ in the both cases.

2.9. Summary of the theoretical models for nonlinear elasticity in materials with internal contacts

Features of each approach

In this section we summarize the theoretical models discussed in sections 2.6-2.8. A brief outline is sketched in Table 2.9.1. All three models are intended to reproduce hysteretic behavior of the stress-strain dependencies observed in materials with internal contacts. The physical mechanics underlying hysteresis in the adhesion (section 2.6) and adhesion hysteresis (section 2.7) models is related to the presence in the system of a double-well potential due to the adhesion phenomenon. In that case, the state of the system correspond to a point "trapped" at one of minima of the potential energy. An external action modifies the

shape of the potential function so that one of the two minima can disappear. If this occurs the system state obviously corresponds to the remaining potential minimum. In the opposite case, the system stays at the potential minimum in which it was before. Certainly, spontaneous transitions can happen especially when the characteristic potential barrier is comparable to kT; this phenomenon produces a number of dynamical effects not considered here. All three models are quasi-static i.e. the result of a protocol execution does not depend on the execution rate.

	Adhesion (2.6)	**Adhesion hysteresis (2.7)**	**Friction (2.8)**
Physical mechanism	Double-well potential*	Double-well potential*	Dry friction, dissipative*
Memory carrier	State of a crack*	Adhesive neck*	Tangential displacement*
Preisach element	Crack*	Asperity*	No physical entity*
Normal interactions	Lennard-Jones + roughness	Asperities+ JKR	Continuous roughness
Tangential interactions	Not considered*	Not considered*	Coulomb friction law*
Crack orientation	Aligned	Distribution	Distribution
Comparison to data	Qualitative	Qualitative	Quantitative
Typical displacements	~ or > atomic scale*	~ atomic scale*	» atomic scale*
Mechanism relevance	Marginal	Important for small strains	Important for small and large strains

Table 2.9.1. Comparison of models described in chapter 2. Symbol "*" marks properties of fundamental character; absence of "*" means that this feature is not critical and can be removed or upgraded.

The physical mechanism for the crack friction model is different and related to dissipative and threshold effects rather than double-well potentials. However, in that case the bistability is also present; for a given tangential displacement between the crack faces the system can be either in the state of siding either in the stick state. The former occurs when the shear stress applied to the crack surface reaches a threshold determined by the normal stress while latter takes place in the opposite case (the shear stress is less that the threshold). These features are inherent properties of all three models (marked with stars in Table 2.9.1)

Hysteresis means the presence of memory in the system, but a physical "carrier" of the memory is different in the considered three cases. In the adhesion model, each hysteretic crack is bistable due to the existence of finite pull-off force; in one (adhesive) state this pull-off force is exerted, in the other state it equals zero since the crack faces are separated at a distance exceeding the adhesion force range. In the adhesion hysteresis model, a full-off force at the level of a crack is not required; however, it should be present at the level of asperity. Two asperities separated by some distance that does not exceed a critical one can be connected via the adhesive neck or not. The presence or absence of adhesive necks depends on history; therefore the adhesive necks play the role of the physical carrier of memory in the system. In the crack friction model, the memory mechanism is different. For a given state of stress, some of cracks slide and some do not. The tangential displacements for sliding cracks are determined from the equilibrium conditions Eq. (2.8.1), whereas for non-sliding cracks the tangential displacements remain unchanged and therefore "store" the information about history.

All three models allow one using the Preisach formalism; however, the sense of a hysteretic element $\hat{\gamma}$ (Fig. 2.2.1 (a)) is not the same. The hysteretic element for the adhesion model, although not rectangular, is the dependence of the mean gap g between crack faces on strain (see Fig. 2.6.3 in which parameter s is introduced instead of strain). In the adhesion hysteresis model, the Preisach element corresponds to the JKR force-displacement relationship (Fig. 2.7.4). Note that a non-rectangular element just means that a non-hysteretic component is present in the element $\hat{\gamma}$ but the Preisach description itself still holds. The crack friction model assumes the Preisach description too, but in that case an element does not correspond to any physical entity. Some cracks slide, some do not, and the collective effect of their evolution can be described via the Preisach formalism since criterions A and B are satisfied.

Certainly, all three models take into account normal contact interactions, although in a different way. The adhesion model uses the Lennard-Jones potential adapted for rough surfaces, but, in fact any model assuming not-zero pull-off force will do. The adhesion hysteresis model is based on existence of adhesive necks; the Whitehouse-Archard decomposition of continuous roughness into a collection of asperities and JKR approximation for the adhesion force is only an example. The crack friction model can use any model of adhesionless normal interaction but we preferred a recent approach based on continuous roughness in which an ambiguous concept of asperity is not required. The tangential interactions are taken into account only by the crack friction model.

The adhesion model discussed here does not take into account crack orientations while the other two do so; the orientation account can be added in the former model as well.

The important feature of the adhesion model is that for the resistance of a bistable (hysteretic) crack some specific selection of parameters is required while the other to produce the relevant effect in any situation. Therefore, the effect of the adhesion-induced crack bistability should be considered as marginal, whereas the two other mechanisms always work. There is, however, an essential difference in the applicability of the adhesion hysteresis and friction models. The maximum size of the adhesive necks is comparable to the atomic size to that their effect is significant only for small strains. At large deformations crack faces displacements becomes of macroscopic scale so that, due to the known adhesion paradox [Ful-75], their effect becomes negligible. Therefore adhesion hysteresis can not be responsible for pronounced hysteretic behavior appearing in stress-strain curves (see Figs. 2.5.4, 2.8.7, 2.8.8, etc) at millistrain range. This behavior is due to friction as it was demonstrated by the successful theory-experiment comparison in section 2.8: the quantitative agreement has been reached.

The models considered here only capture some aspects of micromechanical behavior of consolidated materials with internal contacts, in particular issues related to the Preisach hysteresis. There exist much more systematic approaches to micromechanics e.g. ones summarized in [Dor-16]. Questions related to an extensive research area of homogenization [Kac-13] are also not considered here.

Extensions to 3D

It is important to mention that, by default, all models discussed here have been developed for a simple uniaxial (1D) excitation. In reality, this is not critical; the identified physical mechanisms combined with relevant matrix rotations provide 3D (tensorial) stress-strain relationships. In conclusion, we give equations that allow one to calculate stresses Σ_n and Σ_t (see Eq. 2.8.1) applied to crack faces from the macroscopic stress tensor $\hat{\sigma}$ and then, using the calculated mesoscopic displacements *a* and *b*, to retrieve the macroscopic strain tensor $\hat{\varepsilon}$.

For each crack with orientation angles θ and φ it is convenient to introduce a local reference frame (*X*, *Y*, *Z*) in which the *Z*-axis is perpendicular to the crack plane. The stress tensor in the local coordinate system is

$$\hat{\Sigma} = \hat{A}(\varphi,\theta,\psi)\hat{\sigma}\hat{A}^{-1}(\varphi,\theta,\psi), \tag{2.9.1}$$

where

$$\hat{A}(\varphi,\theta,\psi)=\begin{pmatrix}\cos\psi & \sin\psi & 0\\ -\sin\psi & \cos\psi & 0\\ 0 & 0 & 1\end{pmatrix}\begin{pmatrix}\cos\theta & 0 & -\sin\theta\\ 0 & 1 & 0\\ \sin\theta & 0 & \cos\theta\end{pmatrix}\begin{pmatrix}\cos\varphi & \sin\varphi & 0\\ -\sin\varphi & \cos\varphi & 0\\ 0 & 0 & 1\end{pmatrix} \tag{2.9.2}$$

The free angle ψ is selected so that the local stress tensor

$$\hat{\Sigma}=\begin{pmatrix}\Sigma_{XX} & \Sigma_{XY} & \Sigma_t\\ \Sigma_{XY} & \Sigma_{XX} & 0\\ \Sigma_t & 0 & \Sigma_n\end{pmatrix} \tag{2.9.3}$$

has two zero components. The components Σ_{XX}, Σ_{XY}, and Σ_{YY} do not affect the state of the crack and therefore are not needed. The components Σ_n and Σ_t are required for solving Eq. (2.8.1) that produces displacements *a* and *b*. The displacements are necessary for calculation of a contribution of this particular crack into the macroscopic strain defined in (*X*, *Y*, *Z*)-coordinates:

$$d\hat{\Gamma}=S_V\begin{pmatrix}0 & 0 & b\\ 0 & 0 & 0\\ b & 0 & a\end{pmatrix}\Psi(\varphi,\theta)\sin\theta d\varphi d\theta, \tag{2.9.4}$$

with $\Psi(\varphi,\theta)$, the orientation distribution function. The total strain tensor $\hat{\varepsilon}$ in usual (*x*, *y*, *z*) coordinates is then obtained by the inverse matrix rotation and integration:

$$\hat{\varepsilon}=\hat{\gamma}+\int\hat{A}^{-1}(\varphi,\theta,\psi)d\hat{\Gamma}\hat{A}(\varphi,\theta,\psi), \tag{2.9.5}$$

over spherical angles θ and φ.

In fact, in section 2.8 Eq. (2.8.11) and other equations for uniaxial stress compression were obtained as a particular case of the procedure described above. However, the procedure does not include torsion and therefore is not absolutely general yet.

3. Fundamental solutions for the frictional interaction

3.1. Brief history

As we have seen, contact models play the key role in successful properties description of materials with internal contacts. Theoretical results essentially depend on factors taken into account or neglected by a particular contact model underlying the description at the material (macroscopic) level. This chapter is devoted to the fundamental mechanical problem of frictional contact between two solids having certain surface profiles.

The history of the contact problem started in 1880s when H. Hertz (see [Lan-93]) published the classical solution for two elastic spheres compressed by a normal force. In absence of adhesion and plasticity, this solution is fully reversible. However, the addition of a tangential force and friction ([Cat-38], [Min-49]) makes the problem hysteretic and memory-dependent. It was noted that even a small tangential force acting on two pre-compressed spheres results in appearance of a slip annulus at the periphery of the contact circle where the surfaces are compressed weakly. The coexistence of the stick (central) and slip (peripheral) zones actually means mixed-type boundary conditions that correspond to zero local tangential displacement in the central region and, in the slip annulus, to the Coulomb friction relationship written for local tangential (τ) and normal (σ) stresses, $\tau=\mu\sigma$ (here μ is friction coefficient considered as a constant for two contacting materials). The increase in the tangential force results in the slip propagation towards the contact center. If now the tangential force starts decreasing, a new slip annulus develops at the contact periphery in which $\tau=-\mu\sigma$. Hence, the same values of the normal (N) and tangential (T) forces can correspond to different distributions of stresses and displacements in the contact zone. This fact explains a complex hysteretic character of the solution.

Allowing the normal force to evolve [Min-53] adds a new complexity factor to the problem. The matter is that the slip zone always arises at the contact border where $\sigma=0$ and propagates inward, but, if the normal force increases, the contact border itself propagates outward. The result depends on the value of the derivative dN/dT.

Finally, the introduction of general contact geometry instead of spherical profiles introduces even more complexity into the description. Indeed, for two rough surfaces, the contact zone consists of a multitude of contact spots having random geometry. For changing normal force, those contact spots can merge or split. Further, each of them supports slip and stick zones, and traction distribution in the stick zones can contain residual stresses left from

the previous moments of evolution. With continuously varying normal and tangential loading, this complicated pattern continuously evolves.

Our objective is to essentially modernize the classical results by developing more universal approaches applicable for a wide range of excitation protocols and contact geometries.

3.2. Geometric extensions

The geometric aspect of the problem can be successfully dealt with by using the Reduced Elastic Friction Principle (REFP, see [Jäg-95], [Jäg-97], [Jäg-03], [Cia-98a], [Cia-98b] that, under some restrictions, makes it possible to replace an arbitrary contact geometry by a pair of axisymmetric profiles.

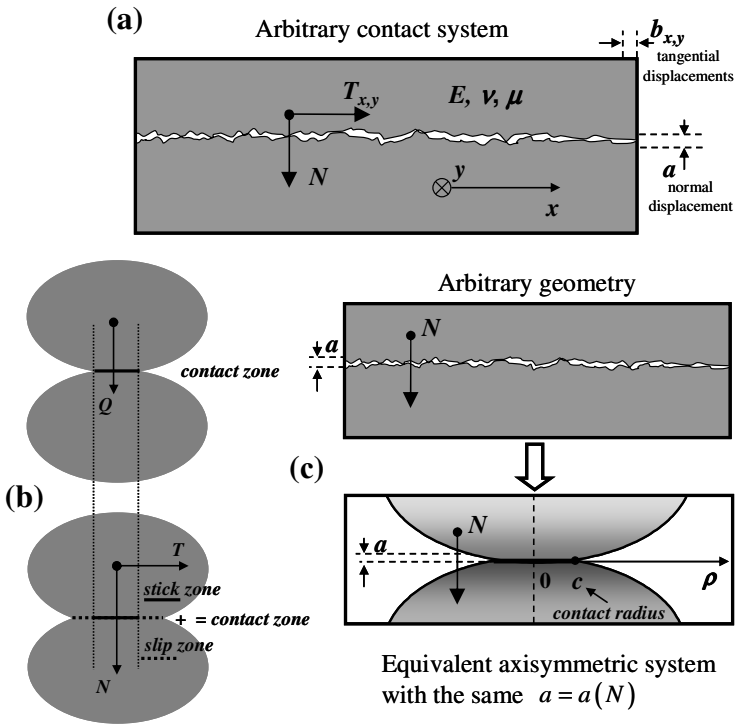

Fig. 3.2.1. (a) Forces and displacements in a general contact system (case of rough surfaces is shown). (b) Reduced elastic friction principle for axisymmetric bodies. (c) Equivalent axisymmetric system that has the same normal reaction as an original one (e.g. contact of rough surfaces).

The geometry of the considered contact mechanical problem is illustrated in Fig. 3.2.1 (a). Both materials are linear elastic with equal for simplicity elastic constants E and ν. Friction between the bodies is described by a single friction coefficient μ (possible differences between static and dynamic friction are ignored). The contact system is loaded by a remote

force $\{N, T_x, T_y\}$ with one normal (N) and two tangential (T_x, and T_y) components. The bodies experience displacement $\{a, b_x, b_y\}$ where the components are defined in the analogous way. For constant loading i.e. when the system is loaded first by a constant normal force and then by a constant tangential force, the notations $\{N, T\}$ and $\{a, b\}$ for the vector force and displacement are accepted. The general problem consists in establishing a link between $\{N, T_x, T_y\}$ and $\{a, b_x, b_y\}$ for both force-driven and displacement-driven systems. For 2D loading case considered here, the force and displacement vectors stay in one plane so that the notations $\{N, T\}$ and $\{a, b\}$ are more suitable.

The objective of this section is to show how to take into account various contact geometries. This can be made by substituting a given contact geometry with a pair of axisymmetric profiles with the same normal reaction law. Such a possibility is guaranteed by the REFP at least as a good approximation.

The REFP is an important theorem of contact mechanics which states that, for constant loading and for a wide range of contact geometries, the tangential force and displacement can be expressed through the normal force and displacement. This principle is illustrated in Fig. 3.2.1 (b) for axisymmetric bodies. Consider two situations: first one when the system is loaded only by normal force Q, and second one when both force components, N and T, are applied ($N>Q$). The force values are chosen in such a way that the stick zone in the second case coincides with the contact zone in the first case. Then the tangential force and displacement in the second situation are given by

$$\begin{cases} T = \mu\left(N - Q\right) \\ b = \theta\mu\left(a\left(N\right) - a\left(N\right)\big|_{N=Q}\right) \end{cases}, \tag{3.2.1}$$

where the dependency of the normal displacement on the normal force $a=a(N)$ is supposed to be known, and θ is a material constant that depends only on Poisson's ratio ν,

$$\theta = \frac{2-\nu}{2\left(1-\nu\right)}. \tag{3.2.2}$$

An important feature of Eq. (3.2.1) is that it does not contain any geometry-related characteristics. Thus a simple consequence of the REFP is a statement that, for two contact systems with the same normal response, the tangential responses are also identical (see Fig. 3.2.1(c)). Consequently, a contact between surfaces of almost arbitrary topography can be replaced by an equivalent axisymmetric system. The related restrictions that limit the class of the considered contact types are discussed in [Jäg-95], [Jäg-97], [Jäg-03], [Cia-98a], [Cia-98b]. In Fig. 3.2.1 the word "arbitrary" should be understood in that context. The idea of

geometric extensions for contact problems in widely used in the Method of Dimensionality Reduction (MDR, [Pop-13], [Pop-15]).

The existing solution for an axisymmetric system with a circular contact area A of radius c, $A=\pi c^2$, has the following form ([Gal-61], [Sne-65], [Jäg-95]):

$$N(c)=\frac{2E}{1-\nu^2}\left(ca-\int_0^c\frac{\rho z(\rho)}{\sqrt{c^2-\rho^2}}d\rho\right), \tag{3.2.3}$$

$$a(c)=\int_0^c\frac{cz'(\rho)}{\sqrt{c^2-\rho^2}}d\rho, \tag{3.2.4}$$

$$\sigma(c,\rho)=\frac{E}{\pi(1-\nu^2)}\int_\rho^c\left(\int_0^r\frac{z'(p)+pz''(p)}{\sqrt{r^2-p^2}}dp\right)\frac{dr}{\sqrt{r^2-\rho^2}}, \tag{3.2.5}$$

where ρ is the radial coordinate, $z(\rho)$ is a function describing the gap between the two bodies, and $z'(\rho)$ and $z''(\rho)$ are its first and second derivatives, respectively (see Fig. 3.2.1(a)). Eqs. (3.2.3) and (3.2.4) can be used to define a parametric expression for the normal force-displacement relationship $a=a(N)$ or $N=N(a)$.

It is straightforward to verify that Eqs. (3.2.3)-(3.2.5) yield the classical Hertz solution [Lan-93] for two equal spheres i.e. when

$$z(\rho)=R-\sqrt{R^2-\rho^2}$$

is assumed, with R, the radius of the spheres. In this derivation, only the lowest term in the expansion over the small parameter c/R is kept.

It can be numerically demonstrated [Poh-15] the precision of the REPF becomes worse in the case of a very strong asymmetry in the contact shape i.e. the situation when one dimension (say, x) considerably exceeds another one (y) . For moving along x the effective θ will deviate from the effective θ for movements along y-axis.

Another, more detailed form of the REFP for an arbitrary 3D relief with possible multiple contacts is

$$\tau(\vec{r})=\mu\left(\sigma(A,\vec{r})-\sigma(S,\vec{r})\right) \tag{3.2.6}$$

$$T=\mu\left(N(A)-N(S)\right), \tag{3.2.7}$$

$$b=\theta\mu\left(a(A)-a(S)\right), \tag{3.2.8}$$

Here, $\vec{r}$ is the coordinate in the global contact plane, A is real the contact area, S is the stick area, and the value of θ is close to Eq. (3.2.2).

The consideration of this assumption certainly deserves some further comments.

(i) First of all, the above hypothesis can only be made under the standard set of assumptions typical for contact theories of this kind: the bodies are elastic, the normal directions for all individual contacts are aligned and stay aligned when sheared, the local Coulomb's law is postulated, and torsion is absent.

(ii) If the materials are different then, strictly speaking, the approach discussed here is only valid for elastically similar materials with the Dundur's constant

$$\beta = \frac{G_2(\kappa_1 - 1) - G_1(\kappa_2 - 1)}{G_2(\kappa_1 + 1) + G_1(\kappa_2 + 1)}$$

equal to 0 (here $G_{1,2}$ are shear moduli, $\kappa_{1,2} = 3 - 4\nu_{1,2}$, and $\nu_{1,2}$ are Poisson's ratios $\nu_{1,2}$ of the materials; see, for instance, [Cia98b]). In the latter paper, $\nu_{1,2}$=0 is required in addition. The analysis for dissimilar bodies is much more complicated, since partial slip then may occur even for purely normal loading. However (see [Jäg-95], [Jäg-03]), the error produced by neglecting dissimilarity effects, in many practical cases, is within the variation error of the friction coefficient in Coulomb's law. A more detailed discussion, including quantification of the dissimilarity effects, is presented in [Mun-92] and [Mun-94].

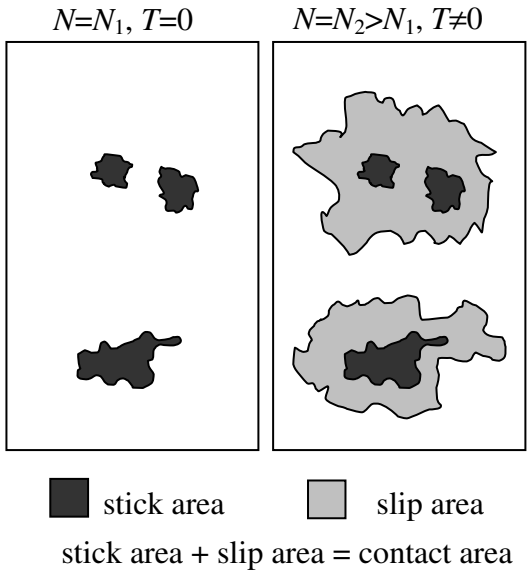

Fig. 3.2.2. Illustration of an important assumption related to the reduced friction principle for arbitrary multiple contacts. The left set shows a configuration of contact zones for a specific normal force. Upon increasing the normal force and then gradually applying a tangential force, the configuration of stick zones at the right set will fully coincide with the configuration of the contact zones at the left for a certain value of the tangential force.

(iii) The expressions and notations used in Eqs. (3.2.6)-(3.2.8) in which the stick area S can substitute the contact area A reflect the acceptance of the assumption illustrated in Fig. 3.2.2.

Suppose that for a certain applied normal load $N=N_1$ the contact zone has the configuration shown on the left-hand side figure, with a total area A_1 that, in the absence of tangential action, coincides with the zone of stick, $S_1=A_1$. Upon increasing the normal force to a larger value (N_2), the contact zone increases too, as shown in the figure on the right, and some individual contact spots may merge. If we then apply a tangential force such that the stick area shrinks and forms an area S_2 that equals A_1, the configuration of the stick zones at the right will perfectly repeat the configuration of the contact zone for $N=N_1$ at the left, including the number and shapes of all individual contacts.

General form of the REPF (Eqs. 3.2.6-3.2.8) assumes another version more suitable for axisymmetric profiles:

$$\tau(\rho)=\mu\left(\sigma(c,\rho)-\sigma(s,\rho)\right) \tag{3.2.9}$$

$$T=\mu\left(N(c)-N(s)\right), \tag{3.2.10}$$

$$b=\theta\mu\left(a(c)-a(s)\right), \tag{3.2.11}$$

in which c is the contact radius, s is the stick zone radius, ρ is the radial coordinate. The dependencies $\sigma(c,\rho)$ $N(c)$ and $a(c)$ are provided by the known normal solution. Expressions $\sigma(s,\rho)$ $N(s)$ and $a(s)$ just mean that in the above functional dependencies representing the normal solutions c is substituted by s. Comparison of the axisymmetric representation Eqs. (3.2.9)-(3.2.11) and the short form of the REFP Eq. (3.2.1) suggests the following interpretation of the parameter Q: Q is the virtually reduced normal force at which the corresponding virtually reduced contact radius coincides with the actual stick zone radius. In other words, Q is the stick zone radius in the force-related coordinate η given by the mapping

$$\eta=N(c)\big|_{c=\rho} \tag{3.2.12}$$

in which $N(c)$ is the normal solution, as previously.

A short form of the REFP Eq. (3.2.1) does not contain any parameters directly related to the contact geometry. All geometric information is contained in the dependency $N=N(a)$ linking the normal force and the normal displacement. This dependency is one of forms of the normal solution and is supposed to be known. For axisymmetric profiles it is given by Eqs. (3.2.3)-(3.2.4). For rough surfaces, a model Eqs. (2.8.28)- (2.8.32) discussed in the previous chapter can be used. Anyway, the REFP theorem in the form Eq. (3.2.1) means that any arbitrary contact satisfying the theorem's conditions behaves in the same way in terms of displacement and forces as an equivalent single-contact axisymmetric system having the same normal reaction.

3.3. Preisach approach

The strength of the Preisach approach is in the possibility to automatically calculate the response for any kind of excitation protocol. In this section we reproduce without demonstration results proven elsewhere (**[Ale-09a], [Ale-11a], [Ale-11b], [Ale-12a], [Ale-12b], [Ale-13a]**) on the basis of particular solutions of frictional contact mechanics. It is important to note that the contact system characterized by the normal reaction $N(a)$ and friction coefficient μ represents the Preisach system in the case when

- loading is in 2D i.e. force $\{N, T\}$ and displacement $\{a, b\}$ always stay in one plane;
- there exists a so-called loading condition i.e. a functional relation $N=N(T)$ for a force-driven system or $a=a(b)$ for a displacement-driven system; in that case the number of inputs in the system is one (T-protocol or b-protocol) which is necessary for the existence of a scalar hysteretic dependence of the type $y_H(x)$.

Case of absence overloading

For definiteness, consider first the case of the force-driven system. Changing force components simultaneously produce two effects: variations in the tangential force are accompanied by generation of slip that propagates from the contact periphery inwards, to the contact center, while changing normal force influences the contact area itself. In that situation, a regime can occur in which the process of contact growth dominates the process of inward slip propagation. This regime called sometimes "complete overlapping" ([Jäg-98], [Jäg-03]) or "overloading" **[Ales-12a]** means that the contact grows so rapidly that slip has no time to develop. The terms "rapidly" or "slowly" for quasi-static processes indicate just a relationship linking the proper derivatives that has the form

$$\left(\mu\frac{dN}{dT}\geq 1 \quad and \quad I=+1\right) \; or \; \left(\mu\frac{dN}{dT}\leq -1 \quad and \quad I=-1\right) \tag{3.3.1}$$

in which

$$I=\operatorname{sgn}\left(dT/dt\right). \tag{3.3.2}$$

The opposite situation i.e. when the condition Eq. (3.3.1) is never satisfied is much easier to consider. It can be shown **[Ales-12a]** that in this case the initial loading curve has the same form as Eq. (3.2.1) (REFP solution):

$$\begin{cases} T=I\mu\left(N-Q\right) \\ b=I\theta\mu\left(a\left(N\right)-a\left(Q\right)\right) \end{cases}, \tag{3.3.3}$$

and after passing the M-th extremum T_M of the protocol it becomes

$$\begin{cases} T = T_M + I\mu\left(N + N_M - 2Q\right) \\ b = b_M + I\mu\theta\left(a\left(N\right) + a\left(N_M\right) - 2a\left(Q\right)\right) \end{cases}, \tag{3.3.4}$$

with N_M=$N(T_M)$. Eq. (3.3.4) directly confirms the criterion B of the Preisach system formulated in section 2.2: all hysteresis loops corresponding to the same extremum values of the input parameter are congruent. Indeed, as we notice in section 2.8, criterion B is fulfilled when the shape of the curve depends only on the last extremum point T_M and not on other points of the protocol. The shape i.e. the dependency $b(T)$ that contains T_M as a parameter can be obtained from Eq. (3.3.4) by excluding Q. Note that, in this dependency, b_M is present as an additive term and does not influence the shape but only the shift of the loop.

Checking of the criterion A is also analogous to section 2.8. For that, we have to assume that the tangential force protocol contains a decreasing sequence of maxima and increasing sequence of minima (see Fig. 3.3.1 (a)) and then consider the situation when T is about to reach $T_{M\text{-}1}$. It can be easily shown using Eq. (3.3.4) that points T_M and $T_{M\text{-}1}$ will cancel out, and the evolution will continue accordingly to Eq. (3.3.4) in which M is replaced by M-2, as if the M-1-th and M-th extrema never occurred. In other words, two points of the protocol are wiped out, and the system forgets the inner loops after exiting it.

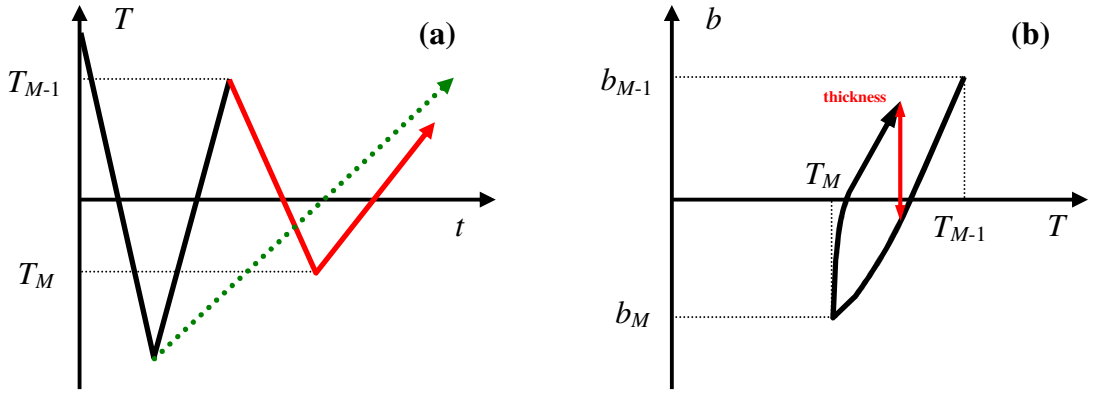

Fig. 3.3.1. (a) Protocol containing a decreasing sequence of maxima and increasing sequence of minima used for the criterion A verification is depicted in black and red. When T reaches $T_{M\text{-}1}$ the red segment disappears from the history and is replaced by the green dotted line. (b) Loop used for calculation of the Preisach density by differentiating its thickness (shown in red) over T and T_M.

Since it is now demonstrated that the considered case can be described via the Preisach formalism (the complete demonstration would include the proof of Eq. (3.3.4)), it is possible to calculate the key parameters of the Preisach description: the Preisach density, the

non-hysteretic contribution, and the initial configuration of open and closed elements as prescribed in section (2.1).

To obtain the Preisach density, we have to calculate the double derivative of the loop thickness or, more precisely, of the difference between down-going the curve connecting point ($T_{M\text{-}1}$, $b_{M\text{-}1}$) with point (T_M, b_M) and the up-going curve connecting point (T_M, b_M) with point (T, b) (see Fig. 3.3.1 (b)). The double derivation is made over T_M and T, therefore the derivative of the former curve disappears. Indeed, the curve ($T_{M\text{-}1}$, $b_{M\text{-}1}$)→(T_M, b_M) is given by Eq. (3.3.4) in which M should de replaced by M-1 and consequently does not depend on T_M. Hence, its is enough to write

$$\Pi\left(T_M, T\right) = \frac{\partial^2 b}{\partial T \partial T_M}$$

in which

$$b = b_M + \mu\theta\left(a\left(N\left(T\right)\right) + a\left(N\left(T_M\right)\right) - 2a\left(Q\right)\right)$$

with

$$Q = \frac{T_M - T}{2\mu} + \frac{N\left(T_M\right) + N\left(T\right)}{2}.$$

This double differentiation ultimately provides the result

$$\Pi\left(T_o, T_c\right) = \frac{\theta}{2\mu}\left(\mu N'\left(T_c\right) + 1\right)\left(\mu N'\left(T_o\right) - 1\right) a''\left(\frac{T_c - T_o}{2\mu} + \frac{N\left(T_c\right) + N\left(T_o\right)}{2}\right) \tag{3.3.5}$$

rewritten in common coordinates: T_o replaces T, T_c replaces T_M (here T>T_M and T_o>T_c). Here primes mean derivatives.

For a full description, the Preisach density has to be supplemented by the non-hysteretic component $b_{NH}(T)$ and by the initial configuration of the hysteretic elements. It is possible to obtain the non-hysteretic contribution using the following reasoning. On the one hand, by rewriting the general representation Eqs. (2.2.2)- (2.2.3) for the decreasing (for definiteness) branch $b(T)$ started at point (T_M, b_M), we obtain

$$b\left(T\right) - b_M = b_{NH}\left(T\right) - b_{NH}\left(T_M\right) - \int_T^{T_M} dT_o \int_T^{T_o} \Pi\left(T_o, T_c\right) dT_c \,.$$

On the other hand, the decreasing branch is given by Eq. (3.3.4) with I=-1. Comparison of the two equations, taking into account the above-deduced Preisach density Eq. (3.3.5), yields

$$b_{NH}\left(T\right) - b_{NH}\left(T_M\right) = \theta \int_{T_M}^{T} \left.\frac{da}{dN}\right|_{N=N\left(T^*\right)} dT^* \,. \tag{3.3.6}$$

Equation (3.3.6) defines the function $b_{NH}(T)$ apart from an arbitrary constant:

$$b_{NH}(T) = \theta \int_0^T \left. \frac{da}{dN} \right|_{N=N(T^*)} dT^* + C \,. \tag{3.3.7}$$

The constant C can be calculated by referring to the state when all elements are closed. To do this, we first obtain the limits of the Preisach space $T_{\min}$ and $T_{\max}$ assuming Q=0 in Eq. (3.3.3) for I=+1 and I=-1, respectively, with the result

$$T_{\max} = \mu N(T_{\max}),\ T_{\min} = -\mu N(T_{\min}). \tag{3.3.8}$$

Reaching these limits will provoke total sliding in the system. If we set T=$T_{\min}$ and close all hysteretic elements, the corresponding displacement

$$b(T_{\min}) = b_{NH}(T_{\min}) + C$$

will not contain any contribution of the Preisach density. Substituting Eqs. (3.3.3) and (3.3.7) into the above equation, we get

$$C = -\theta\mu a\left(N(T_{\min})\right) + \theta \int_{T_{\min}}^0 \left. \frac{da}{dN} \right|_{N=N(T^*)} dT^* \,, \tag{3.3.9}$$

and then also the final expression for the Preisach representation:

$$b(T) = -\theta\mu a\left(N(T_{\min})\right) + \theta \int_{T_{\min}}^T \left. \frac{da}{dN} \right|_{N=N(T^*)} dT^* + \iint_{\Omega_T} \Pi(T_o, T_c)\, dT_o dT_c \tag{3.3.10}$$

with the Preisach density given by Eq. (3.3.5)

Finally, in order to determine the initial configuration of the domains filled with open and closed elements, we assume that the boundary between the two areas can be described by a curve T_c=$F(T_o)$ (see Fig. 3.3.2 (a)). Derivation of the man equation of the Preisach formalism yields

$$db/dT = db_{NH}/dT + \int_{F(T)}^T \Pi(T_o = T, T_c)\, dT_c \,, \tag{3.3.11}$$

for I=+1, where db/dT is at the same time the derivative of the solution Eq. (3.3.3) for the first loading curve. Substitution of the respective contributions, given by Eqs. (3.3.7) and (3.3.5), into Eq. (3.3.11) yields an expression for T_c=$F(T_o)$ in the form

$$T_c + \mu N(T_c) = -T_o + \mu N(T_o). \tag{3.3.12}$$

Using the above equation (3.3.12), it is straightforward to show that the derivative dT_c/dT_o is negative for $\mu\, dN/dT_o$<1, which implies that the function T_c=$F(T_o)$ delimiting the open and closed zones decreases in the entire interval $0 \le T_o \le T_{\max}$ (see Fig. 3.3.2 (a)). Correspondingly, any vertical line T=T_o ($0 \le T_o \le T_{\max}$) has only one intersection with the curve T_c=$F(T_o)$.

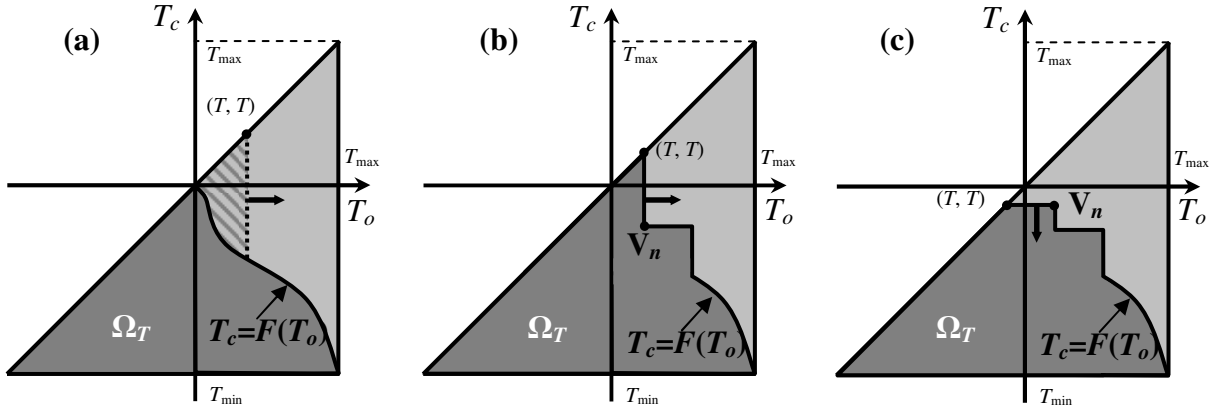

Fig. 3.3.2. (a) Curve $T_c=F(T_o)$ delimiting the open area (dark gray, marked Ω_T) and the closed area (light gray) at the first moment of time t=0; if T increases for t>0 the hatched area will open. (b, c) Typical configuration of open and closed areas for opening (b) and closing (c).

The other plots in Fig 3.3.2 (plots (b) and (c)) illustrate opening (increasing T, I=+1) and closing (decreasing T, I=-1) processes. The curvilinear part of the delimiting line coexist with the staircase line unless T reaches one of outer limits $T_{\min}$ or $T_{\max}$ of the Preisach space i.e. total sliding develops.

In accordance with the concept developed in section 2.5, we give also an expression for the integrated Preisach density:

$$H\left(T_o,T_c\right)=\mu\theta a\left(N\left(T_o\right)\right)+\mu\theta a\left(N\left(T_c\right)\right)-2\mu\theta a\left(\frac{T_c-T_o}{2\mu}+\frac{N\left(T_c\right)+N\left(T_o\right)}{2}\right) \tag{3.3.13}$$

For the displacement-driven system, the appropriate solutions have the forms: the principal equation of the Preisach representation

$$T\left(b\right)=T_{NH}\left(b\right)-\iint\limits_{\Omega_o}\Theta\left(b_o,b_c\right)db_o db_c\,, \tag{3.3.14}$$

the Preisach density

$$\Theta\left(b_o,b_c\right)=\frac{1}{2\mu\theta^2}\left(1+\mu\theta a\left(b_c\right)\right)\left(1-\mu\theta a\left(b_o\right)\right)\,N''\left(\frac{b_c-b_o}{2\mu\theta}+\frac{a\left(b_c\right)+a\left(b_o\right)}{2}\right) \tag{3.3.15}$$

in which $a(b)$ is the loading condition and $N(a)$ is the normal loading curve, and the non-hysteretic contribution

$$T_{NH}\left(b\right)=-N\left(a\left(b_{\min}\right)\right)+\frac{1}{\theta}\int\limits_{b_{\min}}^{b}\left.\frac{dN}{da}\right|_{a=a\left(b^*\right)}db^*\,. \tag{3.3.16}$$

The curve defining the initial configuration of elements is given by an implicit dependency

$$b_c+\mu\theta a\left(b_c\right)=-b_o+\mu\theta a\left(b_o\right). \tag{3.3.17}$$

Case when overloading is allowed

The above results are related to the case when overloading in prohibited i.e. the condition Eq. (3.3.1) is never satisfied. The same condition for the displacement-driven system transform into

$$\left(\mu\theta\frac{da}{db}\geq 1 \quad and \quad I=+1\right) \; or \; \left(\mu\theta\frac{da}{db}\leq -1 \quad and \quad I=-1\right). \tag{3.3.18}$$

If, however, for some input values (T or b) it is fulfilled, the situation becomes more complicated. Indeed, for these input values the formal use of Eq. (3.3.5) or Eq. (3.3.15) is not possible since density $\Pi(T_o,T_c)$ becomes negative and $\Theta(b_o,b_c)$ becomes positive which corresponds to the energy generation instead of loss. Therefore, some correction algorithm is needed. Here we reproduce the main result for the general $y(x)$-representation (section 2.1) of the Preisach formalism. The proof can be found in **[Ale-13a]**. The procedure steps are as follows:

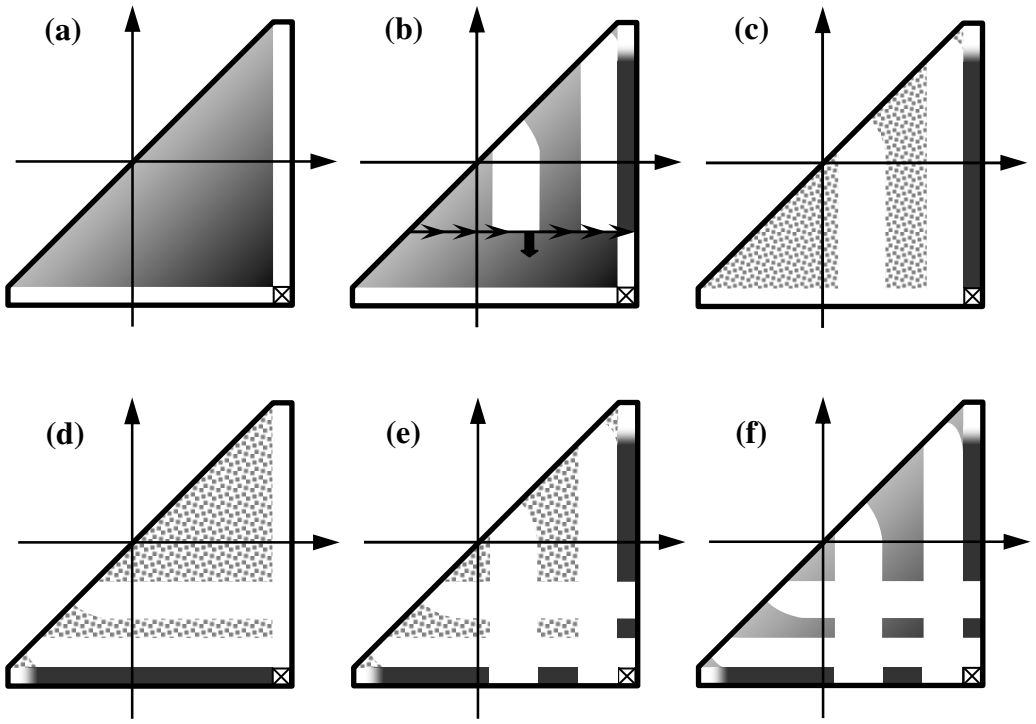

Fig. 3.3.3. Procedure of density correction consisting of steps A-H: (a) take raw density Eq. (3.3.5) or Eq. (3.3.15), place the additional zones of width Δx at the right and at the bottom of the triangle; (b) take a horizontal line, apply the equal area rule, place missing elements at the additional zone at the right if necessary, then shift the horizontal line to cover all the triangle; (c) completing the previous step produces the mask for opening; (d) obtain analogously the mask for closing; (e) combine two masks, extend horizontal bands of the mask to the right and the vertical ones to the bottom; (f) apply the combined and extended mask to the raw density. Everywhere in (a)-(f): the small crossed-over square is never activated and its local density is not important.

A. Extend the Preisach space which is originally confined within the triangle (x_{min}, x_{min}), (x_{max}, x_{max}), (x_{max}, x_{min}) by an arbitrary Δx to the right and to the bottom.
B. Start with the "raw" Preisach density Eq. (3.3.5)/Eq. (3.3.15) for the force/displacement driven system.
C. Take any horizontal line with x_c in [x_{min}, x_{max}].
D. Move a variable point x from the diagonal to the right, setting negative density values to 0, and then adjacent positive values to 0 in order to keep the density integral unchanged. This action may be called the equal area rule.
E. If the right border x_{max} is reached and "negative" areas are not yet compensated by the "positive" ones, add the missing elements into the band Δx. The distribution within Δx is not important and can be uniform.
F. Shift the horizontal line and repeat steps D and E until the whole triangle is covered. All points with zero density values form the mask for I=+1 (opening).
G. Repeat steps C through F for a vertical line and cover again the whole triangle; for each vertical line, the variable point x moves from the diagonal to the bottom border x_{min}. All points with zero density values for the mask for I=-1 (closing).
H. Apply both masks to the "raw" density. Continue the horizontal empty bands till x_o=x_{max}+Δx and the vertical ones till x_c=x_{min}-Δx.

Here x stands for T when considering the force-driven system and for b for the displacement-driven one. The procedure is further explained in Fig. 3.3.3.

Example and conclusions

The result of the algorithm application is a tangential load-displacement curve whose typical behavior is depicted in Fig. 3.3.4. It is seen that the curve exhibits the end-point memory; the congruence property can be easily verified as well. The inset illustrates the applied forces linked by some loading conditions (not shown). The normal forces N is normalized on a characteristic value N_0; the other normalization contacts are μN_0 and $\mu\theta a(N_0)$ for the tangential force T and displacement b, respectively.

The results of this section form a basic of the Preisach representation in frictional contact mechanics. The complex evolution of the shear stress in the contact zone corresponds to the complex structure of the Preisach density. However, constructing the density in an analytical or numerical manner makes it possible to apply a standard procedure (evolutions in the Preisach space) to obtain the response of the system for any kind of excitation protocol. Here, similarly, to section 2.8, hysteretic elements do not correspond to any physical entity in

the system. The elements do not reflect the presence of any statistical ensemble in the system; they are introduced as a mathematical technique that allows us to replace the consideration of cumbersome shear stress distributions by a standard and relatively simple algorithm that has being used in ferromagnetism and elasticity for many years. Of course, the complexity of the initial physical problem can not be avoided "for free", but now it is concentrated in the complex structure of the density that can be reproduced, for instance, in a numerical manner more suitable for practice. The important requirements of the Preisach representation are the existence of a loading condition $N=N(T)$ or $a=a(b)$ and 2D loading (forces and displacements always stay in one plane).

The Preisach representation is cited here in order to illustrate its general applicability for rate-independent hysteresis problems in 1D. In practice, it is recommended to use the method of memory diagrams introduced in the next section.

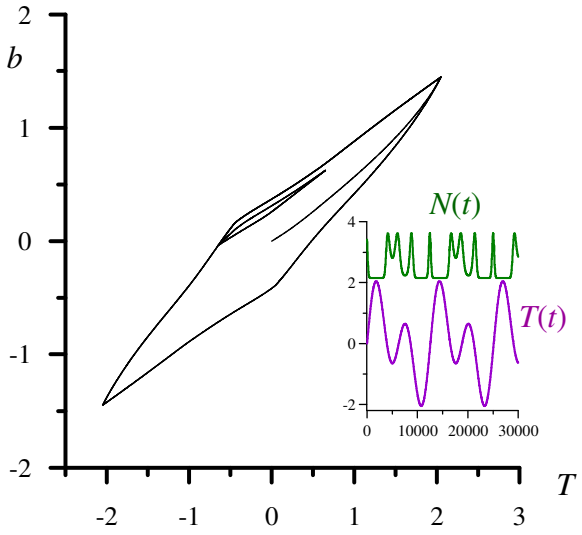

Fig. 3.3.4. Typical hysteretic response of the force-driven system: tangential loading curve $b(T)$. The loading protocol is shown in the inset. The normal reaction curve $a(N)$ needed for calculations correspond to the Hertz solution for spheres.

3.4. Method of memory diagrams

Method of Memory diagrams (MMD, see **[Ale-10], [Ale-11a], [Ale-11b], [Ale-11c], [Ale-12a], [Ale-12b], [Ale-12c], [Ale-12d], [Bol-13], [Ale-14a], [Ale-14b], [Ale-15a], [Ale-15b], [Ale-15c], [Ale-15d], [Ale-15e]**) does not require any specific loading conditions. In 2D, it provides a two parametric output for a two-parametric input i.e. $(N,T)\Rightarrow(a,b)$ for a force-driven and $(a,b)\Rightarrow(N,T)$ for displacements-driven systems. 3D extensions are also possible but are not discussed here. A memory diagram is a simplified form of representing a complex

traction distribution by a graphical object that contains the same amount of information. For the force-driven system, it is convenient to use a force-related variable η, instead of the radial variable ρ, which is defined (see Eq. (3.2.12)) by a nonlinear scaling transformation $\rho \to \eta = N(\rho)$, where ρ formally substitutes c in the normal problem solution $N=N(c)$. Aside from the nonlinear mapping η has the same practical sense as the radial coordinate ρ. Using coordinate ρ does not limit the applicability of results to axisymmetric systems only since, as we have seen in section 3.2, an arbitrary contact system for which the REPF is valid can be replaced by an effective axisymmetric system.

Simplest memory diagrams for an initial curve

In order to introduce the MMD concept, we start with the simplest constant-loading case: we consider a contact zone which is initially free of traction, and then create a traction distribution by applying tangential force T, assuming that the normal force is kept constant during the tangential loading. This particular situation has already been described in section 3.2 (see Eq. (3.2.1) or Eqs. (3.2.9)- (3.2.11)) and is illustrated for the contact of two spheres in Fig. 3.4.1 (a). As required by Coulomb's friction law, the shear stress (traction) within the slip annulus $s<\rho<c$ equals the normal stress times μ. The corresponding memory diagram is a function $D(\eta)$ introduced (see Fig. 3.4.1 (c)) in such a way that the slip annulus $s<\rho<c$ in which $\tau(\rho)=\mu\sigma(c,\rho)$ corresponds to the segment $Q<\eta<N$ with $Q=N(s)$ on which $D(\eta)=1$. More generally, any memory diagram ending by a segment on which $D(\eta)=\pm 1$ indicates the presence of slip in the corresponding annulus of the contact circle. Note that the propagation of slip from the contact boundary $\rho=c$ to a value $\rho=s$ not only creates traction in the slip annulus but also in the stick zone ($\rho<s$) as well, whereas in the memory diagram function $D(\eta)$ on the corresponding segment $0<\eta<Q$ stays unchanged and equals 0. This was a deliberate assumption as the traction distribution in that zone can be easily calculated using Eq. (4) with known c and s (or N and Q) and does not contain any additional information.

The force balance equation in terms of traction distributions reads

$$2\pi\int_0^c \tau(\rho)\,\rho\, d\rho = T\,.$$

In the language of memory diagrams the balance equation becomes

$$\int_0^N D(\eta)\, d\eta = T/\mu \tag{3.4.1}$$

which can be easily verified, since the integral in Eq. (3.4.1) amounts to N-Q and therefore equals T/μ according to Eq. (3.2.1). Thus, the memory diagram shown in Fig. 3.4.1 (c), on

one hand, contains all elements necessary to calculate the traction distribution in Fig. 3.4.1 (a), and, on the other hand, represents an alternative form of the force balance equation.

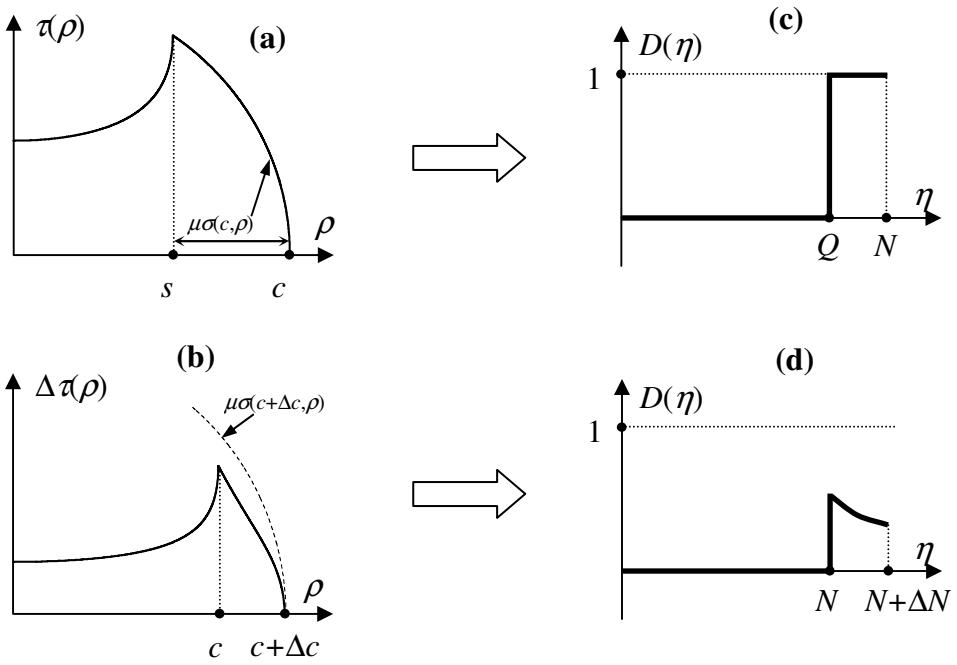

Fig. 3.4.1. Basic traction distributions for a contact between two spheres. (a): Constant N and subsequently constant T forces are applied (a) so that slip progresses from the contact boundary c to a certain value s. In the slip zone $s<\rho<c$ the Coulomb friction condition $\tau(\rho)=\mu\sigma(c,\rho)$ is fulfilled. (b) The forces N and T change simultaneously so that the condition Eq. (3.4.4) is satisfied, slip is absent, and $|\tau(\rho)|<\mu\sigma(c,\rho)$ everywhere in the contact zone. In both cases, the forces have been applied to a traction-free contact (absence of loading history, initial curve). Group (c) and (b): Memory diagrams corresponding to the basic solutions: (c) corresponds to (a), (d) corresponds to (b).

The second principal solution of interest is related to the situation when N does not stay constant during the application of T but rapidly increases so that $(1/\mu)|dT/dN|<1$. This slip-free case is mentioned in section 3.3, and is referred to as "overloading" or "quick" enlargement of the contact zone in **[Ale-12a]** and **[Ale-13a]**, or "complete overlapping" by Jäger ([Jäg-98], [Jäg-03]). The slip-free solution can be derived from the same equations Eqs. (3.2.9)- (3.2.11) as in the previous case using the incremental technique [Min-53]. It consists in assuming a small increment ΔN that enlarges the contact zone from c to a new radius $c+\Delta c$, and a small increment ΔT that produces slip characterized by the radius s. If s lies between c and $c+\Delta c$ no slip occurs. Using Eqs. (3.2.9)- (3.2.11) we write

$$\frac{\Delta\tau(\rho)}{\mu}=\frac{\partial\sigma(c,\rho)}{\partial c}(\Delta c-s+c),$$

$$\frac{\Delta T}{\mu}=\frac{dN}{dc}(\Delta c-s+c),$$

$$\frac{\Delta b}{\theta\mu}=\frac{da}{dc}(\Delta c-s+c),$$

where the last two equations respectively describe slip induced by the force ΔT or by displacement Δb, applied to a contact of radius $c+\Delta c$. Solving for Δc-s+c, we finally obtain

$$\Delta\tau(\rho)=\frac{\partial\sigma(c,\rho)}{\partial c}\frac{dc}{dN}\Delta T=\frac{1}{\theta}\frac{\partial\sigma(c,\rho)}{\partial c}\frac{dc}{da}\Delta b \tag{3.4.2}$$

for the traction increment, and

$$\frac{\Delta b}{\Delta T}=\theta\frac{da}{dN} \tag{3.4.3}$$

for the tangential force and displacement increments, where derivatives dc/dN, dc/da, and da/dN are given by the known normal solution. Besides, the condition representing the absence of slip

$$c<s<c+\Delta c$$

corresponds to the validity condition

$$(1/\mu)\left|\Delta T/\Delta N\right|<1,\ \ \Delta N>0 \tag{3.4.4}$$

for this solution.

Fig. 3.4.1 (b) shows the traction increment corresponding to an exemplar case of the contact between two spheres. In the plot, the increments Δc and $\Delta\tau$ are not small but obtained as a sum of small increments, each satisfying the validity condition of the slip-free solution so that the absolute value of the traction in Fig. 3.4.1 (b) is less than the limiting value $\mu\sigma$ at each point.

In defining the related memory diagram, our intention is to keep the force-balance equation in the form of Eq. (3.4.1) for any current N. The result is shown in Fig. 3.4.1 (d) where the curvilinear piece of the memory function is given by

$$D(\eta)=\frac{1}{\mu}\frac{dT}{dN}\bigg|_{N=\eta}. \tag{3.4.5}$$

The absolute value of the memory function on the new segment $N<\eta<N+\Delta N$ is less than 1 which follows from Eq. (3.4.4). This means that the memory diagram does not end with a segment on which $D(\eta)=\pm1$, and indicates the absence of slip in the considered case.

Similar as in the previous situation of slip, there is an unchanged part $0<\eta<N$ of the memory diagram despite the fact that the traction in the corresponding contact area ($0<\rho<c$)

changes. It is not critical in the MMD since the traction in the whole contact area can be computed from the solution for the normal stress using Eq. (3.4.2), taking into account only those parameters pertaining to the important part $N<\eta<N+\Delta N$ of the diagram. Thus, again, the memory diagram in Fig. 3.4.1 (b) contains all necessary information to retrieve the original traction in Fig. 3.4.1 (d) and, at the same time, satisfies the force balance equation in the form Eq. (3.4.1).

Evolution of memory diagrams

In the general case of an arbitrary loading history, we define the memory diagram as an internal functional dependency $D(\eta)$ satisfying the following three properties.

(I) The memory function $D(\eta)$ is specified on the η-interval limited by the current normal force N ($0<\eta<N$), and evolves in such a way that its integral over this interval always equals T/μ (Eq. 3.4.1) in accordance with the force balance equation.

(II) The absolute value of the memory function can not exceed 1. This requirement is related to the Coulomb friction law and agrees with the procedure established above in this section in which $\left|D(\eta)\right|\le 1$ in the changing part of the diagram, while in the other part $D(\eta)$ is left unaffected.

(III) A possible adjustment of the memory function $D(\eta)$ in the purpose of complying with the principle (I) is made by setting a final segment $Q<\eta<N$ of the memory diagram on which $\left|D(\eta)\right|=1$. This final segment corresponds to the presence of slip that propagates inward until, by proper setting of Q, the condition (I) is satisfied.

In the following paragraphs, we explain how the conditions (I)-(III) determine the evolution of a memory diagram for arbitrary force increments ΔN and ΔT. At each instance, the updated memory diagram allows us to calculate the corresponding displacement increments thus providing the solution to the contact problem. The complete MMD algorithm for an individual step, going from the previous (subscript "p") to the next (subscript "n") values of the parameters, is shown in Fig. 3.4.2. In our notation, the increments are denoted as Δ (e.g. $\Delta N=N_n-N_p$, $\Delta T=T_n-T_p$, etc). Since the normal solution to the contact problem is known, the normal displacement increment

$$\Delta a = a\left(N_n\right) - a\left(N_p\right) \tag{3.4.6}$$

can be calculated directly , while Δb has to be determined as the result of the procedure. The algorithm involves only two binary choices and, therefore, it contains three cases in which the calculations differ. As illustrated in Fig. 3.4.2, we have called these cases YY, YN, and N. In all illustrations, the values of "small force increments" are exaggerated.

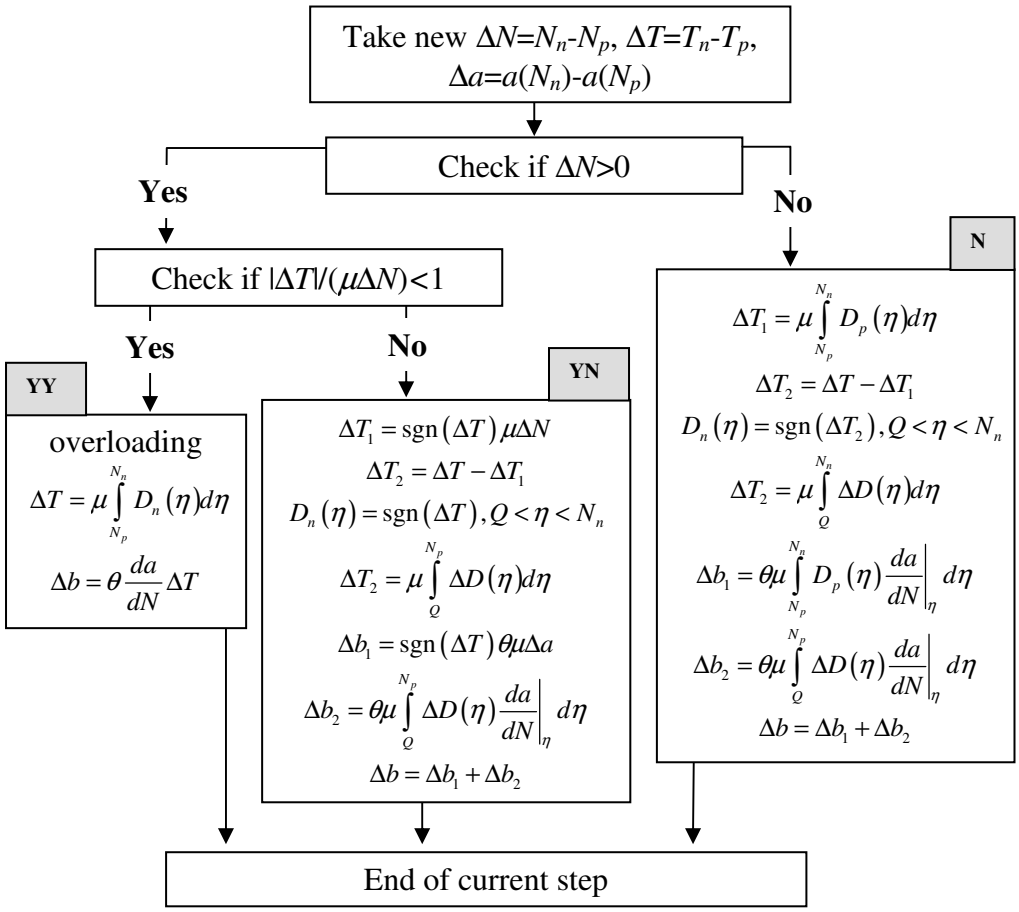

Fig. 3.4.2. Complete algorithm of the method of memory diagrams. The equations displayed in the boxes correspond to Eqs. (3.4.6)-(3.4.23).

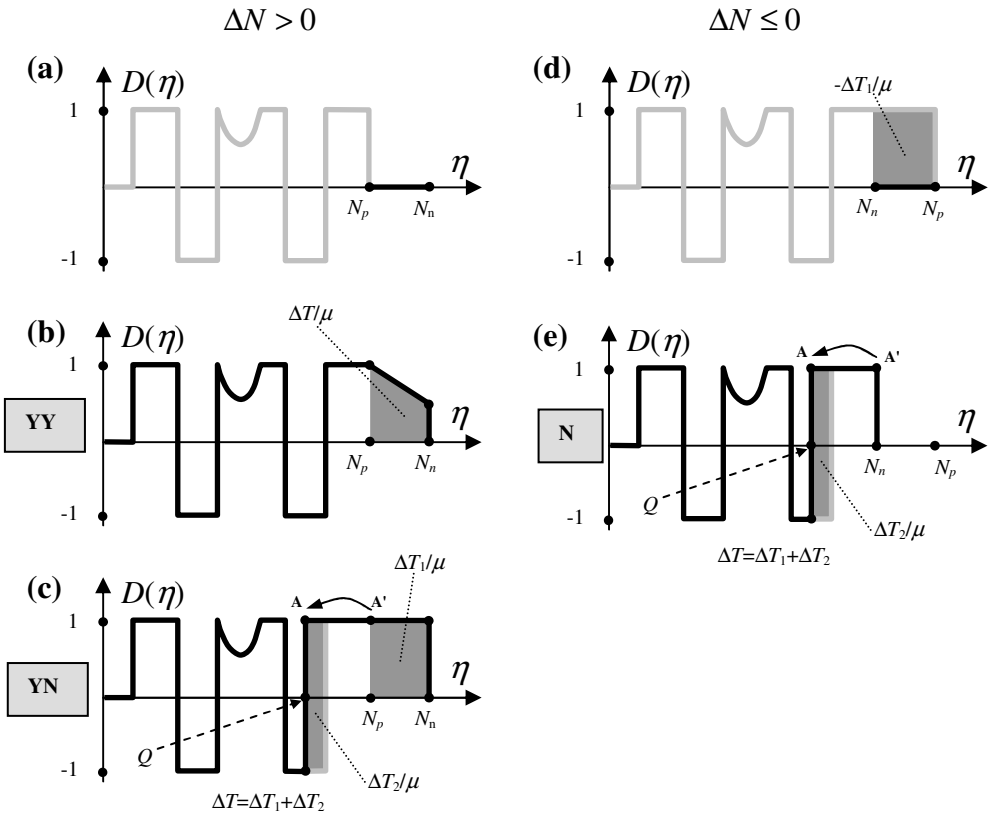

Fig. 3.4.3. Illustrations of the evolution algorithm. (a) Original memory diagram (gray), N increases from N_p to N_n. (b) Case YY i.e. $(1/\mu)|\Delta T/\Delta N|<1,\ \Delta N>0$; The force increment ΔT can be equilibrated by the proper choice of $D(\eta)$ on the new interval $N_p<\eta<N_n$. (c) Case YN i.e. $(1/\mu)|\Delta T/\Delta N|\geq 1,\ \Delta N>0$; The increment ΔT is too large to be equilibrated by setting $D(\eta)=1$ only on the new interval $N_p<\eta<N_n$; Therefore, the slip zone with $D(\eta)=1$ penetrates closer to the contact center. (d) Original memory diagram (gray), N decreases from N_p to N_n releasing force ΔT_1. (e) The residual force increment $\Delta T_2=\Delta T-\Delta T_1$ is equilibrated by a slip propagation. In sets (b), (c), and (e), the thick black lines indicate newly generated parts in the memory diagrams.

Case YY. First al all, the situation is different for increasing and decreasing N. If N increases ($\Delta N>0$, Fig. 3.4.3 (a)-(c)), a new segment $N_p<\eta<N_n=N_p+\Delta N$ should be added to the diagram as shown in Fig. 3.4.3 (a). Then, in order to comply with the condition (I), the memory function is to be updated in such a way that its integral stays equal the tangential force i.e. the integral of the memory function variation $\Delta D(\eta)$ equals $\Delta T/\mu$. Two situations are possible: ΔT can be fitted by updating the memory function on the new segment only (YY), and the opposite situation (YN) which will be discussed later. Indeed, if the area $|\Delta T|$ corresponding to ΔT is small enough i.e.

$$(1/\mu)|\Delta T/\Delta N|<1, \tag{3.4.7}$$

then it is possible to define $D_n(\eta)$ on the new segment $N_p<\eta<N_n$ such that the force balance equation (3.4.1) will be satisfied without any changes to the memory function on the old segment $0<\eta<N_p$:

$$\int_{N_p}^{N_n} D_n(\eta)\,d\eta=\Delta T/\mu, \tag{3.4.8}$$

as illustrated in Fig. 3.4.3 (b). For small increments, linearly approximating the integrand in Eq. (3.4.8) we write

$$\frac{D_n(N_p)+D_n(N_n)}{2}\Delta N=\Delta T/\mu, \tag{3.4.9}$$

where $|D_n(N_n)|<1$ which ensures that the rule (II) is respected. Here $D_n(N_p)=D_p(N_p)$ since we modify the memory function only on the new interval, leaving it unchanged on the old one (compare thick gray line in Fig 3.4.3 (a) for the old diagram $D_p(\eta)$ with the thick black line in Fig. 3.4.3 (b) for the new one, $D_n(\eta)$). Correspondingly, Eq. (3.4.9) defines the updated value $D_n(N_n)$. Thus, the condition (I) is already fulfilled, and the use of the rule (III) is not required.

The inequality $\left|D_n\left(N_n\right)\right|<1$ means that the end of the diagram does not contain a section on which $D(\eta)$ equals either +1 or -1 which corresponds to slip-behavior. In other words, in this situation, the tangential force change can be "absorbed" by the system without producing slip, i.e. by a purely elastic deformation of the contacting bodies, and consequently, the slip-free solution Eqs. (3.4.2), (3.4.3) is applicable since condition Eq. (3.4.4) is fulfilled. Hence, the corresponding solution for Δb is given by Eq. (3.4.3).

Case YN. Now we consider the situation when the normal force increases, $\Delta N>0$, but $\left(1/\mu\right)\left|\Delta T/\Delta N\right|\geq 1$. Then, in general, the balance of forces in the system (Eq. 3.4.1) cannot be achieved by a simple definition of the memory function on the new segment $N_p<\eta<N_n$ only. Even if we set

$$D_n\left(\eta\right)=\mathrm{sgn}\left(\Delta T\right),\ N_p<\eta<N_n, \tag{3.4.10}$$

assuming slip on the new segment (see rule (III)), this would be only enough to fit ΔT in a degenerated case $\left(1/\mu\right)\left|\Delta T/\Delta N\right|=1$. In a more general situation $\left(1/\mu\right)\left|\Delta T/\Delta N\right|>1$, the force increment ΔT can not be equilibrated via a proper selection of the memory function on a new interval only. Defining the memory function according to Eq. (3.4.10) will only correspond to a partial force increment ΔT_1 that equals

$$\Delta T_1=\mathrm{sgn}\left(\Delta T\right)\mu\Delta N, \tag{3.4.11}$$

while the other part

$$\Delta T_2=\Delta T-\Delta T_1 \tag{3.4.12}$$

is left unbalanced for the moment. In order to take into account the unbalanced part, it is necessary to also include the old interval $0<\eta<N_p$. The process to properly do this is fixed by the rule (III) which allows us to modify the memory function at any η-value starting from the contact boundary value $\eta=N_n$ (remember that η has the sense of a generalized radial coordinate) and to use the slip solution expressed in Eqs. (3.2.9)-(3.2.11). The situation is illustrated in Fig. 3.4.3 (c) where the case of positive slip with $D=+1$ is shown for definiteness, while in a general case D should be set to $\mathrm{sgn}(\Delta T_2)=\mathrm{sgn}(\Delta T)$. Firstly, the memory function $D(\eta)$ has been set to $\mathrm{sgn}(\Delta T)$ on the interval $N_p<\eta<N_n$, thereby equilibrating the partial force increment $\Delta T_1=\mu\Delta N$. Subsequently, the remaining part $\Delta T_2=\Delta T-\Delta T_1$ is compensated for by setting $D_n(\eta)=1$ in the contact zone adjacent to the new segment $N_p<\eta<N_n$. In other words, we have to shift point A in Fig. 3.4.3 (c) starting from position A' and setting the memory function to $\mathrm{sgn}(\Delta T)$ on the interval AA' until the desired value $\Delta T_2/\mu$ is reached for which:

$$\int_{Q}^{N} \Delta D(\eta)\, d\eta = \Delta T_2 / \mu\,, \tag{3.4.13}$$

where Q is the new boundary between the stick and slip zones in the η-space, and $D_n(\eta)$=sgn(ΔT)=sgn(ΔT_2). In fact, Eq. (3.4.13) should be considered as an equation for Q.

Once $\Delta T_{1,2}$ and Q are determined, the solution for the displacement increment corresponding to ΔT_1 easily follows from Eq. (3.2.11) and reads

$$\Delta b_1 = \mathrm{sgn}(\Delta T)\,\theta\mu\Delta a\,, \tag{3.4.14}$$

while the remaining part Δb_2 is given by

$$\Delta b_2 = \theta\mu \int_{Q}^{N_p} \Delta D(\eta) \left.\frac{da}{dN}\right|_{N=\eta} d\eta \tag{3.4.15}$$

where Q is known (see further comments on Eq. (3.4.15) below). Finally, it suffices to sum both contributions to obtain the total displacement increment:

$$\Delta b = \Delta b_1 + \Delta b_2\,. \tag{3.4.16}$$

Certainly, penetration of the slip zone towards the contact zone can happen via many scenarios. For instance, in the scenario shown in Fig. 3.4.3 (c), the zone $\eta<N_n$ ends with a segment where $D(\eta)$ is equal to 1, to that setting $D(\eta)$ to 1 in this segment does not compensate anything, and we have to address a zone closer to η=0. On the other hand, when the memory diagram is such that the old contact area $\eta<N_n$ ends with a value of $D(\eta)$ different from 1, the update produces an immediate contribution. Furthermore, it is entirely possible that the developing slip zone erases a certain part in the structure of the memory function by setting it to 1. This would happen in Fig. 3.4.3 (c) if ΔT were large so that point Q would have progressed further to the left thereby completely eliminating the segment with $D(\eta)$=-1 and eventually also other segments. Point Q can even reach η=0 resulting in a gross sliding behavior. The strength of the proposed approach is that it automatically complies with the force balance without specifying or classifying all structural changes that can potentially occur to the memory diagram.

Case N. We now consider the situation in which the normal force is constant or decreasing, $\Delta N \le 0$. In this case, the memory diagram should shrink to the new size N_p, and therefore release some tangential force ΔT_1, as shown in Fig. 3.4.3 (d):

$$\Delta T_1 = \mu \int_{N_p}^{N_n} D_p(\eta) d\eta \tag{3.4.17}$$

(ΔT_1=0 in a particular case when ΔN=0). In order to balance the force equation, we have to account only for the partial force increment

$$\Delta T_2 = \Delta T - \Delta T_1 . \tag{3.4.18}$$

As previously, there is no other option than to allow slip to penetrate closer to the contact center (except in a particular case when ΔT_2 coincidentally equals 0). This means that we have to shift point A, starting from position A' (Fig. 3.4.3 (e)), while setting

$$D_n(\eta) = \mathrm{sgn}(\Delta T_2) \tag{3.4.19}$$

on interval AA', until the force balance equation

$$\Delta T_2 = \mu \int_Q^{N_n} \Delta D(\eta) d\eta \tag{3.4.20}$$

is satisfied. As previously mentioned, various slip scenarios are possible depending on the structure of the memory function on the segment $0<\eta<N_n$.

Once the values of ΔT_1 and ΔT_2 are determined for this case, the related b-increments then read

$$\Delta b_1 = \theta\mu \int_{N_p}^{N_n} D_p(\eta) \left.\frac{da}{dN}\right|_{N=\eta} d\eta , \tag{3.4.21}$$

$$\Delta b_2 = \theta\mu \int_Q^{N_p} \Delta D(\eta) \left.\frac{da}{dN}\right|_{N=\eta} d\eta , \tag{3.4.22}$$

with the total

$$\Delta b = \Delta b_1 + \Delta b_2 . \tag{3.4.23}$$

Eqs. (3.4.17)-(3.4.23) then represent the full solution to the problem in case N.

The solutions that allow slip (i.e. hysteretic), as found in the cases YN and N, have an interesting feature. In the case YN when the normal force increases, the maximal setting $|D(\eta)|=1$ in the new segment is not enough for equilibrating the tangential force, so that we have to engage the older segments. As ΔT_1 and ΔT_2 have the same sign (which also equals the sign of ΔT), the direction of slip always coincides with the direction of the tangential force increment. However, in the case N, corresponding to normal unloading, this is not always true. Decreasing the normal force releases some force ΔT_1 whose value and sign are defined by the system's history, and therefore completely independent on the increment ΔT. In the situation presented in Fig. 3.4.3 (e), the direction of slip is positive since $D_n(\eta)=+1$ at the end of the new diagram, but the released area $\Delta T_1/\mu$ is larger than the area $\Delta T_2/\mu$ generated by slip. This implies that the sum $\Delta T=\Delta T_1+\Delta T_2$ is negative, and the slip direction is opposite to the direction of the tangential force change.

The above rules composing the solution procedure only represent a first-order approximation since, in particular, Eq. (3.4.9) has the precision of $o(\Delta N)$. In addition, the

instruction "shift point A until the force balance equation is satisfied" actually implies an implicit, and therefore in practice, approximate character of the procedure. However, despite the fact that the procedure of building up memory diagrams is approximate, the solution for the displacements corresponding to a predetermined memory diagram is exact. This is elaborated on in the next paragraph.

"Reading" memory diagrams

In the previous section, we have formulated the evolution rules for a memory diagram governing the behavior of the force-driven system. The choice of arguments (forces or displacements) depends only on the context in which the contact problem is posed, and does not affect the physics of the contact interaction. In particular, the following reasoning is valid. Any complex traction distribution within the contact zone corresponding to a certain local tangential displacement field can be represented by a memory diagram $D(\eta)$ as described above. Based on $D(\eta)$, we can then use Eq. (3.4.1) to calculate the tangential force. On the other hand, the solution represented in Eqs. (3.2.10)-(3.2.11) warrants that the MMD is completely symmetric with respect to the argument's choice. Therefore, it is possible to introduce a memory diagram $D(\alpha)$ in the space of a displacement-related argument parameter α given by $\alpha=a(\rho)$ where ρ formally substitutes the argument c in the normal problem solution $a(c)$. Then, similarly to Eq. (3.4.1), the tangential displacement is given by the following simple relationship

$$\int_0^a D(\alpha)\,d\alpha = b/(\theta\mu)\,. \tag{3.4.24}$$

At the same time, the memory diagrams $D(\eta)$ and $D(\alpha)$ are related to the traction distribution and local tangential displacement distribution which correspond to the same deformation state of the body. Hence, the two diagrams are structurally identical, and can be obtained by different scale transformations of the original ρ-coordinate. This yields the following relationships:

$$T = \mu\int_0^a D(\alpha)\left.\frac{dN}{da}\right|_{a=\alpha} d\alpha\,, \tag{3.4.25}$$

$$b = \theta\mu\int_0^N D(\eta)\left.\frac{da}{dN}\right|_{N=\eta} d\eta\,. \tag{3.4.26}$$

Obviously, this also leads to the following symmetric representation using the original radial coordinate ρ:

$$T = \mu\int_0^c D(\rho)\left.\frac{dN}{dc}\right|_{c=\rho} d\rho\,, \tag{3.4.27}$$

$$b = \theta\mu \int_0^c D(\rho) \left. \frac{da}{dc} \right|_{c=\rho} d\rho \,. \tag{3.4.28}$$

With this representation, the rest of the MMD equations have to be modified accordingly.

To give an example, in Fig. 3.4.4 we plot a traction distribution for a contact between two spheres

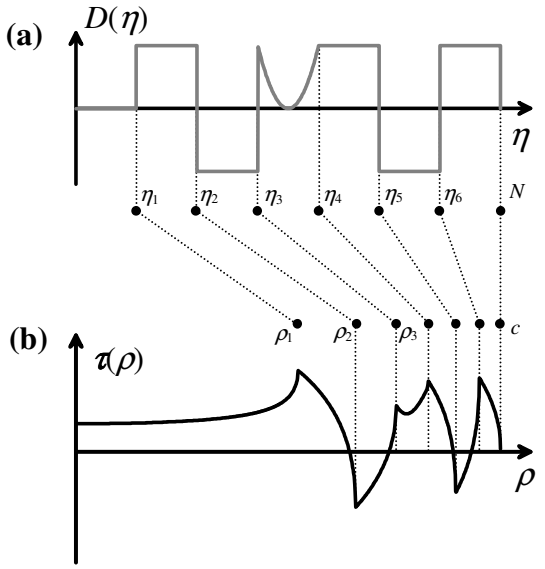

Fig. 3.4.4. Memory diagram (a) and corresponding traction distribution (b) for contact of two identical spheres. The scale transformation is given by $\rho = \left(KR\eta\right)^{1/3}$, equation immediately following from the Hertz theory.

In conclusion, the integral formulations Eqs. (3.4.1), (3.4.24)-(3.4.28) present a simple way of "reading" the memory diagrams in η, α, and ρ-spaces. In all cases, the memory functions consist of constant or curvilinear sections, as shown in Fig. 3.4.3. The difference only resides in a nonlinear stretching of the horizontal axis.

Numerical implementation and examples

The MMD formulation discussed in the previous paragraphs does not impose any requirements with respect to the numerical implementation procedure. The simplest numerical implementation can consist in introducing a fixed-point grid η_i on the η-axis and in defining the corresponding function values $D(\eta_i)$ on that grid. However, this method is time consuming and inaccurate. We have implemented a more precise technique that uses the fact that the memory function is constant on certain intervals and thus can be represented only by the pairs of the two boundary values of η defining the intervals. For curvilinear sections, not only the interval boundaries but all intermediate points η=$N(t_i)$ are to be memorized (here $N(t)$

is the normal force loading history and t_i are discrete observation moments, $\Delta N=N(t_{i+1})-N(t_i)$, $\Delta T=T(t_{i+1})-T(t_i)$, etc.). Thus, in general, the function $D(\eta)$ can be defined on a non-equidistant and adaptive grid. In those cases where the memory function has to be determined in between two points of a curvilinear section, we use a linear interpolation. As a result, the complexity of this numerical code exceeds only slightly the complexity of the method itself (see Fig. 3.4.3).

A simple example illustrating all three cases (or regimes) YY, YN, and N is shown in Fig. 3.4.5. for a monotonous time dependence of the tangential force $T(t)$ (see the inset in Fig. 3.4.5 (a)), the response $b(T)$ (main figure 3.4.5(a)) is monotonous as well. However, the normal force $N(t)$ in Fig 3.4.5(a) is not monotonous that makes it possible to see various regimes in the corresponding memory diagrams (see Fig. 3.4.5(b-e) corresponding to moments of time t=0.25, 0.4, 0.5, 0.9 in arbitrary units, marked by dotes lines in Fig. 3.4.5(a)). The curve $N(t)$ begins with an increasing segment on which the condition Eq. (3.4.7) is fulfilled (case YY, thick gray lines in Fig. 3.4.5(a)). According to the given explanation, a curved-line segment appears in the memory diagram (Fig. 3.4.5(b)). Further, $N(t)$ still increases but the condition Eq. (3.4.7) is not satisfied anymore thus resulting in appearance of the regime YN (thick black line in Fig. 3.4.5(a)). A typical behavior is shown in Fig. 3.4.5(c); a straight-line segment $Q<\eta<N$ on which $D(\eta)$=1 corresponds to slip. Slip propagates inward erasing the previously saved curvilinear segment. At the moment t=0.5 the normal force starts decreasing, therefore the total length of the memory diagram shrinks (future evolution of the memory diagrams is shown with arrows in all sets (b)-(e)), and the system runs in the regime N (Fig. 3.4.5(d)). Then, point Q shifts closer to the left end of the memory diagram η=0 (Fig. 3.4.5(e)); at the moment t=1 Q reaches 0 which means that partial slip transforms into total sliding when $T=\mu N$.

Two more general cases of the MMD application are presented in Fig. 3.4.6. Fig. 3.4.6(a) illustrates the particular situation when the two force arguments, N and T, are linked by a functional relationship, $N=N(T)$, so that actually there is only one independent argument but it evolves in a non-trivial manner. The resulting curve $b(T)$ shown in Fig. 3.4.6(a) is typical for one-parametric hysteresis response: it exhibits closed loops for periodic $T(t)$, partial increase in the argument T on a globally decreasing branch results in the creation of an inner loop, and each completed inner loop has the property of end-point memory, where the curve exits the outer loop with the same tangent as just before entering it, etc. The curves were calculated with the same parameters as curves in Fig. 3.3.4 for the Preisach method, the results coincide with a precision related to numerical discretization. These methods use different equations and completely independent codes.

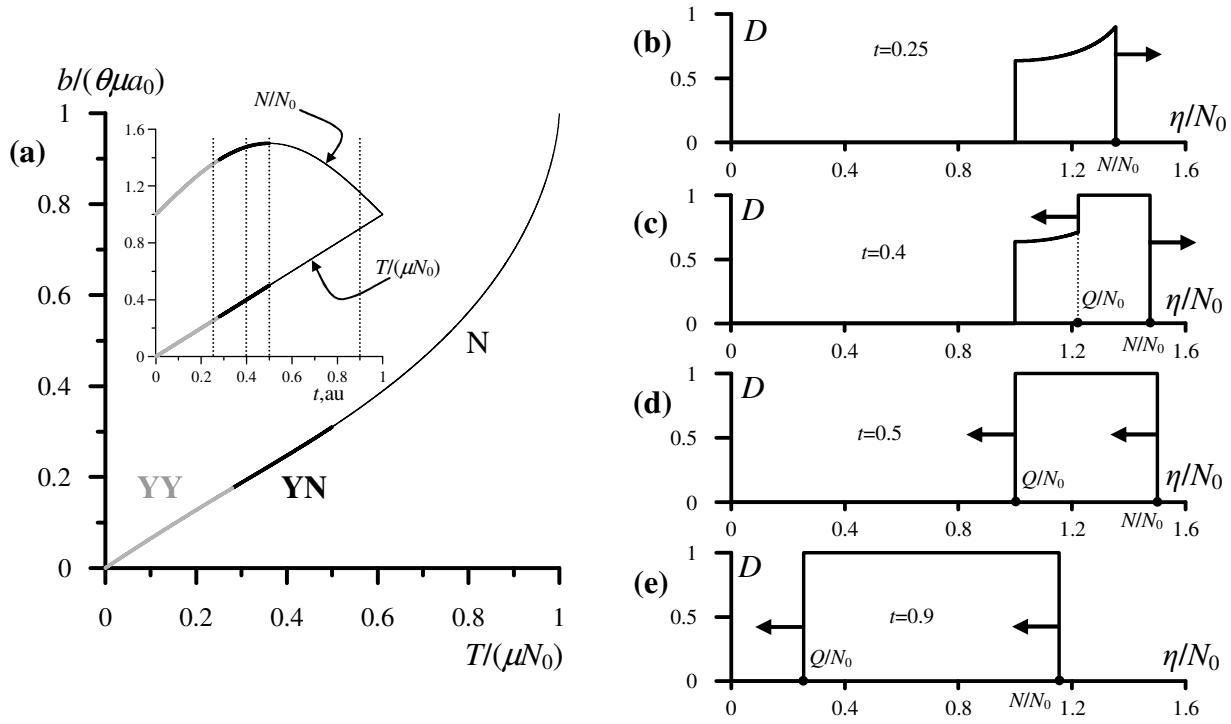

Fig. 3.4.5. Tangential force displacement relationship in which three regimes (cases YY, YN, and N) can be identified (gray, thick black, and thin black lines, respectively). In the inset: loading protocol i.e. time dependencies of normal and tangential forces; the regimes are marked as in the main figure. Four moments of time are selected; memory diagrams at these moments are shown in sets (b)-(e). In all plots, N_0 is a characteristic value of the normal force; $a_0=a(N_0)$.

In the more general case of two independent arguments, N and T without functional relationship, the hysteretic behavior differs considerably. Since variations in N are not linked to the $T(t)$-protocol, it occurs that, even for a periodic $T(t)$ loading history, the "loops" are not necessarily closed, on the contrary. Indeed, as illustrated in Fig. 3.4.6(b), the same $T(t)$-history as used in Fig. 3.4.6(a) produces a curve in which all monotonous parts are shifted, bent, etc. It is important to emphasize that the generation of such curves via the direct analysis of the traction and without the use of the MMD is an extremely cumbersome task. The formulation in terms of MMD strongly reduces the complexity.

Finally, it can be analytically verified that all classical results, as discussed in [Min-53], for spheres loaded by an oblique force follows in a simple and straightforward manner from the MMD equations. As such we have validated our novel approach in numerous exemplary situations.

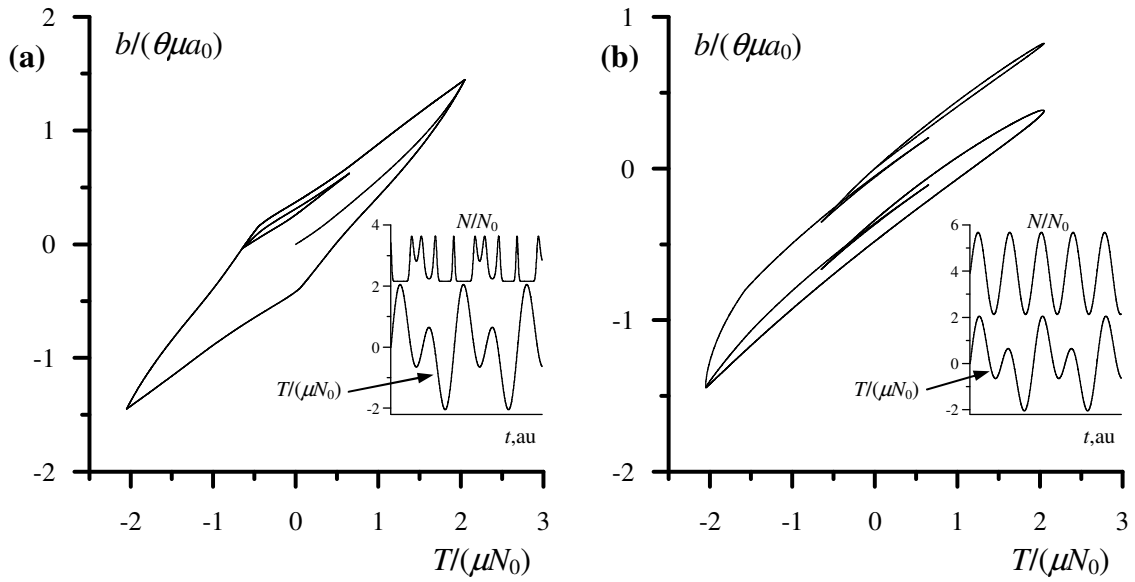

Fig. 3.4.6. Tangential force-displacement curves for some particular loading histories as shown in the insets. (a) One-parametric hysteresis, in which N and T are linked via a functional dependence, same as Fig. 3.3.4. (b) Two-parametric hysteresis in which N and T are independent. In all plots, N_0 is a characteristic value of the normal force; $a_0=a(N_0)$.

3.5. Summary of the fundamental solutions for the frictional interaction

Chapter 3 is devoted to derivation of fundamental solutions for frictional contact mechanics applicable for arbitrary loading protocols. Our objective was to find a solution (i.e. normal (a) and tangential (b) displacements) to the frictional contact problem with an arbitrary geometry of contacting profiles and for an arbitrary loading history in terms of the normal (N) and the tangential (T) forces. Two methods have been elaborated: the Preisach approach (section 3.3) valid when a specific loading condition is prescribed and method of memory diagrams (section 3.4) valid both in the presence or absence of such a condition. For the both methods, the following assumptions have been accepted.

1. Loading is in one plane only (i.e. in 2D) and quasi-static.
2. The Coulomb friction law with friction coefficient μ is postulated for contact stresses.
3. $|T|<\mu N$ so that only partial slip is considered; the opposite for quasi-static loading is trivial.
4. Plasticity and adhesion are ignored.
5. All individual contact spots are aligned (i.e. they have the same normal directions) and stay aligned during loading.

6. The normal solution $a=a(N)$ is independent of the tangential loading and is known from previous studies.
7. Dissimilarity effects are neglected.
8. The reduced friction principle is valid for the considered geometry.

The methods are valid for a wide range of contact geometries (see section 3.2). For instance, multiple contact spots can merge and split. The analysis is essentially based on the reduced friction principle which allows us to replace the arbitrary body shapes by a pair of effective axisymmetric profiles having the same normal reaction $a(N)$ or $N(a)$ which is supposed to be known. Once the effective profile is determined, we use one of the two methods for the effective axisymmetric contact and deduce a computer-assisted analytical solution. The methods are formulated both for force-driven and displacement-driven systems.

4. Numerical modeling of acoustic waves in materials with frictional cracks

4.1. Introduction

This chapter concerns the use of the developed contact model for building up a numerical toolbox (called here MMD-FEM software or code) capable of simulating wave propagation and vibrations in sample containing cracks of known geometry. Such a toolbox represents a numerical support for nonlinear nondestructive testing (NDT) methods that have been created during last decades for detection and visualization of defects in machinery, automobile and aeronautical components, for health monitoring of buildings, bridges and other structures. Numerical modeling of physical processes underlying the NDT experiments offers a complete access to all calculated parameters and fields and therefore dramatically increases the "transparency" of all experimental procedures. Moreover, modeling allows one to estimate physical parameters of damage such as crack size and/or crack opening and finally try to assess the serviceability or lifetime of the sample.

The contact model developed in chapter 3 is especially suitable for that goal. Indeed, on one hand, the purely analytical solutions of the Hertz-Mindlin type [Min-53] and their extensions are not directly applicable to arbitrary loading histories and acoustic excitations; an automated account for friction-induced memory effects is needed. On the other hand, purely numerical approaches in contact mechanics suitable for virtually any geometries and movement types are extremely time consuming, since all geometrical elements including microscopic ones have to be adequately meshed. The automated semi-analytical solutions represent a successful compromise since the implemented multi-scale approach make is possible to integrate the influence of microscopic features into mesoscopic-level response. At the same time, the method is based on analytical solutions and has therefore the advantage of a high computational speed; the algorithmic part is needed only for automated calculations of the analytical solutions' parameters.

The numerical tool described in this chapter consists of two parts: the contact model (chapter 3) and the solid mechanics unit. The solid mechanics unit is created using available finite element software (COMSOL in our study). Features of COMSOL allow one to implement user-defined boundary conditions at internal boundaries including the boundary conditions obtained as a result of algorithm execution.

The account for interface roughness is essential for the proposed approach, as it leads to a different formulation of the problem when compared to the case of ideally flat crack

surfaces that are subject to the Coulomb friction law. In the latter case, depending on the loading conditions, one of the three following cases can occur at each pair of close points located at opposite faces. First, if contact between the surfaces is lost, the local normal (σ) and tangential (τ) stresses both equal zero, while local normal and tangential displacements between this pair of points are defined by external conditions and not by the crack model itself. Second, in the case where $|\tau| < \mu\sigma$ (μ is the coefficient of friction), the normal displacement equals zero and the tangential one does not change, i.e. the stick event occurs. Finally, when $|\tau| = \mu\sigma$ the event of slip takes place. In that situation, a certain tangential displacement is developed which depends on external conditions, whereas the normal displacement still equals zero. It is important to note that the case $|\tau| > \mu\sigma$ is prohibited by the Coulomb friction law. In addition, the normal displacement can be negative (corresponding to a locally open interface) or equal zero (in the presence of contact), but is never positive for ideally flat surfaces since they do not have any asperities receding under load (remember that we assume positive normal characteristics in compression).

Thus, the Coulomb friction law for flat contact faces does not provide an explicit load-displacement relationship that could be easily used as the boundary condition by the solid mechanics part. Below we show how the use of the MMD helps solve the problem of explicit calculations of loads from displacements.

The results discussed in chapter 4 were published in **[Del-16a]**, **[Del-16b]**, **[Del-17a]**, **[Del-17b]**, **[Del-17c]**, **[Del-18]**, **[Ale-17]**, **[Ale-18]**. The COMSOL implementation has been done by Dr. Steven Delrue (KU Leuven, Campus Kortrijk).

4.2. Complete friction model accounting for partial slip, total sliding, and contact loss

The MMD in the formulation given in chapter 3 does not produce the sought-for boundary conditions at internal contact boundaries directly.

First of all, it addresses contact between two bodies with some surface profile (including rough surfaces) remotely loaded by forces *N* and *T*, while in materials containing cracks under acoustical excitation the load is distributed. To extend the method onto this case, we introduce a number of mesoscopic cells containing various parts of a crack (Fig. 4.2.1 (a)) such that load can be considered uniform within each cell (Fig. 4.2.1 (b)). It is then appropriate to introduce mean mesoscopic stresses (normal -*N* and tangential *T*) defined by normalization of forces

$$N \to N / A_n,\ T \to T / A_n \tag{4.2.1}$$

by unit nominal contact area A_n. Note that now the mean normal stress equals $-N$ since according to the usual conventions normal stress is negative in compression while in chapter 3 compression corresponds to $N>0$ and $a>0$.

Secondly, the MMD only accounts for partial slip when some points in the contact zone slip and some do not; otherwise the concept of equilibrium that underlies the MMD is not valid anymore. Hence, it is necessary to split the total tangential displacement into two parts: one part, b_0, corresponding to total sliding and the other one, $\tilde{b}$, to partial slip (Fig. 4.2.1 (d), (e)):

$$b = b_0 + \tilde{b}, \tag{4.2.2}$$

The idea **[Ale-18]** behind this separation can be illustrated as follows. Suppose the tangential loading increases under a fixed normal compression $N=N(a)$, corresponding to a certain normal displacement a. Asperities recede under load in both normal and tangential direction. In addition, the tangential receding $\tilde{b}$, in contrast to the normal one, a, is accompanied by partial slip. According to the MMD based on the Coulomb friction law, $\tilde{b}$ is not allowed to grow infinitely. Once the maximum value $\tilde{b}_{\max} = \theta\mu a$ is achieved, the asperities can not deform anymore and a total sliding process develops when the very last stick point belonging to one face separates from its neighbor at the opposite one. The tangential displacement between those points is denoted b_0 and corresponds to the contribution from total sliding. In other words, b_0 is a reference point mismatch, in some sense.

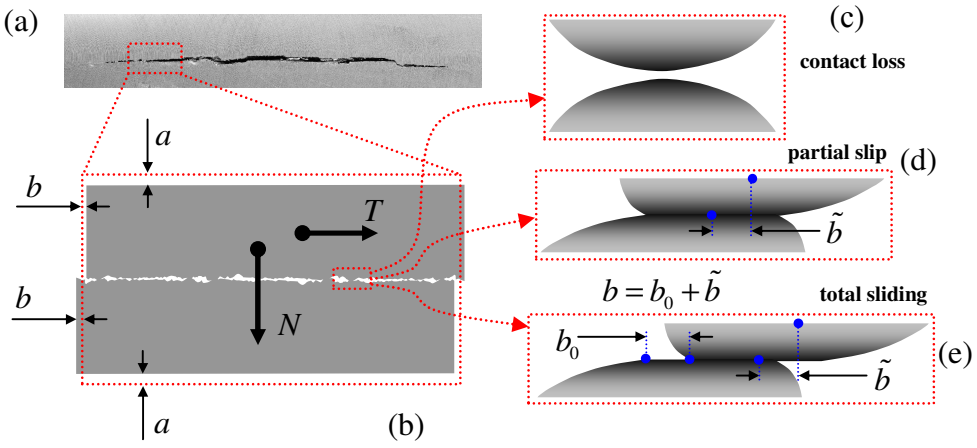

Fig. 4.2.1. Illustration of the proposed multiscale contact model. (a) Macro-level of the sample. (b) Mesoscopic cell in which mean contact stresses and displacements are defined. (c)-(e) Contact states illustrated at the microscopic level (level of asperities): (c) contact loss, (d) partial slip, (e) total sliding.

In case where the normal compression is also allowed to vary, the maximum value $\tilde{b}_{\max} = \theta\mu a$ changes too. In addition, the contact in a particular mesoscopic cell can be lost at some moment so that both stick and slip zones disappear (Fig. 4.2.1 (c)). Thus the full contact model includes three cases: partial slip, total sliding, and contact loss. The MMD algorithm applies in the case of partial slip only. It is fed by a pair (a, $\tilde{b}$) and is displacement-driven. The displacement-driven MMD is fully analogous to the case considered in chapter 3 (Eqs. (3.4.24) and (3.4.25)); the argument of the memory function is denoted α that has the dimension of displacement.

Crack state	If	Then	Memory diagram
(i) Contact loss	$a < 0$	$\tilde{b} := 0 \quad b_0 := b$ $T = N = 0$	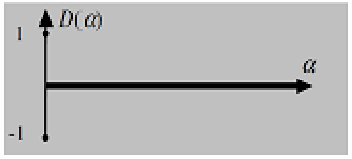
(ii) Total sliding	$a \geq 0$ $\lvert\tilde{b}\rvert \geq \theta\mu a$	$\tilde{b} := \pm\theta\mu a \quad b_0 := b - \tilde{b}$ $T = \pm\mu N$	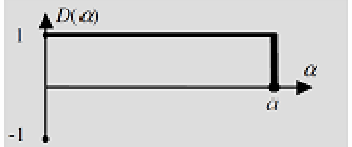
(iii) Partial slip	$a \geq 0$ $\lvert\tilde{b}\rvert < \theta\mu a$	$b_0 := b_0 \quad \tilde{b} := b - b_0$ $T = MMD(\tilde{b})$	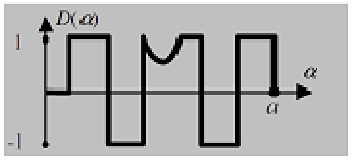

Fig. 4.2.2. Three possible contact states in the model of cracks with rough surfaces. For each case, the following information is supplied: conditions under which the case occurs, solutions for components b_0 and $\tilde{b}$, solutions for mean contact stresses -N and T, and memory diagrams.

Figure 4.2.2 provides an overview of the full concept **[Ale-18]** in case where both normal and tangential displacements a and b evolve in an arbitrary manner. The scheme explains how to calculate the mean contact stresses -N and T for any given value of displacements a and b. In order to do so, the tangential displacement components b_0 and $\tilde{b}$, together with the corresponding memory diagram should be updated. The updating operation for the tangential displacement components is denoted using the assignment operator ":=", which means that values obtained at the previous time step are overwritten by new ones. The full model in Fig. 4.2.2 assumes three possible contact states: contact loss when there is no contact between any two corresponding points from opposite crack faces, total sliding when slip occurs at each contact point and $|T| = \mu N$ according to the Coulomb friction law, and

partial slip when both stick and slip areas are present in the contact zone. Below we consider these three states in more detail.

Contact loss. If $a<0$ the contact is lost which obviously means that $N=T=0$. In this case, the repartition in Eq. (4.2.2), as well as the memory diagram, has not much sense. However, it is useful to formally define these characteristics even in the absence of contact, having in mind that at the next time step contact can be reestablished. If so, the process should start with a "virgin" memory diagram $D(\alpha)=0$, since the contact zone contains no residual tangential stress. The asperities are not strained at this moment, meaning that $\tilde{b} := 0$, and hence $b_0 = b$. Accepting these modifications will guarantee the correct evolution representation once the crack faces will ever get in contact.

Total sliding. Suppose now that $a \geq 0$ and that the old (i.e. obtained at the previous time step) value of $\tilde{b}$ is such that $\left|\tilde{b}\right| \geq \theta\mu a$, with a, the newly calculated normal displacement. In this case, the new value of $\tilde{b}$ should obviously be corrected, since the maximum tangential displacement corresponding to the elastic deformation of asperities can only be $\tilde{b}_{\max} = \theta\mu a$, and any attempt to further increase the tangential action will result in total sliding. We therefore have to set the new $\tilde{b} := \pm\theta\mu a$, with the sign corresponding to the direction of sliding. The remaining part of the tangential displacement corresponds to the total sliding contribution, $b_0 := b - \tilde{b}$. In other words, the reference point for measuring the tangential deformation of asperities is shifted. In accordance to the Coulomb friction law, $T = \pm\mu N$ and $D(\alpha) = \pm 1$, with the sign again corresponding to the sliding direction. The magnitude of the normal force per unit area $N = N(a)$ is calculated using the known normal reaction curve.

Partial slip. Assume now that $a \geq 0$ and the old value of $\tilde{b}$ is such that $\left|\tilde{b}\right| < \theta\mu a$. In this situation, some points of the contact zone stick, and slip, if it occurs at all, can only be partial. The reference value b_0 corresponding to total sliding is therefore not affected, which is symbolically expressed by assigning $b_0 := b_0$. Obviously, the remaining part of the tangential displacement corresponds to the partial slip contribution, $\tilde{b} := b - b_0$. In this regime, the MMD algorithm should be executed using $\tilde{b}$ as an argument, i.e. $T = MMD\left(\tilde{b}\right)$. The magnitude $N = N(a)$ is again calculated using the known normal reaction curve. Note that for this partial slip case, there is, however, the risk that the new $\left|\tilde{b}\right|$ will exceed $\theta\mu a$, even

though the old $|\tilde{b}|$ does not. Such a situation should be additionally checked for, and if this happens, the appropriate solution should be taken as discussed in the total sliding regime.

The algorithm in Fig. 4.2.2 completes the description of the crack model. The result is the possibility to calculate contact forces per unit area, *N* and *T*, for any normal and tangential displacement, *a* and *b*, i.e.:

$$N = N(a),\ T = T(b,a). \tag{4.2.3}$$

This is the main difference of the proposed approach when compared to the simple flat crack model. The introduction of roughness on internal contacting surfaces and the account for partial slip allowed us to organize and perform calculations in an explicit manner. The advancement of this approach is related to the fact that accounting for roughness, or an equivalent axisymmetric contact shape, produces the Coulomb sliding condition for displacements, in the form $|\tilde{b}| = \theta\mu a$, instead of the traditional form $|T| = \mu N$, written for forces (or mean contact stresses).

Numerical example

In order to illustrate the work of the full crack model algorithm, we study the following numerical example. Suppose a contact system is fed by time-dependent displacement protocols *a* and *b*, depicted in Fig. 4.2.3 (a). Both protocols consist of three sine waves with different frequencies and amplitudes. Each curve contains about ten local extrema, and therefore the contact system experiences a lot of "switching" events when either the normal or the tangential loading is reverted. In view of practical applications, one should think of the exemplary protocols as short fragments of a real ultrasonic signal coming from the direct wave propagation, possible reverberations, mode conversions, etc. Time in Fig. 4.2.3 is represented in time steps of the algorithm. The actual time interval corresponding to these steps is not essential since our contact model is quasi-static.

An intermediate result of the protocol execution is the repartitioning of the tangential displacement *b* in the components b_0 and $\tilde{b}$ related to respectively the total sliding shift and the partial slip accompanied by deformation of asperities relative to this shift. Both components are shown in Fig. 4.2.3 (b). The final outcome of the algorithm, i.e. the calculated normal and tangential forces per unit area as functions of time are shown in Fig. 4.2.3 (c) in which, for the tangential force, the absolute value is plotted. A closer look at Fig. 4.2.3 allows us to easily identify the three contact states. The total sliding regime occurs when $|T| = \mu N$ (Fig. 4.2.3 (c)). In this case, the component b_0 evolves since the reference points at both faces shift (Fig. 4.2.3 (b)). The other component $\tilde{b}$ changes as long as *a* is not constant, since the

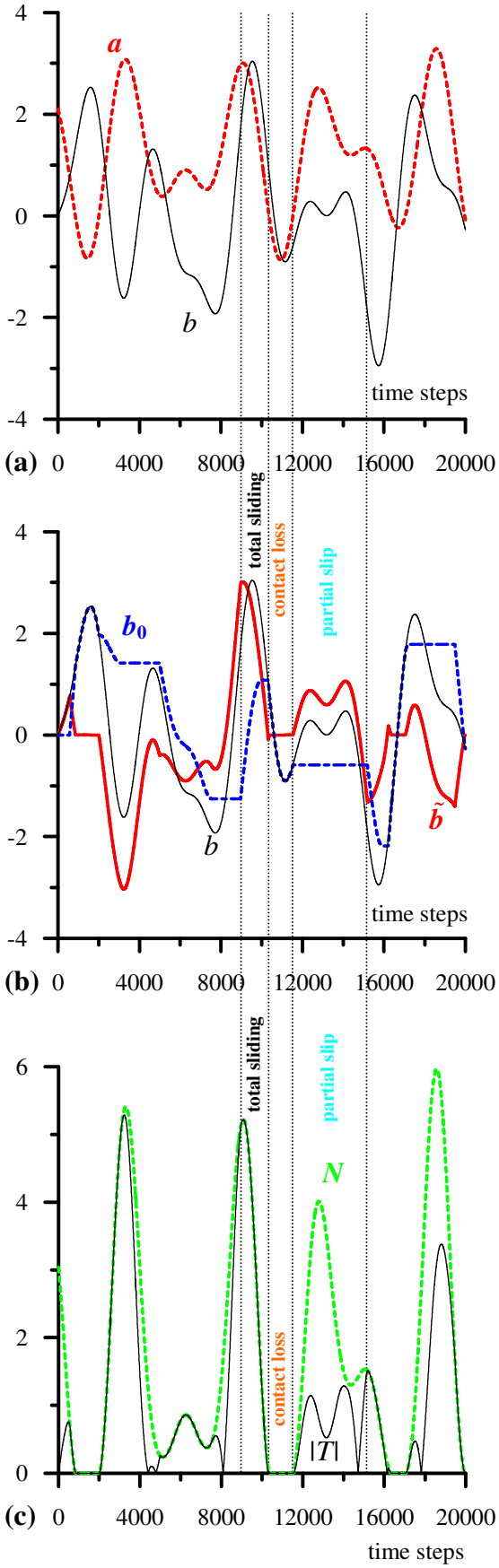

Fig. 4.2.3. (a) Excitation protocol in the considered example: normalized normal and tangential displacements, a and b, as a function of time. (b) Calculated components b_0 and $\tilde{b}$

in the considered numerical example. (c) The appropriate forces N and T calculated in our crack model.

maximum tangential deformation of asperities depends on the normal compression. In the case marked as "total sliding" in Fig. 4.2.3, the normal displacement a decreases, and therefore $\tilde{b}$ diminishes as well. The state of contact loss is also easy to identify. When a becomes negative (Fig. 4.2.3 (a)), $\tilde{b}$ is set to zero since no asperity deformation is possible (Fig. 4.2.3 (b)), and the normal force equals zero too (Fig. 4.2.3(c)). There are two different identification criteria for the partial slip regime: (1) b_0 does not change as the reference points do not shift, and (2) $|T|$ is less than μN. In Fig. 4.2.3, only one instance for each contact state is shown, however, using the above criteria, it is possible to identify the states at each time instance of the loading history.

The calculations have been performed assuming the normal contact reaction in the form

$$N(a) = C^2 a^2, \tag{4.2.4}$$

where $C = 6 \cdot 10^{10}$ $\mathrm{Pa}^{1/2}\mathrm{m}^{-1}$, corresponding to the value obtained by matching the experimental relation between the contact pressure and the gap distance, as exemplified by Biwa et al. [Biw-04] and used in the numerical study of contact between two solid blocks of aluminum by Yuan et al. [Yua-15] (see discussion the part "Normal contact interactions: theoretical approach" of section 2.8).

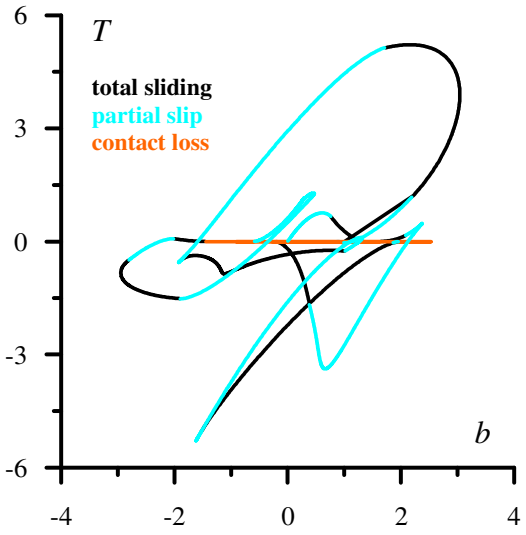

Fig. 4.2.4: The tangential load-displacement curve calculated for the displacement protocol from Fig. 4.2.3.

Finally, using the parametric representations $b(t)$ and $T(t)$, the desired dependency of the tangential force per unit area T on the displacement b is plotted in Fig. 4.2.4. The code allows one to rapidly generate such responses for any excitation protocol. Clearly, this would be extremely difficult without an automated accounting of the memory-dependent processes.

Note that in Figs. 4.2.3-4.2.4, the mean stresses and displacements are normalized on values N_0 and a_0, respectively. Here, N_0 is a typical stress magnitude of elastic waves propagating in the system. The link between normalization constants N_0 and a_0 is given by the quadratic dependency $N_0 = C^2 a_0^2$ corresponding to Eq. (4.2.4).

In the next section, we present some numerical examples of wave propagation in a 2D aluminum bar containing a crack.

4.3. Finite element simulations using the MMD-based contact model

Modeling of elastic wave propagation in cracked samples requires two different components, the first of which is needed to describe the microscopic normal and tangential behavior of the crack faces, whereas the second describes the wave propagation itself. In this study, the Structural Mechanics Module [COM-15a] of the finite element-based, software package COMSOL Multiphysics is used. On the one hand, this specific module has been particularly designed to solve elastic wave propagation problems, while, on the other hand, it contains specific tools accepting external user-supplied contact models. These contact models do not necessarily have to be implemented as closed form equations in the software itself, but can also be written as external functions in MATLAB which can be easily introduced in COMSOL using the LiveLink for MATLAB [COM-15b]. Using this approach, the contact model from the previous section can be directly linked to COMSOL. In our MMD-FEM code, the both components interact in the following way:

(a) Calculation of displacements in Structural Mechanics Module of COMSOL

At each particular time step of the procedure, relative normal and tangential displacements Δu_n and Δu_t are calculated at the discretization points on the crack interface and transferred to the displacement-driven crack model implemented in MATLAB.

(b) Calculation of contact stresses in MATLAB

From the relative normal and tangential displacement values, the contact model in MATLAB allows to directly and explicitly calculate normal and tangential contact stresses ($-N$ and T), which are then considered as an input in COMSOL to update the boundary conditions at the crack interface.

(c) Repeated calculations of displacements and contact stresses

Steps (a) and (b) are repeated for the next time step, until the desired calculation time is reached.

The above-mentioned approach allows the problem of wave propagation in a sample containing a crack with rough surfaces to be numerically solved in a simple and straightforward way. Since roughness is only considered at the microscopic level, crack faces at the mesoscopic level can be modeled as flat in the Structural Mechanics Module of COMSOL.

Numerical implementation of the constitutive crack model

Cracks are introduced as internal boundaries using the "thin elastic layer" feature [COM-15a] that allows one to implement user-defined boundary conditions. These conditions are defined on discretization points located at the same positions but related to different sides of a crack. In other words, the actual number of nodes is doubled. Relative movement of both sides occurs due to the action of forces denoted by F_n for the normal component and F_t for the tangential component (here forces per unit area are meant). The relative normal and tangential displacements between the crack faces are here denoted by Δu_n and Δu_t, respectively. The appropriate choice of boundary conditions makes it possible to separately model various contact phenomena, e.g. to avoid crack faces to freely penetrate into each other or to use the normal reaction curve of the kind of Eqs. (4.2.4), to "switch" on and off friction, etc.

Technically, in theoretical contact mechanics and in the Structural Mechanics Module of COMSOL different notations are used. To help the reader identify the correct forces and displacements which are necessary to introduce into COMSOL, we provide here the explicit link:

$$\Delta u_n = -2a,\ \Delta u_t = 2b, \tag{4.3.1}$$

$$F_n = -N(a) + F_0,\ F_t = T(b,a). \tag{4.3.2}$$

The terms $N(a) \equiv N$ and $T(b,a) \equiv T$ are solutions of Eq. (4.2.3) for the contact forces per unit area provided by the constitutive contact model. The mean normal and shear contact stresses at the mesoscopic level equal

$$-N = F_n - F_0,\ T = F_t$$

respectively. They are created by the contact interactions at the internal boundaries and can be calculated for any value of normal and tangential displacements Δu_n and Δu_t depending on the current contact state (contact loss, total sliding or partial slip). The term F_0 ($F_0 \geq 0$) is introduced to account for a possible pre-stress created as a result of another physical process

such as plasticity, fatigue, thermal changes, irregularities of molecular structure, etc. When differing from zero, the pre-stress induces both positive a and $N(a)$ in a situation where any external excitation, such as an acoustic wave, is absent.

Test sample geometry and physical parameters

In order to illustrate the potential of the proposed model, two instructive examples of a shear wave propagating in a 2D rectangular aluminum sample of 50 mm width and 100 mm height containing a crack are studied. The aluminum sample has a density ρ=2700 kg/m^3, Young's modulus E=70 GPa, and Poisson's ratio ν=0.33. A crack with a length of 20 mm is positioned in the center of the sample. In the first example, the crack orientation is horizontal, whereas in the second example the crack is inclined at 20 degrees, as illustrated in Fig. 4.3.1. In both examples, a continuous shear wave excitation with a frequency of 100 kHz and tangential displacement amplitude of 100 nm is defined on the top boundary of the sample. At the side and bottom boundaries of the sample, non-reflecting boundary conditions were applied in order not to mask the crack-wave interactions by parasite reflections. At the internal crack boundaries, a thin elastic layer boundary condition is specified. The friction coefficient value μ=1 was used, which is close to known data for aluminum on aluminum [eng-17].

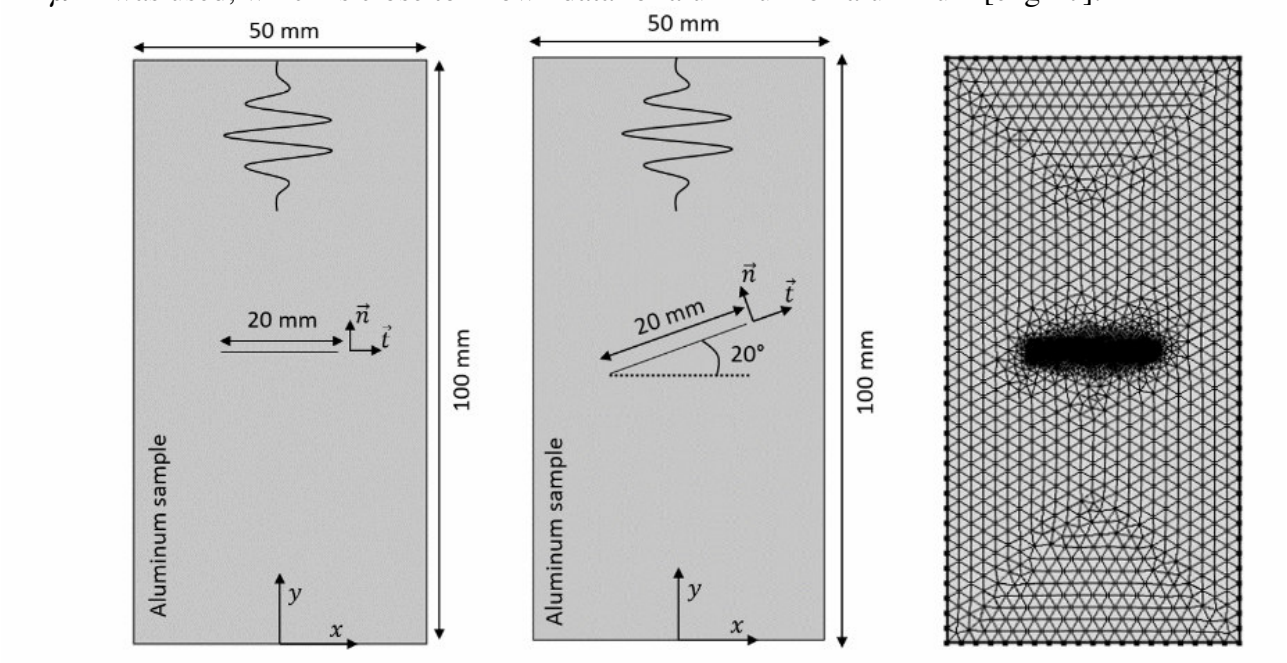

Fig. 4.3.1. Illustration of two geometries implemented in COMSOL together with the mesh generated for one of the geometries. The samples represent 2D rectangles of aluminum with cracks (horizontal and inclined at 20 degrees) of finite length positioned in the center of the rectangle. Both geometries are meshed with triangular mesh elements, with a higher mesh density in the region of the crack.

As illustrated in Fig. 4.3.1, the full geometry is meshed using triangular elements with a maximum size of approximately 2.6 mm (i.e. 12 second-order mesh elements per wavelength). At the internal crack boundary, however, a fixed number of 150 mesh elements (i.e. element size of approximately 0.13 mm) were used. By choosing such small elements, the macroscopic elastic fields used in the MMD algorithm can be considered uniform enough within each mesh cell. The solution to the problem is calculated using the implicit generalized alpha time-dependent solver typically used for structural mechanics problems in COMSOL. Accurate solutions are obtained using a time step Δt=25 ns, corresponding to 400 time steps per wave cycle.

Nonlinear hysteretic tangential behavior of horizontal crack

In the first example, the interaction of the excited shear wave, propagating in the vertical direction, with a horizontal crack is considered, with a particular focus on the influence of pre-stress on wave propagation. At a weak pre-stress value, a sufficiently high wave amplitude may engender total sliding, while strong compression can only induce partial slip. To avoid the influence of the clapping effect (repeated opening and closing of crack faces) and concentrate on tangential interactions only, the weak pre-stress should be still large enough to keep the crack faces always in contact.

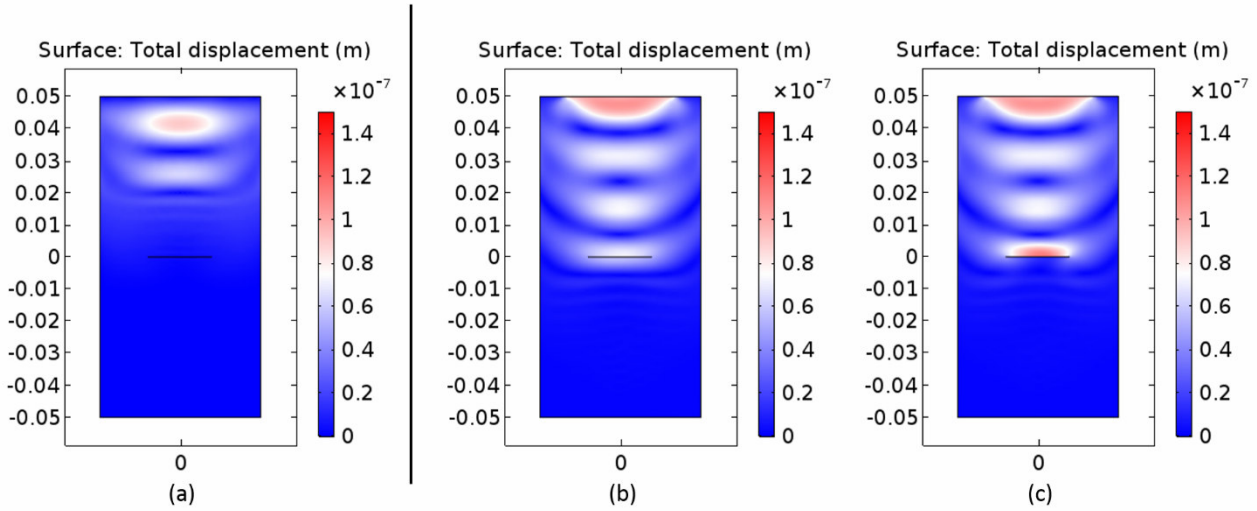

Fig. 4.3.2. Snapshots of the calculated total displacement in the cracked aluminum sample. (a) t=10 μs: shear wave has not reached the crack yet. (b) t=18 μs and F_0=0.36 MPa: shear wave propagation is practically not influenced by the crack. (c) t=18 μs and F_0=0.09 MPa: shear wave propagation is highly influenced by the crack.

In this study, we consider two pre-loading magnitudes, F_0=0.36 MPa and F_0=0.09 MPa, satisfying those criterion for the chosen shear wave excitation with tangential

displacement amplitude of 100 nm. Figure 4.3.2 shows snapshots of the calculated total displacement in the cracked aluminum sample illustrating the interaction of the ultrasonic shear wave with the crack. In set (a), a snapshot at t=10 μs is shown. In this case, the wave has not yet reached the crack. In figures (b) and (c), snapshot at t=18 μs are presented for both pre-loading magnitudes. The 2D color plots illustrate the situation in general; fine nonlinear effects are not visible in this representation. However, the difference between the two cases is clearly seen. Partial slip practically does not modify the linear propagation (Fig. 4.3.2(b)), whereas total sliding domination results in strong refection (Fig. 4.3.2(c)).

Two other pictures, Figs. 4.3.3 and 4.3.4, justify our choice of the pre-stress magnitudes. The figures display contact displacements $\Delta u_n = -2a$ and $\Delta u_t = 2b$ as well as the mean contact stresses $-N$ and T at the center of the crack, for F_0=0.36 MPa and F_0=0.09 MPa, respectively. In both situations, application of the normal pre-loading closes the crack, resulting in the appearance of a negative normal displacement Δu_n due to the fact that asperities in contact can recede under load. The normal displacement Δu_n increases with increasing pre-load F_0. Figure 4.3.3 illustrates the case with the largest pre-loading which forces the crack to stay in the state of partial slip. Indeed, the condition $|T| < \mu N$ is satisfied everywhere (except at one short instant in time). It can be verified (not shown here) that this will also be the case for other positions on the crack. In the case of weaker pre-loading (Fig. 4.3.4), $|T|$ often equals μN, i.e. the contact state frequently switches between partial slip and total sliding. In this case as well, it can be verified (not shown here) that at other positions on the crack the stresses behave in the same way.

The hysteretic tangential load-displacement curves corresponding to the shear wave excitation are shown in Fig. 4.3.5 for both selected pre-stress values. The partial slip and total sliding regime are indicated with different colors. Again, the total sliding regime frequently appears for the weaker pre-stress (bottom figure) whereas stronger pre-compression (top figure) disables this regime. Correspondingly, contact acoustic nonlinearity is much stronger in the weak pre-compression case. However, it is clearly discernible for the higher pre-stress as well, as hysteresis in the upper set of Fig. 4.3.5 is still strongly pronounced. The same effect can be seen in Fig. 4.3.3, in which the shape of the stress and displacement signals are visibly different. This confirms the fact that contact acoustic nonlinearity remains relatively strong, even in situations of high pre-loading due to the partial slip effects and highly nonlinear normal reaction.

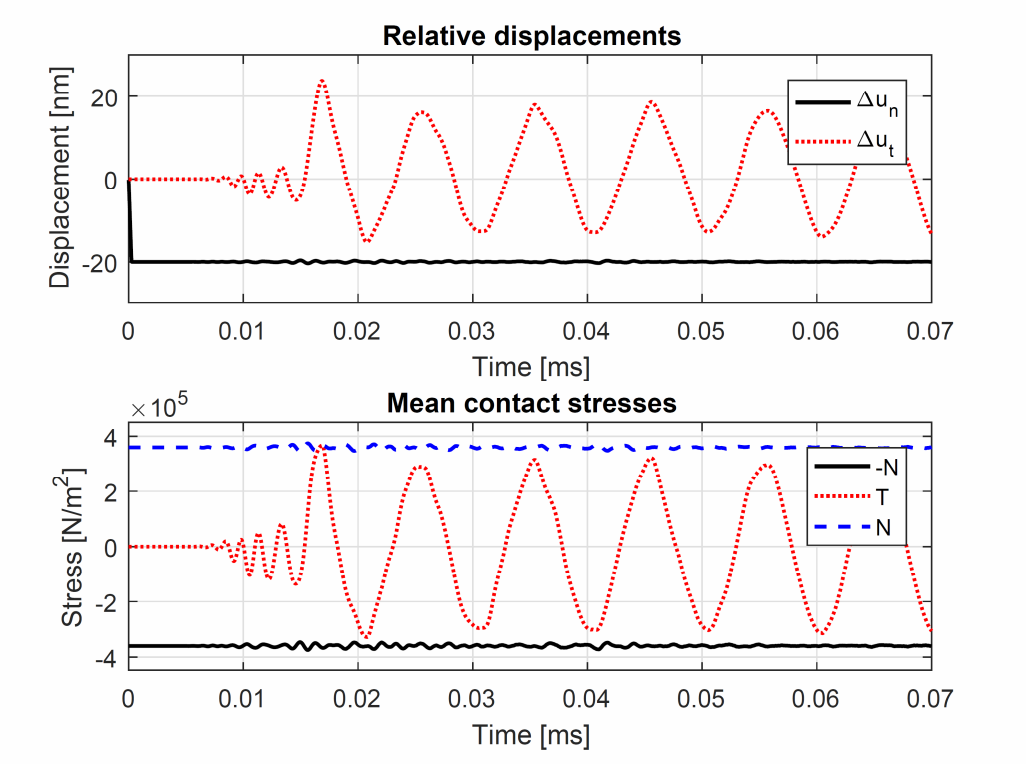

Fig. 4.3.3. Calculated normal and tangential relative displacements Δu_n and Δu_t (upper set), and mean contact stresses *-N* and *T* (lower set) at the central point on the crack interface in case of a shear wave excitation at 100 kHz with amplitude of 100 nm, and a pre-loading F_0=0.36 MPa. The curves for both *-N* and *N* are included to show that shear stress *T* always lies in between them (μ=1 in our examples).

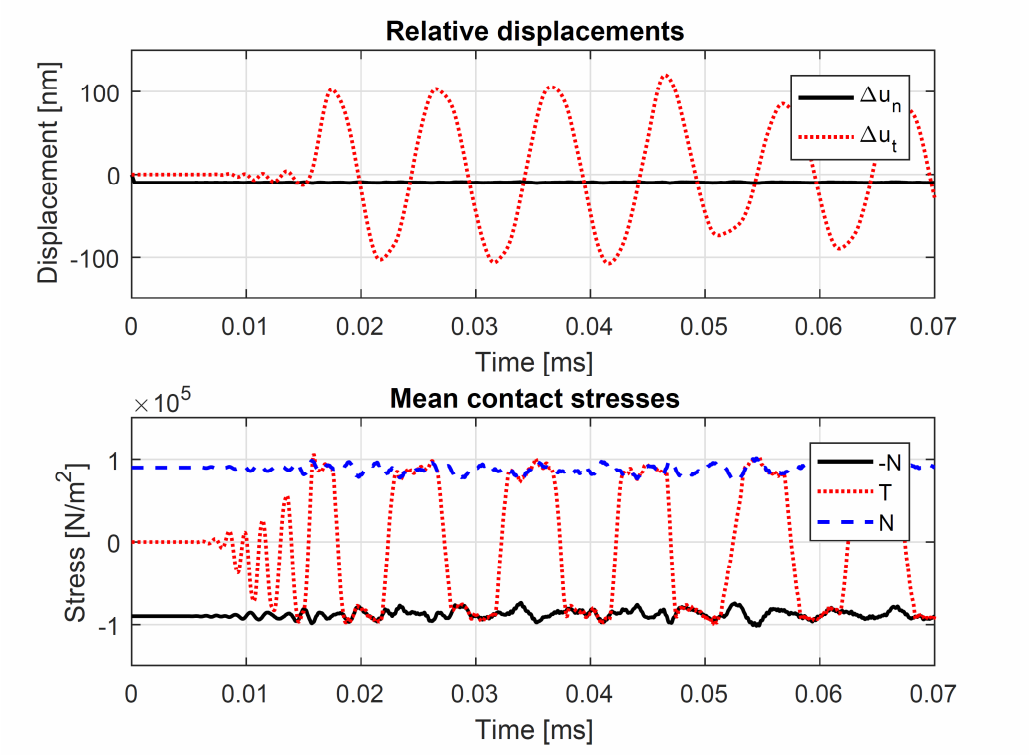

Fig. 4.3.4. Calculated normal and tangential relative displacements Δu_n and Δu_t (upper set), and mean contact stresses *-N* and *T* (lower set) at the central point on the crack interface in

case of a shear wave excitation at 100 kHz with amplitude of 100 nm, and a pre-loading F_0=0.09 MPa. The curves for both -N and N are included to show that shear stress T always lies in between them (μ=1 in our examples).

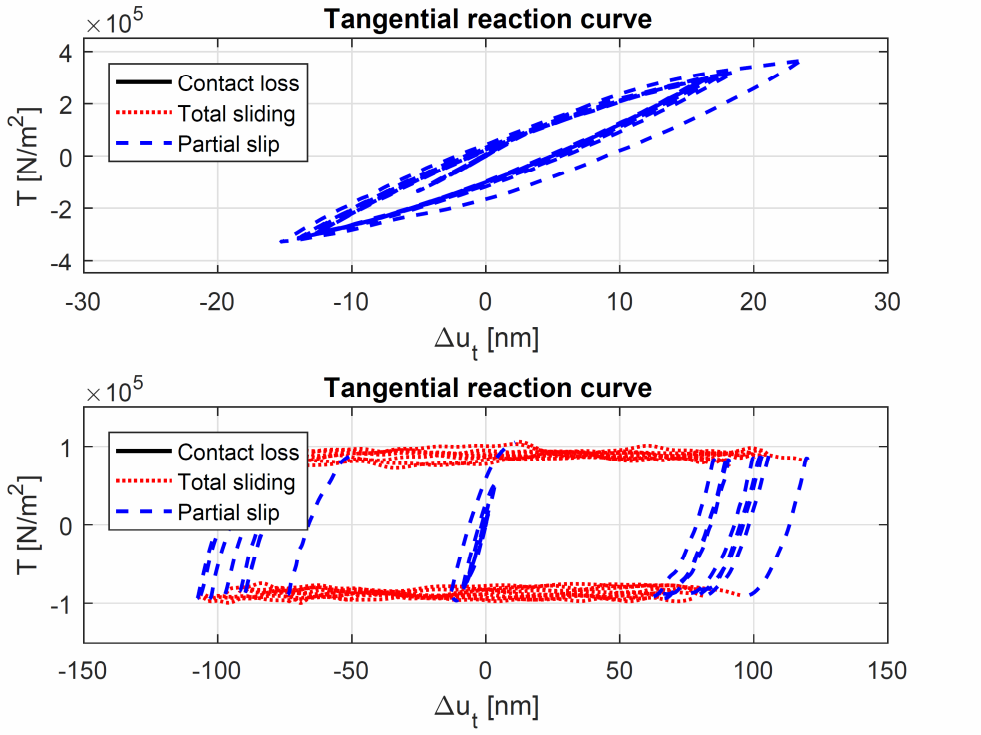

Fig. 4.3.5. Tangential reaction curves at the central point on the crack interface in case of a shear wave excitation at 100 kHz with a tangential displacement amplitude of 100 nm. (a) Hysteretic curve in case of partial slip (pre-load F_0=0.36 MPa), (b) Hysteretic curve in case of partial slip and total sliding (pre-load F_0=0.09 MPa).

Nonlinear normal and tangential behavior of inclined crack

The second example illustrates the interaction of the excited shear wave with an inclined crack. No pre-loading has been introduced in this example. Due to crack's inclination, both clapping (i.e. opening and closing) and friction at the crack interface are efficiently excited.

In Fig. 4.3.6, relative normal and tangential displacements and mean contact stresses are plotted as functions of time. The normal displacement time curve is highly asymmetric as negative excursions of Δu_n meet much higher counter-action. Indeed, negative normal displacements engender both straining of surrounding material layers and the resistance of the deformed asperities. In contrast, positive excursions (contact loss regime) only strain the surrounding material; the reaction of asperities is not activated. Moments of contact and contact loss in the upper figure can be identified in the contact stress curves at the bottom. When contact is lost both normal and tangential contact stresses equal zero. The absolute

value of the negative (in compression) normal stress is plotted in order to show that the Coulomb friction law is fulfilled; the tangential stress can only reach the Coulomb threshold but never exceeds it.

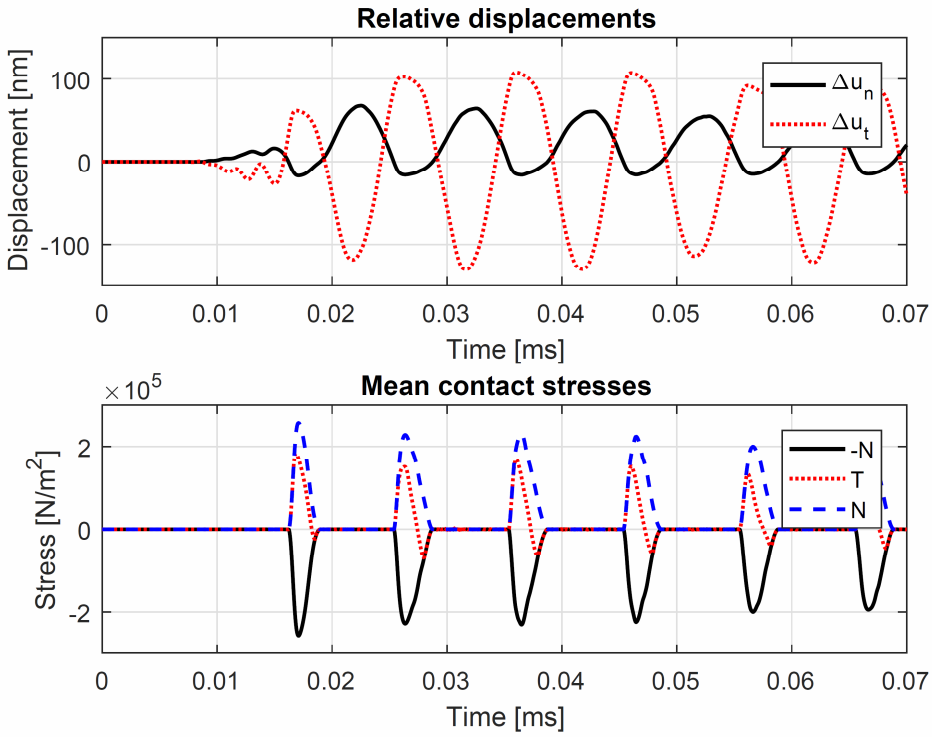

Fig. 4.3.6. Calculated relative displacements Δu_n and Δu_t (upper set) and mean contact stresses $-N$ and T (lower set) at the central point on the crack interface in case of a shear wave excitation at 100 kHz with amplitude of 100 nm, and no pre-loading. The curves for both $-N$ and N are included to show that shear stress T always lies in between them (μ=1 in our examples).

Fig. 4.3.7 shows the normal and tangential reaction curves calculated at the central point on the inclined crack. According to our assumptions, the mean normal stress $-N$ differs from zero only in case of contact (i.e. $a>0$ or $\Delta u_n<0$) and is fully reversible. This can be observed in the Fig. 4.3.7 (upper set). On the other hand, the tangential reaction curve (lower set) is hysteretic. Depending on loading conditions, all three contact regimes appear which is shown in the lower set with different colors.

Mechanical contact interactions are highly nonlinear due to the nonlinear normal reaction curve, as well as due to hysteretic friction effects. Therefore, the crack behaves as a source of secondary nonlinear waves. Fig. 4.3.8 provides an overview of both linear and nonlinear wave dynamics. In particular, the top figures show the time evolution of the normal and shear contact stresses ($-N$ and T) at all positions along the crack interface in the sample excited by the shear wave at 100 kHz with an amplitude of 100 nm. The figures clearly

demonstrate the dynamic switching that occurs between the non-contact (N=T=0) and contact states (N>0, $T \neq 0$), with different behavior for different positions on the crack.

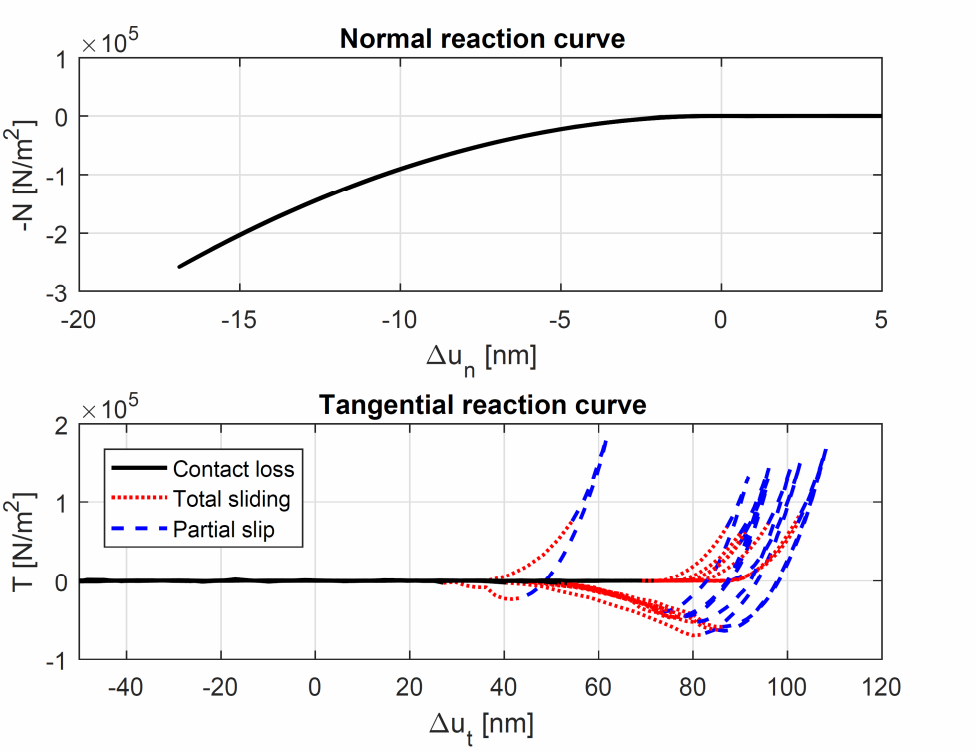

Fig. 4.3.7. Normal (upper set) and tangential (lower set) reaction curves at the central point on the crack interface in case of a shear wave excitation at 100 kHz with a tangential displacement amplitude of 100 nm.

The set of figures in the second row shows snapshots of the displacement component u_x in the aluminum sample at four instances in time, thus illustrating the propagation of the incident wave. The considered time instances are also indicated by the vertical white lines in the top figures. The third row and bottom set of figures illustrate the nonlinear wave propagation. To evaluate the nonlinear wave components, the Scaling Subtraction Method (SSM) [Sca-08] has been used. This method exploits the distorted scaling of the received signals with increasing excitation amplitude due to nonlinearity. To use the SSM, a sample has to be excited twice, once at a low excitation amplitude A_{low}, and once at a high excitation amplitude $A_{high} = n\, A_{low}$, where n denotes the scaling factor. By subtracting the properly scaled relative displacement signals obtained using the low and high excitation amplitudes, all linear contributions in the signals are eliminated and the nonlinearities are enhanced. Here, two simulations were performed, one at a low excitation amplitude A_{low} = 10 nm, and another one at a high excitation amplitude A_{high} = 100 nm. Hence, snapshots of respectively the scale subtracted normal and tangential displacement signals, u_n and u_t, at four instances in time (same as the ones used before) are shown. The color scale in each set of snapshot figures runs

from blue (most negative displacement value over time) over green (zero displacement) to yellow (most positive displacement value over time).

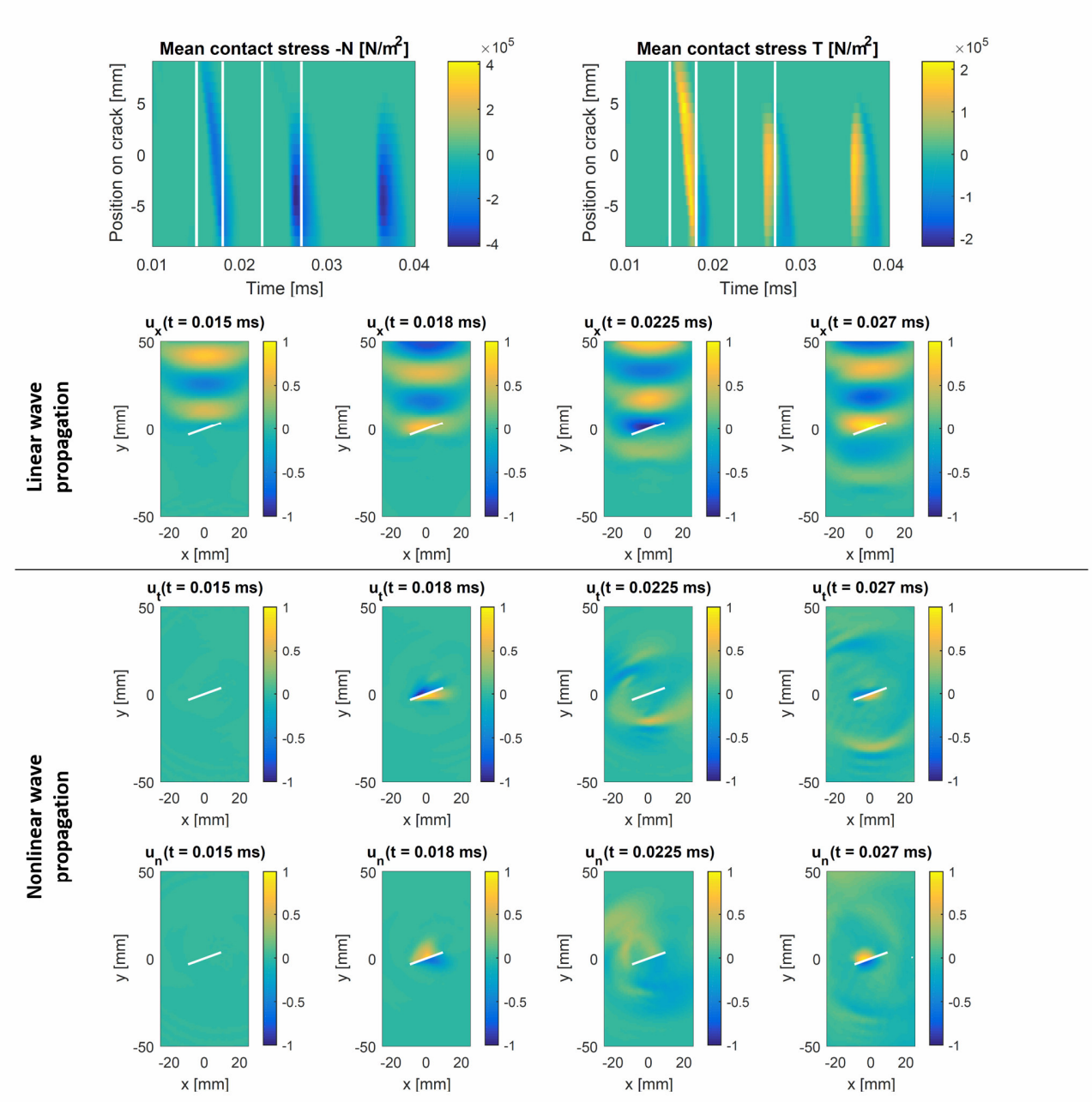

Fig. 4.3.8. First row: color coded plots illustrating the time evolution of the normal (-*N*) and shear (*T*) contact stresses at the crack interface in case of a shear wave excitation at 100 kHz with a tangential displacement amplitude of 100 nm; contact is lost when both contact stresses equal zero. Second row: snapshots of the displacement component u_x in the aluminum sample at four different moments of time. Third and fourth row: snapshots of respectively the scale subtracted normal and tangential displacements u_n and u_t at four different moments of time. The four time instances are marked by white vertical lines in the top figures.

At the first time instant (t=15 μs), there is no sign of nonlinearities at all. This is due to the fact that it takes the excited shear wave approximately 16 μs to travel from the top boundary to the crack (shear wave velocity v_S=3122 m/s). Once the first part of the shear wave has reached the crack, the dynamic wave-crack interaction starts, resulting in the generation of both normal and tangential nonlinearities at the crack interface, as illustrated by the snapshots at t=18 μs, for u_n and for u_t, respectively. The contact stress evolution (top figures) shows that around $t \approx 20$ μs the entire crack is again in an open state. In this case, the crack faces temporarily do not interact contact nonlinearities are not activated, which can for instance be seen in the snapshots at time t=22.5 μs. Yet, at that particular time, the previously generated nonlinear wave components have propagated some distance in the sample, while generation of new nonlinear components is not detected. As the energy of a localized source is redistributed circularly for 2D cases, the amplitude quickly diminishes. At $t \approx 25$ μs, the contact between crack faces is reestablished, inducing again the nonlinear ultrasound generation at the crack faces, clearly observed at the snapshot at time t=27 μs. The performed time evolution study of the nonlinear content in the wave propagation confirms that a crack starts to behave as a nonlinear source when triggered by a wave-crack interaction. The signals excited by this nonlinear source and detected at the surface of the object can in turn be used for defect detection, localization and/or characterization, provided the recorded amplitudes are measurable.

4.4. Conclusions

In this chapter, we developed a theoretical and numerical approach to model elastic wave propagation in solid structures containing cracks at known positions. The key component of the created numerical MMD-FEM toolbox is a contact model accounting for friction and roughness of crack faces. The model allows one to calculate the load-displacement relationships in three different contact states: contact loss, total sliding and partial slip. The first one occurs when there is no contact between every two corresponding points from opposite crack faces. Total sliding occurs when both crack faces are sliding against each other. The last case corresponds to the situation when both stick and slip areas are present in the contact zone and appears due to surface roughness. The load-displacement relationship in the partial slip regime is obtained with the help of the method of memory diagrams that allows one to automate the account for friction-induced hysteresis by introducing an internal functional dependency responsible for all memory effects in the contact system.

The load-displacement relationship represents a boundary condition that has to be defined at internal boundaries, such as cracks. To do this, the constitutive model has been combined with an elastic wave propagation model of final element type. We have used the Structural Mechanics Module of the commercially available finite element based software package COMSOL Multiphysics. Using the LiveLink for MATLAB feature, the crack model, implemented in MATLAB, was incorporated into COMSOL in a simple and straightforward way.

The working principle of the numerical MMD-FEM toolbox is illustrated by means of two instructive examples of shear wave propagation in a 2D rectangular aluminum sample containing a crack with rough surfaces, oriented either horizontally or inclined at 20 degrees. Calculations of all elastic fields in the sample allow one to check the fulfillment of the postulated friction laws, to identify the three contact regimes, to separate the linear and nonlinear components of the waves, to detect several nonlinear signatures including those that can be experimentally measured, etc.

The created MMD-FEM toolbox drastically increases visibility of all wave or vibration processes used in experimental nondestructive testing methods for defect detection and imaging. One of its final objectives is to estimate physical and geometric parameters of defects which is only possible once a relevant nonlinear wave propagation model is implemented.

Positioning the research in the laboratory context

A part of the activity of the Joint International Laboratory LICS/LEMAC of the Institute of Electronics, Microelectronics and Nanotechnologies, IEMN UMR CNRS 8520, is concerned with nonlinear ultrasound NDT and imaging, with the scope of potential applications ranging from microelectronics to aeronautic components. In our group, experimental NDT techniques are being developed in parallel to theoretical studies of contact phenomena. The methodology consists in comparison of measurements carried in a completely controlled environment, with the results produced by a detailed numerical model describing wave propagation in samples with damage. Using the IEMN facilities, a number of samples with artificial defects of fully known structure were produced. The nonlinear signatures measured on these samples are to be compared to results of simulations based on a detailed friction model. Then, if in a completely controlled situation, the agreement between a theory and an experiment is found, the theory and the related numerical tool may be used in conditions when the defects are not pre-fabricated but natural and thus unknown.

There is a number of numerical techniques capable of simulating elastic waves in complex structures. Besides COMSOL software that we have already used **[Del-18]** for modeling of elastic wave propagation in samples with cracks, other numerical implementations are possible. For instance, the discontinuous Galerkin finite element method is proven to be one of the most efficient versions of FEM-based codes and therefore is considered as a working tool in the LEMAC/LICS group **[Bou-13]**.

These studies have been carried out in the framework of two research projects: a national one, ANL-MEMS 2010-2013 "Nonlinear elastic imaging techniques for MEMS reliability assessment" funded by the *Agence Nationale de la Recherche*, and a European FP7 project, ALAMSA "A life-cycle autonomous modular system for aircraft material state evaluation and restoring system".

ANL-MEMS project

Upon arrival at the IEMN in October 2009 and joining the LEMAC/LISC group directed by P. Pernod and V. Preobrazhensky, I started working on preparation and then realization of the ANR project "Nonlinear elastic imaging techniques for MEMS reliability assessment" (ANL-MEMS 2010 BLAN 923 01, commenced in 2010, extended in 2013). The project combines efforts of two research groups; our partner is the LAUM (N. Chigarev, V. Goussev, V. Tournat, J. Blondeau, S. Mezil, and S. Durand). The participants from the IEMN part are O.

Bou Matar, V. Aleshin (me), P. Pernod, V. Preobrazhensky, A. Talbi, and N. Tiercelin. A table below shows the distribution of tasks between the two partners.

	Elaboration of MEMS with calibrated defects	Theoretical investigation of nonlinear acoustic waves interactions with cracks	Numerical simulations of nonlinear acoustic waves propagation and interactions with cracks	Development of the opto-acousto-optic technique	Development of magneto-acoustic wave phase conjugation technique
IEMN	x	x	x		x
LAUM		x		x	

research discussed in chapters 3 and 4 here concerns these two tasks

Table: Tasks of the partners of the ANL-MEMS project

Two experimental methods for defects visualization have been elaborated. The first one is the magneto-acoustic wave phase conjugation technique (IEMN) based on the ultrasound wave front reversal with the aid of the electromagnetic pumping in active magnetic materials. The second one, the opto-acousto-optic technique (LAUM), uses lasers both for generation of sound waves and for detection of the nonlinear acoustic response of cracks, thus representing a fully non contact procedure.

My responsibility was to provide both groups with a detailed theory of mechanical contact interaction for the purpose of development of a numerical tool capable of simulating nonlinear waves in materials with damage.

The ultimate goal of the project was the development two precision techniques for visualization of defects in microstructures and assessment of their size, location and, finally, their potential harmful impact.

ALAMSA European project

In 2012-2016, LICS/LEMAC group participated in a European project abbreviated ALAMSA, "A life-cycle autonomous modular system for aircraft material state evaluation and restoring system". The project consolidated the efforts of ten research and industrial partners: University of Bath, Delft University of Technology, Israel Aerospace Industries, University of

Stuttgart, KU Leuven, DAKEL, and others. Its main objective was developing materials with self-repair and self-monitoring capabilities for aeronautical applications. These materials represent composites that include fibers confining a special kind of epoxy. Breaking fibers releases the epoxy that results in a chemical reaction that finally solidifies the matrix.

The project included an extensive NDT work package that consisted in developing nonlinear imaging techniques for assessment of the healing process efficiency in materials having the self-restoring ability or for optimization of fabrication parameters of existing composites.

The experimental technique elaborated in the IEMN (postdoc N. Smagin, PhD student A. Trifonov, Prof. O. Bou Matar) combines the time reversal principle (focusing of an acoustical signal on its source after wavefront conjugation) with contact elastic nonlinearity used as a damage indicator. A number of schemes based on these ideas have been tested in our group and by other partners; our closest partner is the Wave Propagation and Signal Processing Research Group at KU Leuven Campus Kortrijk.

Theory is numerical modeling discussed in chapters 3 and 4 are related to the content of workpackage 3, “NDT modeling support”. The key component of the workpackage 3 deliverables was the MMD-FEM numerical toolbox that we have created for modeling of nonlinear crack-wave interactions and visualization of acoustic fields in samples of 2D geometry.

Generally, at the level of laboratory, the existing activities and future projects (see below) maps into the research pattern from the point of NDT (collaboration with O. Bou Matar, M. Goueygou), explosive instabilities studies (V. Preobrajenski, Ph. Pernod), phononic crystals (O. Bou Matar), theoretical mechanics (S. Giordano), numerical simulations for wave and vibration problems (O. Bou Matar), microsystems (N. Tiercelin, A. Talbi).

Research project

The MMD-FEM numerical toolbox has strong or even unique advantages for numerical representation of structures, materials or components containing frictional contacts. The objects under study include a variety of cases such as bolted joints, cracks in pieces of machinery, structural elements of composite materials, environmental or operation-induced damage in constructions, etc. The potential of the developed approach is related to the high computational performance achieved due to the implementation of the MMD-based multiscale principle. The automation of the account for frictional interactions makes it possible to model ultrasound excitations, random signals, to obtain and to interpret a whole spectrum of nonlinear signatures.

My research project has two principal components that concern the improvement and the use of proposed theoretical and numerical concept and the related code.

Development of the MMD-FEM numerical toolbox

The existing version of the numerical tool **[Ale-18]**, **[Del-18]** consists of a solid mechanics unit and an external MMD-based contact model implemented in 2D under some number of limitations. Advances are possible in the following directions:

- include more interaction laws and movement types;
- extend modeling to 3D;
- account for heat production and diffusion;
- experimental verification.

The Coulomb friction law is a traditional but not always precise approximation for the frictional interaction. Its principal disadvantage is in neglecting dynamic effects that can be significant (e.g. the difference between static and dynamic friction coefficients can reach 20%). In addition, other effects such as adhesion become especially important in many situations including nanoscale simulations, adhesive materials, self-healing materials, etc. This feature explains the necessity of account for more advanced interaction laws. At the same time, movement types in realistic structures include not only shift but also rolling and torsion. An excellent opportunity for extending the range of interaction and movement types are offered by the MDR-based applications [Pop-15].

Another important step towards better universality is related to 3D extensions. The MMD accepts a direct 3D generalization **[Ale-16]**, but for the price of an additional approximation. Further study in this direction is necessary.

A potential important advance is related to the account for the friction-induced heat production and subsequent heat diffusion. Modeling for this effect has important applications such as thermography. Moreover, heat generation can induce feedback action because of material dilatation; even small temperature-induced stresses can be considerably amplified in contact systems due to the stress concentration phenomena.

Finally, a most important stage in the development of the numerical tool is its experimental verification. This is probably the most complicated task to be completed. At the moment, the results produced by the existing simulation system have not been compared to measurements. The only argument for the validity of the method is the fact that it follows from fundamental principles of contact mechanics. This is certainly not enough, and an extensive verification program is necessary. A particular difficulty appears while attempting to represent contact behavior in real materials containing cracks with an unknown pre-stress distribution. Indeed, due to unknown residual stresses existing in every material subject to loading, the resulting stress distribution after cracking is also unknown. An important step of the validation procedure is the work with engineered samples of composites with delaminations at known locations created by insertion of non-adhesive films during the fabrication process. The fabrication technique has been elaborated in the framework of the ANL-MEMS and ALAMSA European projects.

Use of the MMD-FEM numerical toolbox

The use of the created numerical tool is planned in the area of nondestructive testing and imaging, and in other engineering applications such as optimization of materials' properties, studies of wear and fatigue, applications related to friction-induced instabilities. A long-term part of the project concerns the creation of novel materials whose properties are based on behavior of engineered internal contacts. Examples can include nonlinear acoustic metamaterials and structures exhibiting an explosive instability, both using contact nonlinearity.

Nondestructive testing

The result of the experimental verification stage can be directly used as a numerical support for the nonlinear NDT. The established theory-experiment agreement or at least correlation provides an opportunity to solve the following problems:

- estimate geometric parameters of damage;

- reveal the absence or presence of damage by comparing the synthetic response of a damaged sample with actual measurements;
- accept or reject various hypotheses on the location and strength of damage;
- drastically increase the visibility of physical processes used in the NDT techniques.

The application of the numerical toolbox in the NDT can hopefully extend the existing or future technological limits. Potential applications domains in NDT can include at least three areas listed below.

Aeronautic components

In the framework of the European ALAMSA project (2012-2016), research efforts of ten partners ware focused on developing new self-healing materials for aeronautical industry and NDT methods capable of timely detecting damage in aeronautical components. We plan to continue these efforts and use the established collaboration network for further progress. The accent will be made on refining the developed techniques having one or more of the following features:

- samples of complex (realistic) geometry;
- damage hidden behind structure elements;
- remote detection;
- high sensitivity techniques, detection of early damage stages;
- rapid imaging methods.

The important advantage of having these methods on the credit side is the access to data and samples, including samples with fabricated defects of known geometry which is crucial for experimental validation of the numerical model. The disadvantage is that the former ALAMSA project personnel is now involved in other projects.

Thermosonics

Thermosonics (or ultrasonic thermography) is one of rather new techniques that can be used for the detection of incipient cracks and delaminations. Thermosonics combines the ultrasonic excitation of a sample with a thermal measurement of the sample surface using a high sensitivity (i.e., down to 20mK) and a high resolution infrared camera covering a large field of viewing area. The presence of internal inhomogeneities can be detected by measuring local temperature variations. In the case of cracks and delaminations, ultrasound-induced mechanical vibrations will generate friction effects at the interfaces of the defect, which generate local heating. The released frictional heat will propagate from the defect to the surface of the sample in a few milliseconds, and as a result, the local surface temperature will rise very soon after the ultrasound has activated the defect. In recent years, the use of

thermosonics to assess incipient damage has gained more interest, mainly because it is one of the only techniques that is capable to fulfill the high demands on quality control for a wide field of materials and applications. The method is safe, non-intrusive, allows inspection of large surfaces and performs these inspections in a relatively fast manner.

In order to extend the MMD-FEM code to the case of heat generation and propagation, two steps have to be completed: its is necessary to theoretically calculate frictional-induced energy losses in the MMD model for an arbitrary loading history, and to add to the description the heat equation via, in the case of COMSOL implementation, the Heat Transfer module. This work is being done in collaboration with the Wave Propagation and Signal Processing Research Group at KU Leuven Campus Kortrijk (Prof. K. Van den Abeele, Dr S. Delrue, and K. Truyaert (PhD student in 2016-2019).

Passive structural health monitoring

This research direction is planned to develop in the framework of project funded by the *Agence Nationale de la Recherche* (ANR) and abbreviated PANSCAN, Passive Ambient Noise-based Structural monitoring through exploitation of Contact Acoustic Nonlinearity. The project concerns structural health monitoring and is to be realized by three French partners, the IEMN (combined efforts of the groups of the Valenciennes University and our LICS/LEMAC laboratory), *Institut Langevin "Ondes et Images"* (UMR CNRS 7587), and the LaMCoS laboratory (UMR CNRS 5259).

The project exploits the principle of coda wave interferometry, a technique that compares two coda waves measured in slightly different situations. The slight difference in wave propagation conditions can be due to temperature variations, stress-induced perturbations, or the influence of a low-frequency wave which is then filtered out from coda. The coda waves, because of multiple reflections and scattering, accumulate the weak changes induced by the physical process under study and finally make them measurable. The version with the low-frequency pumping has even higher sensitivity to damage presence since the high-frequency coda can be modified by the low-frequency pump wave only due to the nonlinear process engendered by contact nonlinearity.

The originality of the proposed approach is in the use of passive low-frequency sources; we hope that the technique can be made sensitive enough to detect damage excited even by ambient noise used as pumping or at least to use operation-induced structure vibrations as a "passive" source.

The theoretical part of the project is entirety based on the application of the MMD-FEM code. The coda wave experiment is an excellent practical test for the theoretical and modeling concept we develop; the question is whether the MMD-FEM simulation is capable

of imitating coda wave behavior and of successful describing accumulating weak changes in extremely long signals with a huge number of oscillations.

Engineering applications

Besides NDT, the semi-analytical solutions for frictional contact interaction and their FEM implementations can be of use in other engineering applications, related to properties optimization, fatigue and wear, as well as potential explanations of friction-induced instabilities.

Properties optimization for existing materials with microstructure

In the framework of the ALAMSA project, the nonlinear acoustic imaging techniques have been applied for estimation of the final efficiency of the self-healing process of the fabricated composites. At the same time, properties of the existing composite materials, such as carbon- and glass fiber reinforced plastics can also be enhanced. Even for the traditional composites, the manufacturing process has a large number of technological parameters, such as temperatures and pressures at various stages, contents of various components, etc. Their influence on final material's performance is usually estimated by simple destructive tests e.g. measurements of the ultimate tensile strength, or of resistance to repeated bending. The high precision NDT techniques present a much better opportunity for estimating materials performance, since they are capable of seeing hidden defects at early stages of their development. Accompanied by an adequate modeling tool, they become more transparent to the user and allow visualizing all acoustical fields everywhere in the sample.

These features make us hope that modeling-assisted nonlinear NDT can help optimize the fabrication parameters of existing materials in a much finer way than traditional destructive tests. The MMD-FEM is potentially capable of estimating defects sizes and therefore brings additional information about materials performance.

Studies of wear and fatigue

Typically, machinery components have sensible spots such as joints (e.g. bolted joints) where damage is mostly accumulated. Damage is manifested not necessarily as cracking also as fatigue or wear. Therefore, for a number of engineering applications, it is of interest to model fatigue and wear processes in vicinity of frictional contacts. The MMD-FEM software can calculate stress fields and frictional energy losses in frictional contact systems remotely excited by elastic waves or vibrations of any shape including random signals. Supplemented

by an adequate fatigue/wear model, the MMD-FEM code can become a working tool for modeling fatigue and wear in machinery.

Friction-induced instabilities

It is well-known that under some conditions frictional interactions can produce instabilities accompanied by an important energy conversion into vibrations and acoustical emission. Those effects can have strong negative consequences on serviceability and lifetime of machinery, transport vehicles, etc. Theoretically, instabilities can appear during the interaction of nonlinear oscillators. The interacting nonlinear oscillators can also be frictional contact systems or several parts of one contact experiencing different loading regimes. The contact systems obviously interact once they are mechanically connected or just represent various parts of the same piece. Again, the MMD-FEM code can be a suitable tool for modeling interactions of this kind between oscillators with contact frictional nonlinearity.

Besides practical applications in contact systems exhibiting harmful instabilities, the application of the MMD-based approach is a theoretical novelty in this area, since frictional nonlinearity has never been considered in the theory of nonlinear coupled oscillators.

Creation of novel materials

The MMD-FEM software represents a sort of numerical toolbox that can also be used for designing new materials. Below we consider two examples.

Nonlinear acoustic metamaterials

Metamaterials now attract considerable attention of researchers due to their exceptional properties useful for particular applications, such as sound isolation in a selected frequency band and for selected wavefronts orientations, a possibility for directed and controlled wave propagation, stress mitigation, etc.

Existing metamaterials can be categorized into three classes: (1) linear [Hla-16], [Zig-14], [Nor-15], (2) containing nonlinear materials in perfect contact [Dey-13], [Gue-15], (3) based on nonlinear contact interactions [Leo-13], [Leo-14a], [Leo-14b], [Li-12]. My expectations focus on the third class of metamaterials. Contact interactions are especially attractive once nonlinear metamaterials are concerned, since contact nonlinearity is typically much stronger than other nonlinearity types (geometric and material) and can be made controllable or tunable.

Metamaterials design requires a purposeful optimization of geometry and properties of all constituents. This means that a critical part of metamaterials research is numerical

modeling for acoustical waves propagating in artificial structures comprising many contacts between the elements. Thus the metamaterials design represents another application area for the numerical toolbox that, on one hand, successfully describes the behavior of test structures and, on the other hand, has a strong predictive potential.

The use of modern contact mechanical models for describing structure properties and optimizing future materials performance is a new and open area for an exploratory research. It is expected that a combination of strong nonlinearity and the band gap structure induced by internal resonances will result in a material that is (1) highly opaque for sound in certain frequency range, and (2) generate strong higher harmonics so that the acoustic energy is efficiently transferred from low to high frequencies which can be damped easier. Therefore, a possible application of the approach is the creation of a super sound absorber in certain frequency range. In addition, the contact nonlinearity strength can be modulated by external pre-stress applied to the structure thus offering an opportunity of dynamic tuning.

The MMD-FEM numerical toolbox can replace expensive real experimentation by numerical modeling at the level of concept design.

Structures for producing and using the explosive instability effect

The unusual properties of the artificial materials based on contact nonlinearity do not necessarily include sound absorption only. It is possible to do the opposite i.e. to construct a material in which sound amplitude rapidly grows. As we have shown **[Pre-17]**, there exist a particular case when, due to the three-phonon interaction, the sound amplitude experiences an explosive instability i.e. demonstrates theoretically infinite values at some finite moment of time. In the considered example, a Lamb wave propagates in an antiferromagnetic plate in the presence of a harmonically oscillating magnetic field and a shear resonance. In this situation, the magnetic pumping induces a backward phase conjugate Lamb wave. Thus the system supports three phonons: two of the Lamb waves and one of the shear resonant mode. The appropriate synchronization conditions guarantee the appearance of instability i.e. huge amplification of the acoustic waves and extremely efficient energy conversion from the magnetic subsystem into the mechanical one.

The effect can become even more pronounced when material nonlinearity is replaced by contact one modulated by another physical process, e.g. by the magnetic field as in the mentioned example. Similarly, the considered nonlinearity modulation mechanism is possible to extend onto systems of different physical nature and to apply in acousto-electronics, electro- and hydrodynamics and in microsystems designing. The role of the numerical toolbox remains the same; the properties of the future system should be predicted numerically before performing actual experiments with real structures.

Project positioning in the framework of the I-SITE concept

This section concerns the positioning of the planned future activity in the framework of the research management policy in France, in particular, of the concept of *Initiative Science-Innovation-Territoires-Économie* (I-SITE). I-SITE is a special type of research project that can be submitted by a university; at the same time, I-SITE is a label granted to a university whose project has been accepted. The objective is to concentrate research efforts on most critical areas of science from the point of global perspectives. The *Université Lille-Nord-de-France* has been recently granted the I-SITE label for the project related to three fields (called hubs) of primary strategic importance for the society in general:

- Precision Human Health
- Science for a Changing Planet
- Human-Friendly Digital World

The "Precision Human Health" topic concerns precision medicine and, in a more general sense, biomedical research and applications, clinical sciences, molecular biology genetics, bioinformatics, social and environmental sciences. "Science for a Changing Planet" is related to challenges induced by global changes at the level of humanity and the planet, such as climate change, pollution, ecology, energy use, as well as impacts of these issues on the society. "Human-Friendly Digital World" research domain should respond to growing requirements of the human to the security of the private life and to the information safety, to problems related to new modes of life, new methods of teaching and cognition, easy use of information technologies at the personal, industrial or health-care level. This hub can include mathematics, physical sciences, data analysis, sociology, etc.

Within each hub considered as an attraction center for scientific activities, two actions are proposed: sustain and expand. The "sustain" action concerns research areas falling into the scope of one of the three global topics considered. “Expand” means make efforts in order to bring a particular research area closer to one (or more) of hubs (see figure below).

The I-SITE initiative suggests every researcher an excellent opportunity to estimate the social effect of his research and to see how his efforts maps into the global strategic pattern. As such, the MMD-FEM completed study and research project can be seen in the expansion of the Science for a Changing Planet and Human-Friendly Digital World hubs.

Indeed, NDT methods and their numerical support are directly related to transportation and infrastructure safety and risk preventions - the issues of significant importance in the context of growing human-generated impact on the planet and the corresponding need for frugal use of resources. Every year, companies have to withdraw or recall thousands of products due to the presence of unwanted defects, e.g. delaminations and cracks caused by a

malfunction in the production process or by excessive wear during operation. Apart from defects in products, flaws in the machinery itself may cause unplanned shutdowns and often require the replacement of certain components of the equipment. It is obvious that these problems can cause a significant loss of revenue, often making companies face huge deficits. On the other hand, the undetected presence of defects in materials during operation may also reflect on the social level, as it may be the cause of unsafe conditions. A small defect in a crucial material component of a car, plane, ship, building, bridge, etc., has the potential to uncontrollably grow and ultimately lead to a possibly life-threatening accident.

On the other hand, the MMD-FEM research project is also related to the digital applications sphere since it targets an increased digital "transparency" of imaging techniques providing an access to all wave fields and their components and potentially allowing a 3D visualization. This is certainly a new numerical imaging technology at the research and industrial level that could be created once (if) the sought-for agreement between theory and experiment is established in nonlinear acoustics with contact frictional nonlinearity.

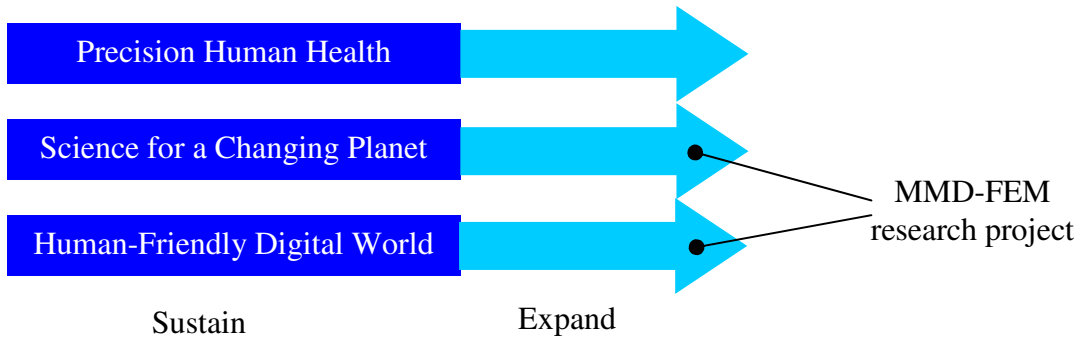

Figure: three research "hubs" and two "actions" proposed in the framework of the I-SITE concept.

References

[Ale-03] Aleshin, V., Gusev, V., Zaitsev, V., 2003. Propagation of initially bi-harmonic acoustic signals in materials with hysteretic quadratic nonlinearity. Ultrasonics International, Granada, Spain.

[Ale-03] Aleshin, V., Gusev, V., Zaitsev, V., 2003. Propagation of initially bi-harmonic acoustic signals in materials with hysteretic quadratic nonlinearity. Ultrasonics International, Granada, Spain.

[Ale-04a] Aleshin, V., Gusev, V., Zaitsev, V., 2004. Propagation of initially bi-harmonic sound waves in a 1D semi-infinite medium with hysteretic non-linearity. Ultrasonics 42, 1053.

[Ale-04a] Aleshin, V., Gusev, V., Zaitsev, V., 2004. Propagation of initially bi-harmonic sound waves in a 1D semi-infinite medium with hysteretic non-linearity. Ultrasonics 42, 1053.

[Ale-04b] Aleshin, V., Van Den Abeele, K., 2004. Micro-potential model for acoustical hysteresis. 18th International Congress on Acoustics, Kyoto, Japan.

[Ale-04b] Aleshin, V., Van Den Abeele, K., 2004. Micro-potential model for acoustical hysteresis. 18th International Congress on Acoustics, Kyoto, Japan.

[Ale-04c] Aleshin, V., Gusev, V., Zaitsev, V., 2004. Propagation of acoustics waves of non-simplex form in a material with hysteretic quadratic nonlinearity: analysis and numerical simulations. J. Comput. Acoust. 12(3), 319-354.

[Ale-04c] Aleshin, V., Gusev, V., Zaitsev, V., 2004. Propagation of acoustics waves of non-simplex form in a material with hysteretic quadratic nonlinearity: analysis and numerical simulations. J. Comput. Acoust. 12(3), 319-354.

[Ale-04d] Aleshin, V., Van Den Abeele, K., 2004. Micro-potential models for stress-strain hysteresis of microcracked media. 9th International Workshop on Nonlinear Elasticity in Materials, Karlskrona, Sweden.

[Ale-04d] Aleshin, V., Van Den Abeele, K., 2004. Micro-potential models for stress-strain hysteresis of microcracked media. 9th International Workshop on Nonlinear Elasticity in Materials, Karlskrona, Sweden.

[Ale-04e] Aleshin, V., Van Den Abeele, K., 2004. Micro-potential model for elasticity of hysteretic materials. 6th International Congress on Mathematical Modeling, Nizhni Novgorod, Russia.

[Ale-04e] Aleshin, V., Van Den Abeele, K., 2004. Micro-potential model for elasticity of hysteretic materials. 6th International Congress on Mathematical Modeling, Nizhni Novgorod, Russia.

[Ale-05a] Aleshin, V., Desadeleer, W., Wevers, M., Van Den Abeele, K., 2005a. Integrated Preisach density as a characterisation for rocks. 10th International Workshop on Nonlinear Elasticity in Materials, Taormina, Italy.
[Ale-05a] Aleshin, V., Desadeleer, W., Wevers, M., Van Den Abeele, K., 2005a. Integrated Preisach density as a characterisation for rocks. 10th International Workshop on Nonlinear Elasticity in Materials, Taormina, Italy.
[Ale-05b] Aleshin, V., Van Den Abeele, K., 2005. Micro-potential model for stress-strain hysteresis of micro-cracked materials. J. Mech. Phys. Solids 53(4), 795.
[Ale-05b] Aleshin, V., Van Den Abeele, K., 2005. Micro-potential model for stress-strain hysteresis of micro-cracked materials. J. Mech. Phys. Solids 53(4), 795.
[Ale-05c] Aleshin, V., Van Den Abeele, K., 2005. Micro-level based constitutive equations in elasticity and acoustics of materials with internal contacts. 12th International Congress on Sound and Vibration, Lisbon, Portugal.
[Ale-05c] Aleshin, V., Van Den Abeele, K., 2005. Micro-level based constitutive equations in elasticity and acoustics of materials with internal contacts. 12th International Congress on Sound and Vibration, Lisbon, Portugal.
[Ale-05d] Aleshin, V., Van Den Abeele, K., 2005. Physical constitutive equations for nonlinear acoustics of materials with internal contacts. 17th International Symposium on Nonlinear Acoustics, State College, Pennsylvania, USA.
[Ale-05d] Aleshin, V., Van Den Abeele, K., 2005. Physical constitutive equations for nonlinear acoustics of materials with internal contacts. 17th International Symposium on Nonlinear Acoustics, State College, Pennsylvania, USA.
[Ale-05e] Aleshin, V., Van Den Abeele, K., 2005. Microcontact-based theory for acoustics in microdamaged materials. 10th International Workshop on Nonlinear Elasticity in Materials, Taormina, Italy.
[Ale-05e] Aleshin, V., Van Den Abeele, K., 2005. Microcontact-based theory for acoustics in microdamaged materials. 10th International Workshop on Nonlinear Elasticity in Materials, Taormina, Italy.
[Ale-06a] Aleshin, V., Van Den Abeele, K., 2006. Micro-potential model for stress-strain hysteresis and PM space, in “The universality of nonclassical nonlinearity, with applications to NDE and Ultrasonics", Ed. P.P Delsanto, Springer, New York, Chapter 11.
[Ale-06a] Aleshin, V., Van Den Abeele, K., 2006. Micro-potential model for stress-strain hysteresis and PM space, in “The universality of nonclassical nonlinearity, with applications to NDE and Ultrasonics", Ed. P.P Delsanto, Springer, New York, Chapter 11.

[Ale-06b] Aleshin, V., Van Den Abeele, K., 2006. Adhesion hysteretic mechanism for nonlinear acoustics of solids with internal contacts. 8ème Congrès Français d'Acoustique, 2006, Tours, France.
[Ale-06b] Aleshin, V., Van Den Abeele, K., 2006. Adhesion hysteretic mechanism for nonlinear acoustics of solids with internal contacts. 8ème Congrès Français d'Acoustique, 2006, Tours, France.
[Ale-06c] Aleshin., V., 2006. Adhesion and friction models for nonlinear elasticity of materials with internal contacts. International colloquium devoted to 25 years anniversary of Le Mans Laboratory of Acoustics, Le Mans, France.
[Ale-06c] Aleshin., V., 2006. Adhesion and friction models for nonlinear elasticity of materials with internal contacts. International colloquium devoted to 25 years anniversary of Le Mans Laboratory of Acoustics, Le Mans, France.
[Ale-06d] Aleshin, V., Van Den Abeele, K., 2006. Physical friction-based model for a tensorial description of stress-strain in materials with internal contacts. 11th International Workshop on Nonlinear Elasticity in Materials, 2006, Sorrento, Italy.
[Ale-06d] Aleshin, V., Van Den Abeele, K., 2006. Physical friction-based model for a tensorial description of stress-strain in materials with internal contacts. 11th International Workshop on Nonlinear Elasticity in Materials, 2006, Sorrento, Italy.
[Ale-07a] Aleshin, V., Van Den Abeele, K., 2007. Microcontact-based theory for acoustics in microdamaged materials. J. Mech. Phys. Solids 55, 366-390.
[Ale-07a] Aleshin, V., Van Den Abeele, K., 2007. Microcontact-based theory for acoustics in microdamaged materials. J. Mech. Phys. Solids 55, 366-390.
[Ale-07b] Aleshin, V., Van Den Abeele, K., 2007.Constitutive models for solids containing rough cracks: from micro to macro. 4th International Conference on Emerging Technologies in Non-Destructive Testing, Stuttgart, Germany.
[Ale-07b] Aleshin, V., Van Den Abeele, K., 2007.Constitutive models for solids containing rough cracks: from micro to macro. 4th International Conference on Emerging Technologies in Non-Destructive Testing, Stuttgart, Germany.
[Ale-07c] Aleshin, V., Van Den Abeele, K., 2007. Constitutive models for nonlinear elasticity in materials with microstructure. Ecole Thématique “Acoustique Et Ondes Non Linéaires Et Applications”, Oléron, France.
[Ale-07c] Aleshin, V., Van Den Abeele, K., 2007. Constitutive models for nonlinear elasticity in materials with microstructure. Ecole Thématique “Acoustique Et Ondes Non Linéaires Et Applications”, Oléron, France.

[Ale-07d] Aleshin, V., Van Den Abeele, K., 2007. Friction in unconforming grain contacts as a mechanism for tensorial stress-strain hysteresis. J. Mech. and Phys. Solids 55, 765-787.
[Ale-07d] Aleshin, V., Van Den Abeele, K., 2007. Friction in unconforming grain contacts as a mechanism for tensorial stress-strain hysteresis. J. Mech. and Phys. Solids 55, 765-787.
[Ale-07e] Aleshin, V., Gusev, V., Tournat, V., 2007. Acoustic modes propagating along the free surface of granular media. J. Acoust. Soc. Am. 121 (5), 2600-2611.
[Ale-07e] Aleshin, V., Gusev, V., Tournat, V., 2007. Acoustic modes propagating along the free surface of granular media. J. Acoust. Soc. Am. 121 (5), 2600-2611.
[Ale-08] Aleshin, V., Desadeleer, W., Van Den Abeele, K., 2008. Characterization of hysteretic elasticity in materials using the integrated Preisach density. Int. J. Nonlin. Mech. 43, 151-163.
[Ale-08] Aleshin, V., Desadeleer, W., Van Den Abeele, K., 2008. Characterization of hysteretic elasticity in materials using the integrated Preisach density. Int. J. Nonlin. Mech. 43, 151-163.
[Ale-09a] Aleshin, V., Van Den Abeele, K., 2009. Preisach analysis of the Hertz-Mindlin system. J. Mech. Phys. Solids 57, 657-672.
[Ale-09a] Aleshin, V., Van Den Abeele, K., 2009. Preisach analysis of the Hertz-Mindlin system. J. Mech. Phys. Solids 57, 657-672.
[Ale-09b] Aleshin, V., Van Den Abeele, K., 2009. Is there physics behind the PM-space? 14th International Conference on Nonlinear Elasticity in Materials, Lisbon, Portugal.
[Ale-09b] Aleshin, V., Van Den Abeele, K., 2009. Is there physics behind the PM-space? 14th International Conference on Nonlinear Elasticity in Materials, Lisbon, Portugal.
[Ale-10] Aleshin, V., Van Den Abeele, K., 2010. General solutions to the contact problem of two spheres with friction. 15th International Conference on Nonlinear Elasticity in Materials, Otranto, Italy.
[Ale-10] Aleshin, V., Van Den Abeele, K., 2010. General solutions to the contact problem of two spheres with friction. 15th International Conference on Nonlinear Elasticity in Materials, Otranto, Italy.
[Ale-11a] Aleshin, V., Van Den Abeele, K., 2011 Frictional contact of two spheres for arbitrary 2D loading: memory diagrams and Preisach analysis. 16th International Conference on Nonlinear Elasticity in Materials, Prague, Czech Republic.
[Ale-11a] Aleshin, V., Van Den Abeele, K., 2011 Frictional contact of two spheres for arbitrary 2D loading: memory diagrams and Preisach analysis. 16th International Conference on Nonlinear Elasticity in Materials, Prague, Czech Republic.

[Ale-11b] Aleshin, V., Van Den Abeele, K., 2011 Frictional contact of two spheres for arbitrary 2D loading: memory diagrams and Preisach analysis. Proceedings of Meetings on Acoustics, 2011, Vol. 13, 045004.

[Ale-11b] Aleshin, V., Van Den Abeele, K., 2011 Frictional contact of two spheres for arbitrary 2D loading: memory diagrams and Preisach analysis. Proceedings of Meetings on Acoustics, 2011, Vol. 13, 045004.

[Ale-11c] Aleshin, V., Van Den Abeele, K., 2011. Frictional contact of two spheres for arbitrary 2D loading. 20ème Congrès Français de Mécanique, Besançon, France.

[Ale-11c] Aleshin, V., Van Den Abeele, K., 2011. Frictional contact of two spheres for arbitrary 2D loading. 20ème Congrès Français de Mécanique, Besançon, France.

[Ale-12a] Aleshin, V., Van Den Abeele, K., 2012. Hertz-Mindlin problem for arbitrary oblique 2D loading: General solution by memory diagrams. J. Mech. Phys. Solids 60, 14-36.

[Ale-12b] Aleshin, V, 2012. On the origin of the contact acoustical nonlinearity: general solutions to the mechanical contact problem. GDRE workshop "Nonlinearities in acoustics, specially contact nonlinearities", Oléron, France.

[Ale-12c] Aleshin, V, 2012. General solutions to the mechanical contact problem. GDR MePhy workshop, 2012, Agay, France.

[Ale-12d] Aleshin, V, 2012. Frictional contact of solids of arbitrary shapes with arbitrary loading histories. 17th International Conference on Nonlinear Elasticity in Materials, Cefalu, Italy.

[Ale-13a] Aleshin, V., Van Den Abeele, K., 2013. General solution to the Hertz-Mindlin problem via Preisach formalism. Int. J. Non-Linear Mech. 49, 15–30.

[Ale-13b] Aleshin, V., Van Den Abeele, K., Bou Matar., O., 2013. On general solutions to the mechanical contact problem with friction: extending the method of memory diagrams. 18th International Conference on Nonlinear Elasticity in Materials, Ascona, Switzerland.

[Ale-14a] Aleshin, V., Bou Matar, O., 2014. Elastic frictional contact problem for arbitrary surface shapes and arbitrary 2D loading history: method of memory diagrams. Proc. Contact Mechanics International Symposium, Abu Dhabi, February 3-5, 2014.

[Ale-14b] Aleshin, V., 2014. Method of memory diagrams for solving frictional contact problems in 3D. 19th International Conference on Nonlinear Elasticity in Materials, Fréjus, France.

[Ale-15a] Aleshin, V., 2015. Method of memory diagrams for solving frictional contact problems and its application to materials with contact nonlinearity. Workshop on Advances in Tribology: Science, Technology and Education, 2015, Karlovy Vary, Czech Republic.

[Ale-15b] Aleshin, V., Bou Matar., O., 2015. Contact mechanical problem for arbitrary 3D loading histories. 12th International Conference on Surface Effects and Contact Mechanics, Valencia, Spain.

[Ale-15c] Aleshin, V., Bou Matar., O., 2015. Frictional contact of solids subject to arbitrary loading history in 3D. GDR MePhy workshop, Agay, France.

[Ale-15d] Aleshin, V., Bou Matar., O., 2015. Contact mechanical models for nonlinear elasticity in materials. 20th International Conference on Nonlinear Elasticity in Materials, Bruges, Belguim.

[Ale-15e] Aleshin, V., Bou Matar., O., Van Den Abeele, K., 2015. Method of memory diagrams for mechanical frictional contacts subject to arbitrary 2D loading, Int. J. Sol. Struct. 60-61, 84-95.

[Ale-16] Aleshin, V., Bou Matar, O., 2016. Solution to the frictional contact problem via the method of memory diagrams for general 3D loading histories. Physical Mesomechanics 19, 130-135.

[Ale-17]. Aleshin, V.V., Delrue, S., Bou Matar, O., Van Den Abeele, K., 2017. Modelling of acoustic waves and vibrations in materials containing frictional cracks with rough faces. Workshop "New Mathematics for a Safer World: Wave Propagation in Heterogeneous Materials", Edinburgh, UK.

[Ale-18] Aleshin, V.V., Delrue, S., Trifonov, A., Bou Matar, O., Van Den Abeele, K., 2018. Two dimensional modeling of elastic wave propagation in solids containing cracks with rough surfaces and friction - Part I: Theoretical background. Ultrasonics, 2018, Vol. 82, 11-18.

[And-04] Andreotti, B., 2004. The Song of Dunes as a Wave-Particle Mode Locking, Phys. Rev. Lett. 93, 238001.

[Ber-98] Bertotti, G., 1998. Hysteresis in magnetism: for physicists, materials scientists, and engineers. Academic Press San Diego.

[Bil-68] Bilby, B. A., Eshelby, J. D. 1968. Dislocations and the theory of fracture. In: Fracture, an Advanced Treatise, Vol. 2, ed. H. Liebowitz. New York.: Academic Press.

[Biw-04] Biwa, S., Nakajima, S., Ohno, N., 2004. On the acoustic nonlinearity of solid-solid contact with pressure-dependent interface stiffness. Journal of Applied Mechanics 71(4), 508–515.

[Boi-97] Boitnott, G.N., 1997. An experimental characterization of the non-linear rheology of rock, Int. J. Rock Mech. Min. Sci. 34, 3-4.

[Bol-13] Boltachev, G.Sh., Aleshin, V., 2013. Shift and torsion contact problems for arbitrary axisymmetric normal stress distributions. Int. J. Solids Struct. 50, 2894–2900.

[Bou-13] Bou Matar, O., Guerder, P.-Y., Zhou, H., Aleshin, V., 2013. Nonlinear elastodynamic simulations using the Discontinuous Galerkin Finite Element Method on graphics processors. 18th International Conference on Nonlinear Elasticity in Materials, Ascona, Switzerland.

[Bow-39] Bowden, F., Tabor, D., 1939. The area of contact between stationary and between moving surfaces. Proceedings of the Royal Society of London: Mathematical, Physical and Engineering Sciences 169, 391–413.

[Bre-02] Brent, R.P., 2002. Algorithms for Minimization without Derivatives, Dover.

[Car-08] Carbone, G., Bottiglione, F., 2008. Asperity contact theories: do they predict linearity between contact area and load? J. Mech. Phys. Solids 56, 2555-2572.

[Cat-38] Cattaneo, C., 1938. Sul contatto di due corpi elastici: distribuzione locale degli sforzi. Accad. Lincei Rend. 27(6), 342–348.

[Cha-01] Chapman, D.M.F, Godin, O.A., 2001. Dispersion of interface waves in sediments with power-law shear speed profiles. II. Experimental observations and seismo-acoustic inversions, J. Acoust. Soc. Am. 110, 1908.

[Cia-98a] Ciavarella, M., 1998. The generalized Cattaneo partial slip plane contact problem. I - Theory, II - Examples. Int. J. Solids Struct. 35, 2349-2362.

[Cia-98b] Ciavarella, M., 1998. Tangential loading of general 3D contacts. ASME J. Appl. Mech. 65, 998–1003.

[COM-15a] COMSOL AB, Structural Mechanics Module, User's Guide, COMSOL Multiphysics v. 5.2 (Stockholm, Sweden, 2015).

[COM-15b] COMSOL AB, LiveLink for MATLAB, User's Guide, COMSOL Multiphysics v. 5.2 (Stockholm, Sweden, 2015).

[Dav-38] Davidenkov, N., 1938. Energy dissipation in vibrations, Journal of Technical Physics 8.

[Del-16a] Delrue, S., Aleshin, V.V., Bou Matar, O., Van Den Abeele, K., 2016. Modeling of elastic wave propagation in samples containing cracks with friction. 21th International Conference on Nonlinear Elasticity in Materials, Lake Tahoe, California, USA.

[Del-16b] Delrue, S., Aleshin, V.V., Bou Matar, O., Van Den Abeele, K., 2016. 2D modeling of elastic wave propagation in solids containing closed cracks with friction. COMSOL Conference 2016 Munich, Munich, Germany.

[Del-17a] Delrue, S., Aleshin, V.V., Sorensen, M., De Lathauwer, L., 2017. Simulation study of the localization of a near-surface crack using an air-coupled ultrasonic sensor array, Sensors 17 (4), 1-21.

[Del-17b] Delrue, S., Aleshin, V.V., 2017. Numerical code for describing acoustic wave propagation in solids containing cracks of known geometry. 24th International Congress on Sound and Vibration, London, UK.

[Del-17c] Delrue, S., Aleshin, V.V., 2017. 2D modeling for acoustic waves in solids with frictional cracks. 23ème Congrès Français de Mécanique, Lille, France.

[Del-18] Delrue, S., Aleshin, V.V., Truyaert, K., Bou Matar, O., Van Den Abeele, K., 2018. Two dimensional modeling of elastic wave propagation in solids containing cracks with rough surfaces and friction – Part II: Numerical implementation. Ultrasonics 82, 19-30.

[Dey-13] Deymier, P.A., 2013. Acoustic Metamaterials and Phononic Crystals, Springer Heidelberg New York.

[Dor-16] Dormieux, L., Kondo, D., 2016. Micromechanics of Fracture and Damage John Wiley & Sons.

[Dro-04] Drozd, J.J., 2004. Computer Simulation of Granular Matter: A Study of An Industrial Grinding Mill, Thesis, Univ. Western Ontario, Canada.

[eng-17] http://www.engineershandbook.com/Tables/frictioncoefficients.htm, accessed on Sept. 14, 2017.

[Fin-11] Fintland, T.W., 2011. Measurements of young's modulus on rock samples at small amplitude and low frequency, M.Sc. thesis in Physics and Mathematics, Norwegian University of Science and Technology, Department of Physics.

[Ful-75] Fuller, K. N. G., Tabor, D., 1975. The effect of surface roughness on the adhesion of elastic solids. Proc. R. Soc. Lond. A 345, 327.

[Gal-61] Galin, L.A., 1961. Contact Problems in the Theory of Elasticity. Raleigh, North Carolina State College.

[God-90] Goddard, J.D., 1990. Nonlinear elasticity and pressure dependent wave speed in granular media, Proc. R. Soc. London, Ser. A 430, 105-131.

[Gol-09] Golick, L.A., Daniels, K.E., 2009. Mixing and segregation rates in sheared granular materials, Physical Review E. 80: 042301

[Gra-56] Granato, A., Lucke, K., 1956. Theory of mechanical damping due to dislocations, J. App. Phys. 27, 583-593.

[Gre-66] Greenwood, J.A., Willianson, J.B.R., 1966. Contact of nominally flat surfaces. Proc. Roy. Soc. London A, 295(1442), 300-319.

[Gue-15] Guerder, P.-Y., 2015. Theoretical and numerical study of nonlinear phononic crystals, PhD thesis, École Centrale de Lille and University of Arizona.

[Gus-02] Gusev, V., Aleshin, V., 2002. Strain wave evolution equation for nonlinear propagation in materials with mesoscopic mechanical elements. J. Acoust. Soc. Am. 112(6), 2666.

[Gus-06a] Gusev, V., Aleshin, V., Tournat, V., 2006, Acoustic waves in an elastic channel near the free surface of a granular medium. Dygram 2006 Workshops: Granular Dynamics, Jamming, Rheology, and Instabilities, Rennes, France.

[Gus-06b] Gusev, V., Aleshin, V., Tournat, V., 2006. Acoustic waves in an elastic channel near the mechanically free surface of granular media. Phys. Rev. Lett. 96, 214301.

[Gus-06c] Gusev, V., Aleshin, V., Tournat, V., 2006. Dispersion des ondes acoustiques transverses horizontales en sub-surface de milieux granulaires non consolidés. 8ème Congrès Français d'Acoustique, Tours, France.

[Hel-01] Helbig, K., and P. N. J. Rasolofosaon, 2001. A theoretical paradigm for describing hysteresis and nonlinear elastricity in arbitrary anisotropic rocks. In Anisotropy 2000, eds. Ikelle, L., and Gangi, A., Soc. Expl. Geophys., Open File Publ., 6, 383-398.

[Hel-98] Helbig, K., 1998. A formalism for the consistent description of non-linear elasticity of anisotropic media. Ed. P. N. J. Rasolofosaon, Rev. Inst. Fran. Pét., 53, 693-708.

[Hin-05] Hinrichsen, H., Wolf, D.E., Eds, 2005. The Physics of Granular Media, chapter 13, Wiley.

[Hla-13] Hladky-Hennion, A.-C., Vasseur, J.O., Haw, G., Croënne, C., Haumesser, L., Norris, A.N., 2013. Negative refraction of acoustic waves using a foam-like metallic structure, Appl. Phys. Lett. 102, 144103.

[Hyu-07] Hyun, S., Robbins, M.O., 2007. Elastic contact between rough surfaces: Effect of roughness at large and small wavelengths. Tribol. Int. 40, 1413-1422.

[Ins-07] Inserra, C., Tournat, V., Aleshin, V., Gusev, V., Catagnède, B., 2007. On some aspects of acoustic diagnostics of unconsolidated granular media. 4th International Conference on Emerging Technologies in Non-Destructive Testing, Stuttgart, Germany. [Izr-85] Israelachvili, J.N., 1985. Intermolecular and Surface Forces, Academic Press.

[Jac-07] Jacob, X., Tournat, V., Aleshin, V., Gusev, V., 0227. Evaluation of the mechanical properties of granular media at low pressures. International Congress on Acoustics, Madrid, Spain.

[Jac-08a] Jacob, X., Aleshin, V., Tournat, V., Leclaire, P., Lauriks, W., Gusev, V., 2008. Acoustic waves propagation along mechanically free surface of unconsolidated granular porous media. Acoustics'08, Paris, France.

[Jac-08b] Jacob, X., Aleshin, V., Tournat, V., Leclaire, P., Lauriks, W., Gusev, V.E., 2008. Acoustic probing of the jamming transition in an unconsolidated granular medium. Phys. Rev. Lett. 100, 158003.

[Jäg-03] Jäger, J., 2003. Properties of equal bodies in contact with friction. Int. J. Solids Struct. 40, 5051–5061.

[Jäg-95] Jäger, J., 1995. Axisymmetric bodies of equal material in contact under torsion or shift. Archive of Applied Mechanics 65, 478-487.

[Jäg-97] Jäger, J., 1997. Half-planes without coupling under contact loading. Archive of Applied Mechanics 67, 247–259.

[Jäg-98] Jäger, J., 1998. A new principle in contact mechanics. J. Tribol. 120(4), 677-684.

[Joh-85] Johnson, K.L., 1985. Contact Mechanics. Cambridge University Press, Cambridge.

[Kac-13] Kachanov, M., Sevostianov, I, (ed.), 2013. Springer Dordrecht, Heidelberg, New York, London.

[Kra-83] Krasnosel'skii, M.A. and Pokrovskii, A.V., 1983. Systems with Hysteresis. Nauka, Moscow (or 1989, Springer, Berlin).

[Lan-93] Landau, L.D., Lifshitz, E.M., 1993. Theory of Elasticity. Pergamon Press, Oxford.

[Law-98] Lawn, B.R., D.B. Marshall, 1998. Nonlinear stress-strain curves for solids containing closed cracks with friction. J. Mech. Phys. Solids 46(1), 85-113.

[Lec-07a] Leclaire, P., Jacob, X., Aleshin, V., Tournat, V., Dazel, O., Allard, J.-F., Lauriks, W., Gusev, V., 2007. Guided acoustic modes for testing surface layers of unconsolidated granular media. 4th International Conference on Emerging Technologies in Non-Destructive Testing, Stuttgart, Germany.

[Lec-07b] Leclaire, P., Tournat, V., Dazel, O., Aleshin, V., Lauriks, W., Allard, J.-F., Gusev, V., 2007. Guided acoustic waves near the free surface of unconsolidated granular materials. International Congress on Acoustics, Madrid, Spain.

[Leo-13] Leonard, A., Fraternali, F., Daraio, C., 2013. Directional wave propagation in a highly nonlinear square packing of spheres, Experimental Mechanics 53, 327-337.

[Leo-14a] Leonard, A., Ponson, L., Daraio, C., 2014. Exponential stress mitigation in structured granular composites, Extreme Mechanics Letters 1, 23–28.

[Leo-14b] Leonard, A., Chong, C., Kevrekidis, P.G., Daraio, C., 2014. Traveling waves in 2D hexagonal granular crystal lattices, Granular Matter 16, 531-542.

[Li-12] Li, F., Ngo, D., Yang, J., Daraio, C., 2012. Tunable phononic crystals based on cylindrical Hertzian contact, Appl. Phys. Lett. 101, 171903.

[Mak-04] Makse, H.A., Gland, N., Johnson, D.L., Schwartz, L.M., 2004. Granular packings: nonlinear elasticity, sound propagation, and collective relaxation dynamics, Phys. Rev. E 70, 061302.

[May-85] Mayergoyz, I.D., 1985. Hysteretic models from the mathematical and control theory points of view, J. Appl. Phys. 57(1), 3803-3805.

[May-91] Mayergoyz, I.D. 1991. Mathematical Models of Hysteresis and Their Applications. Springer-Verlag.

[McC-96] McCall, K., and Guyer, R., 1996. A new theoretical paradigm to describe hysteresis, discrete memory and nonlinear elastic wave propagation in rock, Nonlinear processes in geophysics 3, 89-101.

[Min-49] Mindlin, R. D., 1949. Compliance of elastic bodies in contact. J. Appl. Mech. 16, 259–268.

[Min-53] Mindlin, R.D., Deresiewicz, H., 1953. Elastic spheres in contact under varying oblique forces. J. Appl. Mech., Trans. ASME 20, 327-344.

[Mue-98] Mueth, D., Jaeger, H., Nagel, S., 1998. Force distribution in a granular medium, Physical Review E 57 (3): 3164.

[Mun-92] Munisamy, R.L., Hills, D.A., Nowell, D., 1992. Contact of similar and dissimilar elastic spheres under tangential loading. In: Contact Mechanics, Int. Syrup., 447-461. Presses polytechniques et universitaires romandes, Lausanne.

[Mun-94] Munisamy, R.L., Hills, D.A., Nowell, D., 1994 Static axisymmetrical Hertzian contacts subject to shearing forces. ASME J. Appl. Mech. 61, 278–283.

[Naz-00] Nazarov, V.E., Kolpakov, A.B., 2000. Experimental investigation of nonlinear acoustic phenomena in polycrystalline zinc, J. Acoust. Soc. Am. 107, 1915-1921.

[Naz-15] Nazarov, V, Radostin, A., 2015. Nonlinear Acoustic Waves in Micro-Inhomogeneous Solids, Wiley.

[Nem-01] Nemati, K.M., Stroeven, P., 2001. Stereological analysis of micromechanical behavior of concrete, Materials and Structures 34 (242), 486-494.

[Nes-01] Nesterenko, V.F., 2001. Dynamics of Heterogeneous Materials, Springer, New York.

[Nor-15] Norris, A., 2015. Acoustic cloaking, Acoustic Today 11(1), 38-46.

[Oni-73] Onions, R.A., Archard, J.F, 1973. The contact of surfaces having a random structure. J. Phys. D 6, 289-304.

[Ort-92] Ortin, J., 1992. Preisach modeling of hysteresis for a pseudoelastic Cu-Zn-Al single crystal. J. Appl. Phys. 71(3), 1454.

[Ost-01] Ostrovsky, L.A., Johnson, P. A., 2001. Dynamic nonlinear elasticity in geomaterials, Rivista del Nuovo Cimento, 24 (7), 1-46.

[Pag-10] Paggi, M., Ciavarella, M., 2010. The coefficient of proportionality between real contact area and load, with new asperity models. Wear 268, 1020–10.

[Pag-14] Paggi, M., Pohrt, R., Popov, V., 2014. Partial-slip frictional response of rough surfaces, Scientific Reports 4, 5178.

[Per-02] Persson, B., Bucher, F., Chiaia, B., 2002. Elastic contact between random rough surfaces: Comparison of theory with numerical results. Phys. Rev. B 65(18), 184106.

[Poh-12] Pohrt, R., Popov, V., 2012. Normal contact stiffness of elastic solids with fractal rough surfaces. Phys. Rev. Lett. 108, 104301.

[Poh-13] Pohrt, R., Popov, V., 2013, Contact stiffness of randomly rough surfaces, Scientific Reports 3, 3293.

[Poh-15] Pohrt, R., personal communication.

[Pop-13] Popov, V.L., 2013. Method of reduction of dimensionality in contact and friction mechanics: A linkage between micro and macro scales. Friction 1(1), 41–62.

[Pop-15] Popov, V.L., Heß, M., 2015. Method of Dimensionality Reduction in Contact Mechanics and Friction, Springer Heidelberg New York Dordrecht London.

[Pre-17] Preobrazhensky, V.L., Aleshin, V.V., Pernod, Ph., 2017. Resonance of Feshbach-type and explosive instability of magnetoelastic waves in solids. Wave Motion, submitted, also in: Preobrazhensky, V.L., Aleshin, V.V., Pernod, Ph.,. Feshbach resonance and explosive instability of magnetoelastic waves. 24th International Congress on Sound and Vibration, 2017, London, UK.

[Pre-35] Preisach, F., 1935. Über die magnetische Nachwirkung. Z. Phys. 94, 277.

[Rud-76] Rudenko, O. V., Soluyan, S. I., 1976. Theoretical Foundations of Nonlinear Acoustics. Consultants Bureau, New York.

[Sac-80] Sachs, W, Pao, Y., 1980. On the determination of phase and group velocities of dispersive waves in solids, J. Appl. Phys. 49, 4320-4327.

[Sca-08] Scalerandi, M., Gliozzi, A., Bruno, C., Masera, D., Bocca, P., 2008. A scaling method to enhance detection of a nonlinear elastic response, Appl. Phys. Lett. 92, 101912.

[Sne-65] Sneddon, I.N., 1965. The relation between load and penetration in the axisymmetric Boussinesq problem for a punch of arbitrary profile. Int. J. Eng. Sci. 3, 47-57.

[Ten-04] TenCate, J.A., Pasqualini, D., Habib, S., Heitmann, K., Higdon, D., Johnson, P.A., 2004. Nonlinear and nonequilibrium dynamics in geomaterials. Phys. Rev. Lett. 93(6), 065501.

[Tik-77] Tikhonov, A.N. Arsenin, V.A., 1977. Solutions of Ill-posed Problems. Winston & Sons, Washington.

[Tou-04] Tournat, V., Zaitsev, V., Gusev, V., Nazarov, V., Béquin, P., Castagnède, B., 2004. Probing weak forces in granular media through nonlinear dynamic dilatancy: clapping contacts and polarization anisotropy, Phys. Rev. Lett. 92, 085502.

[Tou-07a] Tournat, V., Gusev, V., Aleshin, V., Jacob, X., Inserra, C., 2007. Acoustique non linéaire et milieux granulaires. École Thématique "Acoustique Et Ondes Non Linéaires Et Applications", Oléron, France.

[Tou-07b] Tournat, V., Gusev, V., Jacob, X., Inserra, C., Aleshin, V., 2007. Linear and nonlinear acoustic waves in unconsolidated granular media: opportunities for new fundamental wave processes and quantitative evaluation. Statics and Dynamics of Granular Media and Colloidal Suspensions, Naples, Italy.

[Tut-98] Tutuncu, A.N., Podio, A.L., Sharma, M.M., 1998. Nonlinear viscoelastic behavior of sedimentary rocks; Part II, Hysteresis effects and influence of type of fluid on elastic moduli, Geophysics 63(1), 195-303.

[Van-00a] Van Den Abeele, K., De Visscher, J., 2000a. Damage assessment in reinforced concrete using spectral and temporal nonlinear vibration techniques, Cement and Concrete Research 30(9), 1453-1464.

[Van-00b] Van Den Abeele, K., Carmeliet, K., TenCate, J.A., Johnson, P.A., 2000. Nonlinear Elastic Wave Spectroscopy (NEWS) techniques to discern material damage, Part II: Single Mode Nonlinear Resonant Acoustic Spectroscopy (SIMONRAS), Res. Nondestr. Eval. 12(1), 31-42.

[Van-03] Van Den Abeele, K., Schubert, F., Aleshin, V. 2003. Modeling of wave distortion phenomena in media with localized microdamage. 5th World Congress on Ultrasonics, Paris, France.

[Van-04] Van Den Abeele, K, Schubert, F, Aleshin, V, Windels, F., Carmeliet, J., 2004. Resonant bar simulations in media with localized damage. Ultrasonics. 42, 1017.

[Van-05a] Van Den Abeele, K., and Vanaverbeke, S., 2005. Multiscale approach and simulations of wave propagation and resonance in media with localized microdamage: 1D and 2D cases, in "The universality of nonclassical nonlinearity with applications to NDE and Ultrasonics", Ed. P.P. Delsanto, Chapter 12.

[Van-05b] Van Den Abeele, K., Katkowski, T., and Mattei, C., 2005b. Nonlinear Acoustic and Ultrasonic NDT of Aeronautical Components, Proceedings of the 17th International Symposium on Nonlinear Acoustics, State College, PA.

[Van-06]Van Den Abeele, K., Vanaverbeke, S., Aleshin, V., 2006. Multiscale approach to nonlinear and hysteretic elastodynamics in one- and two dimensions, in "The universality of

nonclassical nonlinearity, with applications to NDE and Ultrasonics", Springer, New York, Chapter 9.

[Van-12] Van Den Abeele, K, Delrue, S. Haupert, S., Aleshin, V., 2012. Modeling nonlinear response from distributed damage and kissing bonds. Proceedings of Meetings on Acoustics 16, 045020.

[Whi-70] Whitehouse, D.J., and Archard, J.F., 1970. The properties of random surfaces of significance in their contact. Proc. Roy. Soc. London A 316(1524), 97-121.

[Yua-15] Yuan, M., Zhang, J., Song, S., Kim, H., 2015. Numerical simulation of Rayleigh wave interaction with surface closed cracks under external pressure. Wave Motion 57, 143–153).

[Zai-00] Zaitsev, V., Sas, P., 2000. Elastic moduli and dissipative properties of microinhomogeneous solids with isotropically oriented defects, Acustica-Acta Acustica 86, 216-228.

[Zig-14] Zigoneanu, L., Popa, B.-I, Cummer, S., 2014. Three-dimensional broadband omnidirectional acoustic ground cloak, Nature Materials 13, 352–355.